

ULTRAFAST ELECTRON DYNAMICS
IN MOLECULES WITHIN
DENSITY-MATRIX-BASED
CONFIGURATION INTERACTION
FRAMEWORK

Kumulative Dissertation

zur Erlangung des akademischen Grades
doctor rerum naturalium (Dr. rer. nat.)
der Mathematisch-Naturwissenschaftlichen Fakultät
der Universität Rostock

vorgelegt am 19. Juni 2023 in Rostock

von

VLADISLAV KOCHETOV,

geboren am 29. Mai 1995 in Rostow-am-Don

https://doi.org/10.18453/rosdok_id00004451

Die vorliegende kumulative Dissertation wurde am 22.09.2023 im Rahmen eines öffentlichen wissenschaftlichen Kolloquiums am Institut für Physik der Universität Rostock erfolgreich verteidigt.

Gutachter der kumulativen Dissertation:

Prof. Dr. Sergey I. Bokarev	Universität Rostock
Prof. Dr. Oliver Kühn	Universität Rostock
Prof. Dr. Jean-Christophe Tremblay	Université de Lorraine

ABSTRACT

The rapid advancement of high-brilliant laser sources has opened up new avenues for studying isolated electron dynamics at sub-femtosecond and attosecond timescales. This progress enables the experimental verification of a number of processes and effects that were previously inaccessible.

The main goal of this thesis was to develop a general framework to numerically simulate a range of time-dependent phenomena in molecules starting from charge migration to describing non-linear spectroscopy. During this work, the program module RhoDyn, intended to study ultrafast electron dynamics within the density-matrix-based time-dependent restricted active space configuration interaction framework, has been implemented as a part of the open-source OpenMOLCAS project. The formalism employed in this study provides a comprehensive treatment of electron correlation and spin-orbit coupling effects. It also naturally incorporates energy and phase relaxation effects due to nuclei, photoionization, Auger decay processes, and other dissipative terms, enabling a thorough exploration of the electron dynamics in small molecules.

Another point of this thesis is to present the results of work concerning photon-induced ultrafast spin dynamics being theoretically modeled within the implemented framework of ab-initio calculations. The effect of chemical structure on the ultrafast spin-flip dynamics in core-excited states of transition metal complexes has been studied. It was shown that slight variations in the coordination sphere do not lead to qualitative differences in dynamics, whereas the nature of the central atom is more critical. Detailed analysis of spin-orbit coupling-driven dynamics in core-excited states, based on the preselection of states and utilizing the Wigner-Eckart theorem, is conducted to outline and facilitate future experimental investigations.

Keywords: *Multi-reference/multi-configurational methods, non-equilibrium dynamics, open quantum systems, highly-excited/core-excited states, density matrix, highly correlated states, many-body dynamics, time-dependent configuration interaction.*

ZUSAMMENFASSUNG

Der rasante Fortschritt hochbrillanter Laserquellen eröffnet neue Möglichkeiten für die Erforschung isolierter Elektronendynamiken auf der Sub-Femtosekunden- und Attosekundenzeitskala. Dieser Fortschritt ermöglicht die experimentelle Bestätigung einer Vielzahl von Prozessen und Effekten, die zuvor unzugänglich waren.

Das Hauptziel dieser Arbeit bestand darin, einen allgemeinen Rahmen zur numerischen Simulation zu entwickeln, der zeitabhängigen Phänomene in Molekülen von Ladungsmigration bis zur nichtlinearen Spektroskopie umfasst. Im Laufe dieser Arbeit wurde das Programmmodul RhoDyn als Teil des Open-Source-Projekts OpenMOLCAS implementiert, das zur Untersuchung ultraschneller Elektronendynamiken im Rahmen der dichtematrixbasierten zeitabhängigen Konfigurationswechselwirkung im eingeschränkten aktiven Raum entwickelt wurde. Der in dieser Studie verwendete Formalismus bietet eine umfassende Behandlung der Elektronenkorrelation und des Spin-Bahn-Kopplungseffekts. Es integriert auch auf natürliche Weise nichtadiabatische Effekte, Photoionisation, Auger-Zerfallsprozesse und andere dissipative Terme, was eine gründliche Erforschung der Elektronendynamik von kleinen Molekülen ermöglicht.

Ein weiterer Aspekt dieser Arbeit besteht darin, die Ergebnisse der theoretischen Simulation der photoninduzierten ultraschnellen Spin-Dynamik innerhalb des implementierten Rahmenwerks ab-initio Berechnungen vorzustellen. Der Einfluss der chemischen Struktur auf die ultraschnelle Spinflipp-Dynamik in kernangeregten Zuständen von Übergangsmetallkomplexen wurde untersucht. Es wurde gezeigt, dass geringfügige Variationen in der Koordinationssphäre keine qualitativen Unterschiede in der Dynamik bewirken, während die Art des zentralen Atoms entscheidend ist. Eine detaillierte Analyse der durch Spin-Bahn-Kopplung gesteuerten Dynamik in kernangeregten Zuständen, basierend auf der Vorauswahl von Zuständen und der Verwendung des Wigner-Eckart-Theorems, wird durchgeführt, um zukünftige experimentelle Untersuchungen zu skizzieren und zu erleichtern.

Stichworte: *Multi-Referenz-/Multi-Konfigurationsmethoden, Nicht-Gleichgewichtsdynamik, Offene Quantensysteme, Hoch angeregte/kernangeregte Zustände, Dichtematrix, Hochkorrelierte Zustände, Viele-Körper-Dynamik, Zeitabhängige Konfigurationswechselwirkung.*

LIST OF ACRONYMS

ADC Algebraic Diagrammatic Construction

CAS Complete Active Space

CASPT2 Complete Active Space Second Order Perturbation Theory

CASSCF Complete Active Space Self-Consistent Field

CI Configuration Interaction

CM Charge Migration

CSF Configuration State Function

DFT Density Functional Theory

DMRG Density Matrix Renormalization Group

DO Dyson Orbital

GAS Generalized Active Space

HHG High Harmonics Generation

MCSCF Multiconfigurational Self-Consistent Field

MCTDHF Multiconfigurational Time-Dependent Hartree-Fock

MO Molecular Orbital

RAS Restricted Active Space

RASPT2 Restricted Active Space Second Order Perturbation Theory

RASSCF Restricted Active Space Self-Consistent Field

RASSI Restricted Active Space State Interaction

RIXS Resonant Inelastic X-ray Scattering

SCF Self-Consistent Field

SF Spin-Free

SO Spin-Orbit

SOC Spin-Orbit Coupling

TD-CASCI Time-Dependent Complete Active Space Configuration Interaction

TD-CASSCF Time-Dependent Complete Active Space Self-Consistent-Field

TD-CI Time-Dependent Configuration Interaction

TD-RASCI Time-Dependent Restricted Active Space Configuration Interaction

TDDFT Time-Dependent Density Functional Theory

TDSE Time-Dependent Schrödinger Equation

TM Transition Metal

WE Wigner-Eckart

XAS X-ray Absorption Spectrum

XPS X-ray Photoelectron Spectroscopy

XFEL X-ray Free Electron Laser

XUV Extreme Ultraviolet

ON THE CONVENTIONS

Unless stated otherwise, the atomic units ($\hbar = m_e = e = 1$) will be used throughout the text in formulae to make the expressions more compact. During the discussion of the results, mostly electronvolts (eV) are used as energy units for electronic transitions and femtoseconds (fs) as time units. The following notation is used in equations: \hat{O} – operators, \mathcal{A} – superoperators, \mathbf{a} – vectors. Symbol \Im denotes taking the imaginary part of a complex number.

CONTENTS

I	Introduction	1
1.1	Ultrafast spin dynamics	3
1.2	Theoretical approaches to ultrafast electron dynamics	5
1.3	State-of-the-art experiments	7
1.4	Thesis structure	9
II	Theoretical framework	10
2.1	Quantum Chemistry	10
2.2	Perturbation Theory	14
2.3	State Interaction and Spin-Orbit Coupling	15
2.4	Density matrix based TD-RASCI	17
2.5	Wigner–Eckart theorem	20
2.6	Numerical aspects	21
III	Selected Results	23
3.1	General Framework	24
3.2	Spin-Flip Dynamics	28
3.3	Analysis of dynamics with state multipoles and preselection schemes	30
3.4	Photoionization	32
3.5	Outlook	34
	References	35
IV	Publications and Manuscripts	52
	[VK1] published in <i>The Journal of Chemical Physics</i> 153 , 044304 (2020)	54
	[VK2] published in <i>Journal of Chemical Theory and Computation</i> 18 , 46-58 (2022)	71
	[VK3] published under <i>arXiv:2306.06737 physics.comp-ph</i> (2023)	97
V	Publications not included in the thesis	113
	Acknowledgments	115

I INTRODUCTION

Quantum mechanics is a precise and accurate framework for describing the natural world. It has given birth to many other subbranches of this science: fundamental research, quantum technologies, quantum information and computing, quantum biology, and many others. However, as these fields have developed, technical language has become increasingly specialized, creating a barrier to understanding for those outside a particular area. Here we discuss everything within and from the viewpoint of quantum chemistry – a special and mostly theoretical field that studies the interaction of atoms and molecules and applies the principles of quantum mechanics to provide a theoretical basis for molecular behavior. This specialized focus necessitates using jargon and terminology unique to the field in the current work.

Studying molecular and atomic phenomena has been performed for a while, and scientists have made significant strides in understanding the static properties of matter and explaining a wide range of phenomena. Much of this knowledge can be found in classical texts [1–3], but the field continues to evolve as we strive to uncover new insights into the fundamental behavior of our world. In recent decades, scientists have focused their efforts on studying dynamic phenomena, particularly through the development of tools capable of experimentally “keeping an eye” on molecular processes, which occur over a short period of time. Interpreting the results of these experiments is a critical component of this research. Researchers rely on various tools to study dynamic processes, including sources of electromagnetic radiation, optics, and detectors. The quality of these tools must meet exceptionally high standards to accurately capture and analyze the complex behavior of molecules over time. As a result, much of modern research centers on advancing the capabilities of these tools along with the theory facilitating and rationalizing the experiments. The current work is a purely theoretical study; however, discussing the area’s experimental side is also essential.

Energy domain. Firstly, one should clarify the characteristic time and energy scales touched upon in this thesis. While visible light interacts primarily with the outer valence electrons, the highly energetic X-ray electromagnetic radiation can reach deeply lying core energy levels. X-ray radiation, either incoherent or in the form of laser pulses, attracts great attention since they allow for atom-specific excitations due to the energetic separation of the core levels of different elements. Valence electrons are bound with comparable energies in most atoms and molecules, and that’s why they usually interact with light in the same spectral range. In contrast, when electrons are excited from them, localized core orbitals give information about the local electronic structure of a particular atom in its environment. Extreme Ultraviolet (XUV) light (10 – 100 eV) and soft X-rays (100 – 1000 eV) possess wavelengths commensurate with the energy of processes occurring inside electronic shells. Soft X-rays covering the water window region (280 – 530 eV) are essential for studying core excitations in light atoms and early transition metals. The thesis will not consider hard X-rays (more than one keV), typically used to reach

the lowest energy levels, such as $1s$ (K-edge) of heavier elements.

The variety of X-ray spectroscopies [4–6] that focus on core electrons goes along with an exhaustive list of problems, which they can address: first-order spectroscopies, such as X-ray Absorption Spectrum (XAS) [4, 7], give insights into unoccupied energy orbitals; as well as conventional X-ray Photoelectron Spectroscopy (XPS) [8] providing direct information on the energies of orbitals (energy levels, in general) based on the energy and angular distribution of outgoing electrons, etc. The second-order spectroscopy, such as Resonant Inelastic X-ray Scattering (RIXS) [9], provides a comprehensive understanding of electronic structure involving transitions between several electronic states at once. While X-ray spectroscopy has been a long-standing tool in scientific research, recent advancements in light source technologies, which deliver sufficiently bright and short electromagnetic pulses, have pushed the field into the realm of ultrafast science.

What are ultrafast processes? The definition of “fast” is relative, particularly when considering molecular processes. Timescales of the rotational ($\text{ps} \equiv 10^{-12} \text{ s}$), vibrational ($\text{fs} \equiv 10^{-15} \text{ s}$), and electronic ($\text{as} \equiv 10^{-18} \text{ s}$) effects vary depending on the specific process. With the advent of lasers, femtochemistry (speaks for itself) emerged as a field that uses time-resolved spectroscopy, based on the pump-probe approach [10–12], to gain insights into molecular dynamics on a femtosecond timescale. Femtosecond laser pulses have become a standard tool for tracking atomic motion in molecules. Despite this, the relaxation dynamics of core-excited atoms remain beyond the capabilities of femtosecond techniques. When a firmly bound electron in an atomic inner shell is excited, the electronic system undergoes an ultrafast rearrangement, causing the inner-shell core hole to disappear within a few femtoseconds. Modern methods allow for the simultaneous resolution of different characteristic time scales. For example [13], when performing transient XAS with the resolution of 400 as, electron-hole dynamics after strong-field ionization in the NO molecule is observed with the period of 2.7 fs, vibrational dynamics – of 14.5 fs, and rotational alignment – at sub-picosecond (0.1 ps) timescale. The characteristic times vary from one object to another. For instance, core-level X-ray spectroscopy detected ultrafast proton dynamics of a characteristic time of 46 fs in liquid water after ionization [14]. Fundamental research on attosecond phenomena triggered by ultrafast pulses has been carried out, covering a range from atoms [15, 16], quantum dots, solids, and condensed matter to molecules [17, 18]. Spin dynamics as a particular case will be considered in Sec. 1.1 in detail. Here, we notice that this process can be governed by the Spin-Orbit Coupling (SOC) effect, which gives rise to the characteristic times at the (sub-)femtosecond time domain.

Processes of interaction with the field. New light sources such as High Harmonics Generation (HHG) and X-ray Free Electron Laser (XFEL), which will be discussed in detail in Sec. 1.3, offer unprecedented opportunities to increase intensity and coherence and to shorten pulse duration and resolution down to the attosecond scale [19–22]. This advancement enables

the study of electron and molecular dynamics on timescales as short as a few femtoseconds or even sub-femtoseconds, using the ultrashort pulses [23, 24], where the electron dynamics appears to be primarily decoupled from nuclear motion and other effects taking place at longer times. Firstly, ultrashort pulses with a broad linewidth in the frequency domain should generate a superposition of quantum states of a system. This non-stationary superposition then evolves often coherently after the end of the pulse or in the presence of the residual electromagnetic field. Thus, the electron (de)localization as the ultrafast response after attosecond excitation is observed, as was directly probed and reported for the H₂ molecule [25]. Such ultrafast electronic processes induced by prompt ionization occur in simple molecules and can be easily interpreted theoretically [26]. Experimental evidence has demonstrated instances of Charge Migration (CM), [27–29] in which the hole appears to oscillate across a molecule on a timescale of a few femtoseconds when the nuclei are fixed. The driving force behind this process is electron correlation [30], as opposed to the more commonly observed vibrationally mediated charge transfer [31]. However, the dynamics of this process are subject to dephasing due to nuclear motion, which becomes coupled to the evolution of the nuclear wave packet [32–35].

The impact of nuclear vibrations on the dynamics can be significant, particularly during the intersection of potential energy curves of states with different multiplicity, known as intersystem crossing [36, 37]. At this point, electron dynamics can no longer be isolated and become strongly affected by nuclear motion. Ultrafast non-adiabatic dynamics resulting from this coupling have been observed and extensively studied [32, 38], although this thesis is not concerned with such phenomena. In addition to coherent evolution, plenty of processes occur without coherence, often triggered by intensive X-ray/XUV pulses. These processes can include ionization and Auger decay, leading to irreversible changes and dephasing of the initial superposition of states [39, 40]. The spin dynamics can be exceptionally intricate, involving multiple spin manifolds, when successive ionizations occur under ultra-intense irradiation [41].

1.1 ULTRAFAST SPIN DYNAMICS

Recent studies have reported another type of coherent dynamics of one of the main interests of the current work: spin dynamics initiated by X-ray or XUV light [42, 43]. In the pioneering work of Wang and coworkers [42] in the Molecular Quantum Dynamics Group of the University Rostock, it was shown that once a core hole is created at the L_{2,3} absorption edge in transition metal complexes, it leads to a non-stationary mixing of states with different spins, see Fig. 1. In some cases, this process can result in a spin-flip effect taking place within hundreds of attoseconds, which is much faster than conventional spin crossover times driven by nuclear motion during the intersystem crossing, typically on the order of hundreds of femtoseconds or slower [37, 44–47]. The rapid spin transition is explained by strong SOC in electron configurations with 2*p*-hole (2*p*⁻¹3*d*^{*n*+1}) following X-ray excitation. SOC for deeper holes with

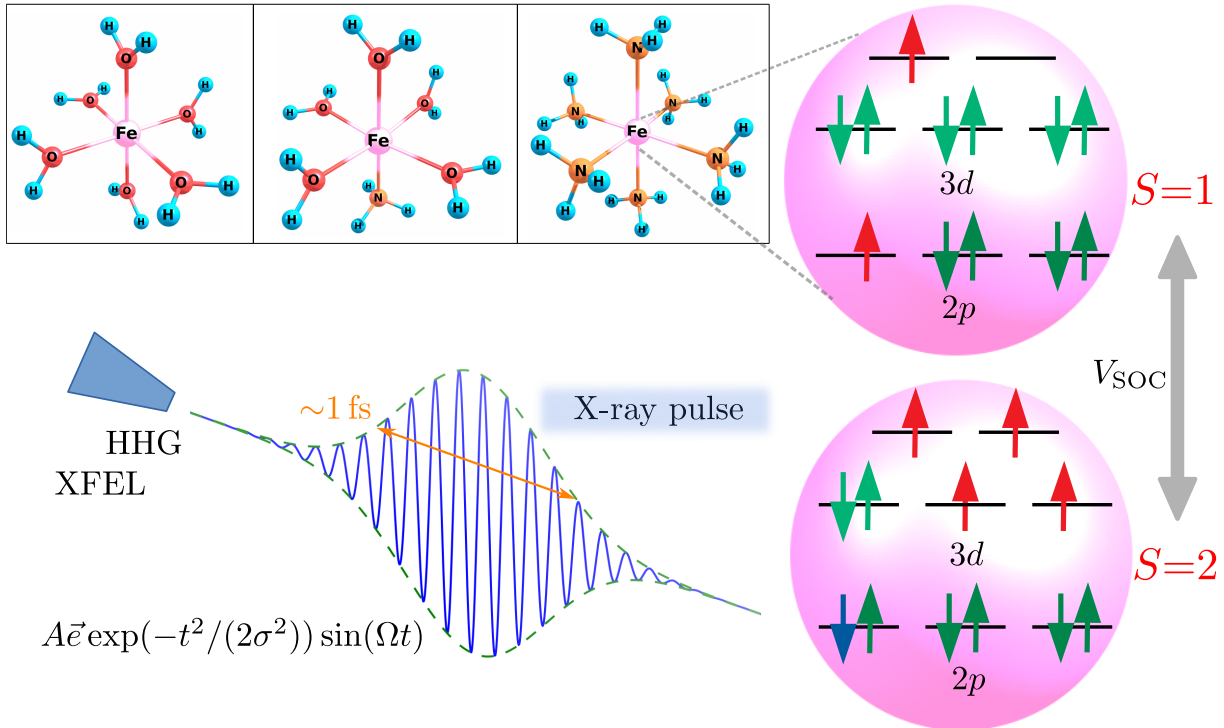


FIGURE 1: SCHEME OF ULTRAFAST SPIN DYNAMICS. DIFFERENT SIX-COORDINATED IRON COMPLEXES, THE MOST PROTOTYPICAL COORDINATION COMPOUNDS, ARE SHOWN ALONG WITH TWO EXEMPLARY ELECTRON CONFIGURATIONS IN THE GROUND AND EXCITED STATES. ULTRASHORT X-RAY PULSE INITIATES THE POPULATION TRANSFER BETWEEN CONFIGURATIONS OF DIFFERENT TOTAL SPIN THAT IS DRIVEN BY SPIN-ORBIT COUPLING.

non-zero angular momentum is generally more prominent than in the shallower holes.

In [48], a new theoretical tool, density matrix-based Time-Dependent Restricted Active Space Configuration Interaction (TD-RASCI), has been adapted to study the many-electron dynamics of the interplay between electron correlation and spin dynamics. Spin dynamics with different initial excitation conditions have been studied on short timescales, where the effect of the nuclear motion is insignificant. The authors have reported conditions to observe the ultrafast spin-flip dynamics driven solely by SOC in the $[\text{Fe}(\text{H}_2\text{O})_6]^{2+}$ complex. Later work of Wang *et al.* [43] has demonstrated that spin dynamics can be triggered by isolated soft X-ray light pulses as well as X-ray pulse trains, with a timescale faster than the lifetime of the $2p$ core hole. Interestingly, the spin dynamics are sensitive to the characteristics of the pulses, such as carrier frequency, pulse duration, and amplitude, allowing for some degree of control over the resulting spin mixture with modest changes in pulse parameters. With multiple pulses, stepwise population pumping occurs, and the characteristics of the individual pulses appear to have less influence on the dynamics. In contrast, the strength of the pulses plays a more critical role. This regime with pulse trains could be more practical in assisting the spin dynamics experimental verification, which is yet to be reached. Regarding the influence of nuclear motion, it must be noted that the inclusion of an electronic-nuclear bath has demonstrated that the electron-

vibrational coupling is small, and its effect can be neglected for the considered $[\text{Fe}(\text{H}_2\text{O})_6]^{2+}$ complex, at least on short timescales below 50 fs.

1.2 THEORETICAL APPROACHES TO ULTRAFAST ELECTRON DYNAMICS

Modern studies would be impossible without the joint work of theoreticians and experimentalists. Time-dependent theory, as an extension to stationary theory, started to develop relatively early, considering the explicit time dependence of the electronic system by evolving the time-dependent wave function in the time domain [49]. Good reviews on the modern time-dependent electronic theory and ones focusing on system-light interactions are published elsewhere [50–54].

A traditional approach to electron dynamics in molecules is Time-Dependent Configuration Interaction (TD-CI) [55–57] in energy representation, i.e., state basis. More generally, the Time-Dependent Complete Active Space Self-Consistent-Field (TD-CASSCF) [58] approaches with a time-dependent basis take into account the orbital relaxation. Mentioned wave-function-based methods, such as Configuration Interaction (CI) and Complete Active Space Self-Consistent Field (CASSCF), are improvements upon the Hartree–Fock method to get precise wave function decomposition fulfilling stationary Schrödinger equation. Besides, more electron correlation is included when using these more sophisticated multi-reference methods, which can be systematically improved up to the Full-CI limit [59]. However, with increasing molecular size or adding more orbitals to include core-excited states, it is crucial to invoke the concepts of Restricted Active Space (RAS) [60] and Generalized Active Space (GAS) [61], which reduce the number of electronic configurations and hence the computational cost. Methods of this group can also be used to take into account nuclear degrees of freedom with the help of other ways for treatment nuclei, for example, simulation of dynamics near a conical intersection: Time-Dependent Complete Active Space Configuration Interaction (TD-CASCI)– or CASSCF–Ehrenfest method [32, 38].

A flexible and reliable method closely related to TD-CASSCF is Multiconfigurational Time-Dependent Hartree-Fock (MCTDHF) [62, 63]. It optimizes both CI coefficients and orbitals by applying the time-dependent variational principle to a many-body wave function ansatz. MCTDHF can also be considered as a version for fermions of the well-established MCTDH method [64–66] for nuclei. While powerful due to its variational flexibility, the MCTDHF equations of motion for the coefficients and orbitals are coupled and difficult to solve in practice.

Versatile methods are formulated in the framework of Algebraic Diagrammatic Construction (ADC) [67], based on the perturbative Green’s function technique. The method can be more accurate when using higher orders of the perturbative expansion. In general, as for CI-based methods, some constraints on the orbitals involved in the excitation should be imposed to allow for computing the high-energy core-level spectrum, which otherwise is not computationally feasible for realistic systems. Such an example is Core-Valence Separated ADC [68]. Extension

of ADC to time domain shows promising results for charge migration simulations [69, 70]. Various Green's function techniques [71, 72] allow obtaining correlated electron dynamics in the second-order Born approximation solving Kadanoff equations for propagation. Such high-quality methods can serve as a standard or reference point for evaluating other methods when studying atoms and small molecules.

The time-dependent coupled-cluster approaches [73, 74] not only use the conventional cluster operator to produce excitations with respect to a reference Slater determinant but also allows for orbital adaptation [75] in the course of evolution in time. The modern development of the method, associated with the core-valence separation technique [76], can be used to simulate pump-probe X-ray experiments on molecules. As opposed to the coupled-cluster technique, a recently implemented method, the time-dependent Density Matrix Renormalization Group (DMRG), [77–79] targets efficiency and large active spaces. The wave function, expressed in terms of matrix product states, can be efficiently optimized with DMRG and then used even to study the ultrafast ionization dynamics in molecules [80] considering a relatively large number of electrons and orbitals, which is out of reach for conventional active space methods. However, it lacks the ability to treat the highly excited states so far, making this method inappropriate for studying the dynamics of core excitations.

Another direction in quantum mechanics (chemistry) computations is the Density Functional Theory (DFT). Rather than the wave function, it is based on such quantity as total electron density [81]. This method was revolutionary in the nineties and is still being actively developed [82]. In general, accurate wave-function-based calculations are computationally extremely expensive, while DFT is much more efficient and is the *de facto* standard for applications to structures with thousands of atoms. Excited-state Linear-Response Time-Dependent Density Functional Theory (TDDFT) usually gives good results for valence-excited states (lying below the ionization potential) with typical errors within half eV. However, problems arise while obtaining Rydberg states, charge-transfer states (because of long-range behavior), and doubly excited states since these are already not of a linear response character and cannot be described in terms of ground state electron density. The concept of Real-Time RT-TDDFT is increasingly adopted for electron dynamics, delivering reasonably good results [83]. However, both Real-Time and Linear-Response versions of TDDFT lack the description of multielectron excitations and are not trustworthy as the system is driven far away from the ground state reference density [84].

The methods mentioned above are based on the wave function (or electron density) decomposition and the subsequent propagation of expansion coefficients. However, it is often necessary to describe open quantum systems more broadly. The density matrix formulation and propagation due to the Liouville-von-Neumann equation offer some advantages [85, 86]. It allows for an implicit inclusion of environmental effects such as dephasing and energy relaxation [43, 87, 88], natural incorporation of (auto)ionization [89, 90] phenomena, and simulation of dynamics in molecular junctions [91]. Moreover, non-linear spectroscopies [92–95]

are usually formulated in terms of perturbation expansion of the density matrix. Thus, one can investigate a broader range of phenomena within the density-matrix-based approach taking into account electron correlation and nuclear motion at a desired level of theory. Namely, the method of choice of the thesis is ρ -TD-RASCI [42, 43, 48], which is implemented in spirit of density-matrix-based TD-CI [89, 90] additionally making benefits of the RAS concept.

1.3 STATE-OF-THE-ART EXPERIMENTS

All the aforementioned processes and experiments would be impossible to observe and perform without high-brilliant laser sources. One of the perspective sources for pulse generation is HHG [19, 96, 97]. HHG is a highly non-linear optical effect observed for atomic and molecular gases as well as for solids [98–100]. When a high-intensity beam with carrier frequency Ω hits an atom or molecule, it irradiates a range of higher harmonics $N\Omega$. By the term HHG, one usually means the spectrum resulting from the recombination of accelerated electrons with their parent ionized atoms. HHG, generated by near single-cycle laser pulses, can produce XUV pulses with duration of several tens of attoseconds [22] and thus enable unprecedented experiments on electronic structure, such as imaging of molecular orbitals [101–103], attosecond interferometry [39, 104], measuring phases of photoionization amplitudes [105, 106], and many more. The low intensity of HHG radiation still limits its applications compared to synchrotron-based radiation.

Development of the XFEL [21, 107–109] facilities makes a step further in terms of intensity and energy. It relies on a linear accelerator design wherein each electron bunch passes the insertion devices only once, in contrast to the conventional synchrotron setup. This results in reduced repetition rates (number of pulses per unit time), where high brilliance (number of monochromatic photons within solid angle area per unit time) is instead achieved by such principles as self-amplified spontaneous emission [110]. The initially unstructured electron bunch interacts with its emission to form structured microbunches, increasing the radiation’s coherence and intensity. Therefore, the peak brilliance of XFELs reaches roughly ten orders of magnitude higher than synchrotrons [107]. The prominent applications of that kind of radiation to time-resolved X-ray spectroscopies can be found in reviews [111, 112]. With the advent of XFELs, few-femtosecond [113] and more recently attosecond [114] X-ray pulses are available with sufficient energy to both initiate and probe the dynamics in cations via single-photon processes. In addition to simplifying the interpretation of the measurement [115], state and atomic site specificity can be attained by varying the probe photon energy. It was shown [116] that using advanced ultrashort X-ray pulses, one can unambiguously monitor the inner valence hole decay with a state-specific, atomically localized probe that does not perturb the dynamics. Fascinatingly, some free-electron lasers provide the so-called “fresh slice” mode to generate two-color pairs of intense X-ray pulses, several fs in duration, with a variable interpulse delay [113].

Attosecond science became possible two decades ago by establishing theory and experi-

ments on sub-fs pulses [19, 97]. After excitation, many body systems with excessive internal energy relax towards lower energy states by rearrangement of molecular, atomic, or nuclear structures. Pump-probe experiments allow studying such processes in real-time with a pump pulse for initiating microscopic dynamics and a delayed probe pulse for detecting transition states of the evolving systems. We briefly highlight current experimental possibilities, bearing in mind that theory and experiment always work in tandem to address various aspects of ultrafast dynamics combining absorption, emission (scattering), and photoionization X-ray techniques [111].

Photoemission, or photoelectron spectroscopy, serves as an essential probe of the sample. The photoelectric effect, first described by Einstein, gives insight into the electronic structure by the fact that photoelectrons ejected have kinetic energy, which depends on the incident photon energy and the electron binding energies. Time-resolved (transient) photoemission spectroscopy [25, 27] was initially implemented in the picosecond time domain and the visible (or later XUV) electromagnetic range, naturally using the first available lasers. Firstly, an isolated attosecond pulse triggers dynamics, usually via ionization, and then follows the delayed second several femtoseconds (several optical cycles) infrared pulse, responsible for subsequent probing of a transient excited state. Then, the energy of dissociated fragments, as an example in [25, 27], can be investigated as a function of the time delay between pulses. Furthermore, by analyzing secondary emitted Auger electrons, one can infer the lifetime of core-excited states, as shown in [117], where a laser-based sampling system, consisting of a few-femtosecond visible light pulse and a synchronized sub-femtosecond soft X-ray pulse, allows tracing these dynamics directly in the time domain with attosecond resolution, thus exploring processes that accompany photoionization. Interpreting signals from attosecond probe pulses poses a challenge due to their wide bandwidth in the energy domain, resulting in the smearing of spectral lines within the signal. Establishing regular attosecond pulses for routine use is still a challenging task. However, theoretical preparations are being made to support upcoming experiments by ensuring that interpretation remains clear despite shot-to-shot pulse variations and spectral broadening [118, 119].

Historically, the first time-resolved measurements of electron dynamics induced by a strong light field were performed with attosecond tunneling spectroscopy [120], where ions, rather than electrons, were measured for different delays between the XUV and near-infrared pulses. Another prominent example of such a scheme is attosecond streaking [20, 121], where photoelectron spectra are measured for a set of delays. The XUV–near-infrared combination of pulses is very efficient. Time-resolved measurements of impulse-driven charge motion have been relying on an XUV pump–strong infrared probe scheme [29], where the pump pulse is derived from an HHG-based source. It has also been applied in the field of ultrafast solid-state physics, with the measurement of delays in electron photoemission from crystalline solids [122] at attosecond time scale (about 100 as) and also in molecules [123]. Recent developments in liquid-jet techniques have made it possible to apply X-ray spectroscopy to molecules contained

in liquid environments [28, 124, 125].

The same principle is being applied in attosecond transient XAS, but one measures the transmission of an XUV pulse through a sample ionized by a near-infrared pulse. In experiments that elucidate ultrafast molecular dynamics, tuning the central wavelength of the probe pulse tracks the motion of the nuclear wave packet into and out of different regions of the excited-state potential energy surface. Advances in laser-pump–synchrotron-probe techniques have allowed time-resolved X-ray absorption spectra to be collected in this fashion [126]. Transient absorption spectroscopy provided direct evidence for the hole alignment in strong-field-generated atomic ions [127], where it persists for a period of 6.2 fs which is long compared to the SOC time scale, the motion of ionic valence-shell electrons observed with the attosecond resolution [16], and even caught the fastest electron dynamics driven by vibrations at the order of 10 fs [128].

1.4 THESIS STRUCTURE

Given recent cutting-edge experiments (Sec. 1.3) and the anticipated advancements in experimental techniques, there is a growing need for a robust and versatile theoretical framework that can accurately simulate time-dependent phenomena. From the viewpoint of theory, quantum chemistry packages [129, 130] offer precise static electronic structure calculations; however, to meet the challenges of time, one needs to predict electron dynamics in molecules and extended systems on subfemtosecond timescales, which is crucial for improving the interpretation of the experimental data.

To address this, an extension of quantum chemistry into the time domain becomes essential, as supported by numerous theoretical approaches outlined in Sec. 1.2. A notable framework in this regard is presented in [VK2], where the program module RhoDyn, implemented within the OpenMOLCAS project, enables the study of light-induced ultrafast electron dynamics using the density-matrix-based TD-RASCI method. Apart from describing the underlying theory and program workflow, it provides practical examples of its application, such as simulating linear X-ray absorption spectra, high harmonic generation, and charge migration.

Furthermore, the framework described in [VK2] is particularly well-suited for investigating the remarkable process of ultrafast spin-flip dynamics driven by SOC, as outlined in Sec. 1.1. Building upon this foundation, the studies conducted in works [VK1] and [VK3] extend the previous knowledge [42, 43, 48] by simulating spin-flip dynamics in a few transition metal complexes. The effect of the chemical environment and the nature of the central atom is studied in [VK1], while more fundamental work concerning internal symmetries of the operators and propagation itself can be found in [VK3].

An overview of the theoretical basis required for these investigations is detailed in Chapter II of this thesis. The main findings of this research are concisely consolidated in Chapter III, accompanied by relevant original papers [VK1], [VK2], [VK3], which are appended in Chapter IV.

II THEORETICAL FRAMEWORK

We start by laying down the foundations from the basics to describe the collection of methods employed in this work. While the choice of these methods may appear specific, their arrangement and concise explanation serve to equip the reader with the theoretical minimum necessary to comprehend the results presented in Chapters III and IV. Please note that this is not an exhaustive introduction to the theoretical aspects of the work but rather a comprehensive review supplemented with essential references.

2.1 QUANTUM CHEMISTRY

Quantum chemistry, as non-relativistic quantum mechanics for molecules, is governed by Time-Dependent Schrödinger Equation (TDSE)

$$\hat{H}|\Psi(t)\rangle = i|\dot{\Psi}(t)\rangle. \quad (1)$$

For the sake of convenience, atomic units are used wherever otherwise is clear from the equations or stated explicitly. Often it is enough, or at least a good start, to consider the stationary Schrödinger equation

$$\hat{H}|\Psi_i\rangle = E_i|\Psi_i\rangle,$$

where Hamiltonian \hat{H} includes the kinetic energies of all the particles, nuclei \hat{T}_n and electrons \hat{T}_e , and their pairwise Coulombic interactions \hat{V}_{nn} , \hat{V}_{ne} , and \hat{V}_{ee} . The solution of the molecular Schrödinger equation is a many-particle wavefunction of all nuclear $\{\mathbf{R}_i\}$ and electronic $\{\mathbf{r}_i\}$ coordinates, which cannot be found exactly except for a limited number of simple systems; however, it can be represented in a complete basis: $\Psi(\mathbf{R}, \mathbf{r}) = \sum \Phi_i^{\text{nucl}}(\mathbf{R})\Psi_i(\mathbf{R}, \mathbf{r})$, where $\Psi_i(\mathbf{R}, \mathbf{r})$ constitute the set of all solutions to the pure electronic equation, still parametrically dependent on the set of nuclear coordinates, and the expansion coefficients $\Phi_i^{\text{nucl}}(\mathbf{R})$ are nuclear wave functions. To disentangle the nuclear and electronic degrees of freedom, one can use the *Born–Oppenheimer approximation* [131], physically motivated by large masses of the nuclei. Thus, motions of nuclei and electrons can be adiabatically separated by neglecting the non-adiabatic couplings, which are mainly represented by the derivative coupling matrix element $\langle\Psi_i|\nabla_{\mathbf{R}}|\Psi_j\rangle$, where the vector derivative is taken on nuclear coordinates. Adiabatic electron wave functions are the eigenstates of the pure electronic Hamiltonian:

$$\begin{aligned} \hat{H}_{\text{el}} &= \hat{T}_e + \hat{V}_{nn} + \hat{V}_{ne} + \hat{V}_{ee}, \\ \hat{H}_{\text{el}}\Psi(\mathbf{R}, \mathbf{r}) &= E_{\text{el}}\Psi(\mathbf{R}, \mathbf{r}). \end{aligned} \quad (2)$$

The adiabatic states $\Phi_i^{\text{nucl}}(\mathbf{R})\Psi(\mathbf{R}, \mathbf{r})$ can change substantially, especially when they are close in energy, and large nonadiabatic couplings can invalidate the Born-Oppenheimer approximation. The non-adiabatic couplings change the classical dynamics picture of nuclear motion on a

single potential energy surface. A nuclear wave packet then evolves on several potential energy surfaces and can switch among them. If adiabatic states become degenerate and form a conical intersection, the non-adiabatic couplings become singular and need careful treatment [66, 86].

Further, we will work within the *frozen nuclei approximation*, i.e., focus only on the solution of time-independent Eq. (2) followed by dynamical studies in an obtained basis. Whenever the excitation of the system occurs, we assume it is excited far from conical intersections and, thus, not considering the nuclear part of the wave function.

Self-Consistent Field. Electronic structure methods, which computationally solve the electronic Schrödinger equation (can be independently solved for different choices of frozen nuclear geometries), are thus pillars upon which many molecular studies are built. The straightforward way to electronic structure calculations was proposed by Hartree, Fock, and Slater [132, 133]. The method involves solving the Schrödinger equation for a set of electrons interacting with each other and the molecular nuclei, while assuming that each electron moves in an average potential created by all the other electrons, in the so-called *self-consistent field*. Despite its deficiencies, the Hartree–Fock, or Self-Consistent Field (SCF), method still serves as the basis for many of the more advanced approaches.

The core ingredient is a Slater determinant, constructed from a set of Molecular Orbitals (MOs) as an antisymmetrized product $\hat{A} \prod_k \chi_k$:

$$|\Psi_0\rangle = \frac{1}{\sqrt{N!}} |\chi_1, \chi_2, \dots, \chi_a, \chi_b, \dots, \chi_N\rangle. \quad (3)$$

The numerical implementation of MOs χ_k requires their expansion in a finite basis of appropriate functions. For isolated molecular systems, a linear combination of atomic orbitals often proves the best option

$$\chi_k = \sum_{\mu=1}^n c_{\mu k} \phi_{\mu}. \quad (4)$$

These functions ϕ should accurately represent the involved physics to ensure tolerable convergence in the expansion and allow efficient numerical integration to limit the computational cost of construction of the operators. Most atomic-orbital calculations favorably employ basis sets of analytic localized atom-centered forms, such as Gaussian-type and Slater-type orbitals, the former of which has long dominated quantum chemistry. The actual atomic orbitals can be approached in such a basis set given sufficiently many basis functions (n), as the corresponding expansion coefficients $c_{\mu k}$ are optimized to minimize the total energy. The benefit of this approach is that a relatively compact atomic-orbital basis set usually affords at least a qualitative level of accuracy for applications. In contrast, larger basis sets can enable calculations that approach quantitative accuracy concerning experiments. The vast array of available bases for quantum chemistry computations is remarkable [134]. Atomic natural orbital type ANO-RCC basis [135] is used nowadays routinely as it covers a large part of the periodic system with

a basis set of decent quality. It has turned out to be sufficient for all of the results gathered in the thesis; however, sometimes, one should use more delocalized functions like diffuse and polarization basis functions.

The expansion in Eq. (4) turns SCF into a set of equations, the Roothan equations [59], a linear algebra problem highly adaptable to computer architecture to determine the coefficients of an optimal set of basis functions. Both the accuracy and the cost of the calculation scale with the number of included basis functions, which in the limit of a complete basis, converges to the exact Hartree-Fock solution. The resolution-of-the-identity approximation and Cholesky decomposition help to reduce the computational cost in treating two-electron integrals over the basis functions [136].

Configuration Interaction approach. The mean-field SCF approximation is considered to be a good starting point for further correlated treatments. Improving upon the SCF Hartree-Fock method is lifting the restriction of a single-determinant wave function. The *Full-CI* approach provides the exact solution by constructing the wave function as a linear combination of all possible electronic configurations

$$|\Psi^{\text{CI}}\rangle = |\Psi_0\rangle + \sum_{ia} C_i^a |\Psi_i^a\rangle + \sum_{i<j,a<b} C_{ij}^{ab} |\Psi_{ij}^{ab}\rangle + \dots \quad (5)$$

within a given one-electron basis set, see Fig. 2. An optimization procedure is performed for a set of the CI coefficients $\{C_i\}$. All these configurations form the so-called Hilbert space, which grows exponentially fast with the system size, leading to a prohibitive computational cost for real-life molecules. The most natural route to reach Full-CI from HF is to increase the maximum excitation degree of the CI wave function with respect to a reference configuration $|\Psi_0\rangle$.

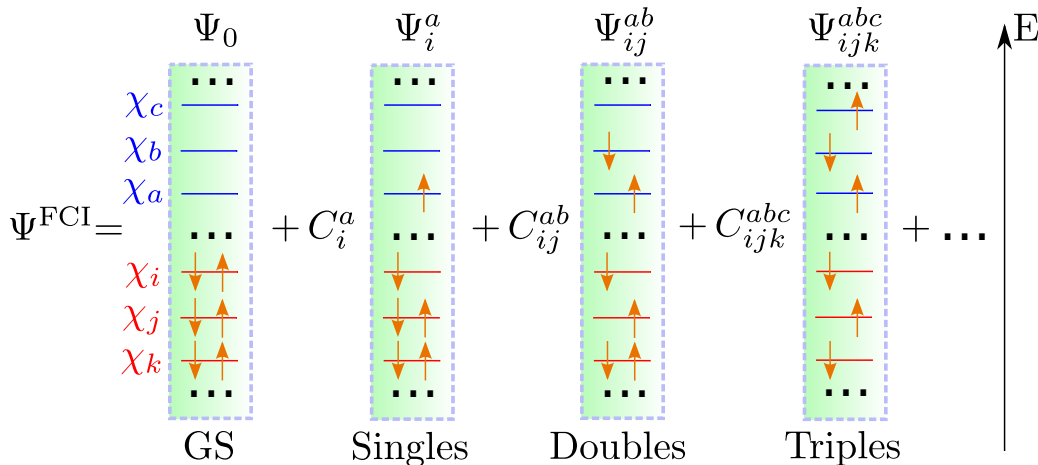


FIGURE 2: CI WAVE FUNCTION'S EXPANSION AS OF EQ. (5). GROUND STATE (GS) CONFIGURATION $|\Psi_0\rangle$ IS NOT NECESSARILY THE HARTREE-FOCK GROUND STATE BUT A REFERENCE CONFIGURATION UPON WHICH OTHER EXCITATION TERMS ARE BUILT. EINSTEIN'S SUMMATION NOTATION OVER REPEATING INDICES IS SUPPOSED.

Modern multiconfigurational methods typically rely on spin-adapted Configuration State Function (CSF)s [59] instead of individual Slater determinants as a basis for expanding the many-body wave function. CSFs are the eigenfunctions of the spin operators \hat{S}^2 and \hat{S}_z , and they can be limited to include only terms that contribute to the overall target spin, defined by the quantum number S . Moreover, given the quantum number M_S related to the spin projection on the z -axis, the energy values for the $2S + 1$ members of the multiplet are degenerate. One can employ the graphical unitary group approach (GUGA) to construct CSF expansion space that does not refer to its determinantal representation [137]. GUGA is a spin-free formalism that completely suppresses the quantum number M_S from the computational procedure. The spin-free approach introduces difficulties in calculating spin-dependent properties [138]. In the state interaction approach, one of the cornerstones of this work and described below in Sec. 2.3, spin-free GUGA representation is used, and the matrix elements over individual spin states are then restored by the Wigner–Eckart theorem [139].

Restricted Active Space concept The next upgrade of the CI method is Multiconfigurational Self-Consistent Field (MCSCF), within which both $\{C_i\}$ and $\{c_{\mu k}\}$ sets of coefficients in expansions (5) and (4) are optimized to minimize the total energy. Underlying Full-CI approach is straightforward but computationally demanding. The Restricted Active Space Self-Consistent Field (RASSCF) method was developed by Swedish pioneers [140, 141] to reduce computational efforts. In applications, not all of the molecular orbitals are of great interest.

In chemistry, often only valence electrons play a significant role by participating in chemical bonding and defining properties of compounds interacting with electromagnetic radiation in the optical region and a wide range of other wavelengths. Then it has the sense to do Full-CI only for some electrons and subspace of orbitals, which these electrons can potentially occupy; this partitioning is called Complete Active Space (CAS). Electrons undergo any excitations within the orbitals chosen in CAS. However, sometimes it is also overcalculation, and one can imply more excitation restrictions. CAS with additional restrictions on the number of electrons in certain orbitals is called RAS, schematically shown in Fig. 3. Full-CI is performed only for a set of orbitals denoted as RAS2. When some electrons are needed to be included in the consideration, usually as single core excitations to discrete spectrum or continuum, this active space should be en-

Occ. Subspace	Opt.		
	$\{\chi\}$	$\{C\}$	
	Deleted	—	—
	Virtual	+	—
	RAS3	+	+
	RAS2	+	+
	RAS1	+	+
	Inactive	+	—
	Frozen	—	—

FIGURE 3: ORBITAL SUBSPACES USED IN THE RASSCF METHOD DISTINGUISHED BY POSSIBLE OCCUPATION NUMBERS AND PERFORMED OPTIMIZATION OF MO $\{\chi\}$ AND CI COEFFICIENTS $\{C\}$.

*: RAS1 (RAS3) ALLOWS FOR A PRE-DEFINED NUMBER OF HOLES (ELECTRONS).

larger. Full-CI is performed only for a set of orbitals denoted as RAS2. When some electrons are needed to be included in the consideration, usually as single core excitations to discrete spectrum or continuum, this active space should be en-

larged with the excitation orbitals put to the RAS1 subspace. Orbitals, which are not supposed to be involved in the interaction, are divided into inactive (occupied) and virtual (unoccupied). Full-CI is not performed for them, only optimization of spin-orbitals χ_k , which corresponds to the SCF level of theory. Notice that the choice of active space for a particular problem should be a matter of thorough study [137, 142, 143] as well as the investigator’s scientific intuition and experience.

2.2 PERTURBATION THEORY

The RASSCF method recovers mainly a static part of electron correlation. A standard way to describe so-called *dynamic correlation* [59, 144] instead is based on non-variational post-MCSCF methods. Suppose Hamiltonian allows the partitioning in two parts, \hat{H}_0 and \hat{V} , one of which can be treated as a small perturbation. Then the perturbation theory is valid to be applied. The most common method for single-determinant reference functions is the Möller-Plesset perturbation theory [145], where the reference Hamiltonian is taken as a sum of Fock operators. This generally improves the SCF solution but breaks down when the static correlation is important. For a simultaneous description of static and dynamic correlation, perturbative treatment should be applied to multi-configurational reference functions. Yet, successful single-state treatments with the second-order perturbation theory exist both for CAS (Complete Active Space Second Order Perturbation Theory (CASPT2)) [146] and RAS (Restricted Active Space Second Order Perturbation Theory (RASPT2)) [147] reference functions. The RASPT2 energy correction is given by the formula of conventional non-degenerate perturbation theory

$$E_i^{(2)} = \sum_k \frac{|\langle \Psi_i | \hat{V} | \Phi_k \rangle|^2}{E_i^{(0)} - \varepsilon_k + \Delta},$$

where Ψ_i is a RASSCF wavefunction of the i th state, and Φ_k is the eigenfunction of the zero-order Hamiltonian $\hat{H}_0 \Phi_k = \varepsilon_k \Phi_k$. This energy is considered as an addition to one-electron energies and takes into account dynamic correlation when active space is not large enough, and contributions from inactive or virtual orbitals should be accounted for.

It must be stressed that RASPT2 calculations cannot be considered a black box and should not be directly trusted. Firstly, the conventional RASPT2 method has the same drawback as the standard perturbation theory, i.e., it is not appropriate for calculations of degenerate states. One should be aware of that, especially calculating the states close to conical intersections. The remedy for this, working only in some cases but worth trying, is using extensions of CASPT2, for example, XDW-CASPT2 [148]. Furthermore, the so-called *intruder state problem* manifests itself when the denominator in the energy correction vanishes due to the accidental degeneracy of the reference state and the perturbed configuration [149]. In this case, one solution is to include such a state into the reference wave function, i.e., to enlarge the active space. It is not always possible or desired and can potentially cause the appearance of new intruder states.

Level shift techniques [150, 151] represent another, more powerful remedy. In addition, several flavors of RASPT2 have been suggested to cope with this problem [146, 152, 153]. In general, for the studied system, when calculations exhibit irregular behavior – i.e., different types of PT2, different shifts, or different active spaces give different results – a thorough search for the right solution is needed. One of the ways to judge the reliability of the RASPT2 results is to compare results produced with different active spaces.

In many cases, see Chapter III, sufficiently good results are already obtained at the RASSCF level of theory. When considering $2p \rightarrow 3d$ excitations, spin-free wave functions and their couplings were reasonably reproduced according to the obtained XAS spectra. CASPT2 was applied only when dealing with valence excitations in the C_6H_6 and HCCI molecules to bring the results closer to experimental values [VK2].

2.3 STATE INTERACTION AND SPIN-ORBIT COUPLING

Any pair of RASSCF wave functions (for example, for different spin multiplicities) are usually optimized separately and thus do not share a common molecular orbital basis resulting in the overlap matrix, not equal unity. One needs to perform the so-called biorthonormalization procedure. The *Restricted Active Space State Interaction (RASSI)* approach allows the calculation of property matrix elements (dipole moment matrix, for instance) for a pair of RASSCF wave function Ψ_1^X and Ψ_2^Y with different bases of MOs χ^X and χ^Y by a transformation of the basis sets and CI coefficients to a biorthonormal basis χ_1^A and χ_2^B . The general algorithm of biorthonormalization of two CASSCF wave functions [154] or RASSCF wave functions [139] includes a calculation of interaction Hamiltonians and particularly the SOC interaction between these functions.

Relativistic effects play an essential role for core electrons in transition metals and heavier atoms; thus, they are crucial for predicting the correct energetics of the system. However, SOC is considered in this thesis mainly as a mechanism coupling electronic states of different spin multiplicities within the *LS*-coupling scheme and leading to spin-forbidden dipole transitions. Scalar relativistic effects can be treated with the one-component Breit-Pauli representation of the spin-orbit operator at the second-order Douglas-Kroll-Hess approximation [155] and *Atomic Mean Field Integrals* [156]:

$$V_{ij} = \langle i | \hat{h} | j \rangle + \frac{1}{2} \sum_k n_k \{ \langle ik | \hat{g} | jk \rangle - \langle ik | \hat{g} | kj \rangle - \langle ki | \hat{g} | jk \rangle \}, \quad (6)$$

where n_k gives the occupancy of the orbitals, \hat{h} and \hat{g} are the one- and two-electron parts of the Breit-Pauli Hamiltonian. The physical picture behind such a representation of Eq. (6) is that of a “mean-field” operator, the performance of which has been thoroughly tested with fascinating results [157–159].

It is instructive to give an explicit expression for the SOC interaction between the electronic

	DET	CSF	Spin-Free (SF)	Spin-Orbit (SO)
Related Operator	-	\hat{S}^2, \hat{S}_z	\hat{H}_{CI}	$\hat{H}_{\text{CI}} + \hat{V}_{\text{SOC}}$
Energies	-	-	E_{SF}	E_{SO}
Size ^a	$\binom{2K}{N}$	$\leq \binom{2K}{N}$	# of roots, N_{SF}	$(2S+1)N_{\text{SF}}$
Wave Function Notation	$ \Psi^{\text{DET}}\rangle$	$ \Psi^{\text{CSF},(S)}\rangle$	$ \Psi_i^{(S)}\rangle$	$ \Psi_i^{(S,M_S)}\rangle$

TABLE 1: NOTATION OF POSSIBLE WAVE FUNCTION BASES THAT CAN BE OBTAINED FROM THE STATE INTERACTION METHOD, SUMMARIZED FOR INFORMATIVE PURPOSES. OPERATORS AND ENERGIES ARE GIVEN IF THE BASIS WAVE FUNCTIONS ARE EIGENFUNCTIONS OF THIS OPERATOR WITH EIGENVALUES EQUAL TO THE ENERGIES.

^a When considering dynamics involving SOC, one has to extend the state basis in accord with spin multiplicity; thus, for example, the number of states in SF and SO bases will be equal. The length of the determinantal expansion as the binomial coefficient of N electrons from $2K$ spin-orbitals holds only at the SCF level of theory.

states. For this, one can define spherical (triplet excitations) operators employing the creation and annihilation operators $\hat{\alpha}, \hat{\beta}$ in the spin-orbital basis $\{\{\chi_k\} \otimes \{\alpha, \beta\}, k = 1..K\}$ (α and β are the two single-electron spin functions for up and down electrons) in the framework of second quantization formalism [160, 161]:

$$\hat{T}_0^1 = \frac{1}{\sqrt{2}}(\hat{\alpha}^\dagger \hat{\alpha} - \hat{\beta}^\dagger \hat{\beta}), \quad \hat{T}_{-1}^1 = \hat{\beta}^\dagger \hat{\alpha}, \quad \hat{T}_1^1 = -\hat{\alpha}^\dagger \hat{\beta},$$

which can be represented in the Cartesian basis:

$$\hat{T}(x) = \frac{1}{2}(\hat{\beta}^\dagger \hat{\alpha} - \hat{\alpha}^\dagger \hat{\beta}), \quad \hat{T}(y) = \frac{i}{2}(\hat{\beta}^\dagger \hat{\alpha} + \hat{\alpha}^\dagger \hat{\beta}), \quad \hat{T}(z) = \frac{1}{\sqrt{2}}(\hat{\alpha}^\dagger \hat{\alpha} - \hat{\beta}^\dagger \hat{\beta}).$$

These tensors lead to the SOC Hamiltonian [139]

$$\frac{1}{\sqrt{2}} \left(V^x (T_{-1}^1 - T_{+1}^1) + \sqrt{2} V^z T_0^1 + i V^y (T_{-1}^1 + T_{+1}^1) \right), \quad (7)$$

where the mean field integrals \mathbf{V} is given by Eq. (6). Notice that Eq. (7) should be contracted with a reduced one-particle density matrix to obtain the matrix of SOC in a required basis.

The electronic Hamiltonian H_{el} (Eq. (2)) constructed in the basis of determinants or CSFs will be denoted as H_{CI} . With the introduced SOC operator, one can diagonalize a total Hamiltonian $\hat{H}_{\text{CI}} + \hat{V}_{\text{SOC}}$ and get a new set of eigenvalues E_{SO} and eigenfunctions having spin S and its projection on the quantization axis M_S . The new eigenstates have the form of a linear combination of spin-free states $|\Psi_j^{(S)}\rangle$, eigenstates of the H_{CI} Hamiltonian:

$$|\Psi_i^{(S,M_S)}\rangle = \sum_j^{N_{\text{SF}}} a_{ij}^{(S,M_S)} |\Psi_j^{(S)}\rangle.$$

Table 1 contains a summary of wave functions used in RASSI: DET (Slater determinants),

CSF, SF, and SO. Depending on the problem, it is convenient to switch between different bases and use its advantages, see Sec. 2.4.

2.4 DENSITY MATRIX BASED TD-RASCI

Once the stage has been set, we can proceed to describe the time-dependent method. In this study, we employ the *Time-Dependent Restricted Active Space Configuration Interaction (TD-RASCI)* method within the density matrix formalism [48]. The formalism enables us to simulate the dynamics of open quantum systems that interact with electromagnetic field in the form of pulses. At the heart of this method lies the Liouville von Neumann equation, specifically a Markovian master equation expressed in the Lindblad form [31]. To carry out the real-time evolution of the reduced density operator $\hat{\rho}$, incorporating the dissipation superoperator \mathcal{D} , the master equation in the form

$$\frac{\partial}{\partial t} \hat{\rho}(t) = i[\hat{H}(t), \hat{\rho}(t)] + \mathcal{D}\hat{\rho}(t) \quad (8)$$

is used, where the time-dependency of the Hamiltonian $\hat{H}(t)$ comes from the interaction of the system with the time-dependent field $\mathbf{E}(t)$

$$\hat{H}(t) = \hat{H}_{\text{CI}} + \hat{V}_{\text{SOC}} - \hat{\boldsymbol{\mu}} \cdot \mathbf{E}(t). \quad (9)$$

The density operator can be defined in any basis available from the state interaction calculations summarized in Sec. 2.3. For instance, in the SO basis, it naturally has the form of

$$\hat{\rho}(t) = \sum_{j,j'} \rho_{j,j'}^{(S,M_S,S',M'_S)}(t) |\Psi_j^{(S,M_S)}\rangle \langle \Psi_{j'}^{(S',M'_S)}|.$$

The flexible choice of the basis, however, is beneficial. CSF basis is preferable for electron correlation dynamics [VK2], SF basis is convenient to be used for spin dynamics [VK1], and the SO basis is used when, for example, dissipation needs to be accounted for [43], or the *a priori* known few SO states should be considered [VK2].

On top of the pure CI Hamiltonian \hat{H}_{CI} , other effects are put within a series of approximations:

- Spin-orbit coupling, \hat{V}_{SOC} , is included within the *LS-coupling* scheme as described in Sec. 2.3.
- Radiation interaction is taken in the *dipole approximation*, $-\hat{\boldsymbol{\mu}} \cdot \mathbf{E}(t)$, where $\hat{\boldsymbol{\mu}}$ is a transition dipole matrix, and $\mathbf{E}(t)$ is an external electric field. For simplicity, the incoming electric field is often chosen to be a single linearly polarized pulse with a temporal Gaussian envelope, as depicted in Fig. 1.

- Dissipation $\mathcal{D}\hat{\rho}(t)$ is responsible for coupling the system to a bath representing nuclear motion and environment. A general Lindblad form of such an operator is the following

$$\mathcal{D}\hat{\rho}(t) = -\frac{1}{2} \sum_l \left[\hat{C}_l \hat{\rho}(t) \hat{C}_l^\dagger + \left[\hat{C}_l, \hat{\rho}(t) \hat{C}_l^\dagger \right] \right],$$

where raising/lowering operators for decay channel l can be chosen as $\hat{C}_l = \sqrt{\Gamma_{ji}} |i\rangle \langle j|$, where Γ_{ji} is the associated dissipation rate between corresponding basis states [89, 90]. \mathcal{D} , often called the Redfield tensor, can be simplified and take a simple parametrized form. The Bloch model [31] decouples population relaxation and coherence dephasing, reducing the fourth-rank Redfield tensor to the second-rank matrix of relaxation rates $k_{i \rightarrow j}$ in the following way

$$\begin{aligned} \mathcal{D}_{ii,jj} &= \delta_{ij} \sum_l k_{i \rightarrow l} - k_{j \rightarrow i} \\ \mathcal{D}_{ij,ij} &= \frac{1}{2} \left(\sum_l k_{i \rightarrow l} + \sum_l k_{j \rightarrow l} \right) \end{aligned} \quad (10)$$

Thus, the dissipation is conveniently represented by the matrix of bath-induced transition rates $k_{i \rightarrow j}$, which can be further calculated within various models; see [43] and [VK1].

- Auger decay plays a vital role in determining the ultra-short lifetime of the core-excited states. It acts effectively as a decay channel and can also be introduced via the \mathcal{D} operator, as has been done in Ref. [43]. In this case, it has the following form:

$$\mathcal{D}_{ab,cd} = \delta_{ab} \delta_{cd} \delta_{ac} \Gamma_a, \quad (11)$$

where Γ_a is a decay rate corresponding to a lifetime of the state $|a\rangle$. Another more feasible way to include the autoionization decay is to estimate matrix elements of the transition operator $|\langle \phi_{el} \Psi_{f+} | \hat{H} - E | \Psi_i \rangle|^2$, where the wave functions of initial Ψ_i and ionized final Ψ_{f+} states are expanded in terms of Slater determinants or CSFs. Then, these matrix elements (Auger rates) can enter the Hamiltonian subblocks, highlighted with **A** letters in Fig. 4, responsible for transitions between different spin manifolds. For the complete theory on calculations of autoionization rates within the RASSCF framework, see Ref. 162. Neglecting the photoelectron wave function ϕ_{el} gives already good approximation to the Auger rates [163].

- Photoionization can be taken into account by an addition to the Hamiltonian, Eq. (9), in the form $\hat{H}_{\text{ion}} = \alpha \hat{D} \langle \mathbf{E}(t) \rangle$, where D_{if} is a matrix of Dyson amplitudes [164], proportional to the photoionization probabilities \tilde{k}_{if} within the *sudden approximation*

$$\tilde{k}_{i \rightarrow f} \approx \alpha \left| \Phi_{if}^{\text{DO}} \right|^2; \quad (12)$$

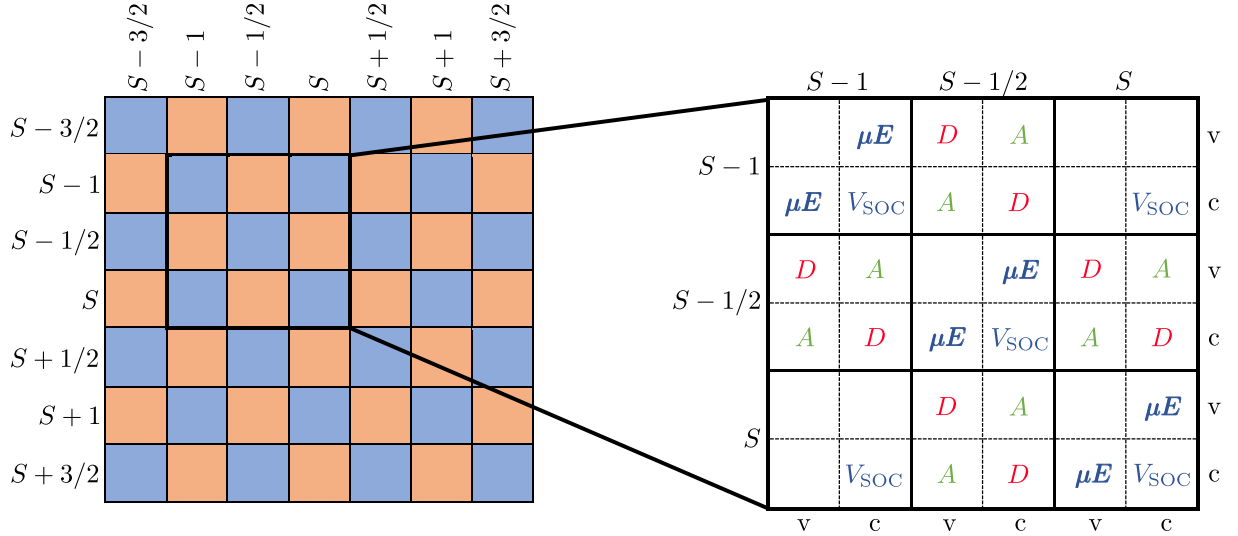


FIGURE 4: THE STRUCTURE OF THE HAMILTONIAN FOR MULTIPLE SPIN MANIFOLDS IN THE BASIS OF SF STATES. LABELS V AND C DENOTE VALENCE- AND CORE-STATE BLOCKS FOR A GIVEN SPIN-SPECIE. V-V SUBBLOCKS OF THE SAME SPIN ARE LEFT EMPTY TO STRESS THAT THE VALENCE V_{SOC} INTERACTION IS WAY SMALLER THAN IN C-C SUBBLOCKS. THE DEFINITION OF OTHER NOTATIONS IS GIVEN IN THE MAIN BODY OF THE TEXT.

α is a scaling parameter that could be determined, e.g., from the sum rule below. This approach effectively approximates the transition dipole moment matrix by squared Dyson Orbitals (DOs) norms. DO is calculated as $\Phi_{if}^{\text{DO}} = \langle \Psi_i | \Psi_{f+}^{N-1} \rangle$, thus within a multiconfigurational ansatz, it is represented as some combination of MOs. In terms of Koopmans theorem [59], the interpretation of DO is straightforward; it corresponds to a pure Hartree–Fock orbital χ_i for the corresponding ionization energy. The constant α is estimated from the following considerations. Roughly speaking, the transition from an initial state i of the N -electron system to a final state $f+$ of $(N-1)$ -electron system is proportional to the squared DO norm. The ionization cross-section [8], by the Golden Rule, is given by

$$\sigma \propto \sum_f \left| \langle \Psi_i | \hat{\mu} | \Psi_{f+}^{N-1} \phi_{el} \rangle \right|^2 \delta(E_f - E_i + \hbar\omega).$$

Then, Eq. (12) can be justified by rearranging the matrix transition element:

$$\tilde{k}_{if} = \left| \langle \Psi_i | \hat{\mu} | \Psi_{f+}^{N-1} \phi_{el} \rangle \right|^2 \approx \left| \langle \frac{\Phi_{if}^{\text{DO}}}{|\Phi_{if}^{\text{DO}}|} | \hat{\mu} | \phi_{el} \rangle \right|^2 \cdot |\Phi_{if}^{\text{DO}}|^2 = \alpha \left| \Phi_{if}^{\text{DO}} \right|^2,$$

The sum rule for oscillator strengths [165] can be applied here to estimate the value of α , i.e., $\sum_f k_{i \rightarrow f} = N$, where N is some constant equal to the number of electrons in the considered (sub)system, e.g., in the active space. Notice that α changes with the gauge change from length to velocity, and one should choose the α parameter with care.

2.5 WIGNER–ECKART THEOREM

One can separate geometric, due to the angular symmetry of the system, and spatial parts of the system's wave function or density matrix. Suppose considering an atomic system with hydrogen-like wave function $|nlm\rangle$, matrix elements of transition dipole moment $\langle nlm|\mu_q|n'l'm'\rangle$ can be simplified in the spherical basis $\{e_q : \hat{e}_{1,-1} = \mp(\hat{x} \pm i\hat{y})/\sqrt{2}, \hat{e}_0 = \hat{z}\}$. Omitting the angular momentum algebra, one obtains dipole moment as a product of Slater integral $F_{nl n'l'}$ [165], which does not depend on m quantum number, and Clebsch–Gordan coefficient $\langle lm|l'1m'q\rangle$. Generally, the Wigner-Eckart (WE) theorem [166] states that for any spherical tensor operator of rang k :

$$\langle j'm'|T_q^k|jm\rangle = \langle j'|T^k|j\rangle \langle j'm'|jkmq\rangle.$$

In the case of a scalar operator, the WE theorem reads

$$\langle j'm'|\hat{O}|jm\rangle = \langle j'|\hat{O}|j\rangle \delta_{j'j}. \quad (13)$$

We are interested in reworking four main components of the propagation technique: $\hat{\rho}$, \hat{H}_{CI} , \hat{V}_{SOC} , and $\hat{\mu}$ to separate geometric and essential dynamical parts of the time-evolution of the system [VK3]. \hat{H}_{CI} and $\hat{\mu}$ are scalar operators in relation to spin terms, and the WE theorem is applied to them according to Eq. (13). The SOC operator (Eq. (6)) is constructed in the basis of the triplet excitation operators, $\hat{T}_{pq}(\alpha)$, [139] being represented as

$$\hat{V}_{\text{SOC}} = \sum_{m=0,\pm 1} (-1)^m \hat{L}_{-m}^1 \otimes \hat{S}_m^1,$$

where $L_{(0,\pm 1)}^1$ and $S_{(0,\pm 1)}^1$ are standard components of angular momentum and spin tensor operators of rank 1. The density matrix is not an operator of any rank in the spherical basis, though every subblock of it with fixed spins S, S' can be expanded in a series of spherical tensors \hat{T}_q^k , see [166]:

$$\rho_{iS,jS'} = \sum_{kq} \langle \rho_{iS,jS'}^{kq} \rangle T_q^k(S,S'), \quad (14)$$

where we have supplemented the state index with its spin to denote the subblock of the density matrix. The *state multipoles* $\langle \rho_{aS,bS'}^{kq} \rangle$ do not depend on spin projections M_S and $M_{S'}$, and the resulting matrices have dimensions $N_{\text{SF}} \times N_{\text{SF}}$ and, thus, the complexity of the problem is reduced approximately by a factor of the squared mean multiplicity. However, the dependence on M is replaced by the dependence on k and q . The master equation (8) can be written in the basis of irreducible spherical tensors and formulated not on the density matrix but on the state multipoles [VK3].

2.6 NUMERICAL ASPECTS

There are plenty of methods dealing with the numerical solution of one of the differential equations of interest: directly TDSE (Eq. (1)), one of the Liouville-von-Neumann type (Eq. (8)), an equation of motion within the RT-TD-DFT formulation [167–169], or of other forms. Without loss of generality, consider the dynamics of an open quantum system, which is described by a master equation

$$\frac{\partial}{\partial t}\hat{\rho}(t) = \mathcal{L}(t)\hat{\rho}(t), \quad (15)$$

where $\mathcal{L}(t)$ is one of the Lindblad-type superoperators, possibly including the dissipation $\mathcal{L}(t) = i[\hat{H}, \cdot] + \mathcal{D}$. Eq. (15) is formally a first-order differential equation. The main goal is to find a so-called *dynamical map* described by the evolution operator, i.e., having an initial density matrix $\rho(t = t_0)$, one should obtain $\rho(t)$ at any arbitrary moment t . The formal solution of Eq. (15) in terms of the evolution operator is given by

$$\rho(t) = U(t_0, t)\rho(t_0), \quad (16)$$

where

$$U(t_0, t) = \hat{T} e^{-i \int_{t_0}^t \mathcal{L}(\tau) d\tau}. \quad (17)$$

Time ordering operator \hat{T} makes it complicated to solve the equation directly if Liouvillian \mathcal{L} depends explicitly on time, which is the case if Hamiltonian \hat{H} is time-dependent. In trying to solve the equation of such a form, one has to calculate the exponent of some matrix operator. It is not a trivial mathematical issue, but so far, there are a number of solutions. The Taylor expansion is not the only one; see the fancy mathematical summary on nineteen ways [170] of doing so.

Solving the master equation (15), one should be careful of the basic structural properties of the density matrix, such as matrix-hermiticity, normalization, and positive semi-definiteness, as well as the unitarity of the evolution operator, all of which should be preserved during propagation. The standard technique is to define the density matrix in a proper state basis and to solve the resulting matrix equation numerically. However, applying such a technique is limited because the number of matrix elements increases polynomially with the number of states. For extensive calculations, it is more feasible to derive the equation $\frac{\partial}{\partial t}\langle \hat{O} \rangle = \frac{\partial}{\partial t} \text{tr}\{\rho(t)\hat{O}\}$ for the time-dependent expectation value of an arbitrary operator \hat{O} of interest.

We will consider different propagation schemes both for Eq. (15) and TDSE, Eq. (1), where the main object is a wave function rather than a matrix. Despite different dimensions, one can formally introduce a unified approach. To show that, we follow Mukamel [171] and consider a two-level system of states $|a\rangle, |b\rangle$. The idea is to reformulate in such a way that the dimension-

ality is reduced and to recast the density matrix into a vector-like form:

$$\begin{pmatrix} \rho_{aa} & \rho_{ba} \\ \rho_{ab} & \rho_{bb} \end{pmatrix} \rightarrow (\rho_{aa} \quad \rho_{bb} \quad \rho_{ab} \quad \rho_{ba});$$

in the case of the two-level system, it is easy to show that:

$$\frac{\partial}{\partial t} \begin{pmatrix} \rho_{aa} \\ \rho_{bb} \\ \rho_{ab} \\ \rho_{ba} \end{pmatrix} = -i \begin{pmatrix} 0 & 0 & -H_{ba} & H_{ab} \\ 0 & 0 & H_{ba} & -H_{ab} \\ -H_{ab} & H_{ab} & H_{aa} - H_{bb} & 0 \\ H_{ba} & -H_{ba} & 0 & H_{bb} - H_{aa} \end{pmatrix} \begin{pmatrix} \rho_{aa} \\ \rho_{bb} \\ \rho_{ab} \\ \rho_{ba} \end{pmatrix}.$$

For an n -state system, the equation of motion can be formally written as

$$\frac{\partial}{\partial t} \rho_{ab} = -i \sum_{cd} (H_{ac} \delta_{bd} - H_{db} \delta_{ac}) \rho_{cd},$$

where ab indices run linearly. It is not practical to implement for calculations of realistic systems, or, at least, such studies are not known to the author. However, this generally shows the perspective to unite wave-function- and density-matrix-based numerical approaches as both objects being vectors but just of different length [171].

Many highly efficient time evolution schemes exist, although many are too specific. Iterative Chebyshev propagation and other polynomial and matrix decomposition methods are designed to solve problems with time-independent Hamiltonians [172, 173]. Lanczos recurrence methods and Krylov space time evolution [76, 79] are appropriate in dealing with scarce matrices. For a general overview of time propagation schemes, see one of the earliest reviews by Kosloff [174] or the modern one by Marquardt and Quack [54]. Local methods, including the Euler method, middle-point approximation, conventional Runge-Kutta of any order, and the Crank–Nicolson scheme, are used routinely for time-dependent problems due to the most straightforward implementation [175]. Accuracy and efficiency can be achieved with adaptive-step methods, such as Runge–Kutta–Fehlberg and Runge–Kutta–Cash–Karp method [176] in general. The variety of such “short-time” (local) schemes enables their straightforward application to the considered problem as a finite difference method to a (partial) differential equation. However, such non-symplectic integrators are unsuitable for large-scale simulations as they become increasingly unstable [177] with increased simulation size and require a fine time grid to maintain stability. One can overcome the disadvantage of local schemes by using Magnus expansion [178] of the evolution operator given by Eq. (17). This alternative approach guarantees that the evolution operator expanded in the Magnus series that is called the Magnus propagator or commutator-free propagator [177–179], strictly preserves the properties of the density matrix obtained with Eq. (16). Due to better stability, the Magnus propagators become widespread in all kinds of calculations, for instance, molecular dynamics simulation [180], DMRG [80], and TDDFT [169].

III SELECTED RESULTS

This study aims to adapt a versatile theoretical framework, density-matrix-based TD-RASCI, to be applicable to a wide range of dynamic phenomena in molecules. All of the studied molecules and molecular complexes are summarized in Table 2, providing references to corresponding works. In the following section, 3.1, we describe the implemented ρ -TD-RASCI framework and overview some applications of less scientific interest but essential from the methodological point of view. These are spectroscopies and light-induced processes nowadays often considered in ultrafast science: linear-response XAS simulation, non-linear HHG, and CM. Among those considered in this thesis phenomena are, in the first place, the SOC-driven ultrafast electron dynamics in transition metal complexes triggered by single X-ray pulses. A series of calculations on different combinations of Transition Metals (TMs) and ligands was performed in [VK1] to dissect the chemical environment effect on the process. Sec. 3.2 gives an overview of the results and repeats the main conclusions, which can be made from the study on the TM row. A brief summary and outlook regarding the spin dynamics, especially in the light of [VK3], is given in Sec. 3.3. Additionally, Sec. 3.4 contains the scheme of considering multiple spin manifolds and ionization channels to outline future studies of that kind of dynamics.

TABLE 2: INVESTIGATED SPECIES AND RESPECTIVE STUDIED SPECTROSCOPIES OR PROCESSES: LINEAR-RESPONSE ABSORPTION (LR), HIGH HARMONIC GENERATION (HHG), CHARGE MIGRATION (CM), AND SPIN DYNAMICS (SD). DETAILS OF THE ELECTRONIC STRUCTURE OF STUDIED COMPLEXES, SUCH AS THE ELECTRONIC CONFIGURATION OF THE GROUND STATE, SPIN MULTIPLICITIES, AND THE TOTAL NUMBER OF ELECTRONIC STATES CONSIDERED IN THE DYNAMICS, ARE REPORTED.

Molecule	Process ^a	Configuration ^b	2S+1	SOC States	Main ref.
H ₂	HHG	$(\sigma_{1s})^2(\sigma_{1s}^*)^0\dots$	1	26 (max)	[VK2]
C ₆ H ₆	CM	$3C(\pi)^63C(\pi^*)^0$	1, 2	595	[VK2]
HCCI	CM	$6C(\pi/\pi^*)^63I(5p)^5$	2	800 (max)	[VK2]
[Fe(H ₂ O) ₆] ²⁺	SD ₊	Fe(2p)(3d) ⁶	3, 5	760	[VK1]
[Fe(H ₂ O) ₅ (NH ₃)] ²⁺	SD ₊				
[Fe(NH ₃) ₆] ²⁺	SD ₊				
[Fe(H ₂ O) ₅ (CN)] ⁺	SD ₊				
[Fe(CO) ₅] ⁰	SD ₊	Fe(2p)(3d) ⁸	1, 3	3766	[VK1]
[TiO ₆] ⁸⁻	SD ₊ , LR	Ti(2p)(3d) ⁰	1, 3	61	[VK1]
TiCl ₄	SD ₊ , LR	Ti(2p)(3d) ⁰	1, 3	61	[VK3]
[Ti(H ₂ O) ₆] ³⁺	SD ₋	Ti(2p)(3d) ¹	2, 4	280	Sec. 3.2
[Cr(H ₂ O) ₆] ³⁺	SD ₋	Cr(2p)(3d) ³	4, 2, 6	1380	[VK1]
[Ni(H ₂ O) ₆] ²⁺	SD ₋ , LR	Ni(2p)(3d) ⁸	3, 1	105	[VK1]

^a lower index of SD indicates if a substantial spin-flip has been observed.

^b Approximate (one-)electron configuration of the ground state, orbitals denote the prevailing contribution from atomic basis function; however, in all cases, the mixing of orbitals is observed, and the distribution of electrons is of multiple orbitals.

3.1 GENERAL FRAMEWORK

The newly developed program module RhoDyn has been incorporated into the open-source OpenMOLCAS program package [130]. A detailed description of the RhoDyn module can be found in [VK2] and the web manual [181]. Effectively, it utilizes the time-independent quantities computed with RASSCF, CASPT2, and RASSI methods (Secs. 2.1, 2.2, 2.3) to construct the Hamiltonian and recast the problem into the time domain by solving the Liouville–von Neumann equation (8); see Fig. 5a for the workflow scheme. The set of multiconfigurational

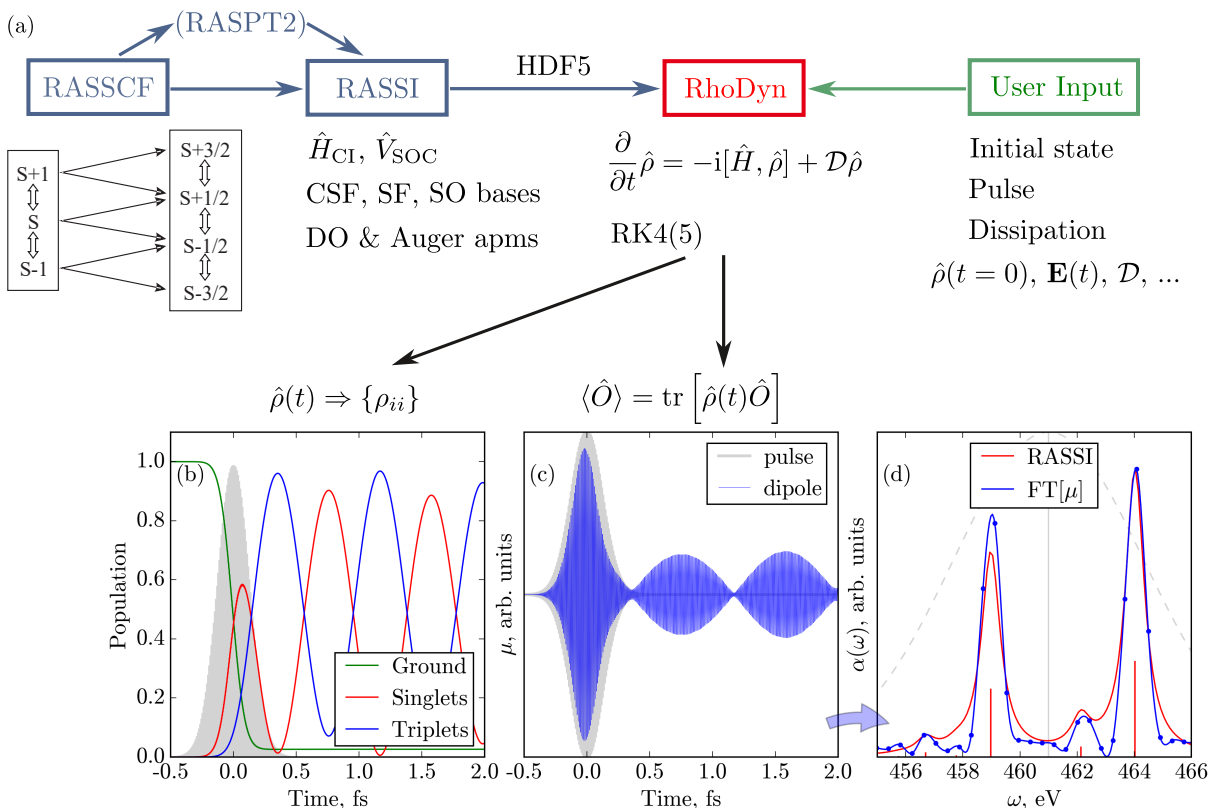


FIGURE 5: ADAPTED FROM [VK2] WITH PERMISSION. WORKFLOW AND DEPENDENCIES OF THE RHO DYN MODULE. (B) TIME EVOLUTION OF POPULATIONS OF GROUND ($S = 0$), SINGLET ($S = 0$), AND TRIPLET ($S = 1$) STATES OF TiCl_4 MOLECULE AFTER THE EXCITATION WITH ULTRASHORT X-RAY PULSE. (C) EXPECTATION VALUE OF THE DIPOLE MOMENT OPERATOR. (D) LINEAR XAS OBTAINED AS THE FOURIER TRANSFORM OF THE DIPOLE MOMENT ACCORDING TO EQ. (18) ALONG WITH THE STATIC RASSI SPECTRUM.

methods guarantees the inclusion of electron correlation effects and the ab initio treatment of SOC effects. These features distinguish the program from other time-dependent frameworks, such as XMDYN [182]. RhoDyn can describe dynamics in coherent and incoherent limits and cases between them via the density-matrix formalism. The nonequilibrium initial state can be prepared by specifying an initial density matrix, e.g., by populating a configuration that is not an eigenstate of the electronic Hamiltonian in a given basis or by introducing an external light field in the form of pulses. As described in Sec. 2.4 and further illustrated in Sec. 3.4, the probabilities of ionization and autoionization (Auger decay) can be computed or defined semiempirically.

RhoDyn allows for a flexible choice of the basis for time propagation depending on the problem under study. In addition to the bases of CSFs, SF and SOC states coming from RASSI step (see Table 1), one can represent the spin part of the density matrix in the basis of spherical irreducible tensors (state multipoles, described in Sec. 2.5). Using correlated states (SF and SOC) as the basis often allows for a substantial decrease in the dimension of the problem in comparison to CSFs. In this respect, a CASPT2 correction to the Hamiltonian might be necessary for better reproducing electronic time scales [VK2]. The implementation is intended to study isolated electronic dynamics when nuclear motion does not play an important role. Such an approach is advantageous for studying dynamics in core-excited states since electron motion is largely decoupled from nuclear effects owing to the characteristic time scales and the ultrashort lifetime of the core hole not exceeding a few fs. To consider the influence of the energy and phase relaxation due to vibronic interactions, the electronic system–vibrational bath partitioning is employed; for details, see [VK1]. The dissipation superoperator \mathcal{D} determines the details of this relaxation by the user-defined matrix of dissipation (relaxation) rates according to Eq. (10). One more thing that the investigator must supply is the characteristics of the pulse. Although for all results presented here, only the single Gaussian-shaped pulses were employed – see, for example, Fig. 1 for an explicit expression – one can flexibly control the number of pulses, their envelopes, carrier frequencies, amplitudes, phases, and even linear frequency chirp. The main output of RhoDyn consists of the time-dependent reduced density matrix; its diagonal elements $\{\rho_{ii}\}$ provide occupation numbers of the basis states $\{\Psi_i\}$. More importantly, the output can be used to compute the expectation value of any operator \hat{O} as $\langle \hat{O} \rangle = \text{tr}\{\rho(t)\hat{O}\}$.

We discuss further three applications of the implemented methodology: using the calculated time-dependent dipole moment to obtain the linear XAS, the molecular high harmonic generation spectrum of the H_2 molecule triggered by a strong-field infrared laser pulse, and the CM process.

Linear-response XAS. The obtained time-dependent dipole moment $\boldsymbol{\mu}(t)$ provides access to linear (XAS or X-ray Emission spectra) and nonlinear spectra of the system (HHG). It can also be used to compute multi-time correlation functions and response functions of any order to simulate and understand non-linear spectra [171]. XAS can be obtained from $\boldsymbol{\mu}(t)$ as

$$\alpha(\omega) = \frac{1}{2\pi} \Im \left[\int_0^{t_f} dt e^{i\omega t} \boldsymbol{\mu}(t) \cdot \mathbf{e} W(t) \right], \quad (18)$$

where the oscillations of $\boldsymbol{\mu}$ are initiated by the incoming pulse with polarization \mathbf{e} , t_f is the length of propagation, and $W(t)$ is a window function used to filter out noise.

One of the exemplary applications is shown on panels (b, c, and d) in Fig. 5 for the TiCl_4 molecule. The calculations have been performed at the RASSCF level of theory with the ANO-RCC-VTZP basis, including three $2p$ and five $3d$ orbitals of titanium atom in the RAS1 and RAS3 spaces allowing for one hole/electron, respectively. Thus, it corresponds to the CI singles

level of theory. This setup is sufficient to accurately describe core excitations in the titanium complexes and has been used for other similar calculations. Here, the propagation length of $t_f=10$ fs has been used to get the spectrum according to Eq. (18). Fig. 5(b) shows the evolution of spin state populations in the TiCl_4 molecule after excitation with the X-ray pulse. Fig. 5(d) displays the steady-state spectrum corresponding to time-independent energies and transition dipole moments obtained from the RASSCF/RASSI calculation and the Fourier transformed spectrum obtained from $\mu(t)$ depicted in panel (c) of the same Figure. Although the time-dependent procedure is redundant with the time-independent one, both results agree reasonably, representing an important consistency check. Another exemplary application can be found in Fig. 2 in work [VK2], displaying the linear $L_{2,3}$ -edge XAS of the $[\text{TiO}_6]^{8-}$ cluster exhibiting similar behavior.

High Harmonic Generation The HHG spectrum is a shining example of a non-linear optical effect; see Sec. 1.3. The calculation of the HHG spectrum was performed for a prototypical example of the H_2 molecule. The following parameters are repeated here for illustrative purposes. Two different basis sets, aug-cc-pVDZ and d-aug-cc-pVDZ, which include diffuse functions, were employed to investigate the effect of the basis and validate the approach. The active space consisted of all unoccupied orbitals (17 and 25 for both bases, respectively) in the RAS3 space, with the only occupied orbital placed in the RAS2 space. Only single excitations to RAS3 were allowed, resulting in 18 and 26 singlet states for the respective bases.

The pulse characteristics were selected to represent a typical experimental pulse from a Ti:Sapphire laser, corresponding to the Keldysh gamma parameter of $\omega\sqrt{2I_p}/E_{max} = 1.13$. In the single polarization case, the HHG spectrum can be calculated in the length form [53]:

$$I_i(\omega) = C\omega^4 \left| \int_0^{t_f} dt e^{-i\omega t} \mu_i(t) e_i(t) W(t) \right|^2,$$

where the time-dependent dipole moment $\mu(t)$ was directly obtained from the RhoDyn simulations. The resulting power spectra I_i reveal typical HHG features and can be seen in Fig. 3 of Ref. [VK2].

For the more compact aug-cc-pVDZ basis, the cutoff frequency is observed around the 17th harmonic, while in the more diffuse d-aug-cc-pVDZ basis, it shifts to approximately the 25th harmonic. This observation highlights the importance of employing a sufficient number of localized Gaussian functions to discretize the relevant continuum in the HHG process. The results are reasonably consistent with previous studies, emphasizing the significance of an appropriately chosen basis set [183–185], including diffuse functions and Rydberg states (e.g., Kaufmann functions [186]).

It is worth noting that ionization losses should be considered by incorporating absorbing boundaries, such as a complex absorbing potential or a heuristic ionization model *a-la* Refs. [90, 187, 188], or by utilizing the DO amplitudes and dissipation rates as described in Sec. 2.4. This

approach leads to a smoother spectrum by reducing artificial scattering at the boundaries of a space where the localized basis functions are confined.

Finally, it should be emphasized that processes like HHG involve numerous stationary electronic states, and careful consideration should be given to the size of the state basis.

Charge Migration. The oscillatory attosecond dynamics in valence excited states have been studied for two molecules, C_6H_6 and HCCI. The former exhibits a “satellite” migration when a superposition of a 1h and the adjacent 2h1p satellite states is created, and the latter is a “pure” hole mixing when different 1h states are involved. This difference in correlation-driven mechanisms is explained by the fact that valence orbitals of benzene molecules span the hole molecule, while the interplay in iodoacetylene occurs between orbitals localized on different atoms, namely iodine and two carbon atoms. CM is often approximated by an immediate removal of an electron from a particular MO. By preparing such an initial state, and letting the system evolve freely, the characteristic oscillations of populations between different MO were observed in both cases. The set of orbitals and the number of states sufficient to reproduce the processes for both molecules are reported in Table 2.

The ρ -TD-RASCI simulations appeared to be consistent with the adaptive TD-CI [189] for C_6H_6 and gave the main period of population migration of about 750 as. By applying the CASPT2 correction, the energy difference between hole-mixed states is calculated more precisely, and then the oscillation period changes to 980 as and agrees with the results of the ADC(3) method, including a large portion of the dynamic correlation, giving 935 as [70], and the TD-DMRG simulations within substantially larger active space, giving 804 as [80]. Therefore, the oscillation period is sensitive to including dynamic correlation. The more realistic initiation of CM was considered for C_6H_6 , in which the non-stationary superposition of states in the $(N - 1)$ system is reached by the transition from the ground state under the excitation with an explicit light pulse. The transition dipole moment between neutral and ionic states has been approximated with Dyson Amplitudes as sketched in Sec. 2.4. Although prominent hole dynamics are happening in this scenario, the simulations reveal no characteristic oscillation time in hole occupation due to preparing a more complex superposition of the ionic states. This result can explain why, despite many theoretical investigations of this system, there is still no direct experimental observation of such kind of dynamics in benzene.

In the case of iodoacetylene, the hole migrates from the iodine atom to the $C\equiv CH$ fragment with a period of 1.95 fs. This result agrees with the experimentally found period of 1.85 fs [190]. The computed period of 1.95 fs is only slightly larger than in other theoretical works [79, 189] with the notably larger active space. Thankfully to the ability of our framework to treat SOC effects, yet another oscillation period was observed in the simulations. The dynamics correspond to pumping the population from the CSF manifold with $S_z = -1/2$ to $S_z = +1/2$ and back with a period of about 12 fs. Its timescale agrees with an average spin-orbit splitting of ionized iodine $5p$ states of 0.3 eV. This finding can further support attempts to design the helical

CM in linear molecules [191].

3.2 SPIN-FLIP DYNAMICS

Implementing the multifunctional framework allowed for extending the prior studies of ultrafast spin-flip dynamics in the core-excited states [42, 43], which have been performed for a single prototypical Fe^{2+} complex. There, the occurrence of the spin transition within the time interval of hundreds of attoseconds has been observed, also dependent on the characteristics of the exciting X-ray light pulse, which should be centered at the $L_{2,3}$ absorption edge. Such a process can be regarded as an elementary step of the conventional spin-crossover driven by nuclear dynamics, similar to CM, an elementary charge transfer step caused by nuclear motion.

Work [VK1] addresses the question of the crucial factor influencing the spin dynamics in terms of the yield of the spin-flipped states. For example, how the central metal ion and surrounding ligands influence the extent of the transition. In particular, the efficiency of the spin-flip should be proportional to the SOC constant. Therefore, one expects the population transfer from states with the spin of the ground state to ones with a different spin to increase from left to right in the periodic table. However, the study on complexes coordinated by different transition metals, $[\text{TiO}_6]^{8-}$, $[\text{Cr}(\text{H}_2\text{O})_6]^{3+}$, $[\text{Fe}(\text{H}_2\text{O})_6]^{2+}$, $[\text{Ni}(\text{H}_2\text{O})_6]^{2+}$, has shown that the situation is more complicated. The so-called spin-flip was observed for the $[\text{TiO}_6]^{8-}$ and $[\text{Fe}(\text{H}_2\text{O})_6]^{2+}$ complexes only, see Table 2, where the “+” sign labels the cases of spin dynamics (SD) with the spin-flip discovered. Although the values of the SOC matrix V_{SOC} responsible for $L_{2,3}$ -splitting are important, the number of multiconfigurational excited states in each spin manifold plays a decisive role. For instance, the SOC strength in $[\text{Ni}(\text{H}_2\text{O})_6]^{2+}$ is three times larger than in $[\text{TiO}_6]^{8-}$, but the small number of accessible spin-flipped states makes the whole process inefficient in the former case, while in the latter, the spin dynamics is much more prominent.

The effect is stable to moderate changes in the coordination sphere. For instance, the exchange of ligands situated close to each other in the spectrochemical series (e.g., H_2O and NH_3 ; see Table 2 for iron complexes) does not lead to qualitative changes in the rate and completeness of the spin dynamics. These ligands neither strongly affect the electronic structure nor the dephasing and relaxation rate of the environment. However, strong-field ligands can substantially change the outer valence shell’s electronic structure, altering the relative energetic stability of the spin states. It is observed for $[\text{Fe}(\text{CO})_5]^0$, where the ground state spin is changed to a singlet in contrast to $[\text{Fe}(\text{H}_2\text{O})_6]^{2+}$ with its quintet ground state. One should also notice that transition metal $M_{4,5}$ absorption edges have been objects of the study but show not-so-strong spin mixing character.

To additionally stress the complex character of the spin dynamics, results for one more titanium complex $[\text{Ti}(\text{H}_2\text{O})_6]^{3+}$ are compared here with $[\text{TiO}_6]^{8-}$. It differs from the previously considered objects $[\text{TiO}_6]^{8-}$ and TiCl_4 , where Ti^{4+} coordinates the ligands, by the additional

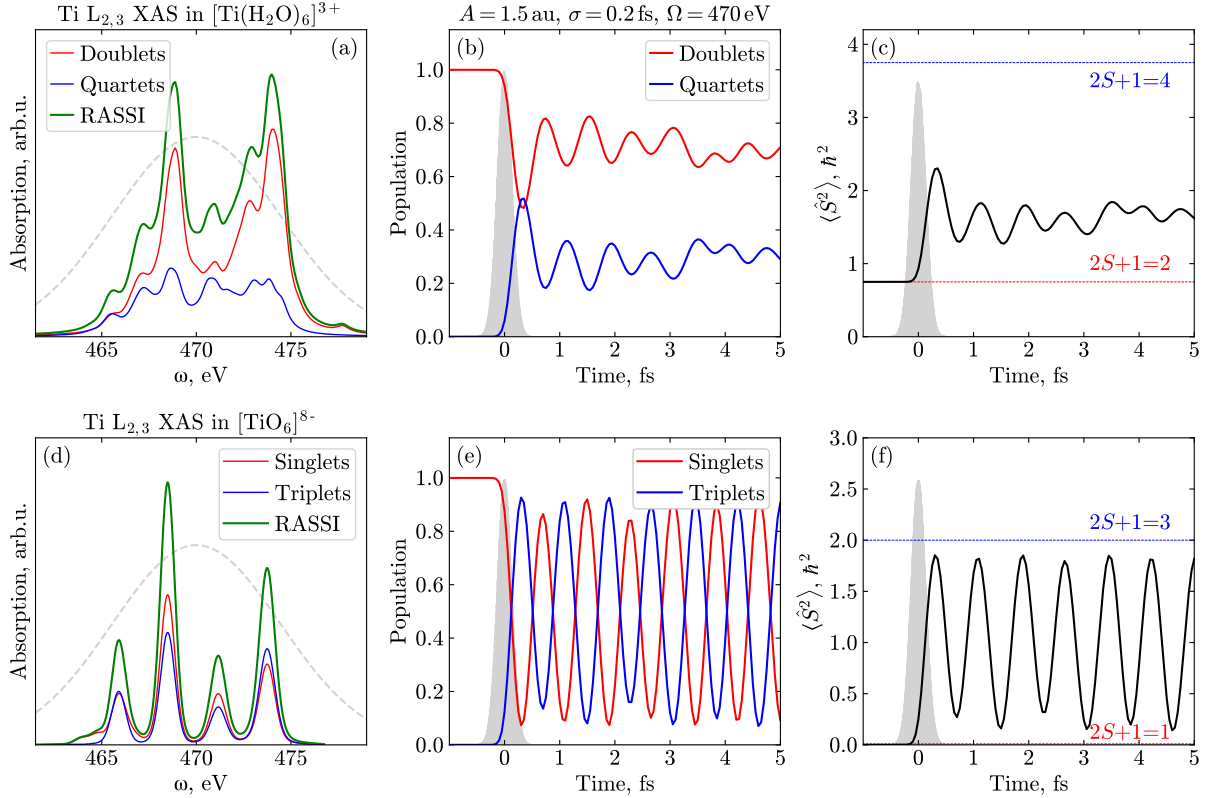


FIGURE 6: SPIN-DYNAMICS IN TWO TITANIUM COMPLEXES: $[\text{Ti}(\text{H}_2\text{O})_6]^{3+}$ (UPPER ROW) AND $[\text{TiO}_6]^{8-}$ (LOWER ROW). FOR EACH COMPLEX, THE STEADY-STATE TI $L_{2,3}$ -EDGE XAS (LEFT COLUMN), THE TIME EVOLUTION OF POPULATIONS SUMMED OVER DIFFERENT SPIN MANIFOLDS (CENTRAL COLUMN), AND THE EXPECTATION VALUE $\langle \hat{S}^2 \rangle$ (RIGHT COLUMN) ARE SHOWN. THE COLORED TEXT IN PANELS (C,F) HIGHLIGHTS VALUES CORRESPONDING TO THE SPIN MULTIPLICITY OF THE GROUND STATE (RED) AND EXCITED FLIPPED STATES (BLUE).

electron occupying primarily Ti 3d orbital. The system with central atom configuration Ti^{3+} stabilizes in a doublet ground state, while ground states of $[\text{TiO}_6]^{8-}$ and TiCl_4 are singlets. This substantially changes the XAS spectrum, as seen in Fig. 6(a,d). The decomposition of the hexaaquatitanium(III) spectra does not demonstrate any prevailing – or at least equal – contribution of quartet states. The dynamics, initiated by the same pulse as for other titanium complexes since the center of $L_{2,3}$ -edge remains the same, are intricate but show only moderate transfer from low- to high-spin states, Fig. 6(b,c), in comparison to the Ti^{4+} structure, Fig. 6(e,f).

To summarize, the exciting pulse should overlap with the spectral regions where “spin-flipped” states dominate. The decomposition of XAS into contributions from different spin states provides a hint about how many states of different multiplicities are presented and the chance to have enough relevant states to observe a target effect. Relevant states are those coupled to the ground states by the dipole matrix elements directly or indirectly through SOC. The relatively small changes in the chemical environment, which do not lead to the change in the ground state spin or qualitative differences in the order of electronic states, cannot be used to

tweak the character of the spin-flip dynamics.

The study [VK1] on the TM row has shown that the character and efficiency of the dynamics have to be analyzed on a case-by-case basis; the rate of spin-flip is firmly dependent on the system, more specifically, the number of states, the value of SOC splitting, and the pulse characteristics.

3.3 ANALYSIS OF DYNAMICS WITH STATE MULTIPOLES AND PRESELECTION SCHEMES

The focus of the current thesis, the SOC-driven dynamics in core-excited states of transition metal complexes, has been partially discussed in the previous Section. As the field is relatively new, much work has been devoted to further enhancing the understanding of the phenomenon and optimizing the computational procedure. Pursuing these goals, a detailed investigation of the state population's evolutions has been conducted, focusing on analyzing contributions from distinct spin projections M . This analysis involves using a graph-drawing algorithm, state preselection schemes, and utilizing the WE theorem.

In [VK1], by using the graph-drawing algorithm [192] helping to perform visual clusterization of states based on the value of matrix elements of transition dipole moment μ and SOC, one observes group(s) of non-participating states in all species. A value $c|(V_{\text{SOC}})| + |\mu|$, where c is a constant governing the ratio of the two factors, has been proposed as a rough characteristic to estimate *a priori* whether the state would be involved in dynamics or stays mainly unpopulated. Due to the inner symmetries of the SOC operator and the selection rules implied by it and the dipole moment, the states were clusterized into two almost equal groups. If the initially populated ground state(s) is (are) located in one of them, the states of another do not participate in the dynamics at all, suggesting the possibility of neglecting the part of states. Then, additionally, the groups are separated per spin projection M .

The study in [VK2] introduces the more advanced preselection of states based on the same values “connecting” different states, which allows performing the dynamics in a reduced (truncated) basis of SOC states, preselected to “participate” in the dynamics. The performed dynamics in such a basis confirmed the earlier suggestions. The characteristic features of population transfer between different spin manifolds of states were reproduced, thus enabling the significant reduction of computational efforts, at least by a factor of two. In such cases as the $[\text{Fe}(\text{CO})_5]^0$ complex, where only a small amount of states have been identified as actively participating in the dynamics, the reduction was especially beneficial.

More scrutinized analysis has been performed using the WE theorem to investigate the properties of the density matrix propagation, which SOC implies on it due to its geometrical nature. In [VK3], the density matrix has been decomposed in moment-distribution-like objects – state multipoles; see Sec. 2.5. The Liouville–von Neumann equation was reformulated in terms of the dynamical coefficients, state multipoles. Such formalism enables the straightforward in-

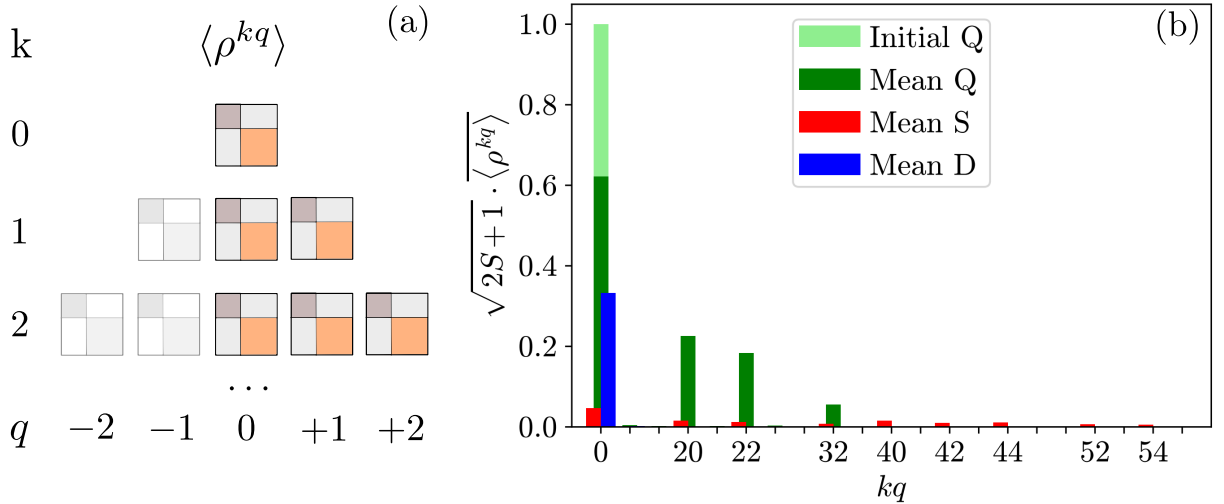


FIGURE 7: TAKEN AND ADAPTED FROM [VK3]. (A) HIERARCHY SCHEME OF STATE MULTIPOLES. DIAGONAL SUBBLOCKS OF EACH MATRIX $\langle \rho^{kq} \rangle$ SHOWN IN COLOR CORRESPOND TO DIFFERENT SPIN MANIFOLDS. PALE MATRICES (STATE MULTIPOLES OF NEGATIVE PROJECTIONS q) ARE NOT CALCULATED DUE TO HERMITICITY; (B) $[Cr(H_2O)_6]^{3+}$ MEAN CONTRIBUTIONS (I.E., ABSOLUTE VALUES OF DIAGONAL ELEMENTS SUMMED ACCORDING TO SPIN MULTIPLICITY AND AVERAGED OVER TIME) OF STATE MULTIPOLES TO THE DENSITY MATRIX. MEAN CONTRIBUTIONS FOR QUINTET (Q), SEXTET (S), AND DOUBLET (D) SPIN MANIFOLDS ARE SHOWN WITH GREEN, RED, AND BLUE COLUMNS, CORRESPONDINGLY. FOR FURTHER DETAILS, SEE [VK3].

terpretation of different terms of the spherical decomposition in kq ranks and projections (see Fig. 7) as either populations or coherences of groups of states with specific M projections. For example, diagonal elements of the $\langle \rho^{00} \rangle$ matrix were directly assigned to the populations of SF states, $\langle \rho^{10} \rangle$ – to the asymmetry between populations of states with $\pm M_S$, and of higher ranks and projections – to the coherences between SOC states with different M_S projections.

For the $[Cr(H_2O)_6]^{3+}$ complex, where higher spin multiplicities and a relatively large number of states are involved (see Table 2), the dynamics of interest could be represented by only a few first spherical basis terms, namely up to $k=2$, $q=1$. Fig. 7(b) shows averaged over time diagonal contributions from different $\langle \rho^{kq} \rangle$ for propagation in the complete spherical basis, where one can see the decrease of the mean contributions with increasing kq . Similar results for the $TiCl_4$ and $[Fe(H_2O)_6]^{2+}$ complexes can be found in [VK3], where the possibility of reduction of the spherical basis is discussed. It was concluded that the efficiency of this reduction depends on the coherence degree of the problem and, thus, depends on the system, its initial state, and the preparation conditions, i.e., the state prior to interaction with an electromagnetic field and the details of such interaction. When a large number of participating states leads to lower coherence due to quasi-equilibration in the electronic reservoir, this reduction is substantial, and the full dynamics can be rather closely reproduced with a relatively low rank and projection threshold for participating state multipoles.

3.4 PHOTOIONIZATION

The influence of Auger decay has been shown to have a minor impact on the spin dynamics character [42], where Auger decay (autoionization) was accounted for phenomenologically, see Sec. 2.4. The loss of the density matrix norm has been ensured by means of diagonal terms of dissipation operator \mathcal{D} (see Eq. (11)), specific for each spin multiplicity. This leads to a uniform exponential decay of populations without explicit consideration of final states.

Within the powerful RhoDyn framework, one can also consider the ionization (as well as autoionization) into the final state spin manifolds by explicitly including them in the Hamiltonian and extending the dimensionality of the density matrix. For example, in analyzing the CM process in the C_6H_6 molecule, two possibilities to trigger the process have been investigated in [VK2]. Either consider instantaneous non-equilibrium $(N - 1)$ -electron state within the $S = 1/2$ manifold only or start from the ground state with $S = 1$ followed by ultrashort pulse and prompt ionization.

Here, yet another example of including the additional decay channels is demonstrated. The high-spin $[\text{Fe}(\text{H}_2\text{O})_6]^{2+}$ complex is promising in this sense. When studying spin dynamics driven by SOC only, it is enough to consider ground quintet ($S = 2$), excited quintet, and excited triplet ($S = 1$) manifolds. The photoionization leads to removing an electron from the system and changes the total spin by $\pm 1/2$. To take into account the effect, one should extend the Hamiltonian to three extra spin manifolds: doublet, quartet, and sextets, as schematically depicted in Fig. 8a. The total number of SOC states, thus, within the given active space (three $2p$ and five $3d$ orbitals) is 2272, see Table 3. Amplitudes of DOs D enable transitions between

$2S+1$	SOC states	Valence	Core
6	96	16	80
5	175	35	140
4	696	174	522
3	585	195	390
2	720	360	360
total	2272	780	1492

TABLE 3: NUMBERS OF SOC STATES PER EACH SPIN MULTIPLICITY IN THE $2p3d$ ACTIVE SPACE FOR THE $[\text{Fe}(\text{H}_2\text{O})_6]^{2+}$ COMPLEX.

S and $S \pm 1/2$ subblocks of the density matrix, see Sec. 2.4. Coefficient α , tuning the strength of ionization, was determined from sum rules to be of the order of one for the system. As the dynamics in extended manifolds, $2S + 1 = 6, 4, 2$, is of no interest to us, the additional decay has been added for these manifolds in the spirit of phenomenological Auger decay (Eq. (11)) and Ref. 90. Introducing the decay coefficient Γ also prevents spontaneous emission. We have chosen it to be the same for all of the states to obtain the depletion of populations in the additional $2S + 1 = 6, 4, 2$ manifolds.

Fig. 8b shows the dynamics obtained, where the dynamics without ionization (without ad-

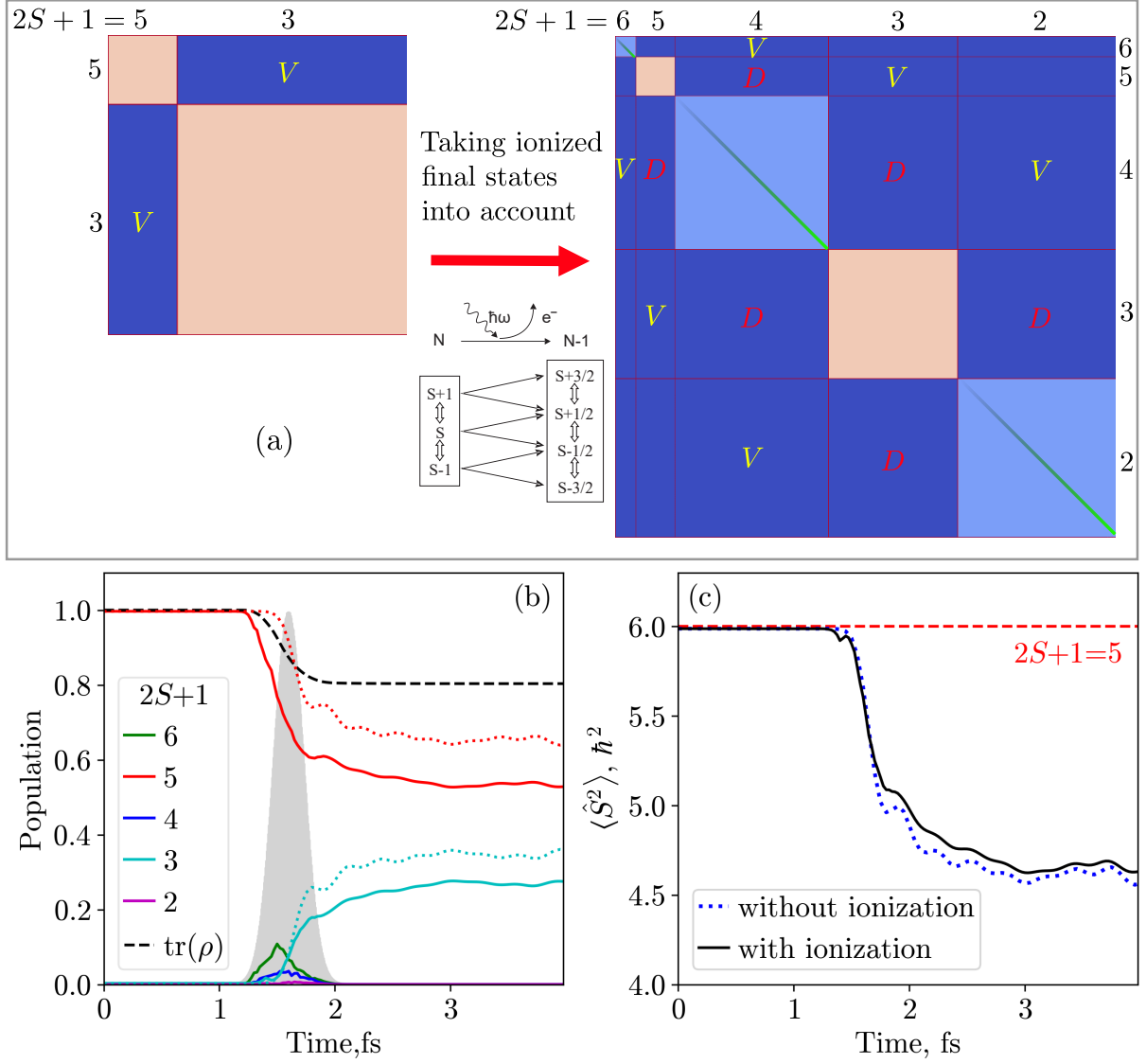


FIGURE 8: (A) SCHEME OF EXTENSION OF THE HAMILTONIAN FOR $[\text{Fe}(\text{H}_2\text{O})_6]^{2+}$ COMPLEX IN THE CASE OF ACCOUNTING FOR IONIZATION FROM THE QUINTET AND TRIPLET MANIFOLDS TO THREE EXTRA MANIFOLDS OF STATES WITH DIFFERENT MULTIPLICITIES. GREEN LINES ON DIAGONALS DENOTE STATES, WHICH ARE SUBJECTED TO FURTHER NOT NORM-CONSERVING DECAY; (B) POPULATION DYNAMICS; (C) TIME EVOLUTION OF THE $\langle \hat{S}^2 \rangle$ VALUE. FOR THE DETAILS ON ELECTRONIC STRUCTURE CALCULATIONS OF $2S+1=5,3$ CASE OR THE PULSE CHARACTERISTICS, SEE [VK1].

ditional manifolds) are denoted with dotted lines. One can notice, at first, that the character of dynamics remains the same despite a notable norm loss of about 20%. When considering the expectation value, $\langle \hat{S}^2 \rangle$, in Fig. 8c, or in other words, some integral characteristic of the total spin of the system, one can notice the smoothing of oscillations. It is an expected effect due to a loss of coherence.

The effect can be considered an initial step to the simulation of phenomena in ultraintense fields, where multiple successive ionizations can occur [41, 193].

3.5 OUTLOOK

This thesis is dedicated to investigating ultrafast electron dynamics using the density-matrix formulation at the complete or restricted active space CI level. The methodology is particularly well-suited for studying electron dynamics lasting a few femtoseconds or less when the system is excited far from conical intersections on the potential energy surface. The approach has two main directions of development that one can follow in the future: going beyond the frozen nuclei approximation and increasing the size of manageable systems. In the future, it is also desirable to enhance the flexibility of the method by incorporating time-dependent orbitals, thus extending it to the TD-RASSCF level in the spirit of Ref. 58. It will allow for orbital relaxation during the dynamics. Additionally, in cases where SOC plays a significant role, the *LS*-coupling approximation for heavy elements and deep hole states must be treated with caution. Two(Four)-component relativistic versions of the multiconfigurational electronic structure method should be then required [194].

Given the potentially large number of states belonging to different spin manifolds in SOC-mediated dynamics, as shown in Sec. 3.4, a scheme for preselecting the participating basis states and the WE reduction scheme require further enhancement. These approaches aim to reduce computational effort. The results of this thesis demonstrate that the dynamics are often remarkably stable, even under loose approximations, and can be reproduced consistently. Besides, additional efficiency gains could be achieved through alternative propagation schemes overviewed in Sec. 2.6. So far, the RhoDyn module supports only local Runge-Kutta-based propagation schemes. Other propagation techniques have appeared either too specific and not appropriate for our case or required not-so-straightforward implementation. Magnus propagators prove to be a better choice in electron dynamics simulations and look promising for our method.

The method represents a general and versatile tool to study dynamics and non-linear processes in molecules. Moreover, analyzing states involved in SOC dynamics holds theoretical interest and significance for experimental science. This study helps outline and facilitate future experimental investigations in this field. Several experimental setups, such as stimulated RIXS [93], spin-resolved photoelectron spectroscopy with elliptically polarized light [195], time-resolved Auger electron spectroscopy [196], or X-ray pump – X-ray probe [116], can be readily employed within the presented framework to explore such effects.

REFERENCES

- [1] L. D. LANDAU and E. M. LIFSHITZ, *Quantum Mechanics: Non-Relativistic Theory*, Pergamon, Oxford (1977).
- [2] B. H. BRANSDEN and C. J. JOACHAIN, *Physics of Atoms and Molecules*, Prentice Hall, Harlow, England ; New York, 2nd ed edition (2003).
- [3] J. J. SAKURAI, *Modern Quantum Mechanics*, Addison-Wesley, Boston, 2nd ed edition (2011).
- [4] F. DE GROOT and A. KOTANI, *Core Level Spectroscopy of Solids*, CRC Press, Boca Raton (2008).
- [5] P. NORMAN and A. DREUW, Simulating X-ray Spectroscopies and Calculating Core-Excited States of Molecules, *Chem. Rev.*, **118** (15), 7208 (2018), doi:10.1021/acs.chemrev.8b00156.
- [6] S. I. BOKAREV and O. KÜHN, Theoretical X-ray spectroscopy of transition metal compounds, *WIREs Comput. Mol. Sci.*, **10** (1), e1433 (2020), doi:10.1002/wcms.1433.
- [7] S. I. BOKAREV, M. DANTZ, E. SULJOTI, O. KÜHN, and E. F. AZIZ, State-Dependent Electron Delocalization Dynamics at the Solute-Solvent Interface: Soft-X-Ray Absorption Spectroscopy and Ab Initio Calculations, *Phys. Rev. Lett.*, **111** (8), 083002 (2013), doi:10.1103/PhysRevLett.111.083002.
- [8] S. HÜFNER, *Photoelectron Spectroscopy: Principles and Applications*, Springer, Berlin, Heidelberg (2003).
- [9] A. KOTANI and S. SHIN, Resonant inelastic x-ray scattering spectra for electrons in solids, *Rev. Mod. Phys.*, **73** (1), 203 (2001), doi:10.1103/RevModPhys.73.203.
- [10] M. DANTUS, M. J. ROSKER, and A. H. ZEWAIL, Real-time femtosecond probing of “transition states” in chemical reactions, *J. Chem. Phys.*, **87** (4), 2395 (1987), doi:10.1063/1.453122.
- [11] N. F. SCHERER, D. M. JONAS, and G. R. FLEMING, Femtosecond wave packet and chemical reaction dynamics of iodine in solution: Tunable probe study of motion along the reaction coordinate, *J. Chem. Phys.*, **99** (1), 153 (1993), doi:10.1063/1.465795.
- [12] A. H. ZEWAIL, Femtochemistry: Atomic-Scale Dynamics of the Chemical Bond, *J. Phys. Chem. A*, **104** (24), 5660 (2000), doi:10.1021/jp001460h.

- [13] N. SAITO, H. SANNOHE, N. ISHII, T. KANAI, N. KOSUGI, Y. WU, A. CHEW, S. HAN, Z. CHANG, and J. ITATANI, Real-time observation of electronic, vibrational, and rotational dynamics in nitric oxide with attosecond soft x-ray pulses at 400 eV, *Optica*, **6** (12), 1542 (2019), doi:10.1364/OPTICA.6.001542.
- [14] Z.-H. LOH, ET AL., Observation of the fastest chemical processes in the radiolysis of water, *Science*, **367** (6474), 179 (2020), doi:10.1126/science.aaz4740.
- [15] M. NISOLI and G. SANSONE, New frontiers in attosecond science, *Prog. Quantum Electron.*, **33** (1), 17 (2009), doi:10.1016/j.pquantelec.2008.10.004.
- [16] E. GOULIELMAKIS, ET AL., Real-time observation of valence electron motion, *Nature*, **466** (7307), 739 (2010), doi:10.1038/nature09212.
- [17] F. KRAUSZ and M. IVANOV, Attosecond physics, *Rev. Mod. Phys.*, **81** (1), 163 (2009), doi:10.1103/RevModPhys.81.163.
- [18] M. NISOLI, P. DECLEVA, F. CALEGARI, A. PALACIOS, and F. MARTÍN, Attosecond Electron Dynamics in Molecules, *Chem. Rev.*, **117** (16), 10760 (2017), doi:10.1021/acs.chemrev.6b00453.
- [19] M. HENTSCHEL, R. KIENBERGER, CH. SPIELMANN, G. A. REIDER, N. MILOSEVIC, T. BRABEC, P. CORKUM, U. HEINZMANN, M. DRESCHER, and F. KRAUSZ, Attosecond metrology, *Nature*, **414**, 509 (2001), doi:10.1038/35107000.
- [20] R. KIENBERGER, ET AL., Atomic transient recorder, *Nature*, **427** (6977), 817 (2004), doi:10.1038/nature02277.
- [21] I. GRGURAŠ, ET AL., Ultrafast X-ray pulse characterization at free-electron lasers, *Nat. Photonics*, **6** (12), 852 (2012), doi:10.1038/nphoton.2012.276.
- [22] T. GAUMNITZ, A. JAIN, Y. PERTOT, M. HUPPERT, I. JORDAN, F. ARDANA-LAMAS, and H. J. WÖRNER, Streaking of 43-attosecond soft-X-ray pulses generated by a passively CEP-stable mid-infrared driver, *Opt. Express*, **25** (22), 27506 (2017), doi:10.1364/OE.25.027506.
- [23] T. SCHULTZ and M. VRAKING (eds.), *Attosecond and XUV Physics: Ultrafast Dynamics and Spectroscopy*, Wiley-VCH, Weinheim (2014).
- [24] L. YOUNG, ET AL., Roadmap of ultrafast x-ray atomic and molecular physics, *J. Phys. B*, **51** (3), 032003 (2018), doi:10.1088/1361-6455/aa9735.
- [25] G. SANSONE, ET AL., Electron localization following attosecond molecular photoionization, *Nature*, **465** (7299), 763 (2010), doi:10.1038/nature09084.

- [26] F. LÉPINE, M. Y. IVANOV, and M. J. J. VRAKING, Attosecond molecular dynamics: Fact or fiction?, *Nat. Photonics*, **8** (3), 195 (2014), doi:10.1038/nphoton.2014.25.
- [27] F. CALEGARI, ET AL., Ultrafast electron dynamics in phenylalanine initiated by attosecond pulses, *Science*, **346** (6207), 336 (2014), doi:10.1126/science.1254061.
- [28] H. J. WÖRNER, ET AL., Charge migration and charge transfer in molecular systems, *Struct. Dyn.*, **4** (6), 061508 (2017), doi:10.1063/1.4996505.
- [29] E. PERFETTO, A. TRABATTONI, F. CALEGARI, M. NISOLI, A. MARINI, and G. STEFANUCCI, Ultrafast Quantum Interference in the Charge Migration of Tryptophan, *J. Phys. Chem. Lett.*, **11** (3), 891 (2020), doi:10.1021/acs.jpcclett.9b03517.
- [30] F. REMACLE and R. D. LEVINE, An electronic time scale in chemistry, *Proc. Natl. Acad. Sci*, **103** (18), 6793 (2006), doi:10.1073/pnas.0601855103.
- [31] V. MAY and O. KÜHN, *Charge and Energy Transfer Dynamics in Molecular Systems*, Wiley-VCH, Weinheim (2011).
- [32] D. MENDIVE-TAPIA, M. VACHER, M. BEARPARK, and M. A. ROBB, Coupled electron-nuclear dynamics: Charge migration and charge transfer initiated near a conical intersection, *J. Chem. Phys.*, **139**, 044110 (2013), doi:10.1063/1.4815914.
- [33] M. VACHER, L. STEINBERG, A. J. JENKINS, M. J. BEARPARK, and M. A. ROBB, Electron dynamics following photoionization: Decoherence due to the nuclear-wavepacket width, *Phys. Rev. A*, **92**, 040502 (2015), doi:10.1103/PhysRevA.92.040502.
- [34] C. ARNOLD, O. VENDRELL, and R. SANTRA, Electronic decoherence following photoionization: Full quantum-dynamical treatment of the influence of nuclear motion, *Phys. Rev. A*, **95** (3), 033425 (2017), doi:10.1103/PhysRevA.95.033425.
- [35] L. YANG, J. R. REIMERS, R. KOBAYASHI, and N. S. HUSH, Competition between charge migration and charge transfer induced by nuclear motion following core ionization: Model systems and application to Li_2^+ , *J. Chem. Phys.*, **151** (12), 124108 (2019), doi:10.1063/1.5117246.
- [36] CH. BRESSLER, ET AL., Femtosecond XANES Study of the Light-Induced Spin Crossover Dynamics in an Iron(II) Complex, *Science*, **323**, 489 (2009), doi:10.1126/science.1165733.
- [37] C. M. MARIAN, Spin-orbit coupling and intersystem crossing in molecules, *WIREs Comput. Mol. Sci.*, **2** (2), 187 (2012), doi:10.1002/wcms.83.

- [38] Z. LI, O. VENDRELL, and R. SANTRA, Ultrafast Charge Transfer of a Valence Double Hole in Glycine Driven Exclusively by Nuclear Motion, *Phys. Rev. Lett.*, **115**, 143002 (2015), doi:10.1103/PhysRevLett.115.143002.
- [39] O. SMIRNOVA, S. PATCHKOVSKII, Y. MAIRESSE, N. DUDOVICH, and M. Y. IVANOV, Strong-field control and spectroscopy of attosecond electron-hole dynamics in molecules, *Proc. Natl. Acad. Sci.*, **106** (39), 16556 (2009), doi:10.1073/pnas.0907434106.
- [40] C. ARNOLD, C. LARIVIÈRE-LOISELLE, K. KHALILI, L. INHESTER, R. WELSCH, and R. SANTRA, Molecular electronic decoherence following attosecond photoionisation, *J. Phys. B*, **53** (16), 164006 (2020), doi:10.1088/1361-6455/ab9658.
- [41] A. RUDENKO, ET AL., Femtosecond response of polyatomic molecules to ultra-intense hard X-rays, *Nature*, **546** (7656), 129 (2017), doi:10.1038/nature22373.
- [42] H. WANG, S. I. BOKAREV, S. G. AZIZ, and O. KÜHN, Ultrafast Spin-State Dynamics in Transition-Metal Complexes Triggered by Soft-X-Ray Light, *Phys. Rev. Lett.*, **118** (2), 023001 (2017), doi:10.1103/PhysRevLett.118.023001.
- [43] H. WANG, T. MÖHLE, O. KÜHN, and S. I. BOKAREV, Ultrafast dissipative spin-state dynamics triggered by x-ray pulse trains, *Phys. Rev. A*, **98** (1), 013408 (2018), doi:10.1103/PhysRevA.98.013408.
- [44] A. HAUSER, Intersystem crossing in Fe(II) coordination compounds, *Coord. Chem. Rev.*, **111**, 275 (1991), doi:10.1016/0010-8545(91)84034-3.
- [45] L. S. FORSTER, Intersystem crossing in transition metal complexes, *Coord. Chem. Rev.*, **250** (15-16), 2023 (2006), doi:10.1016/j.ccr.2006.01.023.
- [46] M. CAMMARATA, ET AL., Sequential Activation of Molecular Breathing and Bending during Spin-Crossover Photoswitching Revealed by Femtosecond Optical and X-Ray Absorption Spectroscopy, *Phys. Rev. Lett.*, **113** (22), 227402 (2014), doi:10.1103/PhysRevLett.113.227402.
- [47] S. MAI and L. GONZÁLEZ, Unconventional two-step spin relaxation dynamics of $[\text{Re}(\text{CO})_3(\text{im})(\text{phen})]^+$ in aqueous solution, *Chem. Sci.*, **10**, 10405 (2019), doi:10.1039/C9SC03671G.
- [48] H. WANG, S. I. BOKAREV, S. G. AZIZ, and O. KÜHN, Density matrix-based time-dependent configuration interaction approach to ultrafast spin-flip dynamics, *Mol. Phys.*, **115** (15-16), 1898 (2017), doi:10.1080/00268976.2017.1294267.
- [49] A. D. MCLACHLAN, A variational solution of the time-dependent Schrodinger equation, *Mol. Phys.*, **8** (1), 39 (1964), doi:10.1080/00268976400100041.

- [50] A. S. MOSKALENKO, Z.-G. ZHU, and J. BERAKDAR, Charge and spin dynamics driven by ultrashort extreme broadband pulses: A theory perspective, *Phys. Rep.*, **672**, 1 (2017), doi:10.1016/j.physrep.2016.12.005.
- [51] J. J. GOINGS, P. J. LESTRANGE, and X. LI, Real-time time-dependent electronic structure theory, *Wiley Interdiscip. Rev.: Comput. Mol. Sci.*, **8** (1), e1341 (2018), doi:10.1002/wcms.1341.
- [52] X. LI, N. GOVIND, C. ISBORN, A. E. DEPRINCE, and K. LOPATA, Real-Time Time-Dependent Electronic Structure Theory, *Chem. Rev.*, **120** (18), 9951 (2020), doi:10.1021/acs.chemrev.0c00223.
- [53] P. SAALFRANK, F. BEDURKE, C. HEIDE, T. KLAMROTH, S. KLINKUSCH, P. KRAUSE, M. NEST, and J. C. TREMBLAY, Molecular attochemistry: Correlated electron dynamics driven by light, in *Advances in Quantum Chemistry*, volume 81, pages 15–50, Elsevier (2020), doi:10.1016/bs.aiq.2020.03.001.
- [54] R. MARQUARDT and M. QUACK, Foundations of Time Dependent Quantum Dynamics of Molecules Under Isolation and in Coherent Electromagnetic Fields, in *Molecular Spectroscopy and Quantum Dynamics*, pages 1–41, Elsevier (2021), doi:10.1016/B978-0-12-817234-6.00006-4.
- [55] P. KRAUSE, T. KLAMROTH, and P. SAALFRANK, Time-dependent configuration-interaction calculations of laser-pulse-driven many-electron dynamics: Controlled dipole switching in lithium cyanide, *J. Chem. Phys.*, **123** (7), 074105 (2005), doi:10.1063/1.1999636.
- [56] T. KLAMROTH, Laser-driven electron transfer through metal-insulator-metal contacts: Time-dependent configuration interaction singles calculations for a jellium model, *Phys. Rev. B*, **68** (24), 245421 (2003), doi:10.1103/PhysRevB.68.245421.
- [57] L. GREENMAN, P. J. HO, S. PABST, E. KAMARCHIK, D. A. MAZZIOTTI, and R. SANTRA, Implementation of the time-dependent configuration-interaction singles method for atomic strong-field processes, *Phys. Rev. A*, **82** (2), 023406 (2010), doi:10.1103/PhysRevA.82.023406.
- [58] T. SATO and K. L. ISHIKAWA, Time-dependent complete-active-space self-consistent-field method for multielectron dynamics in intense laser fields, *Phys. Rev. A*, **88** (2), 023402 (2013), doi:10.1103/PhysRevA.88.023402.
- [59] A. SZABO and N. S. OSTLUND, *Modern Quantum Chemistry*, Dover Publications, Inc., Mineola, N.Y., 1, revised edition (1996).

- [60] H. MIYAGI and L. B. MADSEN, Time-dependent restricted-active-space self-consistent-field theory for laser-driven many-electron dynamics, *Phys. Rev. A*, **87** (6), 062511 (2013), doi:10.1103/PhysRevA.87.062511.
- [61] S. BAUCH, L. K. SØRENSEN, and L. B. MADSEN, Time-dependent generalized-active-space configuration-interaction approach to photoionization dynamics of atoms and molecules, *Phys. Rev. A*, **90** (6), 062508 (2014), doi:10.1103/PhysRevA.90.062508.
- [62] M. NEST, T. KLAMROTH, and P. SAALFRANK, The multiconfiguration time-dependent Hartree–Fock method for quantum chemical calculations, *Journal Chemical Physics*, **122** (12), 124102 (2005), doi:10.1063/1.1862243.
- [63] T. KATO and HIROHIKO KONO, Time-dependent multiconfiguration theory for electronic dynamics of molecules in intense laser fields: A description in terms of numerical orbital functions, *J. Chem. Phys.*, **128** (18), 184102 (2008), doi:10.1063/1.2912066.
- [64] H.-D. MEYER, U. MANTHE, and L. CEDERBAUM, The multi-configurational time-dependent Hartree approach, *Chem. Phys. Lett.*, **165** (1), 73 (1990), doi:10.1016/0009-2614(90)87014-I.
- [65] M. BECK, The multiconfiguration time-dependent Hartree (MCTDH) method: A highly efficient algorithm for propagating wavepackets, *Phys. Rep.*, **324** (1), 1 (2000), doi:10.1016/S0370-1573(99)00047-2.
- [66] V. DESPRÉ, N. V. GOLUBEV, and A. I. KULEFF, Charge Migration in Propiolic Acid: A Full Quantum Dynamical Study, *Phys. Rev. Lett.*, **121** (20), 203002 (2018), doi:10.1103/PhysRevLett.121.203002.
- [67] J. SCHIRMER, L. S. CEDERBAUM, and O. WALTER, New approach to the one-particle Green’s function for finite Fermi systems, *Phys. Rev. A*, **28** (3), 1237 (1983), doi:10.1103/PhysRevA.28.1237.
- [68] J. WENZEL, M. WORMIT, and A. DREUW, Calculating core-level excitations and x-ray absorption spectra of medium-sized closed-shell molecules with the algebraic-diagrammatic construction scheme for the polarization propagator, *J. Comput. Chem.*, **35** (26), 1900 (2014), doi:10.1002/jcc.23703.
- [69] A. I. KULEFF, J. BREIDBACH, and L. S. CEDERBAUM, Multielectron wave-packet propagation: General theory and application, *J. Chem. Phys.*, **123** (4), 044111 (2005), doi:10.1063/1.1961341.
- [70] V. DESPRE, A. MARCINIAK, V. LORIOT, M. C. E. GALBRAITH, A. ROUZE E, M. J. J. VRAKING, LÉPINE, F., and A. I. KULEFF, Attosecond Hole Migration in

- Benzene Molecules Surviving Nuclear Motion, *J. Phys. Chem. Lett.*, **6**, 426 (2015), doi:10.1021/jz502493j.
- [71] N. E. DAHLEN and R. VAN LEEUWEN, Solving the Kadanoff-Baym Equations for Inhomogeneous Systems: Application to Atoms and Molecules, *Phys. Rev. Lett.*, **98** (15), 153004 (2007), doi:10.1103/PhysRevLett.98.153004.
- [72] K. BALZER, S. BAUCH, and M. BONITZ, Time-dependent second-order Born calculations for model atoms and molecules in strong laser fields, *Phys. Rev. A*, **82** (3), 033427 (2010), doi:10.1103/PhysRevA.82.033427.
- [73] P. HOODBHOY and J. W. NEGELE, Time-dependent coupled-cluster approximation to nuclear dynamics. I. Application to a solvable model, *Phys. Rev. C*, **18** (5), 2380 (1978), doi:10.1103/PhysRevC.18.2380.
- [74] D. R. NASCIMENTO and A. E. DEPRINCE, Simulation of Near-Edge X-ray Absorption Fine Structure with Time-Dependent Equation-of-Motion Coupled-Cluster Theory, *J. Phys. Chem. Lett.*, **8** (13), 2951 (2017), doi:10.1021/acs.jpcclett.7b01206.
- [75] S. KVAAL, *Ab Initio* quantum dynamics using coupled-cluster, *J. Chem. Phys.*, **136** (19), 194109 (2012), doi:10.1063/1.4718427.
- [76] A. S. SKEIDSVOLL, T. MOITRA, A. BALBI, A. C. PAUL, S. CORIANI, and H. KOCH, Simulating weak-field attosecond processes with a Lanczos reduced basis approach to time-dependent equation-of-motion coupled-cluster theory, *Phys. Rev. A*, **105** (2), 023103 (2022), doi:10.1103/PhysRevA.105.023103.
- [77] J. HAEGEMAN, C. LUBICH, I. OSELEDETS, B. VANDEREYCKEN, and F. VERSTRAETE, Unifying time evolution and optimization with matrix product states, *Phys. Rev. B*, **94** (16), 165116 (2016), doi:10.1103/PhysRevB.94.165116.
- [78] A. BAIARDI and M. REIHER, Large-Scale Quantum Dynamics with Matrix Product States, *J. Chem. Theory Comput.*, **15** (6), 3481 (2019), doi:10.1021/acs.jctc.9b00301.
- [79] L.-H. FRAHM and D. PFANNKUCHE, Ultrafast *ab Initio* Quantum Chemistry Using Matrix Product States, *J. Chem. Theory Comput.*, **15** (4), 2154 (2019), doi:10.1021/acs.jctc.8b01291.
- [80] A. BAIARDI, Electron Dynamics with the Time-Dependent Density Matrix Renormalization Group, *J. Chem. Theory Comput.*, **17** (6), 3320 (2021), doi:10.1021/acs.jctc.0c01048.
- [81] W. KOHN and L. J. SHAM, Self-Consistent Equations Including Exchange and Correlation Effects, *Phys. Rev.*, **140** (4A), A1133 (1965), doi:10.1103/PhysRev.140.A1133.

- [82] S. KÜMMEL and L. KRONIK, Orbital-dependent density functionals: Theory and applications, *Rev. Mod. Phys.*, **80** (1), 3 (2008), doi:10.1103/RevModPhys.80.3.
- [83] K. LOPATA, B. E. VAN KUIKEN, M. KHALIL, and N. GOVIND, Linear-Response and Real-Time Time-Dependent Density Functional Theory Studies of Core-Level Near-Edge X-Ray Absorption, *J. Chem. Theor. Comput.*, **8** (9), 3284 (2012), doi:10.1021/ct3005613.
- [84] M. R. PROVORSE and C. M. ISBORN, Electron dynamics with real-time time-dependent density functional theory, *Int. J. Quantum Chem.*, **116** (10), 739 (2016), doi:10.1002/qua.25096.
- [85] M. BERMAN and R. KOSLOFF, Time-dependent solution of the Liouville-von Neumann equation: Non-dissipative evolution, *Comput. Phys. Commun.*, **63** (1-3), 1 (1991), doi:10.1016/0010-4655(91)90233-B.
- [86] O. KÜHN, V. MAY, and M. SCHREIBER, Dissipative vibrational dynamics in a curve-crossing system, *J. Chem. Phys.*, **101** (12), 10404 (1994), doi:10.1063/1.467921.
- [87] M. BERMAN, R. KOSLOFF, and H. TAL-EZER, Solution of the time-dependent Liouville-von Neumann equation: Dissipative evolution, *J. Phys. A: Math. Gen.*, **25** (5), 1283 (1992), doi:10.1088/0305-4470/25/5/031.
- [88] X. FAN, A. WEI, T. KLAMROTH, Y. ZHANG, K. GAO, and L. WANG, Ultrafast multi-exciton dynamics in molecular systems: Inclusion of exciton-exciton annihilation, *Phys. Rev. B*, **107** (13), 134301 (2023), doi:10.1103/PhysRevB.107.134301.
- [89] J. C. TREMBLAY, T. KLAMROTH, and P. SAALFRANK, Time-dependent configuration-interaction calculations of laser-driven dynamics in presence of dissipation, *J. Chem. Phys.*, **129** (8), 084302 (2008), doi:10.1063/1.2972126.
- [90] J. C. TREMBLAY, S. KLINKUSCH, T. KLAMROTH, and P. SAALFRANK, Dissipative many-electron dynamics of ionizing systems, *J. Chem. Phys.*, **134** (4), 044311 (2011), doi:10.1063/1.3532410.
- [91] T. ZELOVICH, L. KRONIK, and O. HOD, State Representation Approach for Atomistic Time-Dependent Transport Calculations in Molecular Junctions, *J. Chem. Theory Comput.*, **10** (8), 2927 (2014), doi:10.1021/ct500135e.
- [92] M. F. GELIN, A. V. PISLIAKOV, D. EGOROVA, and W. DOMCKE, A simple model for the calculation of nonlinear optical response functions and femtosecond time-resolved spectra, *J. Chem. Phys.*, **118** (12), 5287 (2003), doi:10.1063/1.1547751.

- [93] S. MUKAMEL, D. HEALION, Y. ZHANG, and J. D. BIGGS, Multidimensional Attosecond Resonant X-Ray Spectroscopy of Molecules: Lessons from the Optical Regime, *Annu. Rev. Phys. Chem.*, **64** (1), 101 (2013), doi:10.1146/annurev-physchem-040412-110021.
- [94] H. ANDO, B. P. FINGERHUT, K. E. DORFMAN, J. D. BIGGS, and S. MUKAMEL, Femtosecond Stimulated Raman Spectroscopy of the Cyclobutane Thymine Dimer Repair Mechanism: A Computational Study, *J. Am. Chem. Soc.*, **136** (42), 14801 (2014), doi:10.1021/ja5063955.
- [95] Y. ZHANG, W. HUA, K. BENNETT, and S. MUKAMEL, Nonlinear Spectroscopy of Core and Valence Excitations Using Short X-Ray Pulses: Simulation Challenges, *Top. Curr. Chem.*, **368**, 273 (2015).
- [96] B. DROMEY, ET AL., High harmonic generation in the relativistic limit, *Nature Phys.*, **2** (7), 456 (2006), doi:10.1038/nphys338.
- [97] P. B. CORKUM and F. KRAUSZ, Attosecond science, *Nature Phys.*, **3** (6), 381 (2007), doi:10.1038/nphys620.
- [98] S. GHIMIRE, A. D. DI CHIARA, E. SISTRUNK, P. AGOSTINI, L. F. DIMAURO, and D. A. REIS, Observation of high-order harmonic generation in a bulk crystal, *Nature Phys.*, **7** (2), 138 (2011), doi:10.1038/nphys1847.
- [99] G. NDABASHIMIYE, S. GHIMIRE, M. WU, D. A. BROWNE, K. J. SCHAFER, M. B. GAARDE, and D. A. REIS, Solid-state harmonics beyond the atomic limit, *Nature*, **534** (7608), 520 (2016), doi:10.1038/nature17660.
- [100] H. LAKHOTIA, H. Y. KIM, M. ZHAN, S. HU, S. MENG, and E. GOULIELMAKIS, Laser picoscopy of valence electrons in solids, *Nature*, **583** (7814), 55 (2020), doi:10.1038/s41586-020-2429-z.
- [101] H. NIIKURA, F. LÉGARÉ, R. HASBANI, A. D. BANDRAUK, M. Y. IVANOV, D. M. VILLENEUVE, and P. B. CORKUM, Sub-laser-cycle electron pulses for probing molecular dynamics, *Nature*, **417** (6892), 917 (2002), doi:10.1038/nature00787.
- [102] J. ITATANI, J. LEVESQUE, D. ZEIDLER, H. NIIKURA, H. PÉPIN, J. C. KIEFFER, P. B. CORKUM, and D. M. VILLENEUVE, Tomographic imaging of molecular orbitals, *Nature*, **432** (7019), 867 (2004), doi:10.1038/nature03183.
- [103] D. M. VILLENEUVE, P. HOCKETT, M. J. J. VRAKING, and H. NIIKURA, Coherent imaging of an attosecond electron wave packet, *Science*, **356** (6343), 1150 (2017), doi:10.1126/science.aam8393.

- [104] O. SMIRNOVA, Y. MAIRESSE, S. PATCHKOVSKII, N. DUDOVICH, D. VILLENEUVE, P. CORKUM, and M. Y. IVANOV, High harmonic interferometry of multi-electron dynamics in molecules, *Nature*, **460** (7258), 972 (2009), doi:10.1038/nature08253.
- [105] M. RICHTER, J. GONZÁLEZ-VÁZQUEZ, Z. MAŠÍN, D. S. BRAMBILA, A. G. HARVEY, F. MORALES, and F. MARTÍN, Ultrafast imaging of laser-controlled non-adiabatic dynamics in NO₂ from time-resolved photoelectron emission, *Phys. Chem. Chem. Phys.*, **21** (19), 10038 (2019), doi:10.1039/C9CP00649D.
- [106] D. YOU, ET AL., New Method for Measuring Angle-Resolved Phases in Photoemission, *Phys. Rev. X*, **10** (3), 031070 (2020), doi:10.1103/PhysRevX.10.031070.
- [107] B. W. J. MCNEIL and N. R. THOMPSON, X-ray free-electron lasers, *Nature Photon.*, **4** (12), 814 (2010), doi:10.1038/nphoton.2010.239.
- [108] P. K. MAROJU, ET AL., Attosecond pulse shaping using a seeded free-electron laser, *Nature*, **578** (7795), 386 (2020), doi:10.1038/s41586-020-2005-6.
- [109] S. SERKEZ, G. GELONI, S. TOMIN, G. FENG, E. V. GRYZLOVA, A. N. GRUM-GRZHIMAILO, and M. MEYER, Overview of options for generating high-brightness attosecond x-ray pulses at free-electron lasers and applications at the European XFEL, *J. Opt.*, **20** (2), 024005 (2018), doi:10.1088/2040-8986/aa9f4f.
- [110] S. V. MILTON, ET AL., Exponential Gain and Saturation of a Self-Amplified Spontaneous Emission Free-Electron Laser, *Science*, **292** (5524), 2037 (2001), doi:10.1126/science.1059955.
- [111] C. MILNE, T. PENFOLD, and M. CHERGUI, Recent experimental and theoretical developments in time-resolved X-ray spectroscopies, *Coord. Chem. Rev.*, **277–278**, 44 (2014), doi:10.1016/j.ccr.2014.02.013.
- [112] P. WERNET, Chemical interactions and dynamics with femtosecond X-ray spectroscopy and the role of X-ray free-electron lasers, *Phil. Trans. R. Soc. A*, **377** (2145), 20170464 (2019), doi:10.1098/rsta.2017.0464.
- [113] A. A. LUTMAN, M. W. GUETG, T. J. MAXWELL, J. P. MACARTHUR, Y. DING, C. EMMA, J. KRZYWINSKI, A. MARINELLI, and Z. HUANG, High-Power Femtosecond Soft X Rays from Fresh-Slice Multistage Free-Electron Lasers, *Phys. Rev. Lett.*, **120** (26), 264801 (2018), doi:10.1103/PhysRevLett.120.264801.
- [114] J. DURIS, ET AL., Tunable isolated attosecond X-ray pulses with gigawatt peak power from a free-electron laser, *Nat. Photonics*, **14** (1), 30 (2020), doi:10.1038/s41566-019-0549-5.

- [115] M. LARA-ASTIASO, D. AYUSO, I. TAVERNELLI, P. DECLEVA, A. PALACIOS, and F. MARTÍN, Decoherence, control and attosecond probing of XUV-induced charge migration in biomolecules. A theoretical outlook, *Faraday Discuss.*, **194**, 41 (2016), doi:10.1039/C6FD00074F.
- [116] T. BARILLOT, ET AL., Correlation-Driven Transient Hole Dynamics Resolved in Space and Time in the Isopropanol Molecule, *Phys. Rev. X*, **11** (3), 031048 (2021), doi:10.1103/PhysRevX.11.031048.
- [117] M. DRESCHER, M. HENTSCHEL, R. KIENBERGER, M. UIBERACKER, V. YAKOVLEV, A. SCRINZI, TH. WESTERWALBESLOH, U. KLEINEBERG, U. HEINZMANN, and F. KRAUSZ, Time-resolved atomic inner-shell spectroscopy, *Nature*, **419**, 803 (2002), doi:10.1038/nature01143.
- [118] G. GRELL, ET AL., Effect of the shot-to-shot variation on charge migration induced by sub-fs x-ray free-electron laser pulses, *Phys. Rev. Research*, **5** (2), 023092 (2023), doi:10.1103/PhysRevResearch.5.023092.
- [119] M. REUNER and D. POPOVA-GORELOVA, Attosecond imaging of photoinduced dynamics in molecules using time-resolved photoelectron momentum microscopy, *Phys. Rev. A*, **107** (2), 023101 (2023), doi:10.1103/PhysRevA.107.023101.
- [120] M. UIBERACKER, ET AL., Attosecond real-time observation of electron tunnelling in atoms, *Nature*, **446** (7136), 627 (2007), doi:10.1038/nature05648.
- [121] J. ITATANI, F. QUÉRÉ, G. L. YUDIN, M. YU. IVANOV, F. KRAUSZ, and P. B. CORKUM, Attosecond Streak Camera, *Phys. Rev. Lett.*, **88** (17), 173903 (2002), doi:10.1103/PhysRevLett.88.173903.
- [122] A. L. CAVALIERI, ET AL., Attosecond spectroscopy in condensed matter, *Nature*, **449** (7165), 1029 (2007), doi:10.1038/nature06229.
- [123] M. SCHULTZE, ET AL., Delay in Photoemission, *Science*, **328** (5986), 1658 (2010), doi:10.1126/science.1189401.
- [124] B. WINTER and M. FAUBEL, Photoemission from Liquid Aqueous Solutions, *Chem. Rev.*, **106** (4), 1176 (2006), doi:10.1021/cr040381p.
- [125] B. WINTER, Liquid microjet for photoelectron spectroscopy, *Nucl. Instrum. Methods. Phys. Res. A*, **601** (1-2), 139 (2009), doi:10.1016/j.nima.2008.12.108.
- [126] C. BRESSLER and M. CHERGUI, Ultrafast X-ray Absorption Spectroscopy, *Chem. Rev.*, **104** (4), 1781 (2004), doi:10.1021/cr0206667.

- [127] L. YOUNG, ET AL., X-Ray Microprobe of Orbital Alignment in Strong-Field Ionized Atoms, *Phys. Rev. Lett.*, **97** (8), 083601 (2006), doi:10.1103/PhysRevLett.97.083601.
- [128] K. S. ZINCHENKO, F. ARDANA-LAMAS, I. SEIDU, S. P. NEVILLE, J. VAN DER VEEN, V. U. LANFALONI, M. S. SCHUURMAN, and H. J. WÖRNER, Sub-7-femtosecond conical-intersection dynamics probed at the carbon K-edge, *Science*, **371** (6528), 489 (2021), doi:10.1126/science.abf1656.
- [129] M. J. FRISCH, ET AL., Gaussian 16 Rev. C.01 (2016).
- [130] G. LI MANNI, ET AL., The OpenMolcas *Web* : A Community-Driven Approach to Advancing Computational Chemistry, *J. Chem. Theory Comput.* (2023), doi:10.1021/acs.jctc.3c00182.
- [131] M. BORN and R. OPPENHEIMER, Zur Quantentheorie der Molekeln, *Ann. Phys.*, **389** (20), 457 (1927), doi:10.1002/andp.19273892002.
- [132] V. FOCK, Näherungsmethode zur Lösung des quantenmechanischen Mehrkörperproblems, *Z. Physik*, **61** (1-2), 126 (1930), doi:10.1007/BF01340294.
- [133] D. R. HARTREE and F.R.S., The calculation of atomic structures, *Rep. Prog. Phys.*, **11** (1), 113 (1947), doi:10.1088/0034-4885/11/1/305.
- [134] T. HELGAKER, P. JØRGENSEN, and J. OLSEN, *Molecular Electronic-Structure Theory* (2000).
- [135] B. O. ROOS, R. LINDH, P.-Å. MALMQVIST, V. VERYAZOV, and P.-O. WIDMARK, New Relativistic ANO Basis Sets for Transition Metal Atoms, *J. Phys. Chem. A*, **109** (29), 6575 (2005), doi:10.1021/jp0581126.
- [136] T. B. PEDERSEN, I. F. GALVÁN, and R. LINDH, The versatility of Cholesky decomposition of electron repulsion integrals, Preprint, Chemistry (2023), doi:10.26434/chemrxiv-2023-579sk.
- [137] B. O. ROOS, R. LINDH, P. Å. MALMQVIST, V. VERYAZOV, and P.-O. WIDMARK, *Multiconfigurational Quantum Chemistry*, Wiley, Hoboken, New Jersey (2016).
- [138] R. F. K. SPADA, M. P. FRANCO, R. NIEMAN, A. J. A. AQUINO, R. SHEPARD, F. PLASSER, and H. LISCHKA, Spin-density calculation via the graphical unitary group approach, *Mol. Phys.*, page e2091049 (2022), doi:10.1080/00268976.2022.2091049.
- [139] P.-Å. MALMQVIST, B. O. ROOS, and B. SCHIMMELPFENNIG, The restricted active space (RAS) state interaction approach with spin-orbit coupling, *Chem. Phys. Lett.*, **357**, 230 (2002), doi:10.1016/S0009-2614(02)00498-0.

- [140] P.-Å. MALMQVIST, A. RENDELL, and B. O. ROOS, The restricted active space self-consistent-field method, implemented with a split graph unitary group approach, *J. Phys. Chem.*, **94** (14), 5477 (1990), doi:10.1021/j100377a011.
- [141] B. O. ROOS, *Björn O. Roos Lecture Notes in Quantum Chemistry European Summer School in Quantum Chemistry*, Springer-Verlag, Lund (1992).
- [142] V. VERYAZOV, P. Å. MALMQVIST, and B. O. ROOS, How to select active space for multiconfigurational quantum chemistry?, *Int. J. Quant. Chem.*, **111** (13), 3329 (2011), doi:10.1002/qua.23068.
- [143] D. CASANOVA, Restricted active space configuration interaction methods for strong correlation: Recent developments, *WIREs Comput Mol Sci*, **12** (1) (2022), doi:10.1002/wcms.1561.
- [144] W. KUTZELNIGG, *Einführung in Die Theoretische Chemie*, Wiley-VCH, Weinheim, Germany (2002).
- [145] CHR. MØLLER and M. S. PLESSET, Note on an Approximation Treatment for Many-Electron Systems, *Phys. Rev.*, **46** (7), 618 (1934), doi:10.1103/PhysRev.46.618.
- [146] K. ANDERSSON, P.-Å. MALMQVIST, B. O. ROOS, A. J. SADLEJ, and K. WOLINSKI, Second-order perturbation theory with a CASSCF reference function, *J. Phys. Chem.*, **94** (14), 5483 (1990), doi:10.1021/j100377a012.
- [147] P. Å. MALMQVIST, K. PIERLOOT, A. R. M. SHAHI, C. J. CRAMER, and L. GAGLIARDI, The restricted active space followed by second-order perturbation theory method: Theory and application to the study of CuO₂ and Cu₂O₂ systems, *J. Chem. Phys.*, **128** (20), 204109 (2008), doi:10.1063/1.2920188.
- [148] S. BATTAGLIA and R. LINDH, Extended Dynamically Weighted CASPT2: The Best of Two Worlds, *J. Chem. Theory Comput.*, page acs.jctc.9b01129 (2020), doi:10.1021/acs.jctc.9b01129.
- [149] S. BATTAGLIA, I. FDEZ. GALVÁN, and R. LINDH, Multiconfigurational quantum chemistry: The CASPT2 method, in *Theoretical and Computational Photochemistry*, pages 135–162, Elsevier (2023), doi:10.1016/B978-0-323-91738-4.00016-6.
- [150] B. O. ROOS and K. ANDERSSON, Multiconfigurational perturbation theory with level shift — the Cr₂ potential revisited, *Chem. Phys. Lett.*, **245** (2-3), 215 (1995), doi:10.1016/0009-2614(95)01010-7.
- [151] N. FORSBERG and P.-Å. MALMQVIST, Multiconfiguration Perturbation Theory with Imaginary Level Shift, *Chem. Phys. Lett.*, **274**, 196 (1997), doi:10.1016/S0009-2614(97)00669-6.

- [152] J. FINLEY, P. Å. MALMQVIST, B. O. ROOS, and L. SERRANO-ANDRÉS, The multi-state CASPT2 method, *Chem. Phys. Lett.*, **288**, 299 (1998), doi:10.1016/S0009-2614(98)00252-8.
- [153] A. A. GRANOVSKY, Extended multi-configuration quasi-degenerate perturbation theory: The new approach to multi-state multi-reference perturbation theory, *J. Chem. Phys.*, **134** (21), 214113 (2011), doi:10.1063/1.3596699.
- [154] P.-Å. MALMQVIST and B. O. ROOS, The CASSCF state interaction method, *Chem. Phys. Lett.*, **155** (2), 189 (1989), doi:10.1016/0009-2614(89)85347-3.
- [155] M. DOUGLAS and N. M. KROLL, Quantum electrodynamical corrections to the fine structure of helium, *Ann. Phys.*, **82** (1), 89 (1974), doi:10.1016/0003-4916(74)90333-9.
- [156] B. SCHIMMELPFENNIG, AMFI, An Atomic Mean-Field Spin-Orbit Integral Program (1996).
- [157] BERND. A. HESS, C. M. MARIAN, U. WAHLGREN, and O. GROPEN, A mean-field spin-orbit method applicable to correlated wavefunctions, *Chem. Phys. Lett.*, **251**, 365 (1996), doi:10.1016/0009-2614(96)00119-4.
- [158] O. CHRISTIANSEN, J. GAUSS, and B. SCHIMMELPFENNIG, Spin-orbit coupling constants from coupled-cluster response theory, *Phys. Chem. Chem. Phys.*, **2** (5), 965 (2000), doi:10.1039/a908995k.
- [159] A. CARRERAS, H. JIANG, P. POKHILKO, A. I. KRYLOV, P. M. ZIMMERMAN, and D. CASANOVA, Calculation of spin-orbit couplings using RASCI spinless one-particle density matrices: Theory and applications, *J. Chem. Phys.*, **153** (21), 214107 (2020), doi:10.1063/5.0029146.
- [160] R. MCWEENY, On the Origin of Spin-Hamiltonian Parameters, *J. Chem. Phys.*, **42** (5), 1717 (1965), doi:10.1063/1.1696183.
- [161] B. L. SILVER, *Irreducible Tensor Methods: An Introduction for Chemists*, number v. 36 in Physical Chemistry, a Series of Monographs, Academic Press, New York (1976).
- [162] G. GRELL, O. KÜHN, and S. I. BOKAREV, Multireference quantum chemistry protocol for simulating autoionization spectra: Test of ionization continuum models for the neon atom, *Phys. Rev. A*, **100** (4), 042512 (2019), doi:10.1103/PhysRevA.100.042512.
- [163] B. N. C. TENORIO, T. A. VOSS, S. I. BOKAREV, P. DECLEVA, and S. CORIANI, Multireference Approach to Normal and Resonant Auger Spectra Based on the One-Center Approximation, *J. Chem. Theory Comput.*, **18** (7), 4387 (2022), doi:10.1021/acs.jctc.2c00252.

- [164] G. GRELL, S. I. BOKAREV, B. WINTER, R. SEIDEL, E. F. AZIZ, S. G. AZIZ, and O. KÜHN, Multi-reference approach to the calculation of photoelectron spectra including spin-orbit coupling, *J. Chem. Phys.*, **143** (7), 074104 (2015), doi:10.1063/1.4928511.
- [165] I. I. SOBEL'MAN, *Introduction to the Theory of Atomic Spectra* (1972).
- [166] K. BLUM, *Density Matrix Theory and Applications*, volume 64 of *Springer Series on Atomic, Optical, and Plasma Physics*, Springer Berlin Heidelberg, Berlin, Heidelberg (2012).
- [167] A. CASTRO, M. A. L. MARQUES, and A. RUBIO, Propagators for the time-dependent Kohn–Sham equations, *J. Chem. Phys.*, **121** (8), 3425 (2004), doi:10.1063/1.1774980.
- [168] K. LOPATA and N. GOVIND, Modeling Fast Electron Dynamics with Real-Time Time-Dependent Density Functional Theory: Application to Small Molecules and Chromophores, *J. Chem. Theory Comput.*, **7** (5), 1344 (2011), doi:10.1021/ct200137z.
- [169] A. GÓMEZ PUEYO, M. A. L. MARQUES, A. RUBIO, and A. CASTRO, Propagators for the Time-Dependent Kohn–Sham Equations: Multistep, Runge–Kutta, Exponential Runge–Kutta, and Commutator Free Magnus Methods, *J. Chem. Theory Comput.*, **14** (6), 3040 (2018), doi:10.1021/acs.jctc.8b00197.
- [170] C. MOLER and C. VAN LOAN, Nineteen Dubious Ways to Compute the Exponential of a Matrix, Twenty-Five Years Later, *SIAM Review*, **45** (1), 3 (2003), doi:10.1137/S00361445024180.
- [171] S. MUKAMEL, *Principles of Nonlinear Optical Spectroscopy*, Oxford Univ. Press, New York (1999).
- [172] H. TAL-EZER and R. KOSLOFF, An accurate and efficient scheme for propagating the time dependent Schrödinger equation, *J. Chem. Phys.*, **81** (9), 3967 (1984), doi:10.1063/1.448136.
- [173] S. GHOSH, A. ANDERSEN, L. GAGLIARDI, C. J. CRAMER, and N. GOVIND, Modeling Optical Spectra of Large Organic Systems Using Real-Time Propagation of Semiempirical Effective Hamiltonians, *J. Chem. Theory Comput.*, **13** (9), 4410 (2017), doi:10.1021/acs.jctc.7b00618.
- [174] R. KOSLOFF, Time-dependent quantum-mechanical methods for molecular dynamics, *J. Phys. Chem.*, **92** (8), 2087 (1988), doi:10.1021/j100319a003.
- [175] W. H. PRESS (ed.), *FORTTRAN Numerical Recipes*, Cambridge University Press, Cambridge, New York, 2nd ed edition (1996).

- [176] J. R. CASH and A. H. KARP, A variable order Runge-Kutta method for initial value problems with rapidly varying right-hand sides, *ACM Trans. Math. Softw.*, **16** (3), 201 (1990), doi:10.1145/79505.79507.
- [177] A. ALVERMANN, H. FEHSKE, and P. B. LITTLEWOOD, Numerical time propagation of quantum systems in radiation fields, *New J. Phys.*, **14** (10), 105008 (2012), doi:10.1088/1367-2630/14/10/105008.
- [178] S. BLANES and P. MOAN, Fourth- and sixth-order commutator-free Magnus integrators for linear and non-linear dynamical systems, *Appl. Numer. Math.*, **56** (12), 1519 (2006), doi:10.1016/j.apnum.2005.11.004.
- [179] A. ALVERMANN and H. FEHSKE, High-order commutator-free exponential time-propagation of driven quantum systems, *J. Comput. Phys.*, **230** (15), 5930 (2011), doi:10.1016/j.jcp.2011.04.006.
- [180] J. JAKOWSKI and K. MOROKUMA, Liouville–von Neumann molecular dynamics, *J. Chem. Phys.*, **130** (22), 224106 (2009), doi:10.1063/1.3152120.
- [181] 4.2.49. RHODYN — Molcas Manual (version 23.02), <https://molcas.gitlab.io/OpenMolcas/sphinx/users.guide/programs/rhodyn.html>.
- [182] B. F. MURPHY, ET AL., Femtosecond X-ray-induced explosion of C₆₀ at extreme intensity, *Nat. Commun.*, **5** (1), 4281 (2014), doi:10.1038/ncomms5281.
- [183] E. LUPPI and M. HEAD-GORDON, The role of Rydberg and continuum levels in computing high harmonic generation spectra of the hydrogen atom using time-dependent configuration interaction, *J. Chem. Phys.*, **139** (16), 164121 (2013), doi:10.1063/1.4824482.
- [184] E. COCCIA, B. MUSSARD, M. LABEYE, J. CAILLAT, R. TAÏEB, J. TOULOUSE, and E. LUPPI, Gaussian continuum basis functions for calculating high-harmonic generation spectra, *Int. J. Quantum Chem.*, **116** (14), 1120 (2016), doi:10.1002/qua.25146.
- [185] I. S. ULUSOY, Z. STEWART, and A. K. WILSON, The role of the CI expansion length in time-dependent studies, *J. Chem. Phys.*, **148** (1), 014107 (2018), doi:10.1063/1.5004412.
- [186] K. KAUFMANN, W. BAUMEISTER, and M. JUNGEN, Universal Gaussian basis sets for an optimum representation of Rydberg and continuum wavefunctions, *J. Phys. B*, **22** (14), 2223 (1989), doi:10.1088/0953-4075/22/14/007.
- [187] S. KLINKUSCH, P. SAALFRANK, and T. KLAMROTH, Laser-induced electron dynamics including photoionization: A heuristic model within time-dependent configuration interaction theory, *J. Chem. Phys.*, **131** (11), 114304 (2009), doi:10.1063/1.3218847.

- [188] M. K. LEE, P. HOERNER, W. LI, and H. B. SCHLEGEL, Effect of spin–orbit coupling on strong field ionization simulated with time-dependent configuration interaction, *J. Chem. Phys.*, **153** (24), 244109 (2020), doi:10.1063/5.0034807.
- [189] J. B. SCHRIBER and F. A. EVANGELISTA, Time dependent adaptive configuration interaction applied to attosecond charge migration, *J. Chem. Phys.*, **151** (17), 171102 (2019), doi:10.1063/1.5126945.
- [190] P. M. KRAUS, ET AL., Measurement and laser control of attosecond charge migration in ionized iodoacetylene, *Science*, **350** (6262), 790 (2015), doi:10.1126/science.aab2160.
- [191] C. LIU, J. MANZ, H. WANG, and Y. YANG, Quantum Engineering of Helical Charge Migration in HCCI, *Chinese Phys. Lett.*, **39** (12), 123402 (2022), doi:10.1088/0256-307X/39/12/123402.
- [192] A. A. HAGBERG, D. A. SCHULT, and P. J. SWART, Exploring Network Structure, Dynamics, and Function using NetworkX, in *Proceedings of the 7th Python in Science Conference*, edited by G. VAROQUAUX, T. VAUGHT, and J. MILLMAN, pages 11–16, Pasadena, CA USA (2008).
- [193] B. RUDEK, ET AL., Ultra-efficient ionization of heavy atoms by intense X-ray free-electron laser pulses, *Nat. Photonics*, **6** (12), 858 (2012), doi:10.1038/nphoton.2012.261.
- [194] C. E. HOYER, L. LU, H. HU, K. D. SHUMILOV, S. SUN, S. KNECHT, and X. LI, Correlated Dirac–Coulomb–Breit multiconfigurational self-consistent-field methods, *J. Chem. Phys.*, **158** (4), 044101 (2023), doi:10.1063/5.0133741.
- [195] A. HARTUNG, ET AL., Electron spin polarization in strong-field ionization of xenon atoms, *Nat. Photonics*, **10** (8), 526 (2016), doi:10.1038/nphoton.2016.109.
- [196] D. SCHWICKERT, ET AL., Charge-induced chemical dynamics in glycine probed with time-resolved Auger electron spectroscopy, *Struct. Dyn.*, **9** (6), 064301 (2022), doi:10.1063/4.0000165.

IV PUBLICATIONS AND MANUSCRIPTS

[VK1]: VLADISLAV KOCHETOV, HUIHUI WANG, and SERGEY I. BOKAREV

Effect of chemical structure on the ultrafast spin dynamics in core-excited states,
The Journal of Chemical Physics **153**, 044304 (2020)

My contribution: The program for simulating spin-flip dynamics developed by **HW** was generalized and incorporated into the OpenMOLCAS program package. I have performed the numerical simulations and produced all the presented figures. Together with **SIB**, the manuscript has been drafted and converged to its final form.

[VK2]: VLADISLAV KOCHETOV and SERGEY I. BOKAREV

RhoDyn: A ρ -TD-RASCI Framework to Study Ultrafast Electron Dynamics in Molecules,
Journal of Chemical Theory and Computation **18**, 46-58 (2022)

My contribution: Together with **SIB**, I have developed the methodology to simulate various time-dependent phenomena. I have extended and optimized the implementation within the OpenMOLCAS program. I have performed the numerical simulations and produced all the presented figures. The results have been analyzed by me and **SIB**. Together with **SIB**, the manuscript has been drafted and converged to its final form.

[VK3]: THIES ROMIG, VLADISLAV KOCHETOV, and SERGEY I. BOKAREV

Spin-flip dynamics in core-excited states in the basis of irreducible spherical tensor operators, *arXiv:2306.06737* [physics.comp-ph] (2023)

My contribution: Together with **TR**, I have implemented the propagation in spherical tensor basis. I have performed the numerical simulations and produced all the presented figures together with **TR**. The results have been analyzed by me and coauthors. Together with coauthors, the manuscript has been drafted and converged to its final form.

[VK1] EFFECT OF CHEMICAL STRUCTURE ON THE ULTRAFAST SPIN DYNAMICS IN CORE-EXCITED STATES

VLADISLAV KOCHETOV, HUIHUI WANG, and SERGEY I. BOKAREV

Reprinted from

VLADISLAV KOCHETOV, HUIHUI WANG, and SERGEY I. BOKAREV, *The Journal of Chemical Physics* **153**, 044304 (2020), with the permission of AIP Publishing.

Copyright © 2020 AIP.

Effect of chemical structure on the ultrafast spin dynamics in core-excited states

Cite as: J. Chem. Phys. 153, 044304 (2020); doi: 10.1063/5.0005940

Submitted: 27 February 2020 • Accepted: 2 July 2020 •

Published Online: 28 July 2020



View Online



Export Citation



CrossMark

Vladislav Kochetov,¹  Huihui Wang,² and Sergey I. Bokarev^{1,a)} 

AFFILIATIONS

¹Institut für Physik, Universität Rostock, A.-Einstein-Strasse 23-24, 18059 Rostock, Germany

²State Key Laboratory of Quantum Optics and Quantum Optics Devices, Institute of Laser Spectroscopy, Shanxi University, 030006 Taiyuan, China

^{a)}Author to whom correspondence should be addressed: sergey.bokarev@uni-rostock.de

ABSTRACT

Recent developments of the sources of intense and ultrashort x-ray pulses stimulate theoretical studies of phenomena occurring on ultrafast timescales. In the present study, spin-flip dynamics in transition metal complexes triggered by sub-femtosecond x-ray pulses are addressed theoretically using a density matrix-based time-dependent configuration interaction approach. The influence of different central metal ions and ligands on the character and efficiency of spin-flip dynamics is put in focus. According to our results, slight variations in the coordination sphere do not lead to qualitative differences in dynamics, whereas the nature of the central ion is more critical. However, the behavior in a row of transition metals demonstrates trends that are not consistent with general expectations. Thus, the peculiarities of spin dynamics have to be analyzed on a case-by-case basis.

Published under license by AIP Publishing. <https://doi.org/10.1063/5.0005940>

I. INTRODUCTION

Novel light sources such as High Harmonic Generation (HHG) and X-ray Free Electron Laser (XFEL) are steadily improving in terms of increasing intensity, energy, and shortening pulse duration and temporal resolution down to attoseconds.^{1–5} Such an advance allows one to study electron dynamics on a few femtosecond and subfemtosecond timescales.^{6,7} The key point is the preparation of a superposition of quantum states by pulses, which have a broad linewidth in the frequency domain. This non-stationary superposition then coherently evolves in time. Examples of such behavior were demonstrated experimentally and reinforced theoretically for the different cases of charge migration.⁸ Due to their ultrafast character, the early electron dynamics appear to be almost isolated from nuclear motion and other effects taking place at longer times.

Another kind of coherent dynamics reported recently and considered in this paper is the spin dynamics initiated by x-ray light.^{9,10} The principle of this process is briefly illustrated in Fig. 1(a) showing the many-body state patterns without [Spin-Free (SF)] and with [Spin-Orbit (SO)] strong Spin-Orbit Coupling (SOC), which are

characteristic for core-excited states. Initially, only the spin-allowed transitions with $\Delta S = 0$, i.e., between the green and red SF states, are occurring upon light absorption. The creation of a core-hole in $2p$ orbitals, i.e., the $L_{2,3}$ -edge absorption, in transition metal complexes is followed by the mixing of states with different spins evolving in time.^{10,11} For certain pulse characteristics, this process leads to a spin-flip, taking place within about a femtosecond, which is extremely fast compared to the conventional spin-crossover times, taking, as a rule, more than 50 fs.^{12–16} However, in exceptional cases, it may take notably less time.¹⁷ Since SOC for the deeper holes with non-zero angular momentum is, in general, much larger than in the valence band, simulating dynamics initiated by high-energy photons is of interest.

From the general viewpoint, the ultrafast spin-flip should occur when a superposition of states with $2p_{3/2}$ and $2p_{1/2}$ core holes is effectively prepared by excitation with a broadband pulse. Thus, one can expect this process to be purely dictated by the properties of these core holes, with the chemical environment and the details of the pulse characteristics being less relevant. However, previous works^{9,10} concluded that the carrier frequency and the width of the pulse are essential to trigger the efficient spin-flip

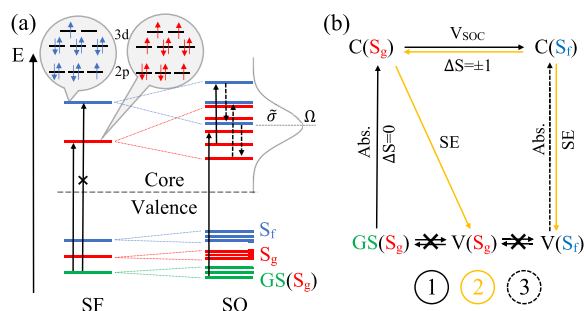


FIG. 1. (a) Scheme of many-electron energy levels in the system without (left) and with (right) SOC. States of different spins are marked with red and blue colors; we additionally distinguish the “ground” states (green), which can be populated due to the finite temperature. The light pulse with carrier frequency Ω and bandwidth $\bar{\sigma}$ is shown in gray; it prepares the superposition of the SOC states. (b) Population pattern of the core (C) and valence (V) states with spins S_g and S_f enabled by the light absorption (Abs.), stimulated emission (SE), and SOC (V_{SOC}). The style of arrows corresponds to the primary, secondary, and tertiary processes.

transition. In particular, the creation of the superposition of the $2p_{3/2}$ and $2p_{1/2}$ core holes was not always a prerequisite for such a spin transition to occur. Moreover, the peculiarities of the dynamics were discussed only for one particular system—hexaaqua iron (II) complex $[\text{Fe}(\text{H}_2\text{O})_6]^{2+}$, where a sub-femtosecond transition from quintet to triplet states has been observed. Therefore, the question of the conditions for the efficient spin transition calls for additional study.

The central question of this article is how the nature of the excited metal atom and its chemical environment (coordination sphere) influences the dynamics and the spin-flip yield. Focusing on the transition metal (Ti, Cr, Fe, and Ni) complexes with different weak- and strong-field ligands, we deduce the compounds, from which one can expect significant changes in the populations of states with different spins, and discuss conditions, at which one can observe them.

This article is organized as follows: First, we present the theoretical method used in this work in Sec. II. Furthermore, the logic behind the choice of the objects under investigation is explained in Sec. III, and the essential parameters of the computation are presented in Sec. IV. The influence of ligands and the nature of the central metal on the dynamics are presented in Sec. V and are further analyzed in Sec. VI. Finally, the conclusions are given in Sec. VII.

II. METHOD

The approach we use for the study of the populations of spin states is the quite general density matrix-based Time-Dependent Restricted Active Space Configuration Interaction (TD-RASCI) described elsewhere.^{11,18} Since the whole process of interest lasts no more than few fs, explicit nuclear motion is neglected in the calculation. Its effect is taken into account implicitly via coupling of the electronic subsystem, having Hamiltonian \hat{H} , to a vibrational heat bath. The dynamics of an open system and its

reduced density operator $\hat{\rho}$ are described by the Liouville–von Neumann equation,¹⁹

$$\frac{\partial}{\partial t} \hat{\rho} = -i[\hat{H}, \hat{\rho}] - \mathcal{R}\hat{\rho}, \quad (1)$$

where \mathcal{R} is a dissipation superoperator. Note that here and below atomic units are used unless stated otherwise. If one writes the Hamiltonian operator in the basis of configuration state functions,²⁰ it has the form

$$\mathbf{H}(t) = \mathbf{H}_{\text{CI}} + \mathbf{V}_{\text{SOC}} + \mathbf{U}_{\text{ext}}(t). \quad (2)$$

Here, \mathbf{H}_{CI} and \mathbf{V}_{SOC} are the Configuration Interaction (CI) Hamiltonian, responsible for electron correlation effects, and the SO interaction part, respectively. The light field contributes to the Hamiltonian with the time-dependent light–matter interaction term $\mathbf{U}_{\text{ext}}(t) = -\mathbf{d} \cdot \vec{E}(t)$ in the dipole approximation, where \mathbf{d} is a transition dipole matrix and $\vec{E}(t)$ is an external electric field.

However, in practical applications to the spin-flip dynamics, the so-called SF basis $\{\Phi_i^{(S_i, M_{S_i})}\}$ is more convenient. These $\{\Phi_i^{(S_i, M_{S_i})}\}$ are the eigenfunctions of \mathbf{H}_{CI} and correspond to a particular spin S and its projection M_S onto the quantization axis and, thus, are the eigenfunctions of the \hat{S}^2 and \hat{S}_z operators. The term \mathbf{V}_{SOC} couples different SF functions such that the eigenfunctions of $\mathbf{H}_{\text{CI}} + \mathbf{V}_{\text{SOC}}$ are the linear combinations of SFs with different spins. The density matrix in the SF basis is given by

$$\rho(t) = \sum_{ij} \rho_{ij}^{(S_i, M_{S_i}), (S_j, M_{S_j})}(t) |\Phi_i^{(S_i, M_{S_i})}\rangle \langle \Phi_j^{(S_j, M_{S_j})}|. \quad (3)$$

Diagonal elements ρ_{ii} in such representation are the populations of the corresponding SF states $|\Phi_i^{(S_i, M_{S_i})}\rangle$. For the simplicity of the analysis, ρ_{ii} with the same total spin S have been summed,

$$P(S) = \sum_i \delta_{SS} \rho_{ii}^{(S_i, M_{S_i}), (S_i, M_{S_i})}. \quad (4)$$

We use the following notation for the different groups of states: $P(\text{GS})$ is the population of a single or several ground states with the spin S_g split by SOC and found in thermal equilibrium at finite temperature. $P(S_g)$ is the population of the excited states with the same spin S_g , which is also called the “main” spin below. $P(S_f)$ is the population of the excited states with the “flipped” spin S_f different from that of the ground one. The mean value of the spin squared operator has been calculated in the SF basis as

$$\langle \hat{S}^2 \rangle = \text{tr}[\hat{\rho} \hat{S}^2] = \sum_i \rho_{ii} S_i^2 = \sum_S P(S) \cdot S(S+1) \quad (5)$$

and is further used as an integral characteristic of the spin-flip process.

For simplicity, the incoming electric field was chosen to be a single linearly polarized pulse with a temporal Gaussian envelope,

$$\vec{E}(t) = A\vec{e} \exp(-t^2/(2\sigma^2)) \sin(\Omega t), \quad (6)$$

although the pulse trains are more efficient to induce spin-flip transitions.¹⁰ Here, A , \vec{e} , and Ω are the amplitude, polarization, and carrier frequency. The pulse width σ was chosen such as to cover a wide range of valence–core excitations; thus, it corresponds to the ultrashort pulse in the time domain.

We apply the following strategy to estimate the influence of phase and energy relaxation due to the vibrational degrees of freedom. We employ a system–bath approach, where we assume that the coupling to the reservoir can be treated in the second order of perturbation theory and the Markov approximation. Furthermore, we distinguish the “intracomplex” (high-frequency) and “outer” (low-frequency) vibrational baths. The high-frequency part is specific to the first solvation shell, coupled to a secondary bath given by the second and further solvation shells. We assume that it represents a collection of harmonic oscillators in thermal equilibrium coupled to the electronic transitions in a Huang–Rhys-like fashion.¹⁹ The modes corresponding to the low-frequency part are usually more delocalized, and the distinction between solvation shells is not meaningful. Hence, we employ the multi-mode Brownian oscillator model²¹ for the “intracomplex” bath and utilize the Ohmic spectral density for the low-frequency one. In total, the effect of the reservoir is described by the spectral density of the form

$$J_{ij}(\omega) = \sum_{\xi} \omega_{\xi}^2 g_{ij,\xi}^2 \frac{\omega \omega_{\xi} \gamma}{(\omega^2 - \omega_{\xi}^2)^2 + \omega^2 \gamma^2} + \theta(\omega) j_0 \omega e^{-\omega/\omega_c}, \quad (7)$$

where i and j label coupled electronic states. With this, we assume no correlation between the two baths; moreover, the low-frequency part is state-independent. In the first term of Eq. (7), ξ is a normal mode with ground-state frequency ω_{ξ} , parameter γ accounts for the influence of the secondary bath, and $g_{ij,\xi}$ is the dimensionless shift of the i 's state harmonic potential energy surface with respect to the potential of state j . The couplings

$$g_{ij,\xi}^2 = \frac{1}{2} \omega_{\xi} (\Delta Q_{gi,\xi} - \Delta Q_{gj,\xi})^2 \delta_{S_i S_j} \delta_{M_{S_i} M_{S_j}} \quad (8)$$

have been obtained in the SF basis from the Cartesian gradients in the excited states i and j at the geometry of the ground state g by projecting them onto a normal mode ξ . These gradients in normal mode coordinates give mass-weighted shifts $\Delta Q_{gi,\xi}$. In the summation in the first term of Eq. (7), only the normal modes with frequencies above 200 cm^{-1} are taken into account since lower-energy vibrations are highly anharmonic and cannot be mapped to a harmonic model. The second Ohmic term compensates for this fact. In this term, $\theta(\omega)$ is the Heaviside step function, j_0 is a coupling strength, and ω_c is a cutoff frequency. For the details of spectral density parameterization, see Sec. IV.

Finally, we employ the Bloch model, which decouples population relaxation and coherence dephasing. In this case, the only non-zero elements of the relaxation matrix $\mathcal{R}_{ab,cd}$ are given by

$$\mathcal{R}_{ii,ij} = \delta_{ij} \sum_l k_{i \rightarrow l} - k_{j \rightarrow i} \quad (9)$$

for population relaxation and

$$\mathcal{R}_{ij,ij} = \frac{1}{2} \left(\sum_l k_{i \rightarrow l} + \sum_l k_{j \rightarrow l} \right) \quad (10)$$

for coherence dephasing. The relaxation rates $k_{i \rightarrow j}$ have been obtained from the spectral density, Eq. (7), as

$$k_{i \rightarrow j} = 2[1 + n(\omega)][J_{ij}(\omega) - J_{ij}(-\omega)], \quad (11)$$

where $n(\omega) = (\exp(\omega/k_B T) - 1)^{-1}$ is the Bose–Einstein distribution function.

In the initial density matrix, SO states were populated according to the Boltzmann distribution: $\rho_{ij}(0) = \delta_{ij} \exp(-E_i/(k_B T))$, which is then transformed to the SF basis for propagation. Pure dephasing due to the Auger decay is neglected for the clarity of discussion; its effect has been estimated elsewhere^{10,11} and does not qualitatively change the picture beyond the relatively uniform decay of diagonal elements ρ_{ii} . Furthermore, for the simplicity of discussion, most of the calculations are performed without dissipation to the environment (nuclear degrees of freedom), i.e., $\mathcal{R} = 0$ in Eq. (1).

Propagation of the density matrix according to Eq. (1) has been performed in the SF basis with the Runge–Kutta–Cash–Karp method^{22,23} of the 4(5) order of accuracy. All the computations for the density matrix propagation are carried out employing the locally modified version of the OpenMOLCAS package.²⁴

III. INVESTIGATED SPECIES

In this study, we have focused on transition metal complexes as convenient objects to study the effect of the chemical structure on the spin dynamics. These complexes exhibit states of different multiplicities that can be close in energy, as shown in Fig. 1. Their relative energies are governed by the interplay of the ligand-field splitting and pairing (exchange) energy and depend on the position of the ligand in the spectrochemical series. In turn, SOC increases from left to right in the row of transition metals. Both effects influence relative stability and spin crossover properties.^{12,13}

When talking about the soft x-ray excitation of metal atoms, the electronic states relevant for such dynamics are of the $2p \rightarrow 3d$ type and are strongly dipole allowed, in contrast to the weaker $2p \rightarrow 4s$ ones. Depending on the number of electrons in the d -shell, the number of these states also varies because of the difference in the available d -holes for an excited $2p$ electron. Variation in the total number of accessible states may also strongly influence the spin dynamics, in addition to differences in SOC strength, and its impact has been studied here. Furthermore, the $3p \rightarrow 3d$ transitions could also be relevant for observing spin dynamics and seem to be more attractive as M-edge absorption requires less energetic radiation, but at the same time, SOC for the $3p$ holes is notably smaller than that for the $2p$ ones. This type of transitions has also been considered in this paper.

Two main sets of compounds have been studied; see Table I. The weak-field d^6 iron hexaaqua complex $[\text{Fe}(\text{H}_2\text{O})_6]^{2+}$ with a quintet ground state is used as a reference as it has been recently studied and demonstrated an efficient spin–flip transition.¹⁰ Set 1 includes this hexaaqua iron (II) complex and its derivatives with the

TABLE I. Details of the geometric and electronic structure of studied complexes: the metal–ligand distance, the number of 3d electrons in the ground state, the magnitude of L₃/L₂ energy splitting, the total number of SOC electronic states with different multiplicities considered in the dynamics, and the global XAS shift for the comparison with the experiment.

Compound	R(M–L) ^a (Å)	3d electrons	L ₃ /L ₂ SOC splitting ^b (eV)	States (2S _g + 1)	States (2S _f + 1)	XAS shift (eV)
<i>Reference</i>						
[Fe(H ₂ O) ₆] ²⁺	2.04, 2.27 [2.095] ²⁵	6	12.8	175 (5)	585 (3)	1.65
<i>Set 1</i>						
[Fe(H ₂ O) ₅ (NH ₃) ²⁺	2.16, 2.20, 2.26 ^c		12.6			1.60
[Fe(NH ₃) ₆] ²⁺	2.30	6	12.6	175 (5)	585 (3)	1.55
[Fe(H ₂ O) ₅ (CN)] ⁺	2.05, 2.11, 1.92 ^c		12.5			1.68
[Fe(CO) ₅] ⁰	1.68, 1.77 [1.810, 1.842] ²⁶	8	11.0	751 (1)	3015 (3)	11.0
<i>Set 2</i>						
[TiO ₆] ⁸⁻	[1.95, 1.98] ²⁸	0	5.3	16 (1)	45 (3)	8.1
[Cr(H ₂ O) ₆] ³⁺	2.00 [1.966] ²⁵	3	7.2	640 (4)	650 (2), 90 (6)	5.9
[Ni(H ₂ O) ₆] ²⁺	2.09 [2.044–2.064] ²⁷	8	17.9	75 (3)	30 (1)	13.5

^aDue to the Jahn–Teller effect or the presence of axial/equatorial ligands, distances may vary. All different distances are given in this case. Values in square brackets correspond to the experiment (where available). Data: Ref. 25 aqueous solution EXAFS, Ref. 26 gas-phase electron diffraction, and Refs. 27 and 28 x-ray diffraction.

^bThe energy splitting between the L₃ and L₂ highest peaks.

^cThe order of distances: equatorial H₂O, axial H₂O, axial NH₃ or CN⁻ ligand.

general formula [FeX_n(H₂O)_{6-n}]²⁺, where water molecules are partially or completely replaced by stronger ligands X = NH₃ (n = 1 or 6), or even stronger CN⁻ (n = 1). This set is intended to test the influence of ligand strength; complexes of *set 1* are listed in Table I in the ascending order of the spectrochemical strength of ligands.

The second set comprises six-coordinated complexes [TiO₆]⁸⁻ and [M(H₂O)₆]ⁿ⁺ with M = Cr, Fe, Ni ordered by the SOC value or equivalently by their nuclear charge. The perovskite building block, [TiO₆]⁸⁻ cluster, has been chosen because of its high relevance to many functional materials; besides, it resembles the reference [Fe(H₂O)₆]²⁺ complex, also having a nearly octahedral coordination sphere of oxygen atoms. It is also interesting from the viewpoint of the number of possible singly excited 2p⁻¹3d¹ configurations as this number is quite small (Table I). The nickel complex, possessing an almost filled d-shell, also features the small number of relevant electronic configurations similar to Ti, but its SOC constant is larger by about a factor of three. The chromium complex has a more intricate electronic structure with the d³ ground state, resulting in lots of excited states similar to the reference iron compound. A standalone compound, in some sense, is [Fe(CO)₅]⁰. Due to the strong-field ligands, it has a singlet ground state, and the spin-state energetic pattern is substantially different from the other high-spin complexes.

IV. COMPUTATIONAL DETAILS

All structures and vibrational frequencies ω_i were obtained at the Density Functional Theory (DFT) level with the B3LYP functional and aug-cc-pVTZ basis set in the Gaussian 09 program package.²⁹ For [TiO₆]⁸⁻, the rutile experimental geometry has been used.²⁸

The calculation of SF states and interstate couplings has been performed at the Restricted Active Space Self-Consistent Field

(RASSCF) level of theory. Scalar relativistic effects were introduced via the Douglas–Kroll–Hess transformation³⁰ up to the second order in perturbation theory in conjunction with the all-electron ANO-RCC basis set³¹ of VTZP quality. The results up to the fourth order are benchmarked in the [supplementary material](#). The active space of eight orbitals (three 2p and five 3d) was found to give a good approximation³² and is used for all species except for [Fe(CO)₅]⁰. Full CI has been done for the 3d subspace (RAS2), while for the 2p subspace (RAS1), only one hole has been allowed; RAS3 subspace has been left empty. For [Fe(CO)₅]⁰, the 3dσ (a₁'), four 3d (e' and e''), and 3dσ* (a₁'*) orbitals were put to the RAS2 as well as four π* orbitals to the RAS3 with only one electron allowed, resulting in 13 orbitals in the active space. Note that all the experimental X-ray Absorption Spectra (XAS) were shifted to be aligned with calculations for the computational consistency as opposed to the conventional way of doing vice versa. The respective shifts can be found in Table I.

The particular construction of basis functions and respective matrices in Eq. (2) has been done as follows: First, molecular orbitals were optimized in a state-averaged RASSCF procedure,³³ where averaging over all possible electron configurations has been performed. These orbitals were kept frozen during the propagation. Thus, the polarizability of ligands is accounted for only statically, and orbital relaxation in the course of dynamics is neglected. The SOC matrix V_{SOC} is computed by means of the state interaction approach,^{34,35} implementing the atomic mean field integral^{36,37} method. It has proven itself to be a versatile tool for computing the L_{2,3}-edge absorption spectra of transition metal complexes.^{32,38–40} The respective calculations have been done with the OpenMOLCAS program package.²⁴

The polarization vector \vec{e} , see Eq. (6), has been selected to point along one of the metal–ligand bonds. Different polarizations have relatively little effect on the dynamics, as has been shown in Ref. 11, and thus have not been addressed here. The width of the light pulse

TABLE II. Summary of the pulse characteristics, see Eq. (6).

Compound	σ (fs)	$\hbar\Omega$ (eV)	A (a.u.)
$[\text{TiO}_6]^{8-}$	0.2	470.0	1.5
$[\text{Cr}(\text{H}_2\text{O})_6]^{3+}$	0.2	588.0	2.5
$[\text{Fe}(\text{H}_2\text{O})_6]^{2+}$	0.2	716.0	6.0
	0.2	713.2	2.5
$[\text{Fe}(\text{CO})_5]^0$	0.2	728.0	6.0
$[\text{Ni}(\text{H}_2\text{O})_6]^{2+}$	0.2	875.0	9.0

σ was set to 0.2 fs in the time domain for all simulations. The carrier frequency Ω was chosen to correspond to the center between the L_3 and L_2 bands, see Table II. The amplitude A of the pulse was adjusted to ensure approximately the same depletion of the ground state in all simulations [$P(\text{GS}) < 0.2$]. The initial population of near-degenerate ground states in the high-spin complexes corresponded to the temperature of $T = 300$ K. Additional calculations for $T = 0$ K are shown in the supplementary material.

To estimate the effect of dephasing due to the width of the vibrational wave function in the initial state on the dynamics, 250 geometries were sampled from the vibrational Wigner function^{41,42} at $T = 300$ K using the tool `wigner.py` provided in the SHARC 2.1 suite.⁴³ For comparison, results for $T = 0$ K are given in the supplementary material.

The couplings to the intracomplex high-frequency heat bath $g_{j,\xi}^2$ in Eq. (7) were computed for SF states from the RASSCF gradients of the excited states at the ground state optimized geometry. The parameters γ and j_0 were chosen to correspond to the rate of vibrational relaxation to the second solvation shell of about $(100 \text{ fs})^{-1}$, i.e., $\gamma = 300 \text{ cm}^{-1}$ and $j_0 = 5.92 \cdot 10^{-4}$. The cutoff frequency ω_c of the Ohmic counterpart of the spectral density was set to 80 cm^{-1} as it corresponds to the characteristic changes in the second solvation shell caused by solute in liquid water.⁴⁴ Relaxation rates, Eq. (11), were computed at $T = 300$ K.

V. RESULTS

In Subsections V A and V B, we analyze the influence of purely electronic factors such as the strength of the ligand field and SOC that are decoupled from the influence of vibrations for simplicity. Nuclear effects are discussed in Subsection V C.

A. Influence of ligand strength

The influence of the surrounding ligand on the dynamics has been studied on the example of Fe^{2+} complexes with H_2O , NH_3 , and CN^- ligands. Despite different positions in the spectrochemical series (especially that of H_2O and CN^-), all these complexes have a quintet ground state, see Table I. XAS for all members of the set represents dipole-allowed transitions from the $2p_{3/2}$ and $2p_{1/2}$ orbitals to the non-bonding $3d(t_{2g})$ and anti-bonding $3d\sigma^*(e_g)$ levels. Although one sees clear differences in the nature and energy of individual transitions between complexes, e.g., in the extent of spin-mixing, these differences are washed out upon lifetime broadening.

Therefore, the XAS spectra of different species are fairly similar, showing only minor variations in the L_3/L_2 energy splitting as well as in the structure of the L_3 edge, see Fig. 2(a).

The spin-flip dynamics occurring in these complexes upon light excitation is illustrated in Figs. 2(b) and 2(c), where the time-dependent values of $\langle \hat{S}^2 \rangle$ are presented. One can see that upon excitation, the expectation value $\langle \hat{S}^2 \rangle$ first quickly drops from the value of $6\hbar^2$, corresponding to the quintet state manifold, and then slowly evolves after the pulse is over, exhibiting some oscillations. However, within the considered time interval, $\langle \hat{S}^2 \rangle$ does not reach the triplet value of $2\hbar^2$, evidencing a notable contribution from quintet states in the superposition. In other words, the closed system reaches a quasi-equilibrium with respect to the influence of \mathbf{V}_{SOC} , and the populations do not change strongly anymore.

Concerning the influence of ligands, the same statement as for XAS can also be made for the dynamics. It can be seen from a similar form of the respective $\langle \hat{S}^2 \rangle$ curves as a function of time in Figs. 2(b) and 2(c) for two different pulses. These pulses have different carrier frequencies and amplitudes and thus involve different groups of states in the dynamics. For instance, the gray pulse [panel (c)], centered between L_3 and L_2 , overlaps with the latter edge in energy, whereas the orange pulse [panel (b)] barely touches it. This fact explains the larger yield of triplet states in the case of the gray pulse. Comparing the curves for different ligands, one can conclude that at least for short pulses (broad in energy), the smearing of the fine

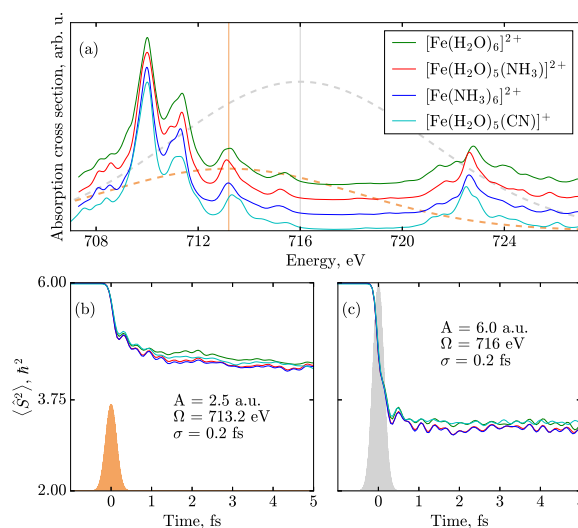


FIG. 2. (a) Calculated XAS of the reference complex $[\text{Fe}(\text{H}_2\text{O})_6]^{2+}$ and complexes from set 1, see Table I. Spectra are shifted vertically for visual clarity. Dashed lines show the shape of the pulses in the frequency domain. [(b) and (c)] Time evolution of $\langle \hat{S}^2 \rangle$ for these complexes for two different pulses; their characteristics are given in the respective panels, and filled curves depict the time envelopes. The centers of the corresponding excitation bands in the frequency domain are also depicted in panel (a) with two vertical lines. The amplitude has been selected to give a comparable depletion of the ground state [$P(\text{GS}) \approx 0.1$].

details of the electronic structure occurs, leveling the differences due to ligands.

To consider a qualitatively different case, we now address the results for $[\text{Fe}(\text{CO})_5]^0$. For this complex, all ligands have a strong field, and in contrast to $[\text{Fe}(\text{H}_2\text{O})_5(\text{CN})]^+$, this results in the low-spin singlet ground state. The $[\text{Fe}(\text{CO})_5]^0$ spectrum is less consistent with the experiment⁴⁵ than that of the $[\text{Fe}(\text{H}_2\text{O})_6]^{2+}$ species [see Fig. 3(a)] as the SOC splitting is underestimated by 2 eV–3 eV, but main spectral features can be clearly recognized. The lower intensity pre-peak at about 720 eV is due to transitions to the $3d\sigma^*$ (a_1^*) orbital and is, thus, somewhat similar to the transitions discussed before for *set 1*. In contrast, the pronounced second peak of the L_3 edge at 722 eV is a fingerprint of a strong π -backdonation⁴⁵ as it mainly corresponds to transitions from the $2p_{3/2}$ to the ligand and π^* orbitals, which are notably mixed with the iron $3d$ orbitals. Thus, excitation with the light pulse occurs from the ground singlet state to predominantly charge-transfer ones because of the larger transition strengths of the latter. The partial contributions of different spin states to the SOC-coupled ones are illustrated in Fig. 3(a). The total intensity is partitioned according to the fraction of the singlet (red curve) and triplet (blue curve) SF state contributions to the respective SOC-state. Essential for the current discussion is that the L_3 states have approximately equal contributions from singlet and triplets SF states, whereas for the L_2 , triplets distinctly dominate.

Dynamics in $[\text{Fe}(\text{CO})_5]^0$ is shown in Fig. 3(b) for the pulse centered between the L_3 and L_2 edges and overlapping with all dipole-allowed transitions. One sees the spin-flip from singlet to triplet happening much faster than the pulse duration, i.e., shortly after the initial singlet–singlet excitation (red curve). Remarkably, in contrast to other iron complexes from *set 1*, the efficient spin transition occurs independent of the pulse characteristics. In this case, the final $\langle \hat{S}^2 \rangle$ is closer to the target triplet value of $2\hbar^2$. Noteworthy, in the case of $[\text{Fe}(\text{CO})_5]^0$, pronounced oscillations in the state populations and the $\langle \hat{S}^2 \rangle$ are observed. The time period of these oscillations (0.35 fs) corresponds to the SOC-splitting of 11.0 eV.

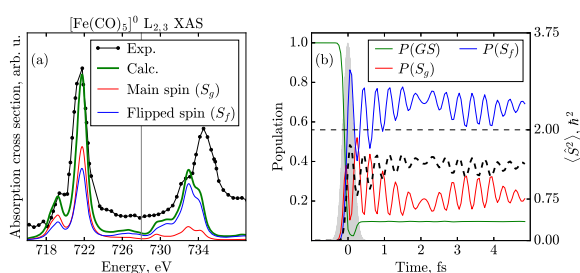


FIG. 3. Results of modeling for the $[\text{Fe}(\text{CO})_5]^0$ complex: (a) Experimental (black dotted line) and calculated (green line) XAS. The total intensity is decomposed according to the fraction of the singlet (red curve) and triplet (blue curve) character of the respective states, see text. (b) Evolution of the population of singlet $S_g = 0$ (red) and triplet $S_f = 1$ (blue) SF states initiated by the pulse with characteristics given in Table II. The dashed line shows the expectation value of the \hat{S}^2 operator. The value of $2\hbar^2$, marked with a horizontal line, corresponds to the pure triplet $S_f = 1$.

Naturally, when the symmetry is changed and the electronic structure is altered by the strong-field ligands and the dominant contributions from the charge-transfer states, the time-evolution changes qualitatively. The reasons for this fact will be further analyzed in Sec. VI.

B. Transition metal series

The influence of the central atom is studied on the example of complexes from *set 2*, see Table I. In the upper row of Fig. 4, the calculated $L_{2,3}$ absorption spectra are presented. Overall, reasonably good agreement with the experiment is reached at the RASSCF level of theory. The SOC splitting between the L_3 and L_2 bands, as well as the ligand-field splitting within the L_3 band, is well reproduced for all systems under study. The $[\text{TiO}_6]^{8-}$ spectrum is compared to the Ti $L_{2,3}$ -edge XAS in SrTiO_3 ⁴⁶ as a reference for the d^0 system in the octahedral field of oxygen atoms. It shows four clear peaks originating from the $2p_{3/2}^{-1}t_{2g}$, $2p_{3/2}^{-1}e_g$, $2p_{1/2}^{-1}t_{2g}$, and $2p_{1/2}^{-1}e_g$ states. A somewhat similar multiplet configuration can be roughly recognized for other species of the row, but one sees an intensity redistribution and appearance of additional peaks due to the stronger multiconfigurational character.

The first row in Fig. 4 depicts the decomposition of spectra in the spin multiplicity of final states (red and blue curves). Note that almost everywhere, the contributions from the states with the main or ground spin S_g (red) are higher than from the ones with the flipped spin S_f (blue). The only exceptions are the L_2 band of $[\text{TiO}_6]^{8-}$ and the 712 eV–727 eV region of $[\text{Fe}(\text{H}_2\text{O})_6]^{2+}$ shown in Figs. 4(a1) and 4(c1), respectively.

The spin dynamics of *set 2* are shown in the lower row of Fig. 4. The $[\text{TiO}_6]^{8-}$ compound features strong oscillations between the main-spin and flipped-spin states with a period of about 0.6 fs, which corresponds to 6.9 eV energy [Fig. 4(a2)], correlating with the L_3/L_2 SOC splitting. Conceivably, it is caused by the relatively small number of states involved in the dynamics giving rise to the Rabi-like oscillations. Other complexes demonstrate the same trend, i.e., oscillations have the characteristic period inversely proportional to the value of SOC splitting, see Table I. However, it is difficult to rationalize why they are very pronounced in some cases and, in others, notably washed out. These oscillations result from the joint behavior of hundreds and even thousands of states and depend on their interference. They should also depend on the interplay with some other energetic differences (and their characteristic timescales), e.g., ligand-field splittings. For instance, in the cases of chromium [Fig. 4(b2)] and iron [Fig. 4(c2)], the oscillations are dumped slowly, which is related to a huge number of involved states. Similar behavior has also been observed for $[\text{Fe}(\text{CO})_5]^0$ (Fig. 3). Note that these oscillations also persist if the inhomogeneous distribution of geometries (Wigner sampling) and relaxation to the environment are taken into account (see Sec. V C).

The prevailing population of states with the flipped spin (blue line in the lower row of panels in Fig. 4) is observed only in $[\text{TiO}_6]^{8-}$ and $[\text{Fe}(\text{H}_2\text{O})_6]^{2+}$ complexes, whereas for $[\text{Cr}(\text{H}_2\text{O})_6]^{3+}$ and $[\text{Ni}(\text{H}_2\text{O})_6]^{2+}$, the spin of the ground state (red line) stays dominant. This behavior is also observed for the $\langle \hat{S}_z \rangle$ curves

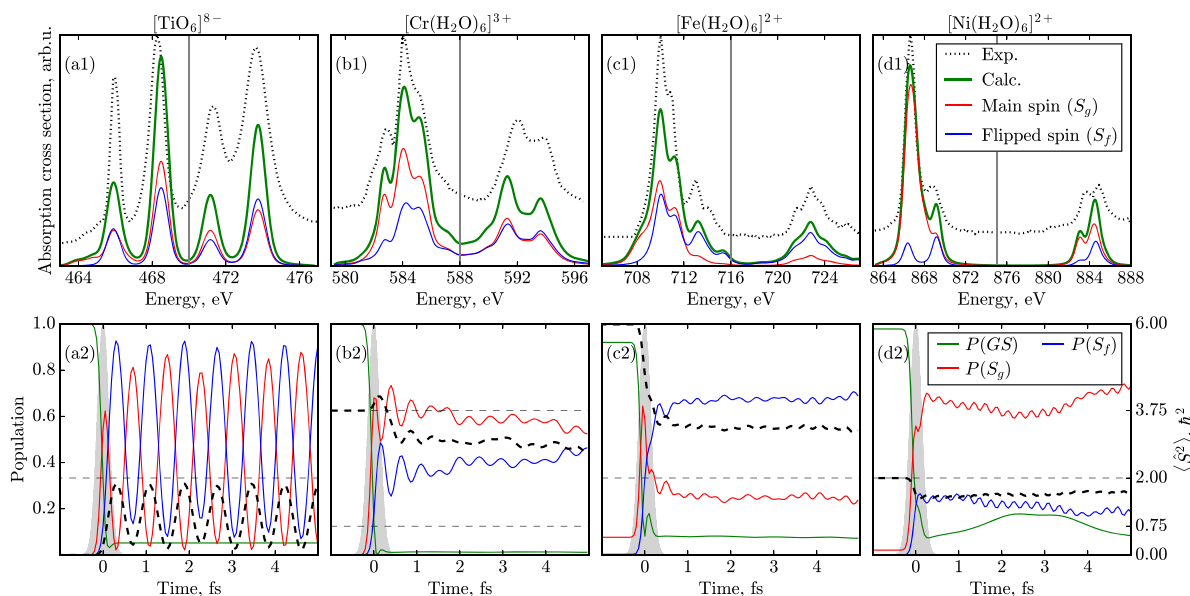


FIG. 4. Results for species from set 2 (Table I): panels (a) $[\text{TiO}_6]^{8-}$, (b) $[\text{Cr}(\text{H}_2\text{O})_6]^{3+}$, (c) $[\text{Fe}(\text{H}_2\text{O})_6]^{2+}$, and (d) $[\text{Ni}(\text{H}_2\text{O})_6]^{2+}$. Upper row: the comparison of the experimental XAS spectra^{38–40,46} with the calculated ones. Lower row: SF-state population dynamics in the corresponding complexes initiated by pulses with characteristics given in Table II. All pulse amplitudes (light-gray) are normalized to the same height for the sake of clarity. Partial populations [Eq. (4)] of the ground states GS, excited states with the same spin S_g , and spin distinct by ± 1 (flipped spin) S_f are depicted in green, red, and blue, respectively. Thick dashed lines give the actual $\langle \hat{S}^2 \rangle(t)$ for a particular complex. Horizontal dashed lines indicate the expectation values $S(S+1)\hbar^2$ of the \hat{S}^2 operator for half-integer and integer spins S relevant for each complex.

(dashed line). For the former two cases, the $\langle \hat{S}^2 \rangle$ significantly deviates from the initial value and tends to the flipped value, namely, the singlet ($0\hbar^2$) to triplet ($2\hbar^2$) transition for $[\text{TiO}_6]^{8-}$ and quintet ($6\hbar^2$) to triplet ($2\hbar^2$) for $[\text{Fe}(\text{H}_2\text{O})_6]^{2+}$. In turn, only a moderate spin transition can be seen for $[\text{Cr}(\text{H}_2\text{O})_6]^{3+}$ (b2) and $[\text{Ni}(\text{H}_2\text{O})_6]^{2+}$ (d2). To summarize, there is no correlation between the efficiency of spin transition and the value of SOC, which is opposite to what can be anticipated from general considerations.

To strengthen this conclusion, one has to exclude the influence of the light pulse because the amplitude has been selected differently for different complexes. It seems natural that the pulse strength notably influences the $\langle \hat{S}^2 \rangle$ for the same system, and one might argue that by substantially increasing the amplitude, one could achieve a more efficient spin conversion. This fact is illustrated in Fig. 5, where the dependence of $\langle \hat{S}^2 \rangle(t)$ on the amplitude of the pulse ranging from 1 a.u. to 7 a.u. for iron (a) and from 4 a.u. to 10 a.u. for nickel (b) is shown. One can see that already at 6 a.u. for iron and 7 a.u. for nickel, there is no further increase in the yield of spin transition. Observed saturation takes place when the ground state population is almost completely depleted. These values of amplitude, at which the total population of the ground states GS drops below 0.1, were chosen for all the complexes to exclude the influence of the pulse strength possibly. In the transition metal row, the characteristic A value increases as we excite in the center of $L_{2,3}$ -edge, meaning that a stronger pulse is needed to overlap with more energetically distant

transitions separated by SOC efficiently. As an example, note in Fig. 5(a) the growing prominence of oscillations with the increasing amplitude, witnessing an involvement of more distant L_3/L_2 groups of states.

Finally, the $3p \rightarrow 3d$ excitations have been considered. The respective XAS spectra are given in the supplementary material. Although SOC is also notable in this case [SOC splittings are up to 6 eV in $[\text{Ni}(\text{H}_2\text{O})_6]^{2+}$], the S_g states are by far prevailing among the

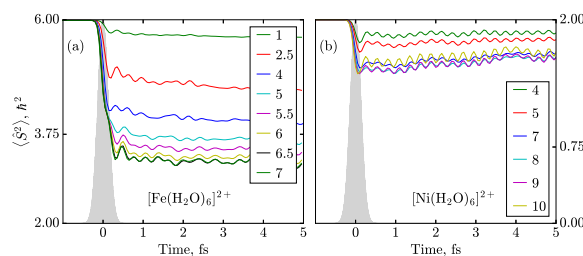


FIG. 5. The dependence of $\langle \hat{S}^2 \rangle(t)$ on the amplitude A of the incoming pulse, which is given in atomic units in the legend, exemplified for (a) $\hbar\Omega = 716$ eV and $\sigma = 0.2$ fs for $[\text{Fe}(\text{H}_2\text{O})_6]^{2+}$ and (b) $\hbar\Omega = 875$ eV and $\sigma = 0.2$ fs for $[\text{Ni}(\text{H}_2\text{O})_6]^{2+}$.

bright states, and no spin-flip dynamics is observed. That is why this case will be not further discussed here.

C. Nuclear effects

The effect of nuclear dynamics on the spin-flip processes can be roughly considered being twofold: the initial nuclear distribution may cause electronic dephasing, and the vibrational degrees of freedom may act as a heat bath causing phase and population relaxation between participating states. The first one refers to the inhomogeneous and the second to the homogeneous broadening of the respective spectroscopic lines. Both effects may be considered as related to the chemical structure discussed herein since the nature of ligands determines their possible contribution. Figure 6 presents the effect of nuclear distribution in the system's initial state on three examples. It shows the time dependence of the population accounting for the width of the initial nuclear wave packet as compared to the results for a single "equilibrium" geometry, corresponding to the center of the distribution.

In $[\text{Fe}(\text{H}_2\text{O})_6]^{2+}$, three lowest SF quintet states lie close to each other in energy, which corresponds to 15 SO states slightly split due to SOC. Different geometries affect the relative energies of these states and notably change equilibrium populations of the lowest five "ground" microstates at $T = 300$ K, i.e., the diagonal elements of the initial density matrix $\rho(0)$. Hence, before the pulse comes, one sees a broad distribution of the populations of these "ground" states and other quintet states, including the other ten closely lying microstates. Since all these states have the same spin ($S = 2$), the $\langle \hat{S}^2 \rangle$ value is sharp before excitation, as indicated in panel (a2). However, the spin-flip dynamics itself is less sensitive to the initial populations and changes in the electronic structure due to different geometries. The scope of population curves (color-filled ranges) is relatively narrow, and most importantly, the curves averaged over 250 geometries closely resemble those for a single optimized geometry, cf. respective solid and dotted lines in Fig. 6(a1). Therefore, Wigner sampling leads to only minor changes. This fact may be rationalized by noting that the potential energy surfaces of the core-excited states in this complex are almost parallel to each other, as has been illustrated for the symmetric Fe–O stretching mode,¹⁰ leading to small dephasing. Interestingly, this dephasing does not destroy fast

oscillations due to the most distant states split by SOC, which is discussed in Sec. V B.

The situation seems to be qualitatively different for $[\text{Fe}(\text{H}_2\text{O})_5(\text{CN})]^+$, see panels (b1) and (b2). In this case, due to the strong-field CN^- ligand, a triplet state comes close to the ground quintet one. Geometries from the flanks of the Wigner function induce a flipped order of the lowest quintet and triplet states. It leads to a very broad distribution of the population curves as the dynamics comprise both quintet \rightarrow triplet and reverse transitions. However, because of the small statistical weight of these points, the averaged dynamics stay almost the same as for a single optimized geometry.

For the third example of $[\text{Ni}(\text{H}_2\text{O})_6]^{2+}$, the initial density matrix, $\rho(0)$, is not influenced that much by geometrical variations. Nevertheless, the averaged dynamics are substantially different from the single-point one. In this case, one might expect a stronger dependence of the slopes of core-excited states' potential surfaces on nuclear displacements, leading to a significant dephasing. One should also note that Wigner sampling leads to a higher S_f yield for the nickel complex.

The influence of ligands due to the dissipation to the vibrational heat bath has been estimated for three Fe^{2+} complexes, having the same ground state and featuring similar non-dissipative dynamics: $[\text{Fe}(\text{H}_2\text{O})_6]^{2+}$, $[\text{Fe}(\text{H}_2\text{O})_5(\text{CN})]^+$, and $[\text{Fe}(\text{NH}_3)_6]^{2+}$. For all these cases, one can barely see the changes in the total populations and $\langle \hat{S}^2 \rangle$ due to relaxation. An example of $[\text{Fe}(\text{H}_2\text{O})_5(\text{CN})]^+$, showing the most pronounced differences, is presented in Fig. 7; the other two examples can be found in the [supplementary material](#). This finding is in accord with the previous study¹⁰ and can be explained by the following two observations: the considered electronic timescale is very short for nuclear dynamics to come into effect, and the number of the k_{ij} 's that are large enough to cause notable relaxation within 5 fs is quite small. The latter statement is illustrated in the panel (a) of Fig. 7 where only few ij pairs out of 52 670 have rate values larger than 0.1 eV. Note that the dissipation results should not be overinterpreted because these largest rates exceed the energetic distances (<0.1 eV– 0.2 eV), which are typical for neighboring core states. Therefore, they approach the applicability limits of the second-order perturbation theory in system-bath coupling.

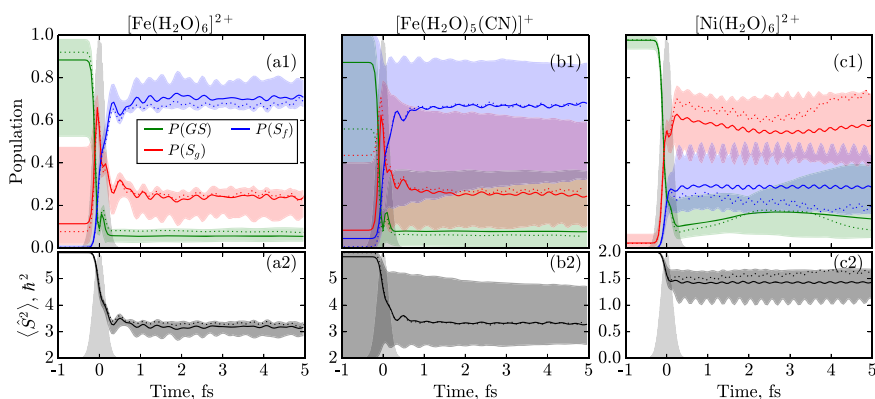


FIG. 6. Spin-flip dynamics accounting for the width of the initial vibrational wave packet in the nuclear phase space (only the distribution of geometries is considered) for $[\text{Fe}(\text{H}_2\text{O})_6]^{2+}$ [panels (a)], $[\text{Fe}(\text{H}_2\text{O})_5(\text{CN})]^+$ [panels (b)], and $[\text{Ni}(\text{H}_2\text{O})_6]^{2+}$ [panels (c)]. Solid lines denote the population dynamics averaged with the Wigner distribution function; color-filled intervals show the overall range of Wigner-sampled trajectories; dotted lines correspond to a single "equilibrium" geometry calculation.

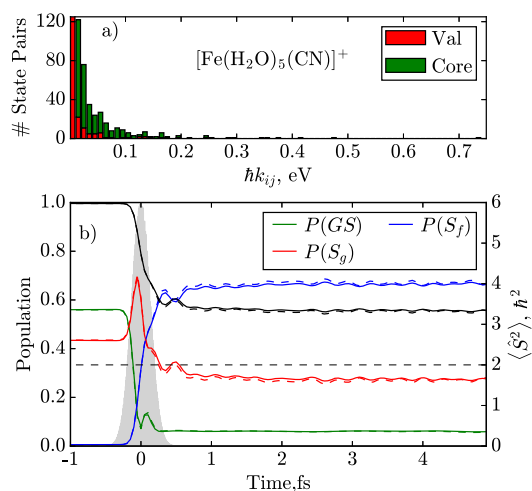


FIG. 7. (a) The distribution of the relaxation rates k_{ij} between the valence- (red bars) and core-excited (green bars) SF states of $[\text{Fe}(\text{H}_2\text{O})_5(\text{CN})]^+$. Note that bars for the range 0.00–0.01 eV are cut not to show all 52 670 rates. (b) Respective spin-dynamics with (solid lines) and without (dashed lines) dissipation.

Of course, different ligands have different fingerprints in relaxation dynamics. For instance, in $[\text{Fe}(\text{H}_2\text{O})_6]^{2+}$, the largest contributions to the rates correspond to the Fe–O symmetric and asymmetric stretching modes. A similar situation is observed in $[\text{Fe}(\text{NH}_3)_6]^{2+}$ where, in addition to Fe–N stretching vibrations, a symmetric NH_3 rocking mode is also contributing. For $[\text{Fe}(\text{H}_2\text{O})_5(\text{CN})]^+$, the prominent modes are (in order of decreasing importance) axial H_2O torsion, axial and equatorial Fe–ligand stretching, and equatorial H_2O wagging modes. However, these individual features are averaged out when the total populations of 175 quintet and 585 triplet states or the integral $\langle \hat{S}^2 \rangle$ are considered on a short timescale. Nevertheless, for longer times, one can expect the relaxation in $[\text{Fe}(\text{H}_2\text{O})_5(\text{CN})]^+$ to be most and for $[\text{Fe}(\text{NH}_3)_6]^{2+}$ least efficient out of these three examples.

VI. DISCUSSION

From the discussion in Secs. V A–V C, one can make four general observations. First, the qualitative character of the dynamics is only barely dependent on the chemical nature of ligands unless the electronic structure is altered completely. The examples are high-spin complexes of *set 1*, demonstrating a very similar behavior, and $[\text{Fe}(\text{CO})_5]^0$, possessing the low-spin ground state and exhibiting a completely different energetic pattern of spin-states. Second, the related differences between the complexes in the dephasing and relaxation rates to the vibrational bath also do not cause substantial changes in the dynamics. The respective structural reorganization responsible for energy dissipation occurs on a notably longer timescale of hundreds of femtoseconds to few picoseconds,^{15,16} whereas the spin-flip is a sub-femtosecond process. Third, in contrast to expectations, the value of SOC splitting does not play a decisive role in the character of dynamics, as seen from the comparison

of different metals. For instance, $[\text{Ni}(\text{H}_2\text{O})_6]^{2+}$ has the largest SOC constant in the considered series but does not show prominent spin-flip dynamics. On the other hand, $[\text{TiO}_6]^{8-}$, with its SOC constant being a factor of three smaller, demonstrates intricate dynamics. Fourth, the critical point is the ratio between the SF states with different spins constituting the SOC-eigenstates. It can be seen from the XAS decomposition into S_g and S_f contributions in Figs. 3 and 4. Indeed, a significant spin-flip was observed for titanium and iron compounds, where bright states with the prevailing amount of the S_f spin contributions are dominating in XAS for the high-energy flank of the L_3 and the whole L_2 edges. It means that at specific energy ranges, more SF flipped states can be accessed by the excitation and SOC mediated population transfer. For the $3p$ excitation, there are no such ranges, and spin-flip is not observed. However, a profound analysis going beyond these simple observations is complicated due to the vast amount of the electronic states, which are coupled in a complex way.

To shed light on the reasons for such behavior and attain a more mechanistic understanding, let us consider a somewhat simplified model, see Fig. 1(b). Assuming that we are working in the saturated regime (Fig. 5) and, thus, can neglect the details of the incoming light pulse for simplicity, the dynamics are governed by two factors—strengths of the dipole transition and that of the SOC. Let us follow the density matrix evolution and, namely, its diagonal elements in the basis of SF states. Initially, an entire population resides in the ground state and the lowest excited states, which are populated according to the respective Boltzmann factors, see Sec. IV. The light pulse couples these initial states with the core ones through the respective transition dipole \mathbf{d} matrix elements. Note that the spin quantum number is conserved $GS \rightarrow S_g$ due to the spin selection rules. Reflecting this fact, in Fig. 4, the red line, $P(S_g)$, rises simultaneously with the arriving pulse. In the SOC picture, states with strictly defined spin do not exist as the spin quantum number is not conserved; thus, the predominant population of the S_g SF states corresponds to a non-stationary superposition of SOC eigenstates. After the initial population of the core-excited S_g states, all SF states get mixed regardless of their spin through \mathbf{V}_{SOC} . That is why the blue S_f line goes up parallel to the red one but after a short delay (see Fig. 4). Once the pulse is switched off, the dynamics are governed solely by the elements of \mathbf{V}_{SOC} . This free dynamics is then determined by the populations accumulated during the pulse in the bright core-excited states with spin S_g and their SO coupling to other states with both S_g and S_f .

Provided a large number of coupled states, we employ a concept widely used in the data analysis to illustrate some trends. Let us start the discussion from the example of the $[\text{Fe}(\text{CO})_5]^0$ complex; see Fig. 8. This figure is obtained with the NetworkX package⁴⁷ implementing the force-directed graph drawing algorithm by Fruchterman and Reingold.⁴⁸ Here, each node corresponds to one of the 3766 SF basis states $\Phi_i^{(S, M_S)}$, and the color encodes their nature, e.g., ground as well as excited states with spins S_g and S_f . The size of the nodes, in turn, denotes whether the state is involved in dynamics (we call it participating) or stays mainly unpopulated (spectator). The distances between nodes are optimized to minimize spring-like forces between them. If the pulse characteristics are left besides the discussion, the force ($F_{ij} = -\kappa_{ij}\Delta x_{ij}$) between nodes i and j corresponds to the spring constant,

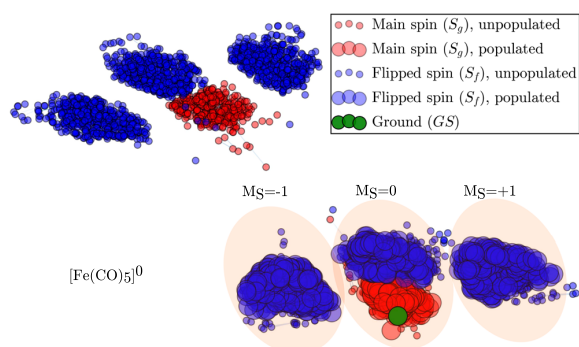


FIG. 8. Force-directed graph showing the clustering of the states of $[\text{Fe}(\text{CO})_5]^0$ according to the transition-dipole and SOC; see Eq. (12). Each node corresponds to one of the 3766 SF basis states $\Phi_i^{(S, M_S)}$: green—GS singlet states, red—excited singlet states, and blue—excited triplet states. Large circles indicate states participating in the dynamics, i.e., having a notable maximal population; small circles correspond to the “spectator” states acquiring no population.

$$\kappa_{ij} = c(|V_{\text{SOC}}|_{ij} + |d_{ij}|), \quad (12)$$

where c is a factor governing the relative importance of the two couplings. It has been adjusted for visual clarity to illustrate the clustering of states. These two quantities in the sum are correlated with the degree of spin conversion. The dipole matrix identifies states that can be directly populated by the light absorption from the initial state manifold (which is denoted as green nodes in Fig. 8). The subsequent dynamics is governed mainly by the strength of SOC. The combination of these two quantities allows considering both effects together.

Looking at Fig. 8, one can note the following peculiarities. According to the above criteria, the states group in two main

clusters, which are separated from each other and, thus, are connected neither by transition dipole nor by SOC. Inside both clusters, one can distinguish four subgroups. The red one corresponds to the singlet (S_g) excited states ($M_S = 0$); the three blue subgroups are triplet (S_f) states grouped by their M_S quantum number. Inside of the smaller subgroups, both \mathbf{d} and V_{SOC} contributions keep nodes together, whereas between them, only the SO interaction is non-zero. This is due to the spin selection rules ($\Delta S = 0$, $\Delta M_S = 0$) for the dipole transitions, causing the blocked structure of \mathbf{d} . Remarkably, the participating states (big nodes) are found only in the cluster, where the single ground state (green node) is entering. Thus, the second big cluster is completely excluded from the dynamics. Even in the former cluster, a relatively small amount of states (about 200 out of 1800) are populated during dynamics. The last important notice is that the amount of the spin-flipped states in this participating cluster is larger than that of the spin-conserved ones.

The graphs for the other compounds of *set 2* and the reference $[\text{Fe}(\text{H}_2\text{O})_6]^{2+}$ complex are presented in Fig. 9. For most of the species {apart from $[\text{Ni}(\text{H}_2\text{O})_6]^{2+}$ }, the states also group in two major clusters. $[\text{TiO}_6]^{8-}$ [panel (a)], however, does not show subdivision according to the M_S quantum number for the triplet states. For this complex, the overall number of states is the lowest among all systems. The singlet ground state enters only one cluster similar to $[\text{Fe}(\text{CO})_5]^0$. Analogously to the latter, the amount of triplet S_f states is dominating over the S_g singlet states. $[\text{Cr}(\text{H}_2\text{O})_6]^{3+}$ and $[\text{Fe}(\text{H}_2\text{O})_6]^{2+}$ systems shown in panels (b) and (c), respectively, demonstrate similar clustering. In these two cases, the M_S -components of the ground state are distributed between two major clusters, thus leading to the involvement of both groups of states into the dynamics. Therefore, almost all considered states are populated within the first femtosecond. However, this behavior depends on the temperature: for low temperatures, only one component of the ground state may be initially populated, and thus, only one cluster is participating. For instance, compare with Figs. S2 and S3 in the [supplementary material](#) for the case of dynamics in $[\text{Fe}(\text{H}_2\text{O})_6]^{2+}$

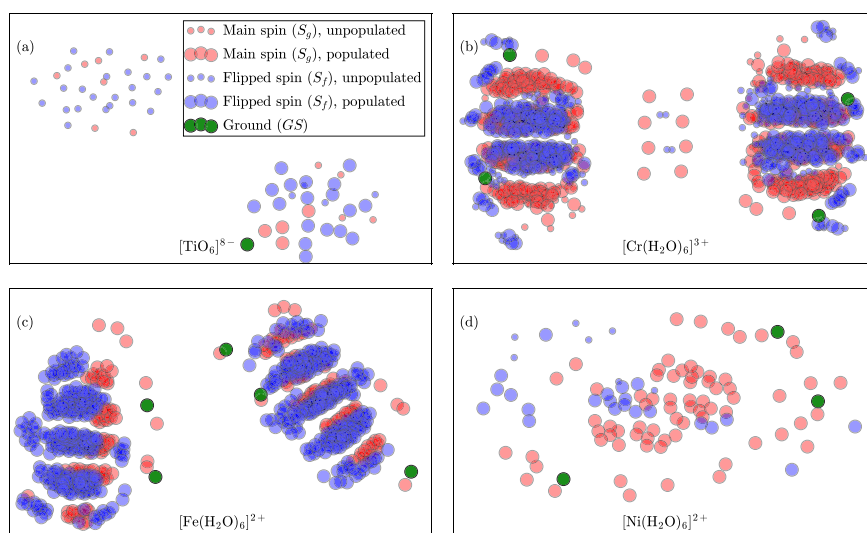


FIG. 9. Clustering of states for the complexes of *set 2*: (a) $[\text{TiO}_6]^{8-}$, (b) $[\text{Cr}(\text{H}_2\text{O})_6]^{3+}$, (c) $[\text{Fe}(\text{H}_2\text{O})_6]^{2+}$, and (d) $[\text{Ni}(\text{H}_2\text{O})_6]^{2+}$; see caption of Fig. 8.

at $T = 0$ K. Both clusters show a distinct splitting according to the M_S quantum number. The difference between the two systems is the ratio between numbers of S_f and S_g states. The flipped states are prevailing in the case of $[\text{Fe}(\text{H}_2\text{O})_6]^{2+}$ and represent a minority in the case of $[\text{Cr}(\text{H}_2\text{O})_6]^{3+}$. $[\text{Ni}(\text{H}_2\text{O})_6]^{2+}$ is somewhat similar to $[\text{TiO}_6]^{8-}$ since the total number of states is quite small. The three components of the ground state are also uniformly distributed throughout the cluster. The overall M_S grouping is less pronounced but still can be seen in the central part of the panel (d). In contrast to other cases, the separation of states into two clusters is not present. One should also note the dominating number of the S_g states.

Although the graphs given in Figs. 8 and 9 provide a convenient visualization of the connections between different states, they do not allow making an unambiguous conclusion about the decisive factors, which could be used for the *a priori* assertion on the efficiency of spin-flip for an arbitrary system. The only factor that seems to favor the efficient transition is the dominating number of spin-flipped states over the states with the ground state spin. Such a situation is observed for $[\text{Fe}(\text{CO})_5]^0$, $[\text{Fe}(\text{H}_2\text{O})_6]^{2+}$, and $[\text{TiO}_6]^{8-}$, being efficient systems, and is not observed for $[\text{Cr}(\text{H}_2\text{O})_6]^{3+}$ and $[\text{Ni}(\text{H}_2\text{O})_6]^{2+}$, showing no prominent spin transition. As described for the case of *set 2*, this domination can be present in some energy ranges and be absent for the other. This fact explains the dependence of the efficiency on the particular pulse characteristics used for the excitation, see Refs. 9 and 10. In this respect, the proper pulse leading to spin transition should necessarily overlap with the spectral regions, where S_f states dominate.

VII. CONCLUSIONS

This article represents an extension of the previous study of the ultrafast spin-flip dynamics in the core-excited states, which has been performed for a prototypical Fe^{2+} complex.^{9,10} There, the occurrence of the spin transition within the time window of hundreds of attoseconds has been observed, being also dependent on the characteristics of the exciting x-ray light pulse. Here, we address the main question: what is the crucial factor influencing the spin dynamics in terms of the yield of the spin-flipped states? For example, how the central metal ion and surrounding ligands influence the extent of the transition.

An intuitive answer can be suggested based on the two-level model, where the probability of the transition between states is proportional to the square of the coupling matrix element.¹⁹ In particular, the efficiency of spin-flip should be proportional to the SOC constant. Therefore, one expects the population transfer from states with the spin of the ground state S_g to ones with a different spin S_f to increase from left to right in the periodic table. However, the situation appears to be more complicated. Although the values of the SOC matrix V_{SOC} responsible for $L_{2,3}$ -splitting are indeed important, the number of the relevant states plays a decisive role. For instance, the SOC strength in $[\text{Ni}(\text{H}_2\text{O})_6]^{2+}$ is three times larger than in $[\text{TiO}_6]^{8-}$, but the small number of the accessible spin-flipped S_f states makes the whole process inefficient in the former case, while in the latter, the spin dynamics is much more prominent.

Importantly, the exciting pulse should overlap with the spectral regions where S_f states dominate. Here, the decomposition of

XAS provides a hint about how many states of different multiplicities are presented and what is the chance to have enough relevant states in order to observe a target effect. Relevant states are those that are coupled to the ground states by the dipole matrix elements either directly or indirectly through SOC.

The effect seems to be stable to moderate changes in the coordination sphere. For instance, the exchange of ligands situated close to each other in the spectrochemical series (e.g., H_2O and NH_3) does not lead to the qualitative changes in the rate and completeness of the spin dynamics. These ligands strongly affect neither the electronic structure nor the dephasing and relaxation rate to the environment. In general, nuclear effects were found to have little influence on the dynamics as their characteristic timescale is longer than the process considered in this article. However, strong-field ligands can substantially change the electronic structure of the outer valence shell, altering the relative energetic stability of the spin states. This is observed for $[\text{Fe}(\text{CO})_5]^0$, where the ground state spin is changed to a singlet in contrast to $[\text{Fe}(\text{H}_2\text{O})_6]^{2+}$ with its quintet ground state. In conclusion, the character and efficiency of the dynamics have to be analyzed on a case-by-case basis as no general trends have been observed.

SUPPLEMENTARY MATERIAL

The [supplementary material](#) contains the $M_{2,3}$ absorption spectra of the complexes of *set 2* and their decomposition in terms of the involved spin states, the results of dynamics and the graph of participating states at $T = 0$ K, the comparison of energies calculated with the second- and fourth-order Douglas-Kroll-Hess transformation, Wigner sampling at $T = 0$ K, and dynamics including relaxation for $[\text{Fe}(\text{H}_2\text{O})_6]^{2+}$ and $[\text{Fe}(\text{NH}_3)_6]^{2+}$.

ACKNOWLEDGMENTS

The authors would like to thank Professor Dr. Oliver Kühn and Dr. Olga S. Bokareva for fruitful discussion. Financial support from the Deutsche Forschungsgemeinschaft (Grant No. BO 4915/1-1) (V.K. and S.I.B.) and the National Natural Science Foundation of China (Grant No. 11904215) (H.W.) is gratefully acknowledged.

DATA AVAILABILITY

The data that support the findings of this study are available within the article and its [supplementary material](#).

REFERENCES

- M. Hentschel, R. Kienberger, C. Spielmann, G. A. Reider, N. Milosevic, T. Brabec, P. Corkum, U. Heinzmann, M. Drescher, and F. Krausz, *Nature* **414**, 509 (2001).
- R. Kienberger, E. Goulielmakis, M. Uiberacker, A. Baltuska, V. Yakovlev, F. Bammer, A. Scrinzi, T. Westerwalbesloh, U. Kleineberg, U. Heinzmann, M. Drescher, and F. Krausz, *Nature* **427**, 817 (2004).
- I. Grguraš, A. R. Maier, C. Behrens, T. Mazza, T. J. Kelly, P. Radcliffe, S. Düsterer, A. K. Kazansky, N. M. Kabachnik, T. Tschentscher, J. T. Costello, M. Meyer, M. C. Hoffmann, H. Schlarb, and A. L. Cavalieri, *Nat. Photonics* **6**, 852 (2012).
- T. Gaumnitz, A. Jain, Y. Pertot, M. Huppert, I. Jordan, F. Ardana-Lamas, and H. J. Wörner, *Opt. Express* **25**, 27506 (2017).

- ⁵P. K. Maroju, C. Grazioli, M. Di Fraia, M. Moiola, D. Ertel, H. Ahmadi, O. Plekan, P. Finetti, E. Allaria, L. Giannessi, G. De Ninno, C. Spezzani, G. Penco, S. Spampinati, A. Demidovich, M. B. Danailov, R. Borghes, G. Kourousias, C. E. Sanches Dos Reis, F. Billé, A. A. Lutman, R. J. Squibb, R. Feifel, P. Carpeggiani, M. Reduzzi, T. Mazza, M. Meyer, S. Bengtsson, N. Ibrakovic, E. R. Simpson, J. Mauritsson, T. Csizmadia, M. Dumergue, S. Kühn, H. Nandiga Gopalakrishna, D. You, K. Ueda, M. Labeye, J. E. Bækhoj, K. J. Schafer, E. V. Gryzlova, A. N. Grum-Grzhimailo, K. C. Prince, C. Callegari, and G. Sansone, *Nature* **578**, 386 (2020).
- ⁶*Attosecond and XUV Physics: Ultrafast Dynamics and Spectroscopy*, edited by T. Schultz and M. Vrakking (Wiley-VCH, Weinheim, 2014).
- ⁷L. Young, K. Ueda, M. Gühr, P. H. Bucksbaum, M. Simon, S. Mukamel, N. Rohringer, K. C. Prince, C. Masciovecchio, M. Meyer, A. Rudenko, D. Rolles, C. Bostedt, M. Fuchs, D. A. Reis, R. Santra, H. Kapteyn, M. Murnane, H. Ibrahim, F. Légaré, M. Vrakking, M. Isinger, D. Kroon, M. Gisselbrecht, A. L'Huillier, H. J. Wörner, and S. R. Leone, *J. Phys. B: At., Mol. Opt. Phys.* **51**, 032003 (2018).
- ⁸H. J. Wörner, C. A. Arrell, N. Banerji, A. Cannizzo, M. Chergui, A. K. Das, P. Hamm, U. Keller, P. M. Kraus, E. Liberatore, P. Lopez-Tarifa, M. Lucchini, M. Meuwly, C. Milne, J.-E. Moser, U. Rothlisberger, G. Smolentsev, J. Teuscher, J. A. van Bokhoven, and O. Wenger, *Struct. Dyn.* **4**, 061508 (2017).
- ⁹H. Wang, S. I. Bokarev, S. G. Aziz, and O. Kühn, *Phys. Rev. Lett.* **118**, 023001 (2017).
- ¹⁰H. Wang, T. Möhle, O. Kühn, and S. I. Bokarev, *Phys. Rev. A* **98**, 013408 (2018).
- ¹¹H. Wang, S. I. Bokarev, S. G. Aziz, and O. Kühn, *Mol. Phys.* **115**, 1898 (2017).
- ¹²A. Hauser, *Coord. Chem. Rev.* **111**, 275 (1991).
- ¹³L. S. Forster, *Coord. Chem. Rev.* **250**, 2023 (2006).
- ¹⁴C. M. Marian, *Wiley Interdiscip. Rev.: Comput. Mol. Sci.* **2**, 187 (2012).
- ¹⁵M. Cammarata, R. Bertoni, M. Lorenc, H. Cailleau, S. Di Matteo, C. Mauriac, S. F. Matar, H. Lemke, M. Chollot, S. Ravy, C. Lahlouh, J.-F. Létard, and E. Collet, *Phys. Rev. Lett.* **113**, 227402 (2014).
- ¹⁶Y. Jiang, L. C. Liu, A. Sarracini, K. M. Krawczyk, J. S. Wentzell, C. Lu, R. L. Field, S. F. Matar, W. Gawelda, H. M. Müller-Werkmeister, and R. J. D. Miller, *Nat. Commun.* **11**, 1530 (2020).
- ¹⁷S. Mai and L. González, *Chem. Sci.* **10**, 10405 (2019).
- ¹⁸J. C. Tremblay, T. Klamroth, and P. Saalfrank, *J. Chem. Phys.* **129**, 084302 (2008).
- ¹⁹V. May and O. Kühn, *Charge and Energy Transfer Dynamics in Molecular Systems* (Wiley-VCH, Weinheim, 2011).
- ²⁰A. Szabo and N. S. Ostlund, *Modern Quantum Chemistry*, 1st ed. (Dover Publications, Inc., Mineola, NY, 1996).
- ²¹S. Mukamel, *Principles of Nonlinear Optical Spectroscopy* (Oxford University Press, New York, 1999).
- ²²J. R. Cash and A. H. Karp, *ACM Trans. Math. Software* **16**, 201 (1990).
- ²³*FORTTRAN Numerical Recipes*, 2nd ed., edited by W. H. Press (Cambridge University Press, Cambridge, NY, 1996).
- ²⁴I. Fernández Galván, M. Vacher, A. Alavi, C. Angeli, F. Aquilante, J. Autschbach, J. J. Bao, S. I. Bokarev, N. A. Bogdanov, R. K. Carlson, L. F. Chibotaru, J. Creutzberg, N. Dattani, M. G. Delcey, S. S. Dong, A. Dreuw, L. Freitag, L. M. Frutos, L. Gagliardi, F. Gendron, A. Giussani, L. González, G. Grell, M. Guo, C. E. Hoyer, M. Johansson, S. Keller, S. Knecht, G. Kovacević, E. Källman, G. Li Manni, M. Lundberg, Y. Ma, S. Mai, J. P. Malhado, P. Å. Malmqvist, P. Marquetand, S. A. Mewes, J. Norell, M. Olivucci, M. Oettel, Q. M. Phung, K. Pierloot, F. Plasser, M. Reiher, A. M. Sand, I. Schapiro, P. Sharma, C. J. Stein, L. K. Sørensen, D. G. Truhlar, M. Ugandi, L. Ungur, A. Valentini, S. Vancouillie, V. Velyazov, O. Weser, T. A. Wesolowski, P.-O. Widmark, S. Wouters, A. Zech, J. P. Zobel, and R. Lindh, *J. Chem. Theory Comput.* **15**, 5925 (2019).
- ²⁵T. K. Sham, J. B. Hastings, and M. L. Perlman, *J. Am. Chem. Soc.* **102**, 5904, 00075 (1980).
- ²⁶B. W. McClelland, A. G. Robiette, L. Hedberg, and K. Hedberg, *Inorg. Chem.* **40**, 1358, 00025 (2001).
- ²⁷Y.-Q. Zheng and Z.-P. Kong, *J. Coord. Chem.* **56**, 967 (2003).
- ²⁸R. W. G. Wyckoff, *Crystal Structures* (Interscience Publishers, New York, 1963), Vol. 1.
- ²⁹M. J. Frisch, G. W. Trucks, H. B. Schlegel, G. E. Scuseria, M. A. Robb, J. R. Cheeseman, G. Scalmani, V. Barone, B. Mennucci, G. A. Petersson, H. Nakatsuji, M. Caricato, X. Li, H. P. Hratchian, A. F. Izmaylov, J. Bloino, G. Zheng, J. L. Sonnenberg, M. Hada, M. Ehara, K. Toyota, R. Fukuda, J. Hasegawa, M. Ishida, T. Nakajima, Y. Honda, O. Kitao, H. Nakai, T. Vreven, J. J. A. Montgomery, J. E. Peralta, F. Ogliaro, M. Bearpark, J. J. Heyd, E. Brothers, K. N. Kudin, V. N. Staroverov, R. Kobayashi, J. Normand, K. Raghavachari, A. Rendell, J. C. Burant, S. S. Iyengar, J. Tomasi, M. Cossi, N. Rega, J. M. Millam, M. Klene, J. E. Knox, J. B. Cross, V. Bakken, C. Adamo, J. Jaramillo, R. Gomperts, R. E. Stratmann, O. Yazyev, A. J. Austin, R. Cammi, C. Pomelli, J. W. Ochterski, R. L. Martin, K. Morokuma, V. G. Zakrzewski, G. A. Voth, P. Salvador, J. J. Dannenberg, S. Dapprich, A. D. Daniels, O. Farkas, J. B. Foresman, J. V. Ortiz, J. Cioslowski, and D. J. Fox, Gaussian 09, Revision D.01, Gaussian, Inc., Wallingford, CT, 2009, Technical Report.
- ³⁰M. Douglas and N. M. Kroll, *Ann. Phys.* **82**, 89 (1974).
- ³¹B. O. Roos, R. Lindh, P.-Å. Malmqvist, V. Velyazov, and P.-O. Widmark, *J. Phys. Chem. A* **109**, 6575 (2005).
- ³²S. I. Bokarev and O. Kühn, *Wiley Interdiscip. Rev.: Comput. Mol. Sci.* **10**, e1433 (2020).
- ³³P. Å. Malmqvist, A. Rendell, and B. O. Roos, *J. Phys. Chem.* **94**, 5477 (1990).
- ³⁴P. Å. Malmqvist, *Int. J. Quantum Chem.* **30**, 479 (1986).
- ³⁵P.-Å. Malmqvist and B. O. Roos, *Chem. Phys. Lett.* **155**, 189 (1989).
- ³⁶B. Schimmelpfennig, AMFI: An Atomic Mean-Field Spin-Orbit Integral Program, 1996.
- ³⁷C. M. Marian, in *Reviews in Computational Chemistry*, edited by K. B. Lipkowitz, D. B. Boyd, and John Wiley & Sons (Wiley-VCH, New York, 2001), Vol. 17, pp. 99–204.
- ³⁸I. Josefsson, K. Kunnus, S. Schreck, A. Föhlich, F. de Groot, P. Wernet, and M. Odelius, *J. Phys. Chem. Lett.* **3**, 3565 (2012).
- ³⁹P. Wernet, K. Kunnus, S. Schreck, W. Quevedo, R. Kurian, S. Teichert, F. M. F. de Groot, M. Odelius, and A. Föhlich, *J. Phys. Chem. Lett.* **3**, 3448 (2012).
- ⁴⁰S. I. Bokarev, M. Dantz, E. Suljoti, O. Kühn, and E. F. Aziz, *Phys. Rev. Lett.* **111**, 083002 (2013).
- ⁴¹J. P. Dahl and M. Springborg, *J. Chem. Phys.* **88**, 4535, 00195 (1988).
- ⁴²R. Schinke, *Photodissociation Dynamics: Spectroscopy and Fragmentation of Small Polyatomic Molecules*, Cambridge Monographs on Atomic, Molecular and Chemical Physics, 1st ed. (Cambridge University Press, Cambridge, 1995), p. 01631.
- ⁴³S. Mai, M. Richter, M. Heindl, M. F. S. J. Menger, A. Atkins, M. Ruckebauer, F. Plasser, L. M. Ibele, S. Kropf, M. Oettel, P. Marquetand, and L. González, SHARC2.1: Surface Hopping Including Arbitrary Couplings—Program Package for Non-Adiabatic Dynamics, 2019.
- ⁴⁴M. Heyden, J. Sun, S. Funkner, G. Mathias, H. Forbert, M. Havenith, and D. Marx, *Proc. Natl. Acad. Sci. U. S. A.* **107**, 12068 (2010).
- ⁴⁵E. Suljoti, R. Garcia-Diez, S. I. Bokarev, K. M. Lange, R. Schoch, B. Dierker, M. Dantz, K. Yamamoto, N. Engel, K. Atak, O. Kühn, M. Bauer, J.-E. Rubensson, and E. F. Aziz, *Angew. Chem., Int. Ed.* **52**, 9841 (2013).
- ⁴⁶J. C. Woicik, E. L. Shirley, C. S. Hellberg, K. E. Andersen, S. Sambasivan, D. A. Fischer, B. D. Chapman, E. A. Stern, P. Ryan, D. L. Ederer, and H. Li, *Phys. Rev. B* **75**, 140103 (2007).
- ⁴⁷A. A. Hagberg, D. A. Schult, and P. J. Swart, in Proceedings of the 7th Python in Science Conference, edited by G. Varoquaux, T. Vaught, and J. Millman, Pasadena, CA, 2008, pp. 11–16 available at http://conference.scipy.org/proceedings/SciPy2008/paper_2/.
- ⁴⁸T. M. J. Fruchterman and E. M. Reingold, *Software: Pract. Exper.* **21**, 1129 (1991).

Supplement

Effect of chemical structure on the ultrafast spin dynamics in core-excited states

Vladislav Kochetov,¹ Huihui Wang,² and Sergey I. Bokarev^{1, a)}

¹*Institut für Physik, Universität Rostock, A.-Einstein-Strasse 23-24, 18059 Rostock, Germany*

²*State Key Laboratory of Quantum Optics and Quantum Optics Devices, Institute of Laser Spectroscopy, Shanxi University, 030006, China*

(Dated: June 11, 2020)

Recent developments of the sources of intense and ultrashort X-ray pulses stimulate theoretical studies of phenomena occurring on ultrafast timescales. In the present study, spin-flip dynamics in transition metal complexes triggered by sub-femtosecond X-ray pulses are addressed theoretically using a density matrix-based time-dependent configuration interaction approach. The influence of different central metal ions and ligands on the character and efficiency of spin-flip dynamics is put in focus. According to our results, slight variations in the coordination sphere do not lead to qualitative differences in dynamics, whereas the nature of the central ion is more critical. However, the behavior in a row of transition metals demonstrates trends that are not consistent with general expectations. Thus, the peculiarities of spin dynamics have to be analyzed on a case-by-case basis.

^{a)}sergey.bokarev@uni-rostock.de

Supplement

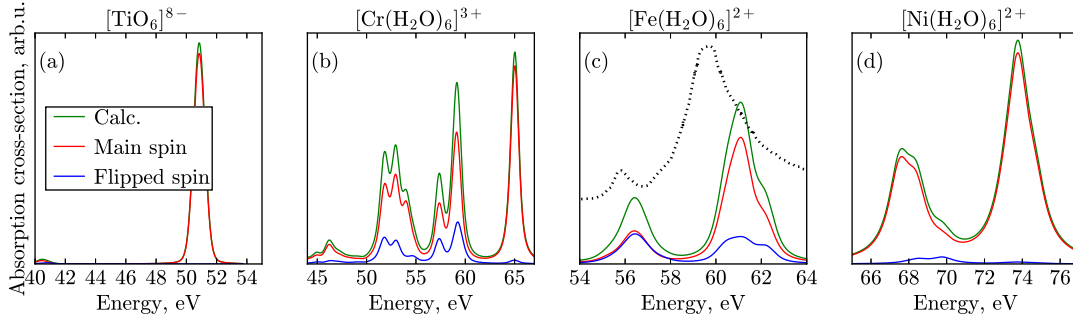


Figure S1. Calculated $M_{2,3}$ -edge absorption spectra for the *set 2* complexes with the decomposition in spin multiplicities denoted in the legend of panel (a). Panel (c) presents in addition the experimental spectrum (black dotted) for the Fe $M_{2,3}$ -edge of Fe_2O_3 [R. Berlasso et al., Phys. Rev. B 73, 115101 (2006)].

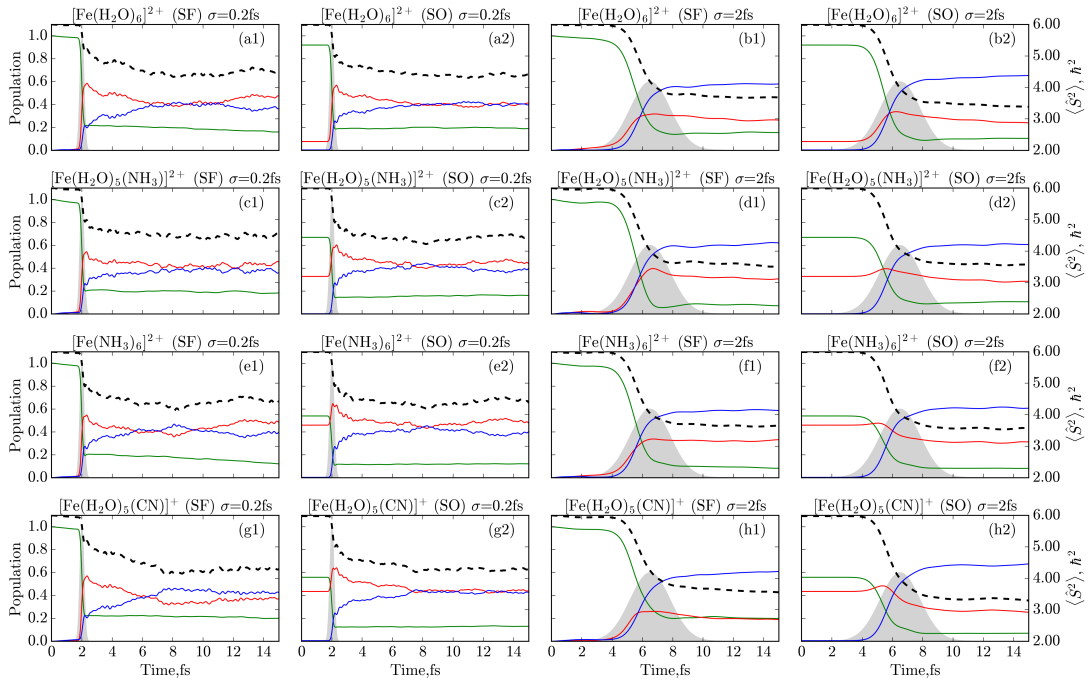


Figure S2. Comparison of the dynamics at $T = 0$ K (panels (a1)-(h1)) and $T = 300$ K (panels (a2)-(h2)) for the compounds of *set 1* and two different pulses. For notation see caption of Figure 4 in the main text. For the longer pulse (panels (b), (d), (f), and (h)): $\hbar\Omega = 713$ eV, $A = 1.5$ a.u., $\sigma = 2$ fs. Short pulse has characteristics given in Table II in the main text.

Supplement

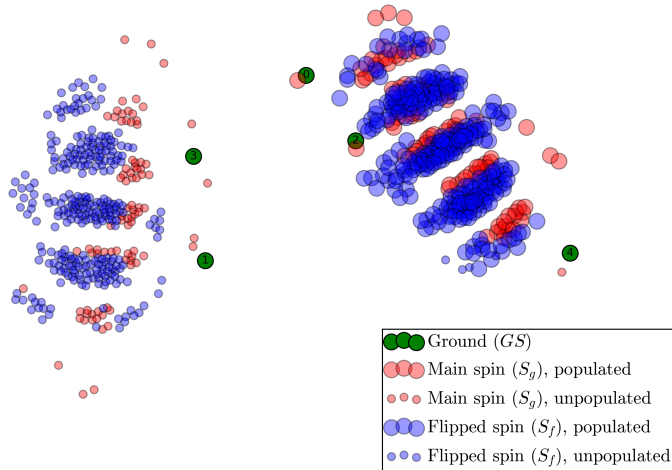


Figure S3. Force-directed graph, showing the clustering of the states of $[\text{Fe}(\text{H}_2\text{O})_6]^{2+}$ at $T = 0$ K. Thus, only the true ground state corresponding to the green node numbered “0” is initially populated. See caption to Figure 8 in the main text.

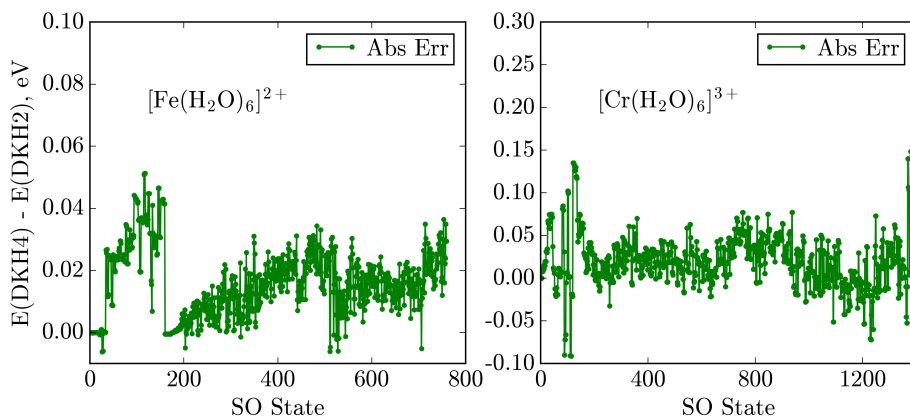


Figure S4. Comparison of the deviations in SF excitation energies using Douglas-Kroll-Hess transformation of the second (DKH2) and fourth (DKH4) orders for $[\text{Fe}(\text{H}_2\text{O})_6]^{2+}$ and $[\text{Cr}(\text{H}_2\text{O})_6]^{3+}$ systems.

Supplement

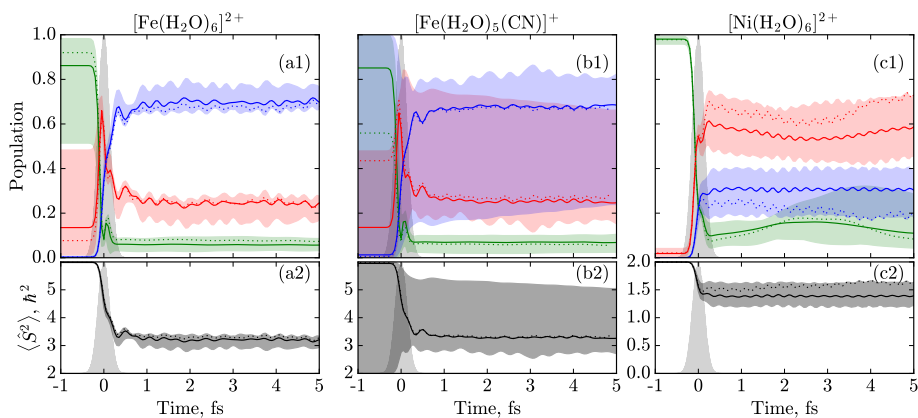


Figure S5. Spin-flip dynamics accounting for the width of the initial vibrational wave packet in the nuclear phase space (only distribution of geometries is considered) at $T = 0$ K for $[\text{Fe}(\text{H}_2\text{O})_6]^{2+}$ (panels (a)), $[\text{Fe}(\text{H}_2\text{O})_5(\text{CN})]^+$ (panels (b)), and $[\text{Ni}(\text{H}_2\text{O})_6]^{2+}$ (panels (c)). For notation see Figure 6 in the main text.

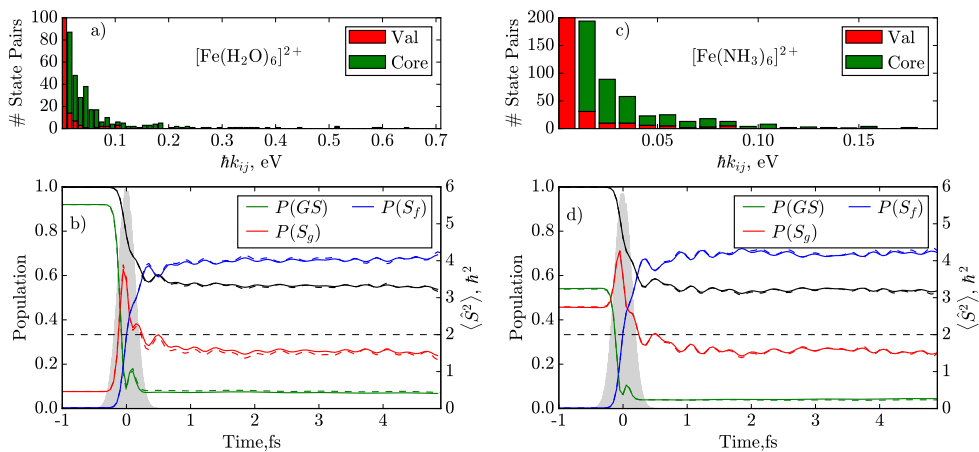


Figure S6. (a) and (c) Distributions of the relaxation rates k_{ij} between valence- (red bars) and core-excited (green bars) states of $[\text{Fe}(\text{H}_2\text{O})_6]^{2+}$ and $[\text{Fe}(\text{NH}_3)_6]^{2+}$. Note that the bars for the range 0.00-0.01 eV are cut not to show all 52670 rates. (b) Respective spin-dynamics with (solid lines) and without (dashed lines) dissipation.

[VK2] RHO_DYN: A ρ -TD-RASCI FRAMEWORK TO STUDY ULTRAFAST
ELECTRON DYNAMICS IN MOLECULES

VLADISLAV KOCHETOV and SERGEY I. BOKAREV

Reprinted (adapted) with permission from

VLADISLAV KOCHETOV and SERGEY I. BOKAREV, *Journal of Chemical Theory and Computation* **18**, 46-58 (2022).

Copyright © 2022 American Chemical Society.

RhoDyn: A ρ -TD-RASCI Framework to Study Ultrafast Electron Dynamics in Molecules

Vladislav Kochetov and Sergey I. Bokarev*

 Cite This: *J. Chem. Theory Comput.* 2022, 18, 46–58

 Read Online

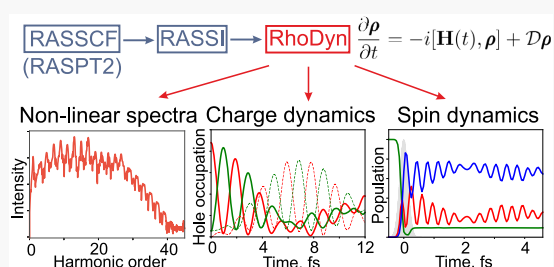
ACCESS |

 Metrics & More

 Article Recommendations

 Supporting Information

ABSTRACT: This article presents the program module RhoDyn as part of the OpenMOLCAS project intended to study ultrafast electron dynamics within the density-matrix-based time-dependent restricted active space configuration interaction framework (ρ -TD-RASCI). The formalism allows for the treatment of spin-orbit coupling effects, accounts for nuclear vibrations in the form of a vibrational heat bath, and naturally incorporates (auto)ionization effects. Apart from describing the theory behind and the program workflow, the paper also contains examples of its application to the simulations of the linear $L_{2,3}$ absorption spectra of a titanium complex, high harmonic generation in the hydrogen molecule, ultrafast charge migration in benzene and iodoacetylene, and spin-flip dynamics in the core excited states of iron complexes.



1. INTRODUCTION

The past decade heralds the gradual change of the ultrafast paradigm in physics and chemistry from the femtosecond to subfemtosecond and even a few tens of attoseconds domain. The fascinating growth in the number of studies of the ultrafast phenomena is owing to establishing new sources such as X-ray free electron lasers (XFELs)^{1–4} and high harmonics generation (HHG) setups^{5,6} which give access to dynamics at electronic time scales.^{7–10} State-of-the-art XFELs allow studying processes with extremely intense ultrashort pulses enabling studies of multiple ionization and radiation damage.^{11,12} HHG, in turn, gives unparalleled pulse durations of several tens of attoseconds⁶ and thus enables unprecedented experiments on electronic structure, such as imaging of molecular orbitals,^{13–15} attosecond interferometry,^{16,17} measuring phases of photoionization amplitudes,^{18,19} and others. Moreover, one of the most intriguing phenomena in ultrafast physics and chemistry, charge migration (CM),^{20,21} already has impressive experimental evidence.^{22–24}

From the viewpoint of theory, quantum chemistry packages provide an accurate static electronic structure. However, to meet the challenges of time and to improve the interpretation of the experimental data, one needs to predict the subfemtosecond electron dynamics in molecules and extended systems. That is why an extension of quantum chemistry to the time domain is warranted.

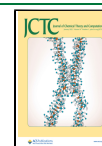
There are plenty of methods dealing with ultrafast phenomena occurring on the attosecond to few femtoseconds time scale.^{25–28} For instance, versatile methods are formulated in the framework of algebraic diagrammatic construction (ADC),^{29,30} the coupled-cluster family of approaches,^{31–33} and time-dependent density functional theory.³⁴ The multiconfi-

gurational time-dependent Hartree (MCTDH)(F) method^{35–39} should be named among the multiconfigurational wave function techniques allowing the study of electron dynamics in real space and time. In energy representation (state basis), a traditional approach to electron dynamics is time-dependent configuration interaction (TD-CI)^{40–43} or, more generally, the time-dependent multiconfigurational self-consistent field (TD-MCSCF)^{44,45} approach. With increasing molecular size or considering deeper-lying core orbitals, it is crucial to decrease computational cost, where the concepts of restricted active space (RAS)⁴⁵ and generalized active space (GAS)⁴⁶ help reduce the number of electronic configurations. Another recently implemented method allowing for larger active spaces is time-dependent density matrix renormalization group (TD-DMRG).^{47–50}

The methods mentioned above are based on the configuration interaction (CI) wave function decomposition and the subsequent propagation of expansion coefficients. However, it is often necessary to describe open quantum systems in a more general way. For instance, the density matrix formulation offers some advantages. It allows for an implicit inclusion of environmental effects such as dephasing and energy relaxation and natural incorporation of (auto-)ionization^{51,52} phenomena. Moreover, nonlinear spectro-

Received: November 2, 2021

Published: December 29, 2021



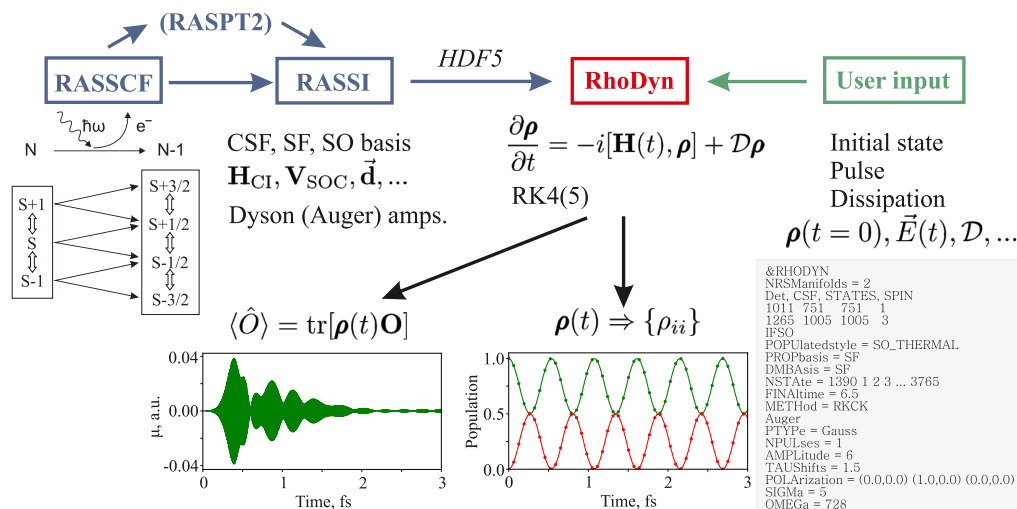


Figure 1. Scheme of the workflow and dependencies of the RhoDyn module on other parts of the OpenMOLCAS package.

copies^{53–56} are usually formulated in terms of perturbation expansion of the density matrix. Thus, a wider range of phenomena can be investigated within the density-matrix-based approach.

In this article, we present an implementation of the density-matrix-based time-dependent restricted active space configuration interaction (ρ -TD-RASCI) method into the OpenMOLCAS program package⁵⁷ within a program module called RhoDyn. The primary goal of this module is to provide access to the various aspects of the ultrafast electron dynamics in molecules, including the influence of spin-orbit coupling (SOC) effects, population and phase relaxation due to the environment, and (auto)ionization. The article is organized as follows: We start from the theory underlying the method in section 2. Section 3 describes the program's functionality. Further, in section 4, we present some exemplary applications to the X-ray absorption spectrum of titanium dioxide, HHG spectrum of the hydrogen molecule, charge-migration dynamics in benzene and iodoacetylene, and spin dynamics in the core excited states of transition metal complexes. Section 5 summarizes the peculiarities of the RhoDyn module and provides an outlook of future developments. To make the discussion in the main text more concise, the details of calculations are given in the Appendix.

2. METHODOLOGY

ρ -TD-RASCI method⁵⁸ is implemented as a core feature of the RhoDyn program module. It is intended to study purely electronic dynamics when nuclear motion does not play an important role, completely altering the dynamics. Such an approach seems to be especially useful to study core-state dynamics since electron dynamics are to a large extent isolated from nuclear effects owing to the characteristic time scale of core electron's motion and the ultrashort lifetime of the core hole not exceeding a few femtoseconds. To still be able to take the influence of the energy and phase relaxation due to vibronic interactions into account, the RhoDyn module allows employing the electronic system–vibrational bath partitioning; for details, see ref 59. In such an approach, the dynamics of an

open system are described via its reduced density operator $\hat{\rho}$ following the Liouville–von Neumann equation

$$\frac{\partial}{\partial t} \hat{\rho} = -i[\hat{H}, \hat{\rho}] - \mathcal{D}\hat{\rho} \quad (1)$$

with a dissipation superoperator \mathcal{D} . Note that here and below atomic units are used unless stated otherwise. The RhoDyn module is inherently interfaced with other core programs of the OpenMOLCAS package, as shown schematically in Figure 1. The matrix (tensor) forms of the $\hat{\rho}$, \hat{H} , and \mathcal{D} operators are written in energy representation using the eigenstates of some zero-order Hamiltonian \hat{H}_0 . The program allows for a flexible choice of the basis. On a basic level, the basis of configuration state functions (CSFs) is utilized. In this latter basis, the Hamiltonian matrix takes the form

$$\mathbf{H}(t) = \mathbf{H}_{\text{Cl}} + \mathbf{V}_{\text{SOC}} + \mathbf{U}_{\text{ext}}(t) \quad (2)$$

Here, \mathbf{H}_{Cl} , \mathbf{V}_{SOC} , and $\mathbf{U}_{\text{ext}}(t)$ are the time-independent CI Hamiltonian responsible for electron correlation effects, spin-orbit (SO) interaction, and time-dependent external potential, e.g., due to interaction with the light field, respectively. The study of electron-correlation-driven dynamics can be conveniently conducted in this basis. However, for more complicated processes, the investigator might prefer to take the eigenfunctions of the $\hat{H}_0 = \hat{H}_{\text{Cl}}$ or $\hat{H}_0 = \hat{H}_{\text{Cl}} + \hat{V}_{\text{SOC}}$ operators as a basis. We will call them spin-free (SF) and SO states in what follows. In its simplest form, the light–matter interaction term is represented as semiclassical dipole coupling $\mathbf{U}_{\text{ext}}(t) = -\mathbf{d} \cdot \vec{E}(t)$, where \mathbf{d} is a transition dipole tensor written in one of the bases mentioned above and $\vec{E}(t)$ is an external electric field; see section 3.

The quantities necessary for the propagation, \mathbf{H}_{Cl} , \mathbf{V}_{SOC} , \mathbf{d} , and the transformation matrices between CSF, SF, or SO bases, are transferred from the RASSCF and RASSI modules of OpenMOLCAS; see Figure 1. In RhoDyn, the user needs to supply the form of the light field $\vec{E}(t)$ and the dissipation tensor \mathcal{D} , which can be obtained numerically as described in detail elsewhere⁵⁹ or take a simple parametrized phenomenological form.

Propagation of the density matrix according to eq 1 is performed with the adaptive Runge–Kutta–Cash–Karp method^{60,61} of the 4(5) order of accuracy or with the fourth-order Runge–Kutta with a fixed time step. In many cases, this method suffices as it approximates the full exponential propagator sufficiently accurately to produce the same results.^{49,62}

The main output of the RhoDyn module consists of the time-dependent reduced density matrix $\rho(t)$, which can be printed out with any convenient time step. Its diagonal provides occupation numbers of the basis states. More importantly, this matrix can be used to compute the expectation value of any operator \hat{O} whose matrix is written in the same basis:

$$\langle \hat{O} \rangle = \text{tr}[\rho(t)\mathbf{O}] \quad (3)$$

In this respect, the most prominent example is the dipole moment $\langle \hat{\mu} \rangle(t)$, as it provides access to linear and nonlinear spectra of the system; see, e.g., sections 4.1 and 4.2. Note that the explicit electronic continuum is currently not implemented and (auto)ionization processes can be accounted only implicitly; i.e., continuum electron stays unobserved. Therefore, the explicit photoelectron observables such as angular distributions, time delays, or phases cannot be calculated and are the subject of future development.

3. COMPUTATIONAL WORKFLOW

The RhoDyn module vastly relies on the infrastructure of the OpenMOLCAS package. The workflow of a dynamical calculation, including the example of input, is illustrated in Figure 1. Representative input files corresponding to the examples of section 4 are given in the Supporting Information to provide further guidance. First, one needs to compute all the wave functions with complete active space self-consistent field (CASSCF) or restricted active space self-consistent field (RASSCF) methods for all state manifolds which are relevant for the dynamics with the RASSCF module; these can be states of different multiplicities coupled via SOC or states with a different number of electrons if photoionization, autoionization, or electron attachment is considered. Thus, comparatively small but highly optimized correlated basis functions are used for time propagation. Although considerably reducing the dimension of the space spanned by the basis and the respective computational cost, it may be less reliable if the electron movement spans a large physical domain or involves a large number of electronic states; see, e.g., section 4.2. One might wish to employ a complete active space second order perturbation theory (CASPT2) or restricted active space second order perturbation theory (RASPT2) energy correction to include dynamic correlation. Finally, the RASSI module implementing the restricted active space state interaction (RASSI) method⁶³ provides \mathbf{H}_{Cl} and \mathbf{V}_{SOC} , and transition dipole matrix \mathbf{d} , entering the Hamiltonian equation (eq 2), in any convenient basis of CSFs, SF, or SO states and the transformation matrices between the bases. The communication of the data from the respective modules to RhoDyn is done via the HDF5 interface.⁶⁴

The user needs to supply RhoDyn with the initial density matrix, which can be, for instance, represented as the thermal ensemble in equilibrium:

$$\rho_{ij}(0) = \delta_{ij} \exp(-E_i/(kT)) \quad (4)$$

However, it can be generally constructed from any state vector $|\Psi\rangle$ in the respective basis $\{|\Phi_i\rangle\}$ as $\rho(0) = \sum_{ij} \langle \Phi_i | \Psi \rangle \langle \Psi | \Phi_j \rangle$ and be read in a matrix form from a separate file.

In the absence of static contribution, the electric field can be derived from the vector potential as $\vec{E}(t) = -\partial \vec{A}(t)/\partial t$; thus, both the oscillatory function and the pulse envelope need to be differentiated. It gives rise to two terms; e.g., for a Gaussian-shaped light pulse with vector potential $\vec{A}(t) = A\Omega^{-1}\vec{e} \exp\{-(t-t_0)^2/(2\sigma^2)\} \cos(\Omega t + \varphi_0)$ (note that the normalization factor of the envelope is included in the amplitude A), the electric field reads

$$\begin{aligned} \vec{E}(t) = & A\vec{e} \exp\{-(t-t_0)^2/(2\sigma^2)\} \sin(\Omega t + \varphi_0) \\ & + \frac{A\vec{e}(t-t_0)}{\Omega\sigma^2} \exp\{-(t-t_0)^2/(2\sigma^2)\} \cos(\Omega t + \varphi_0) \end{aligned} \quad (5)$$

Here, A , \vec{e} , t_0 , and Ω are the amplitude, polarization, time center of the envelope, and carrier frequency. The second correction term ensures that the integral of the electric field over the entire pulse vanishes: $\int_{-\infty}^{\infty} \vec{E}(t) dt = 0$.⁶⁵ However, it should be notable only for small Ω , e.g., valence excitations, when the carrier envelope phase φ_0 matters. For core excitations and pulse durations of more than 200 as, this term is of minor importance.

In RhoDyn, the user can choose between different options for pulse forms, such as Gaussians and more localized $\sin^n(\pi(t-t_0)/(2\sigma))$ or $\cos^n(\pi(t-t_0)/(2\sigma))$ ($n = 2, \dots$). There is also a possibility to select a linearly chirped pulse⁷ with $\Omega(t) = \Omega_0 + a(t-t_0)$. Apart from a single pulse, one can choose a sequence with individual polarization, intensity, duration, time shift, and carrier frequency. Thus, it allows the user to prepare an intricate electronic wave packet and enables calculations of the nonlinear spectra. Currently, in RhoDyn, there are no tools to perform orientational averaging, but this can be done at the postprocessing stage.

The Redfield tensor \mathcal{D} in eq 1 accounts for the coupling to the vibrational bath.^{66,67} The decay rates must be calculated separately; see, e.g., ref 59, and RhoDyn reads them in a matrix form. The user can also complement the diagonal of the Hamiltonian by imaginary numbers to implicitly account for some other decay channels. In this case, the propagation is non-norm-conserving and $\text{tr} \rho < 1$.

4. EXEMPLARY APPLICATIONS

Below we present three different applications of the implemented methodology: (i) using the calculated time-dependent dipole moment to obtain the linear X-ray absorption spectrum (XAS) of $[\text{TiO}_6]^{8-}$ cluster and the high harmonic generation spectrum of the H_2 molecule triggered by a strong-field IR laser pulse, (ii) the charge migration in the benzene and iodoacetylene molecules caused by sudden ionization and short UV pulse, and (iii) the ultrafast spin-flip dynamics in the $[\text{Fe}(\text{H}_2\text{O})_6]^{2+}$ and $[\text{Fe}(\text{CO})_5]^{10}$ complexes in the core excited states triggered by an ultrashort X-ray pulse. Possible applications are, of course, not limited to these types of processes and may include studies of multiple ionization and nonlinear spectroscopies as will be detailed elsewhere.

4.1. Linear XAS. The time-dependent dipole moment $\vec{\mu}(t)$ can be used for computing multi-time correlation functions and response functions of different orders to simulate and understand nonlinear spectra.⁶⁸ The simplest example is a

linear absorption spectrum which can be obtained as a Fourier transform of $\vec{\mu}(t)$:

$$\alpha(\omega) = \frac{1}{2\pi} \text{Im} \left[\int_0^{t_f} dt e^{i\omega t} \vec{\mu}(t) \cdot \vec{e} W(t) \right] \quad (6)$$

Here, the oscillations of $\vec{\mu}$ are initiated by the incoming pulse with polarization \vec{e} , t_f is the length of propagation, and $W(t)$ is a window function used to filter out noise.

An example is given in Figure 2, displaying the $L_{2,3}$ -edge XAS of the $[\text{TiO}_6]^{8-}$ cluster mimicking the bulk TiO_2 . The

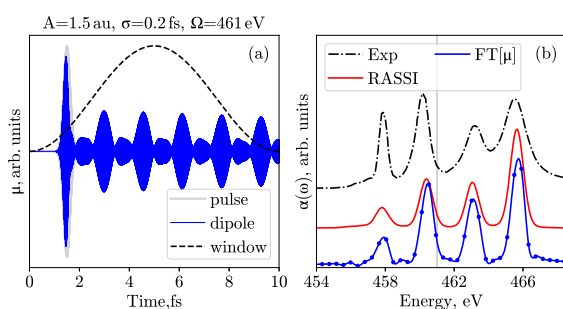


Figure 2. (a) Ultrashort X-ray pulse (gray shaded area) with characteristics given above the panel, time evolution of $\vec{\mu}(t)$ (blue), and Hann window function (dashed) used to simulate the XAS of the $[\text{TiO}_6]^{8-}$ cluster. (b) Comparison of the Fourier transform of $\vec{\mu}(t)$ ($\text{FT}[\vec{\mu}]$, blue) and the static spectrum obtained from RASSI (red) with experiment.⁶⁹ The thin vertical line marks the carrier frequency of the excitation pulse.

pulse, dipole response, and window function are shown in Figure 2a. Figure 2b displays the steady-state spectrum corresponding to time-independent energies and transition dipole moments obtained from the RASSCF/RASSI calculation and the Fourier transformed spectrum. Although the time-dependent procedure is redundant with the time-independent one, both results agree reasonably, representing an important consistency check.

4.2. High-Harmonic Generation. HHG is a highly nonlinear optical effect observed for atomic and molecular gases as well as for solids.^{70–72} As a result of the interaction of a high-intensity light pulse having carrier frequency Ω with the target system, the emission of higher harmonics with frequencies $N\Omega$ occurs; N is odd for the bright harmonics for the isotropic systems. Such a high-energy spectrum is due to the field-driven recombination of the accelerated electron with the ionized target.

HHG spectra can be calculated in the length form as a Fourier transform of the dipole moment's response to the incoming radiation with polarization \vec{e} :¹⁰

$$I(\omega) = A\omega^4 \left| \int_0^{t_f} dt e^{-i\omega t} \vec{\mu}(t) \cdot \vec{e} W(t) \right|^2 \quad (7)$$

The HHG spectrum has been calculated for a prototypical example of the H_2 molecule. Two different basis sets, aug-cc-pVDZ⁷³ and d-aug-cc-pVDZ,⁷⁴ supporting a set of diffuse functions, have been used. Pulse characteristics have been chosen to represent the typical experimental pulse as an output of a Ti:sapphire laser; see the Appendix.

The two resulting HHGs for two bases can be seen in Figure 3b. For the more compact aug-cc-pVDZ basis, the cutoff

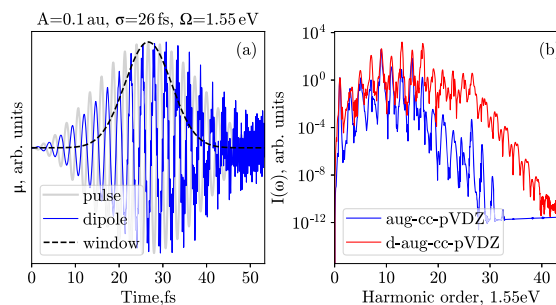


Figure 3. (a) Response of the H_2 dipole moment (blue line) to the IR short and intense laser pulse (gray line) for the aug-cc-pVDZ basis. The filtering window function in eq 7 is also depicted with a dashed line. (b) Resulting HHG spectrum of H_2 molecule for the two basis sets.

frequency is observed around the 17th harmonic whereas for the more diffuse d-aug-cc-pVDZ basis, it shifts to about the 25th harmonic, which demonstrates the importance of taking enough localized Gaussian functions to discretize the continuum relevant for the HHG process. In comparison with previous studies⁷⁵ and available experimental data,⁷⁶ the results are in reasonable agreement, but of course the adequately chosen basis set, including diffuse functions and Rydberg states, e.g., Kaufmann functions,⁷⁷ is of great importance here.^{78–80} One should note that ionization losses should be accounted for by absorbing boundaries, for example, by the complex absorbing potential or heuristic ionization model in the spirit of refs 52 and 81. This procedure delivers a smoother spectrum since the artificial scattering at the boundaries of the localized basis set decreases. Finally, we note that such processes as HHG involve a plethora of stationary electronic states, and the size of the state basis should be chosen with caution.

4.3. Charge Migration. Charge migration represents an attosecond to few femtosecond oscillatory hole dynamics occurring upon ionization of the system when a superposition of several ionic eigenstates is created, e.g., by a broadband laser pulse. This process is often approximated by an instantaneous removal of an electron from a particular molecular orbital (MO).^{20,83} This effect has been mainly studied theoretically,^{21,30,83–86} although recent experimental advancements also address it.^{22–24} Its main driving force is electron correlation, but nonadiabatic couplings can also drive it.⁸⁷ More specifically, the basic correlation-driven mechanisms can be different.^{20,83} Here we consider the hole mixing for two examples, benzene and iodoacetylene, which exhibit different types of charge migration. The former is a “satellite” migration when a superposition of a 1h and the adjacent 2h1p satellite states is created, and the latter is a “pure” hole mixing when different 1h states are involved. It implies some differences summarized in Table 1.

The mechanism of the preparation of the superposition Ψ_{ion} in theoretical simulations can also be different. One can consider the following: (i) the population of a single $N - 1$ -electron configuration or CSF, $\Psi_{\text{ion}} = \Phi_j^{N-1}$, (ii) the direct action of the annihilation operator for a particular orbital on the N -electron ground eigenstate of the un-ionized system

$$\Psi_{\text{ion}} = \mathcal{N} \hat{a}_p \Psi_g^N = \mathcal{N} \sum_j C_{gp} \hat{a}_p \Phi_j^N$$

Table 1. Summary of Charge Migration Simulations in Benzene and Iodoacetylene Molecules

	C ₆ H ₆	HCCI
type of charge migration	1h/2h1p	1h
character of hole density migration	breathing	from 1 to C≡C
experimental period, fs	–	1.85 ²³
theoretical period, this work, fs	0.98	1.95
theoretical period, other works, fs	0.75, ⁶² 0.94, ⁸² 0.80 ⁵⁰	1.83, ⁶² 1.85 ⁴⁹
number of basis CSFs (singlets, doublets)	175, 210	2520, 12096 ^a
number of basis SF/SO states (singlets, doublets) ^b	175, 210	1, 20–800

^aThis number includes CSFs with both $\pm 1/2$ spin projections. ^bThe number of basis states which are actually included in the dynamics.

where \mathcal{N} is a normalization factor, e.g.⁶²

$$\mathcal{N} = 1/\langle \Psi_g^N | \hat{a}_p^\dagger \hat{a}_p | \Psi_g^N \rangle$$

or (iii) the direct action of the light pulse $\vec{E}(t)$ on the ground state wave function that conditionally can be denoted as

$$\Psi_{\text{ion}}(t) = \exp[i\hat{\mu} \cdot \vec{E}(t)t] \Psi_g^N$$

where $\hat{\mu}$ is the dipole operator. The first two ways represent a sudden limit and thus are artificial but convenient in theoretical treatment.

Case (iii) is more realistic and can have a direct correspondence to the experiments. Finally, the initial density matrix can be generally constructed from the respective ionic CI vectors in the basis of CSFs, obtained according to (i) or (ii), as $\rho(0) = \bar{C}_{\text{ion}} \bar{C}_{\text{ion}}^\dagger$.

Benzene. We have chosen benzene (C₆H₆) as a convenient example which is often studied in theoretical works.^{50,62,82} Charge migration, in this case, consists of hole dynamics following the preparation of the initial state by the sudden removal of an electron from the 1b_{1g} MO (Figure 4). The initial state predominantly represents a superposition of the “main” 1b_{1u} 1h state and its 2h1p shakeup satellite due to excitation from the degenerate 1b_{2g} and 1b_{3g} orbitals to a couple of degenerate unoccupied orbitals, 2b_{1u} and 1a_u.⁸² Note that orbital notation is given in the largest Abelian subgroup D_{2h} of the full point symmetry group D_{6h} which coincides with the notation of ref 62 but differs from that of ref 82. It was shown^{88,89} that nuclear motion could lead to the loss of coherence at time scales of a few femtoseconds, even for large molecules. However, the study of dynamics, including vibrational modes of benzene, resulted in the survival of oscillations⁸² providing a basis for the clamped nuclei approximation used in this work.

Figure 4a displays the photoelectron spectrum of benzene computed within the sudden approximation.⁹⁰ It has fewer features than the ADC(3) spectrum of Despré et al.,⁸² because the ionizations from orbitals outside the active space are not included. Nevertheless, it contains all prerequisite states needed to describe the dynamics.

Figure 4b displays the hole occupation dynamics following the instantaneous occupation of a single CSF differing from the main ground state configuration by a hole in the 1b_{1u} orbital. Such an excitation does not break the symmetry of the molecule, and the occupations of the 1b_{2g} and 1b_{3g} orbitals, as well as of 2b_{1u} and 1a_u orbitals (in D_{2h} notation), are the same because these orbitals are degenerate. The time evolution of hole occupations was derived from the diagonal elements of

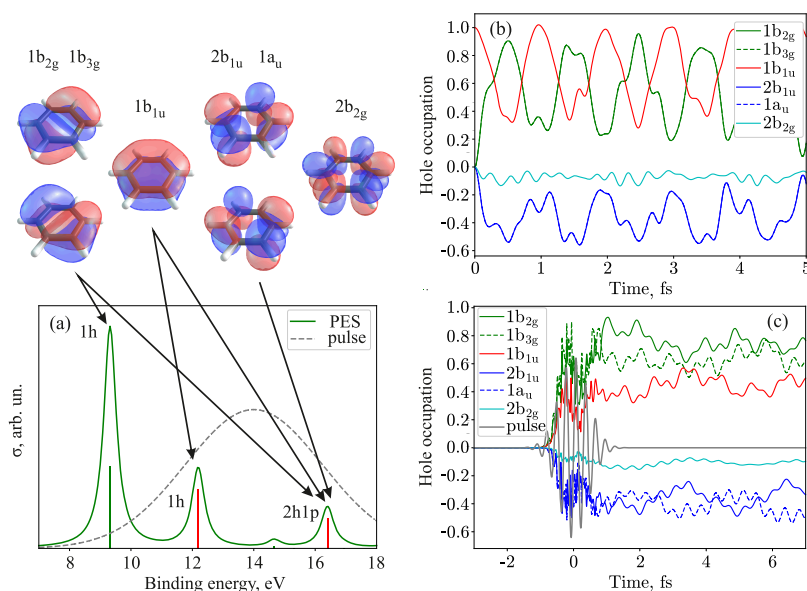


Figure 4. (a) Photoelectron spectrum (PES) of C₆H₆ computed at the CASPT2 level using sudden approximation. The two relevant states/transitions are denoted as red sticks. The dashed line displays the shape of the pulse used for ionization. The upper part shows the MOs included in the active space. Arrows show the orbitals which are relevant to the formation of 1h and 2h1p states. (b) Hole occupation dynamics in C₆H₆ following the population of a single CSF with the hole in the 1b_{1u} orbital, obtained at the CASPT2 level of theory. Negative values correspond to the electron population. (c) Hole occupation dynamics in C₆H₆ initiated by a pulse with $A = 1$ au, $\hbar\Omega = 14$ eV, $\sigma = 0.42$ fs, $\alpha = 0.2$, and pulse polarization parallel to the molecular plane.

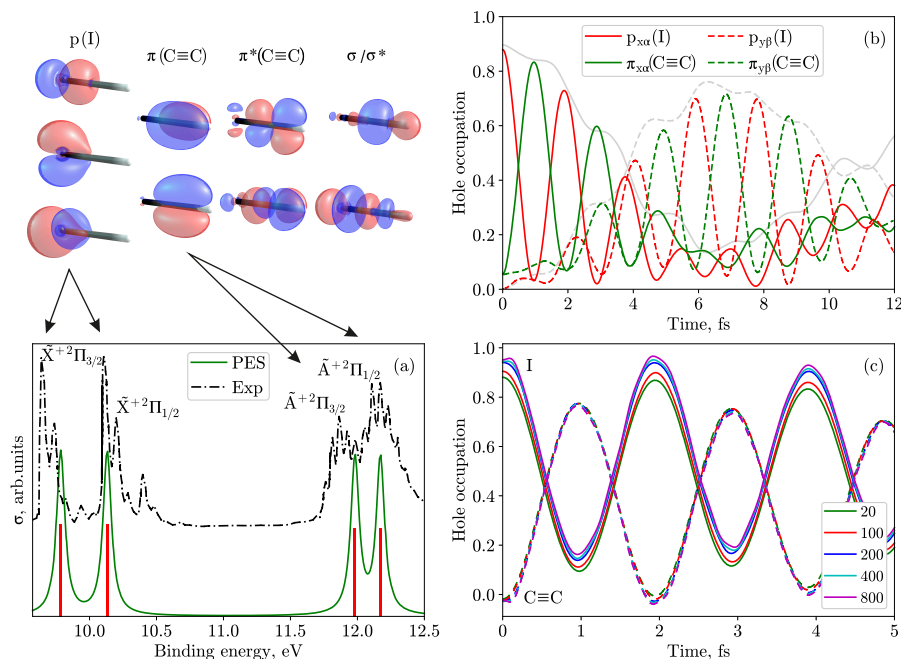


Figure 5. (a) PES of HCCI computed at the CASPT2 level using sudden approximation. The upper part shows the orbitals in the active space; arrows display the assignment of the respective bands. The experimental spectrum was digitalized from ref 92. (b) Hole occupation dynamics in HCCI following the population of a single CSF with the hole in the iodine $p_{x\alpha}$ spin-orbital computed at the CASPT2 level of theory with 100 states. Occupations of α spin-orbitals are shown in solid lines, and those of β spin-orbitals are shown in dashed lines. Also shown are the total populations of CSFs with $S_z = -1/2$ (solid gray line) and $+1/2$ (dashed gray line). (c) Total hole occupation on the I atom (solid lines) and C≡C fragment (dashed lines) as computed with different numbers of basis SO states.

the density matrix, $\rho_{ii}(t)$, in the CSF basis. For instance, for an orbital a , it reads

$$n_{\text{hole},a}(t) = \sum_{i=1}^{N_{\text{CSF}}} \rho_{ii}(t) (n_{\text{GSC},a} - n_{i,a}) \quad (8)$$

where $n_{i,a}$ is the occupation number of orbital a for the i th CSF and $n_{\text{GSC},a}$ is the respective occupation in the main ground state configuration $(1b_{1u})^2(1b_{2g})^2(1b_{3g})^2(2b_{1u})^0(1a_u)^0(2b_{2g})^0$. Hence, the negative hole occupations correspond to the electron occupation.

Figure 4b shows the prominent hole dynamics mainly bouncing between $1b_{1u}$ and the $1b_{2g}/1b_{3g}$ pair of orbitals in agreement with previous works.^{50,62,82} The hole occupation curves demonstrate a bit more wiggle than in the previous works; these features can be assigned to the involvement of the energetically distant ionic states. The total of 210 doublet ionic states spans the energy range of 40 eV in accord with the smallest oscillation period of around 0.2 fs seen in Figure 4b. Calculations at the ρ -TD-CASCI level (not shown) are consistent with the adaptive TD-CI⁶² and also give the main period of population migration of about 750 as. Thus, the additional pair of σ/σ^* included in the active space in ref 62 does not play an important role. If we apply CASPT2, the energy difference between hole-mixed states is calculated more precisely, and then the oscillation period changes to 980 as (Figure 4b) and agrees with the results of the ADC(3) method, including a large portion of the dynamic correlation, giving 935 as,⁸² and the TD-DMRG simulations with the $(26e^-, 26\text{MO})$ active space, giving 804 as.⁵⁰ Therefore, the oscillation period is sensitive to the inclusion of the dynamic

correlation. This conclusion is also supported by a sequence of calculations by Baiardi with increasing active spaces,⁵⁰ leading to the oscillation period's systematic growth.

To address the hole migration dynamics within a more realistic scenario, we employed the Dyson orbital formalism and sudden approximation^{90,91} to populate the ionic state manifold directly from the neutral ground state interacting with the light field. Therefore, the transition dipole moment between neutral and ionic states i and j is approximated as $|\vec{d}_{ij}| = \alpha \|\Phi_{ij}^{\text{DO}}\|^2$. Here, Φ_{ij}^{DO} is the Dyson orbital (DO), and α is the proportionality factor, which is considered a free parameter governing the degree of the depletion of the ground state. Further, we imply that the transition dipole is oriented parallel to the field polarization. With the pulse shown in Figure 4a in the frequency domain (see also the Appendix), one predominantly populates the superposition of the target $1h$ (12.19 eV) and $2h1p$ (16.40 eV) states, but the other state at 9.32 eV binding energy is also involved.

The results are shown in Figure 4c. The degeneracy of states is lifted by the linearly polarized field leading to uneven occupations of the degenerate orbitals. However, although a prominent hole dynamics is happening, the simulations reveal no characteristic oscillation time in hole occupation due to preparing more complex superposition of the ionic states.

Iodoacetylene. In this study, we also focused on the charge migration dynamics in HCCI after the instantaneous creation of the hole in the $5p_x(I)$ orbital, which is perpendicular to the molecular axis. We also assume that we are able to selectively remove a spin-up electron from this orbital. Experimental preparation of such an initial state would require an ensemble

of aligned molecules as in ref 23 but in the presence of the magnetic field directed along the axis of the molecules to create a specific superposition of the components of the total angular momentum eigenstates. However, here we select this initial state to dissect the effect of the electron correlation responsible for the charge migration and the SOC-induced dynamics due to the large SO constant of iodine.

According to the PES presented in Figure 5a, only the states with ionization energies up to 12.5 eV should be relevant for dynamics amounting to eight SO basis states. Here, we also study the influence of the number of SO states, including 20, 100, 200, 400, and 800 states. These choices span the ranges of ionization energies of 16, 21, 24, 28, and 32 eV, respectively. The initial state was prepared by populating the dominant ground-state CSF with a removed electron from the p_{xz} orbital; the dynamics are performed in the basis of SO states.

The photoelectron spectrum, Figure 5a, is obtained in the same way as for the benzene molecule. Four red sticks are of 1h type and correspond to transitions from the ground state $\tilde{X}^1\Sigma^+$ to $\tilde{X}^+ 2\Pi_{3/2}$, $\tilde{X}^+ 2\Pi_{1/2}$, $\tilde{A}^+ 2\Pi_{3/2}$, and $\tilde{A}^+ 2\Pi_{1/2}$ states of the ion. The \tilde{X}^+ pair of bands are primarily associated with the hole in $5p(I)$ orbitals and \tilde{A}^+ in $\pi(C\equiv C)$ orbitals. The experimental spectrum exhibits rich rovibronic structure superimposing on the pure photoionization transitions at 9.71, 10.11, 11.87, and 12.12 eV;⁹² vibrational effects have been not considered in this study. Experimental SOC splittings are found to be 0.4 and 0.25 eV. The computed spectrum displays bands with transition energies of 9.78, 10.13, 11.98, and 12.17 eV, respectively, and is in good agreement with the experiment within the accuracy of 0.1 eV. However, the SO splittings are predicted slightly lower than in the experiment: 0.35 and 0.19 eV for \tilde{X}^+ and \tilde{A}^+ states.

The dynamics simulation results are given in Figure 5b, displaying the population of the four mainly involved orbitals. Since the initial density matrix is in the CSF basis, we performed a nonorthogonal transformation to the truncated SO basis where the number of states is less than the maximum number of SO states. This transformation leads to a slight loss of the total norm ($\text{tr}[\rho] < 1$), as seen in Figure 5c. With the increasing number of SO states, the norm is recovered. Interestingly, the dynamics character is changing neither qualitatively nor quantitatively since the period of charge oscillations stays the same. Only the total hole population on the iodine atom slightly increases. The larger number of SO basis states, i.e., 800, also introduces slight high-frequency oscillations due to the minute involvement of the energetically distant eigenstates. One can conclude that including more eigenstates than indicated by the photoionization spectrum leads only to a minor improvement in accuracy.

As seen in Figure 5b,c, the hole migrates from the iodine atom to the $C\equiv CH$ fragment with a period of 1.95 fs. This result is in good agreement with the experimentally found period of 1.85 fs.²³ The initial dynamics involve the CSFs with $S_z = -1/2$, and thus the hole occupies α spin-orbitals. However, due to the notable SOC of iodine, the hole also populates $p_{y\beta}(I)$ and $\pi_{y\beta}(C\equiv C)$ orbitals, shown with dashed lines. The oscillations in the y -oriented β manifold are slightly retarded compared to the x -oriented α orbitals. Thus, the dynamics correspond to pumping the population from the CSF-manifold with $S_z = -1/2$ to $S_z = +1/2$ and back with a period of about 12 fs as shown with gray lines in Figure 5b. Its time scale agrees with an average SO splitting of the \tilde{X}^+ and \tilde{A}^+

states of 0.3 fs. All other orbitals stay insignificantly occupied with a summed population of less than 0.1.

The computed period of 1.95 fs is only slightly larger than those in other theoretical works^{49,62} with the notably larger active space, including 36 and 22 active orbitals with 16 active electrons, respectively. Again, this fact evidences that some portion of electron correlation, which is essential for the charge migration dynamics, can be recovered by the diagonal CASPT2 correction similar to benzene.

4.4. Ultrafast Spin-Flip dynamics. Another type of dynamical process for which RhoDyn is particularly suited is the dynamics in core excited systems triggered by ultrashort X-ray pulses. For instance, the approach implemented within the RhoDyn module has been used to study spin dynamics for excitation at the L-edge of transition metal complexes.^{43,58,59,93}

We continue discussing these applications here, shifting the focus to methodological issues. The process under study can be understood as follows: After absorption of an X-ray photon, the localized core hole is created. If the angular momentum of the core hole is nonzero, one can use the broad (ultrashort) pulse to create a superposition of pure spin states, which then evolve in time, resulting in spin-mixing or even spin-flip due to the strong SOC for core orbitals. In a sense, it is analogous to electron correlation driven charge migration, but instead of oscillating hole population, one observes SOC-driven spin oscillations. For the first-row transition metals, the SOC constant for the $2p \rightarrow 3d$ excitations is of the order of 10 eV,⁵⁹ giving a characteristic time scale of ≈ 400 (as). Given this time scale and relatively large masses of transition metal atoms and atoms in the first coordination sphere of the typical ligands, one can assume the approximation of clamped nuclei, inherent to RhoDyn, is particularly valid for this case.

As mentioned in section 4.3, even using small and medium-sized active spaces often results in a large number of stationary basis states. Considering all of them to study dynamics can be connected with significant computational efforts or even be impossible. That is why the reduction of dimensionality may be critical. In cases like the charge migration in iodoacetylene, one can preselect basis states based on additional information available from the experiment or other *a priori* considerations. For instance, in the case of HCCI, it was known from ref 23 which states are mainly populated by the incoming light pulse that allowed us to substantially limit the number of basis SO states from 12 096 to numbers below 200; cf. Table 1 and Figure 5c. However, the knowledge about the initial state and characteristics of the excitation pulse can also help to *a priori* reduce the computational effort in general cases. For example, for charge migration, one can decide in favor of some initial CSF and knowing the CI Hamiltonian matrix preselect only those basis CSFs coupled to it by off-diagonal matrix elements directly, indirectly via single configuration, two configurations, and so on. Thus, one builds a kind of CI-like hierarchy of the important states, which can be truncated according to accuracy and computational effort demands.

In the case of spin dynamics triggered by an explicit light pulse, one should take into account the following: (i) the form of the initial state since there often exist several low-lying electronic states or spin components of a multiplet which can be (thermally) populated; (ii) the excitation energy window due to the bandwidth of the light pulse; (iii) the magnitude of the transition dipole matrix elements which connect the initial basis states with those falling within the energy window; (iv) the actual coupling matrix, e.g., the off-diagonal part of \mathbf{H}_{CI} or

V_{SOC} which connects excited states and governs the dynamics. Accounting for (i)–(iv), one preselects first-rank participating states coupled via dipole transition and then the second-rank participating states coupled via SOC. Note that if the pulse is strong enough it may cause stimulated emission populating more states. Therefore, one would require iterative selection of participating states, depicted in Figure 6. In this case, the

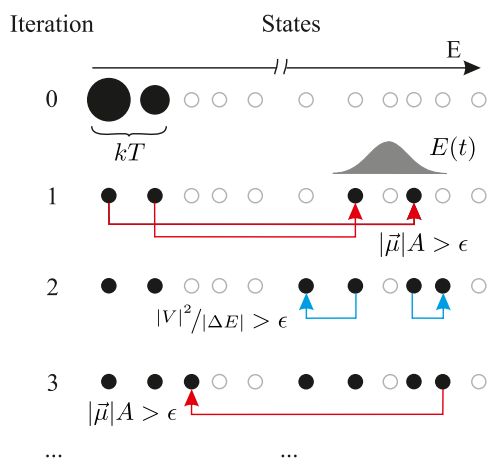


Figure 6. Iterative scheme to preselect states for dynamics. Iteration 0, thermally populated initial states. Iteration 1, light absorption within the energy window of the light pulse. Iteration 2, coupling between excited states. Iteration 3, population due to stimulated emission. Black circles denote participating states; open gray circles denote rejected states.

sorting into participating and spectator states is done according to a single threshold parameter ϵ , where, provided the state i is populated in the previous iteration, the state j is rejected if $|\vec{\mu}_{ij}|A < \epsilon$ and $|V_{ij}|^2/|E_i - E_j| < \epsilon$, with $\vec{\mu}_{ij}$, A , V_{ij} and E_i being the

transition dipole, field amplitude, SOC matrix element, and basis-state energy, respectively.

Below we present the application of selective ultrafast spin dynamics at the L-edge for two iron complexes: $[\text{Fe}(\text{H}_2\text{O})_6]^{2+}$ and $[\text{Fe}(\text{CO})_5]^0$.

Hexaaquairon(II). $[\text{Fe}(\text{H}_2\text{O})_6]^{2+}$ ion is one of the coordination complexes known to have a spin-flip after ultrashort X-ray pulse, i.e., to acquire a spin distinct from its ground state after X-ray excitation.^{43,59} The calculated static $L_{2,3}$ -edge absorption spectrum (Figure 7a) is in good agreement with experiment.⁹⁶ In Figure 7a, one can see the Fourier transformed excitation pulse envelope and the decomposition of the spectrum into spin-free contributions showing that, in some parts, the contribution from the spin (triplet) other than the ground-state one (quintet) is prevailing. The initial density matrix was constructed by populating the lowest SO state, equivalent to zero temperature. Dynamics were triggered by the short pulse excitation with characteristics chosen to cover a wide range of valence core $2p \rightarrow 3d$ excitations and make the ground state undergo substantial depletion up to 90%; see Figure 7a. As displayed in Figure 7b, the initially populated quintet core excited state mixes with triplet states due to strong SOC (12.8 eV constant) resulting essentially in a spin-flip.

For visualization of connections between states due to transition dipole and SOC matrix elements discussed above and used for the selection scheme (Figure 6), we use a force-directed drawing algorithm.^{94,95} The results are shown in Figure 7c. Each node corresponds to one of the 760 SF basis states, and the color encodes their multiplicity, i.e., red quintets and blue triplets; the initially populated state is green. The distances between nodes are optimized to minimize spring-like forces between them. The force ($F_{ij} = -\kappa_{ij}\Delta x_{ij}$) between nodes i and j corresponds to the spring constant $\kappa_{ij} = c(|V_{\text{SOC}}|_{ij}| + |d_{ij}|)$, where c is a factor governing the relative importance of the two couplings. It has been adjusted for visual clarity to illustrate the

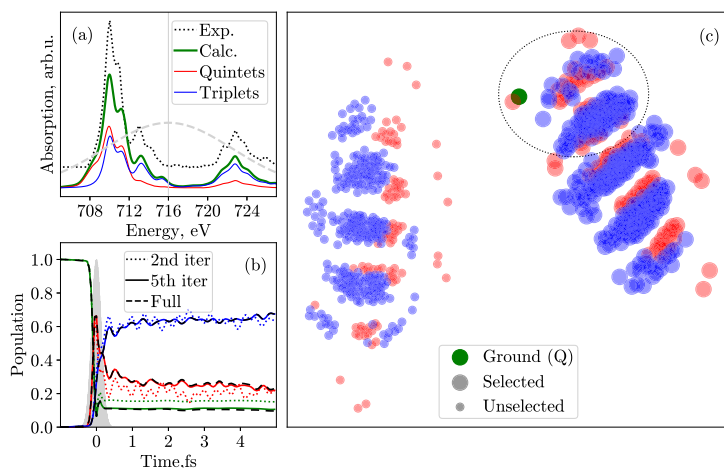


Figure 7. Spin dynamics after the L-edge excitation in the $[\text{Fe}(\text{H}_2\text{O})_6]^{2+}$ complex. (a) Experimental and calculated XAS with its decomposition in spin multiplicities. The dashed gray line shows the incoming pulse in the frequency domain. Pulse characteristics are $A = 6$ au, $\hbar\Omega = 716$ eV, and $\sigma = 0.2$ fs. (b) Time evolution of the population calculated including 128 and 378 preselected states (iterations 2 and 5, dotted and solid color lines, respectively) and using the basis of all 760 SF states (dashed black lines). The filled gray curve shows the time envelope of the pulse. (c) Force-directed graph^{94,95} displaying connections between states due to transition dipole and SO coupling. A circle represents each SF state; large circles correspond to states participating in the dynamics. The color indicates spin multiplicity: red for quintets $S = 2$, blue for triplets $S = 1$, and green for the initially populated quintet state. Dashed ellipse displays the states selected after the second iteration; see text.

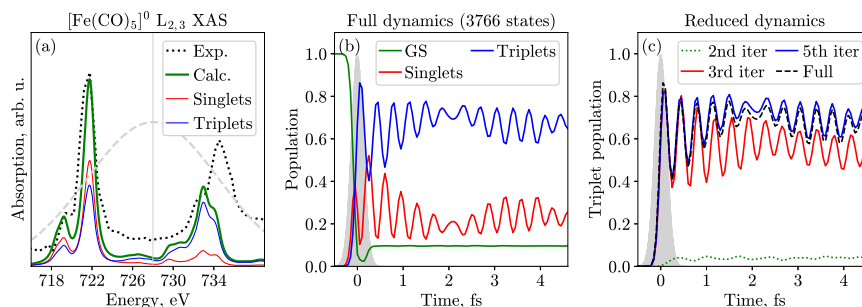


Figure 8. Spin dynamics after the L-edge excitation of the $[\text{Fe}(\text{CO})_5]_0$ complex. (a) Experimental and calculated XAS with its decomposition in spin multiplicities: singlets (red line) and triplets (blue line). The dashed gray line shows the incoming pulse in the frequency domain; pulse characteristics are $A = 6$ au, $\hbar\Omega = 728$ eV, and $\sigma = 0.2$ fs. (b) Time evolution of the population singlet and triplet states calculated including all 3766 SF states. (c) Differences in the population of triplets (equivalent to triplet yield $\langle S_z^2 \rangle / 2$) accounting for the total number of states as compared to the reduced dynamics, including only 111 (green, second iteration), 656 (red, third iteration), and 1882 (blue, fifth iteration) states.

clustering of states. The size of the nodes, in turn, denotes whether the state is involved in dynamics or stays mainly unpopulated. The states are separated into two main clusters, connected strongly neither by dipole transitions nor by SOC, whereas interaction is notable within the clusters. It is natural to expect that half of the states from the left cluster are not participating in the dynamics. Indeed, for the threshold value $\epsilon = 27.2$ meV, the iterative procedure described above (Figure 6) converged after five iterations. The number of states selected at each iteration starting from 0 is 1, 8, 128, 240, 351, and 378. The states selected after iteration 2, i.e., the smallest reasonable basis where dipole and SOC coupling are minimally accounted for, are denoted with the dashed ellipse in Figure 7c. The respective dynamics with 128 states shown in Figure 7b with dotted lines demonstrate correct trends but are still different from the full one with 760 states (black dashed lines). However, after the fifth iteration, the dynamics with 378 are barely different from the full one. Thus, preselecting only half of all states, which are marked with big nodes in Figure 7c, produces the converged result.

One can also analyze how states are added according to their spin magnetic quantum number S_z and SOC selection rules. It can be traced because the states additionally form micro-clusters according to the S_z value within both larger clusters. The initially populated state is the ground state with $S_z = -2$. The quintet states with $S_z = -2$ were selected at the first iteration according to the dipole selection rule $\Delta S_z = 0$. Both triplet and quintet states with $S_z = -1$ are also selected at the second iteration due to the SOC selection rule $\Delta S_z = 0, \pm 1$. These two groups of states correspond to two subclusters encircled with the dashed line in Figure 7c. The further three iterations select consecutively states with $S_z = 0, +1$, and $+2$.

Iron Pentacarbonyl. $[\text{Fe}(\text{CO})_5]_0$ exhibits a significant spin-flip rate from the singlet to the triplet state manifold upon L-edge X-ray excitation⁵⁹ and has also been used to test the preselection procedure. The computational setup (see the Appendix) results in 3766 SO states. Therefore, preselection of states, in this case, is more crucial for efficient computation than it is for $[\text{Fe}(\text{H}_2\text{O})_6]^{2+}$.

The absorption spectrum, full dynamics with 3766 states, and the triplet yield for the different number of selected states are displayed in Figure 8. For $[\text{Fe}(\text{CO})_5]_0$, the transition from singlet to triplet multiplicity is accompanied by strong Rabi-like oscillations. As was shown previously, not all states equally contribute due to different SOC and transition dipole moment

matrix elements. Similar to $[\text{Fe}(\text{H}_2\text{O})_6]^{2+}$, iron pentacarbonyl also shows clustering of states in two groups,⁵⁹ but in contrast, one also has subgroups due to substantially different transition dipole moments as $2p \rightarrow \pi^*$ transitions are more intense than the $2p \rightarrow 3d$ ones.

The threshold value of $\epsilon = 1.36$ eV was applied for the preselection. As for $[\text{Fe}(\text{H}_2\text{O})_6]^{2+}$, the convergence to half of all states was also reached after five iterations. At each iteration starting from 0, the number of qualified states was 1, 9, 111, 656, 1599, and 1882, respectively. As shown in Figure 8c, the convergence to the full result is notably slower in this case. However, the dynamics with 1882 basis states almost quantitatively agree with the full dynamics. We observe that, already at the third iteration with 656 states included, the dynamics are qualitatively reproduced, which is enough to describe such main features as the oscillation period and noticeable spin-flip rate. Finally, we note that the energetic distance between states plays an important role. Since for $[\text{Fe}(\text{CO})_5]_0$ the states lie much denser than for $[\text{Fe}(\text{H}_2\text{O})_6]^{2+}$, the threshold has to be selected about 2 orders of magnitude higher. It is also in accord with the larger transition dipole moments of the $2p \rightarrow \pi^*$ transitions compared to the $2p \rightarrow 3d$ transitions.

5. CONCLUSIONS AND OUTLOOK

In this article, we presented a program module RhoDYN incorporated within the OpenMOLCAS project. Its purpose is to study ultrafast electron dynamics on a level of complete or restricted active space CI in the density-matrix formulation. Thus, it represents a straightforward extension of the stationary quantum chemistry methods available in the OpenMOLCAS package to the time domain. Although the clamped nuclei approximation is inherent to the underlying theory, the effect of nuclear vibrations can still be taken into account in the form of a harmonic vibrational heat bath, ensuring the dissipation dynamics. Thus, the methodology is particularly suited for studies of less than a few femtosecond electron dynamics when a system is excited far from conical intersections on the potential energy surface or when heavy atoms are involved. It can also be applied in cases when SOC is important, staying, of course, within the limits of the applicability of the LS -coupling approximation. Since the number of states belonging to different spin manifolds can be particularly large in the case of SOC-mediated dynamics, the scheme for the preselection of

the participating basis states is suggested. Therefore, the computational effort can be notably reduced.

Several examples illustrate the possible applications of the methodology: computation of (non)linear spectra, i.e., linear XAS of $[\text{TiO}_6]^{8-}$ and HHG in H_2 ; charge migration in benzene and iodoacetylene; and the spin-dynamics in core excited iron complexes. The density-matrix formulation of the CI problem not only allows for the treatment of energy and phase relaxation but also offers a convenient way to incorporate (auto)ionization which will be the subject of our future research.

■ APPENDIX: DETAILS OF CALCULATIONS

$[\text{TiO}_6]^{8-}$. The calculation has been performed on the RASSCF level with the ANO-RCC-VTZP basis, including three 2p and five 3d orbitals of titanium atom in the RAS1 and RAS3 spaces allowing for one hole/electron, respectively. Thus, it effectively corresponds to the CI singles level of theory. The spectrum is globally shifted by 8.1 eV for better comparison with the experiment. For further details of calculations, see ref 59. Here, the propagation length of $t_f = 10$ fs has been used. Pulse characteristics are $A = 1.5$ au, $\sigma = 0.2$ fs, and $\hbar\Omega = 461$ eV. We employ the Hann window $W(t) = \sin^2(\pi n/N)$, where n is the counting number of N sampling points equal to the number of time points.

H_2 . Two different basis sets, aug-cc-pVDZ⁷³ and d-aug-cc-pVDZ,⁷⁴ supporting a set of diffuse functions, have been used. The active space comprised all unoccupied orbitals (17 and 25 for both bases, respectively) in the RAS3 space with the only occupied orbital placed in the RAS2 space; further, only single excitations have been allowed in RAS3. This setup gave a total of 18 and 26 singlet states for both bases, respectively. Pulse characteristics have been chosen to represent the typical experimental pulse as an output of a Ti:sapphire laser with $A = 3.5 \times 10^{15}$ W/cm² (0.1 au), $\hbar\Omega = 1.55$ eV (800 nm), $2\sigma = 53.3$ fs (including 20 optical cycles), $t_0 = 0$ fs, $t_{\text{final}} = 2\sigma$ (see Figure 3a), and the Keldysh parameter $\gamma = \omega\sqrt{2I_p}/E_{\text{max}} = 1.13$. The pulse envelope corresponds to the \cos^2 function. Gaussian window function with a dispersion of 10 fs (see Figure 3a) was applied to the time-dependent dipole moment before Fourier transformation.

C_6H_6 . The active space ($6e^-$, 6MOs) is used containing the complete set of π/π^* orbitals. The ANO-L-VTZ basis has been employed. The dynamics have been computed within the pure ρ -TD-CASCI method and also taking the diagonal energy correction due to dynamic electron correlation outside the active space via CASPT2. The total number of CSF basis functions (equal to the number of accounted SFs) amounts to 175 singlet and 210 doublet states; see Table 1.

HCCI. For HCCI, the active space consists of nine molecular orbitals representing linear combinations of six 2p orbitals of carbon atoms and three 5p orbitals of iodine. The number of active electrons equals 11 for doublet ionized states and 12 for the initial singlet state; the number of CSFs is given in Table 1. The ANO-RCC-VTZP basis set with Douglas-Kroll-Hess (DKH) Hamiltonian correction⁹⁷ was used for electronic structure calculation to take into account scalar relativistic effects. The CASPT2 energy correction was computed with the imaginary shift of 0.1 hartree.

$[\text{Fe}(\text{H}_2\text{O})_6]^{2+}$. The computational scheme for the electronic structure in this work coincides with that of ref 59. We employ the DKH relativistic Hamiltonian,⁹⁷ all-electron ANO-RCC-

VTZP basis set, and RASSCF/RASSI level of theory. A reasonable active space with eight orbitals (three Fe 2p and five Fe 3d) and 12 electrons was used, which resulted in 760 SO basis states.

$[\text{Fe}(\text{CO})_5]^0$. For this complex, active space consists of three 2p orbitals (RAS1, one hole is allowed), $3d\sigma$ (a_1'), four 3d (e' and e''), and $3d\sigma^*$ ($a_1'^*$) (RAS2, full CI), and four π^* orbitals (RAS3, one electron is allowed), resulting in 13 orbitals with 14 active electrons.⁹⁸ Other computational details coincide with $[\text{Fe}(\text{H}_2\text{O})_6]^{2+}$; see also ref 59.

■ ASSOCIATED CONTENT

Supporting Information

The Supporting Information is available free of charge at <https://pubs.acs.org/doi/10.1021/acs.jctc.1c01097>.

Representative input files further illustrating the computational workflow on the selected examples given in section 4 (PDF)

■ AUTHOR INFORMATION

Corresponding Author

Sergey I. Bokarev – Institut für Physik, Universität Rostock, 18059 Rostock, Germany; orcid.org/0000-0003-0779-5013; Email: sergey.bokarev@uni-rostock.de

Author

Vladislav Kochetov – Institut für Physik, Universität Rostock, 18059 Rostock, Germany

Complete contact information is available at <https://pubs.acs.org/10.1021/acs.jctc.1c01097>

Notes

The authors declare no competing financial interest.

■ ACKNOWLEDGMENTS

Financial support from the Deutsche Forschungsgemeinschaft Grant No. BO 4915/1-1 is gratefully acknowledged.

■ REFERENCES

- (1) McNeil, B. W. J.; Thompson, N. R. X-Ray Free-Electron Lasers. *Nature Photon* **2010**, *4*, 814–821.
- (2) Grguraš, I.; Maier, A. R.; Behrens, C.; Mazza, T.; Kelly, T. J.; Radcliffe, P.; Düsterer, S.; Kazansky, A. K.; Kabachnik, N. M.; Tschentscher, T.; Costello, J. T.; Meyer, M.; Hoffmann, M. C.; Schlarb, H.; Cavalieri, A. L. Ultrafast X-Ray Pulse Characterization at Free-Electron Lasers. *Nature Photon* **2012**, *6*, 852–857.
- (3) Maroju, P. K.; et al. Attosecond Pulse Shaping Using a Seeded Free-Electron Laser. *Nature* **2020**, *578*, 386–391.
- (4) Serkez, S.; Geloni, G.; Tomin, S.; Feng, G.; Gryzlova, E. V.; Grum-Grzhimailo, A. N.; Meyer, M. Overview of Options for Generating High-Brightness Attosecond x-Ray Pulses at Free-Electron Lasers and Applications at the European XFEL. *J. Opt.* **2018**, *20*, 024005.
- (5) Hentschel, M.; Kienberger, R.; Spielmann, C.; Reider, G. A.; Milosevic, N.; Brabec, T.; Corkum, P.; Heinzmann, U.; Drescher, M.; Krausz, F. Attosecond Metrology. *Nature* **2001**, *414*, 509–513.
- (6) Gaumnitz, T.; Jain, A.; Pertot, Y.; Huppert, M.; Jordan, I.; Ardana-Lamas, F.; Wörner, H. J. Streaking of 43-Attosecond Soft-X-Ray Pulses Generated by a Passively CEP-Stable Mid-Infrared Driver. *Opt. Express* **2017**, *25*, 27506.
- (7) *Attosecond and XUV Physics: Ultrafast Dynamics and Spectroscopy*; Schultz, T., Vrakking, M., Eds.; Wiley-VCH: Weinheim, 2014.
- (8) Young, L.; et al. Roadmap of Ultrafast X-Ray Atomic and Molecular Physics. *J. Phys. B* **2018**, *51*, 032003.

- (9) Baykusheva, D.; Wörner, H. J. Attosecond Molecular Spectroscopy and Dynamics. *arXiv (Physics.Chemical Physics)*, February 6, 2020, 2002.02111, ver. 1. <https://arxiv.org/abs/2002.02111>.
- (10) Saalfrank, P.; Bedurke, F.; Heide, C.; Klamroth, T.; Klinskusch, S.; Krause, P.; Nest, M.; Tremblay, J. C. Molecular Attochemistry: Correlated Electron Dynamics Driven by Light. *Adv. Quantum Chem.* **2020**, *81*, 15–50.
- (11) Doumy, G.; et al. Nonlinear Atomic Response to Intense Ultrashort X Rays. *Phys. Rev. Lett.* **2011**, *106*, 083002.
- (12) Rudek, B.; et al. Ultra-Efficient Ionization of Heavy Atoms by Intense X-Ray Free-Electron Laser Pulses. *Nature Photon* **2012**, *6*, 858–865.
- (13) Niikura, H.; Légaré, F.; Hasbani, R.; Bandrauk, A. D.; Ivanov, M. Y.; Villeneuve, D. M.; Corkum, P. B. Sub-Laser-Cycle Electron Pulses for Probing Molecular Dynamics. *Nature* **2002**, *417*, 917–922.
- (14) Itatani, J.; Levesque, J.; Zeidler, D.; Niikura, H.; Pépin, H.; Kieffer, J. C.; Corkum, P. B.; Villeneuve, D. M. Tomographic Imaging of Molecular Orbitals. *Nature* **2004**, *432*, 867–871.
- (15) Villeneuve, D. M.; Hockett, P.; Vrakking, M. J. J.; Niikura, H. Coherent Imaging of an Attosecond Electron Wave Packet. *Science* **2017**, *356*, 1150–1153.
- (16) Smirnova, O.; Mairesse, Y.; Patchkovskii, S.; Dudovich, N.; Villeneuve, D.; Corkum, P.; Ivanov, M. Y. High Harmonic Interferometry of Multi-Electron Dynamics in Molecules. *Nature* **2009**, *460*, 972–977.
- (17) Smirnova, O.; Patchkovskii, S.; Mairesse, Y.; Dudovich, N.; Ivanov, M. Y. Strong-Field Control and Spectroscopy of Attosecond Electron-Hole Dynamics in Molecules. *Proc. Natl. Acad. Sci. U. S. A.* **2009**, *106*, 16556–16561.
- (18) Richter, M.; González-Vázquez, J.; Mašín, Z.; Brambila, D. S.; Harvey, A. G.; Morales, F.; Martín, F. Ultrafast Imaging of Laser-Controlled Non-Adiabatic Dynamics in NO₂ from Time-Resolved Photoelectron Emission. *Phys. Chem. Chem. Phys.* **2019**, *21*, 10038–10051.
- (19) You, D.; et al. New Method for Measuring Angle-Resolved Phases in Photoemission. *Phys. Rev. X* **2020**, *10*, 031070.
- (20) Kuleff, A. I.; Cederbaum, L. S. Ultrafast Correlation-Driven Electron Dynamics. *J. Phys. B* **2014**, *47*, 124002.
- (21) Nisoli, M.; Declève, P.; Calegari, F.; Palacios, A.; Martín, F. Attosecond Electron Dynamics in Molecules. *Chem. Rev.* **2017**, *117*, 10760–10825.
- (22) Calegari, F.; Ayuso, D.; Trabattini, A.; Belshaw, L.; De Camillis, S.; Anumula, S.; Frassetto, F.; Poletto, L.; Palacios, A.; Declève, P.; Greenwood, J. B.; Martín, F.; Nisoli, M. Ultrafast Electron Dynamics in Phenylalanine Initiated by Attosecond Pulses. *Science* **2014**, *346*, 336–339.
- (23) Kraus, P. M.; Mignolet, B.; Baykusheva, D.; Rupenyan, A.; Horny, L.; Penka, E. F.; Grassi, G.; Tolstikhin, O. I.; Schneider, J.; Jensen, F.; Madsen, L. B.; Bandrauk, A. D.; Remacle, F.; Wörner, H. J. Measurement and Laser Control of Attosecond Charge Migration in Ionized Iodoacetylene. *Science* **2015**, *350*, 790–795.
- (24) Wörner, H. J.; et al. Charge Migration and Charge Transfer in Molecular Systems. *Struct. Dyn.* **2017**, *4*, 061508.
- (25) Alvermann, A.; Fehske, H.; Littlewood, P. B. Numerical Time Propagation of Quantum Systems in Radiation Fields. *New J. Phys.* **2012**, *14*, 105008.
- (26) Moskalenko, A. S.; Zhu, Z.-G.; Berakdar, J. Charge and Spin Dynamics Driven by Ultrashort Extreme Broadband Pulses: A Theory Perspective. *Phys. Rep.* **2017**, *672*, 1–82.
- (27) Goings, J. J.; Lestrangle, P. J.; Li, X. Real-Time Time-Dependent Electronic Structure Theory. *Wiley Interdiscip. Rev.: Comput. Mol. Sci.* **2018**, *8*, No. e1341.
- (28) Li, X.; Govind, N.; Isborn, C.; DePrince, A. E.; Lopata, K. Real-Time Time-Dependent Electronic Structure Theory. *Chem. Rev.* **2020**, *120*, 9951–9993.
- (29) Schirmer, J.; Cederbaum, L. S.; Walter, O. New Approach to the One-Particle Green's Function for Finite Fermi Systems. *Phys. Rev. A* **1983**, *28*, 1237–1259.
- (30) Kuleff, A. I.; Breidbach, J.; Cederbaum, L. S. Multielectron Wave-Packet Propagation: General Theory and Application. *J. Chem. Phys.* **2005**, *123*, 044111.
- (31) Hoodbhoy, P.; Negele, J. W. Time-Dependent Coupled-Cluster Approximation to Nuclear Dynamics. I. Application to a Solvable Model. *Phys. Rev. C* **1978**, *18*, 2380–2394.
- (32) Kvaal, S. *Ab Initio* Quantum Dynamics Using Coupled-Cluster. *J. Chem. Phys.* **2012**, *136*, 194109.
- (33) Nascimento, D. R.; DePrince, A. E. Simulation of Near-Edge X-Ray Absorption Fine Structure with Time-Dependent Equation-of-Motion Coupled-Cluster Theory. *J. Phys. Chem. Lett.* **2017**, *8*, 2951–2957.
- (34) Lopata, K.; Van Kuiken, B. E.; Khalil, M.; Govind, N. Linear-Response and Real-Time Time-Dependent Density Functional Theory Studies of Core-Level Near-Edge X-Ray Absorption. *J. Chem. Theory Comput.* **2012**, *8*, 3284–3292.
- (35) Meyer, H.-D.; Manthe, U.; Cederbaum, L. The Multi-Configurational Time-Dependent Hartree Approach. *Chem. Phys. Lett.* **1990**, *165*, 73–78.
- (36) Beck, M. The Multiconfiguration Time-Dependent Hartree (MCTDH) Method: A Highly Efficient Algorithm for Propagating Wavepackets. *Phys. Rep.* **2000**, *324*, 1–105.
- (37) Nest, M.; Ludwig, M.; Ulusoy, I.; Klamroth, T.; Saalfrank, P. Electron Correlation Dynamics in Atoms and Molecules. *J. Chem. Phys.* **2013**, *138*, 164108.
- (38) Despré, V.; Golubev, N. V.; Kuleff, A. I. Charge Migration in Propiolic Acid: A Full Quantum Dynamical Study. *Phys. Rev. Lett.* **2018**, *121*, 203002.
- (39) Lode, A. U. J.; Lévêque, C.; Madsen, L. B.; Streltsov, A. I.; Alon, O. E. *Colloquium*: Multiconfigurational Time-Dependent Hartree Approaches for Indistinguishable Particles. *Rev. Mod. Phys.* **2020**, *92*, 011001.
- (40) Krause, P.; Klamroth, T.; Saalfrank, P. Time-Dependent Configuration-Interaction Calculations of Laser-Pulse-Driven Many-Electron Dynamics: Controlled Dipole Switching in Lithium Cyanide. *J. Chem. Phys.* **2005**, *123*, 074105.
- (41) Klamroth, T. Laser-Driven Electron Transfer through Metal-Insulator-Metal Contacts: Time-Dependent Configuration Interaction Singles Calculations for a Jellium Model. *Phys. Rev. B* **2003**, *68*, 245421.
- (42) Greenman, L.; Ho, P. J.; Pabst, S.; Kamarchik, E.; Mazziotti, D. A.; Santra, R. Implementation of the Time-Dependent Configuration-Interaction Singles Method for Atomic Strong-Field Processes. *Phys. Rev. A* **2010**, *82*, 023406.
- (43) Wang, H.; Bokarev, S. I.; Aziz, S. G.; Kühn, O. Ultrafast Spin-State Dynamics in Transition-Metal Complexes Triggered by Soft-X-Ray Light. *Phys. Rev. Lett.* **2017**, *118*, 023001.
- (44) Sato, T.; Ishikawa, K. L. Time-Dependent Complete-Active-Space Self-Consistent-Field Method for Multielectron Dynamics in Intense Laser Fields. *Phys. Rev. A* **2013**, *88*, 023402.
- (45) Miyagi, H.; Madsen, L. B. Time-Dependent Restricted-Active-Space Self-Consistent-Field Theory for Laser-Driven Many-Electron Dynamics. *Phys. Rev. A* **2013**, *87*, 062511.
- (46) Bauch, S.; Sørensen, L. K.; Madsen, L. B. Time-Dependent Generalized-Active-Space Configuration-Interaction Approach to Photoionization Dynamics of Atoms and Molecules. *Phys. Rev. A* **2014**, *90*, 062508.
- (47) Haegeman, J.; Lubich, C.; Oseledets, I.; Vandereycken, B.; Verstraete, F. Unifying Time Evolution and Optimization with Matrix Product States. *Phys. Rev. B* **2016**, *94*, 165116.
- (48) Baiardi, A.; Reiher, M. Large-Scale Quantum Dynamics with Matrix Product States. *J. Chem. Theory Comput.* **2019**, *15*, 3481–3498.
- (49) Frahm, L.-H.; Pfannkuche, D. Ultrafast *Ab Initio* Quantum Chemistry Using Matrix Product States. *J. Chem. Theory Comput.* **2019**, *15*, 2154–2165.
- (50) Baiardi, A. Electron Dynamics with the Time-Dependent Density Matrix Renormalization Group. *J. Chem. Theory Comput.* **2021**, *17*, 3320–3334.

- (51) Tremblay, J. C.; Klamroth, T.; Saalfrank, P. Time-Dependent Configuration-Interaction Calculations of Laser-Driven Dynamics in Presence of Dissipation. *J. Chem. Phys.* **2008**, *129*, 084302.
- (52) Tremblay, J. C.; Klinkusch, S.; Klamroth, T.; Saalfrank, P. Dissipative Many-Electron Dynamics of Ionizing Systems. *J. Chem. Phys.* **2011**, *134*, 044311.
- (53) Gelin, M. F.; Pislakov, A. V.; Egorova, D.; Domcke, W. A Simple Model for the Calculation of Nonlinear Optical Response Functions and Femtosecond Time-Resolved Spectra. *J. Chem. Phys.* **2003**, *118*, 5287–5301.
- (54) Mukamel, S.; Healion, D.; Zhang, Y.; Biggs, J. D. Multidimensional Attosecond Resonant X-Ray Spectroscopy of Molecules: Lessons from the Optical Regime. *Annu. Rev. Phys. Chem.* **2013**, *64*, 101–127.
- (55) Ando, H.; Fingerhut, B. P.; Dorfman, K. E.; Biggs, J. D.; Mukamel, S. Femtosecond Stimulated Raman Spectroscopy of the Cyclobutane Thymine Dimer Repair Mechanism: A Computational Study. *J. Am. Chem. Soc.* **2014**, *136*, 14801–14810.
- (56) Zhang, Y.; Hua, W.; Bennett, K.; Mukamel, S. Nonlinear Spectroscopy of Core and Valence Excitations Using Short X-Ray Pulses: Simulation Challenges. *Top. Curr. Chem.* **2014**, *368*, 273–345.
- (57) Fdez. Galván, L.; et al. OpenMolcas: From Source Code to Insight. *J. Chem. Theory Comput.* **2019**, *15*, S925–S964.
- (58) Wang, H.; Bokarev, S. I.; Aziz, S. G.; Kühn, O. Density Matrix-Based Time-Dependent Configuration Interaction Approach to Ultrafast Spin-Flip Dynamics. *Mol. Phys.* **2017**, *115*, 1898–1907.
- (59) Kochetov, V.; Wang, H.; Bokarev, S. I. Effect of Chemical Structure on the Ultrafast Spin Dynamics in Core-Excited States. *J. Chem. Phys.* **2020**, *153*, 044304.
- (60) Cash, J. R.; Karp, A. H. A Variable Order Runge-Kutta Method for Initial Value Problems with Rapidly Varying Right-Hand Sides. *ACM Trans. Math. Softw.* **1990**, *16*, 201–222.
- (61) FORTRAN Numerical Recipes, 2nd ed.; Press, W. H., Ed.; Cambridge University Press: Cambridge, U.K., 1996.
- (62) Schriber, J. B.; Evangelista, F. A. Time Dependent Adaptive Configuration Interaction Applied to Attosecond Charge Migration. *J. Chem. Phys.* **2019**, *151*, 171102.
- (63) Malmqvist, P.-Å.; Roos, B. O.; Schimmelpfennig, B. The Restricted Active Space (RAS) State Interaction Approach with Spin-Orbit Coupling. *Chem. Phys. Lett.* **2002**, *357*, 230–240.
- (64) High-Performance Data Management and Storage Suite; The HDF Group.
- (65) Paramonov, G. K.; Kühn, O. State-Selective Vibrational Excitation and Dissociation of H_2^+ by Strong Infrared Laser Pulses: Below-Resonant versus Resonant Laser Fields and Electron-Field Following. *J. Phys. Chem. A* **2012**, *116*, 11388–11397.
- (66) May, V.; Kühn, O. *Charge and Energy Transfer Dynamics in Molecular Systems*; Wiley-VCH: Weinheim, 2011.
- (67) Blum, K. *Density Matrix Theory and Applications*; Springer Series on Atomic, Optical, and Plasma Physics 64; Springer: Berlin, 2012.
- (68) Mukamel, S. *Principles of Nonlinear Optical Spectroscopy*; Oxford University Press: New York, 1999.
- (69) Woicik, J. C.; Shirley, E. L.; Hellberg, C. S.; Andersen, K. E.; Sambasivan, S.; Fischer, D. A.; Chapman, B. D.; Stern, E. A.; Ryan, P.; Ederer, D. L.; Li, H. Ferroelectric Distortion in SrTiO_3 Thin Films on $\text{Si}(001)$ by x-Ray Absorption Fine Structure Spectroscopy: Experiment and First-Principles Calculations. *Phys. Rev. B* **2007**, *75*, 140103.
- (70) Ghimire, S.; DiChiara, A. D.; Sistrunk, E.; Agostini, P.; DiMauro, L. F.; Reis, D. A. Observation of High-Order Harmonic Generation in a Bulk Crystal. *Nature Phys.* **2011**, *7*, 138–141.
- (71) Ndabashimiye, G.; Ghimire, S.; Wu, M.; Browne, D. A.; Schafer, K. J.; Gaarde, M. B.; Reis, D. A. Solid-State Harmonics beyond the Atomic Limit. *Nature* **2016**, *534*, 520–523.
- (72) Lakhota, H.; Kim, H. Y.; Zhan, M.; Hu, S.; Meng, S.; Goulielmakis, E. Laser Picoscopy of Valence Electrons in Solids. *Nature* **2020**, *583*, 55–59.
- (73) Kendall, R. A.; Dunning, T. H.; Harrison, R. J. Electron Affinities of the First-row Atoms Revisited. Systematic Basis Sets and Wave Functions. *J. Chem. Phys.* **1992**, *96*, 6796–6806.
- (74) Pritchard, B. P.; Altarawy, D.; Didier, B.; Gibson, T. D.; Windus, T. L. New Basis Set Exchange: An Open, Up-to-Date Resource for the Molecular Sciences Community. *J. Chem. Inf. Model.* **2019**, *59*, 4814–4820.
- (75) White, A. F.; Heide, C. J.; Saalfrank, P.; Head-Gordon, M.; Luppi, E. Computation of High-Harmonic Generation Spectra of the Hydrogen Molecule Using Time-Dependent Configuration-Interaction. *Mol. Phys.* **2016**, *114*, 947–956.
- (76) Mizutani, H.; Minemoto, S.; Oguchi, Y.; Sakai, H. Effect of Nuclear Motion Observed in High-Order Harmonic Generation from D_2 H_2 Molecules with Intense Multi-Cycle 1300 Nm and 800 Nm Pulses. *J. Phys. B* **2011**, *44*, 081002.
- (77) Kaufmann, K.; Baumeister, W.; Jungen, M. Universal Gaussian Basis Sets for an Optimum Representation of Rydberg and Continuum Wavefunctions. *J. Phys. B* **1989**, *22*, 2223.
- (78) Luppi, E.; Head-Gordon, M. The Role of Rydberg and Continuum Levels in Computing High Harmonic Generation Spectra of the Hydrogen Atom Using Time-Dependent Configuration Interaction. *J. Chem. Phys.* **2013**, *139*, 164121.
- (79) Coccia, E.; Mussard, B.; Labeye, M.; Caillat, J.; Taïeb, R.; Toulouse, J.; Luppi, E. Gaussian Continuum Basis Functions for Calculating High-Harmonic Generation Spectra. *Int. J. Quantum Chem.* **2016**, *116*, 1120–1131.
- (80) Ulusoy, I. S.; Stewart, Z.; Wilson, A. K. The Role of the CI Expansion Length in Time-Dependent Studies. *J. Chem. Phys.* **2018**, *148*, 014107.
- (81) Klinkusch, S.; Saalfrank, P.; Klamroth, T. Laser-Induced Electron Dynamics Including Photoionization: A Heuristic Model within Time-Dependent Configuration Interaction Theory. *J. Chem. Phys.* **2009**, *131*, 114304.
- (82) Despré, V.; Marciniak, A.; Loriot, V.; Galbraith, M. C. E.; Rouze e, A.; Vrakking, M. J. J.; Lépine, F.; Kuleff, A. I. Attosecond Hole Migration in Benzene Molecules Surviving Nuclear Motion. *J. Phys. Chem. Lett.* **2015**, *6*, 426–431.
- (83) Breidbach, J.; Cederbaum, L. S. Migration of Holes: Formalism, Mechanisms, and Illustrative Applications. *J. Chem. Phys.* **2003**, *118*, 3983.
- (84) Mignolet, B.; Levine, R. D.; Remacle, F. Localized Electron Dynamics in Attosecond-Pulse-Excited Molecular Systems: Probing the Time-Dependent Electron Density by Sudden Photoionization. *Phys. Rev. A* **2012**, *86*, 053429.
- (85) Cooper, B.; Averbukh, V. Single-Photon Laser-Enabled Auger Spectroscopy for Measuring Attosecond Electron-Hole Dynamics. *Phys. Rev. Lett.* **2013**, *111*, 083004.
- (86) Jia, D.; Manz, J.; Yang, Y. De- and Recoherence of Charge Migration in Ionized Iodoacetylene. *J. Phys. Chem. Lett.* **2019**, *10*, 4273–4277.
- (87) Timmers, H.; Li, Z.; Shivaram, N.; Santra, R.; Vendrell, O.; Sandhu, A. Coherent Electron Hole Dynamics Near a Conical Intersection. *Phys. Rev. Lett.* **2014**, *113*, 113003.
- (88) Arnold, C.; Vendrell, O.; Santra, R. Electronic Decoherence Following Photoionization: Full Quantum-Dynamical Treatment of the Influence of Nuclear Motion. *Phys. Rev. A* **2017**, *95*, 033425.
- (89) Vacher, M.; Bearpark, M. J.; Robb, M. A.; Malhado, J. P. Electron Dynamics upon Ionization of Polyatomic Molecules: Coupling to Quantum Nuclear Motion and Decoherence. *Phys. Rev. Lett.* **2017**, *118*, 083001.
- (90) Grell, G.; Bokarev, S. I.; Winter, B.; Seidel, R.; Aziz, E. F.; Aziz, S. G.; Kühn, O. Multi-Reference Approach to the Calculation of Photoelectron Spectra Including Spin-Orbit Coupling. *J. Chem. Phys.* **2015**, *143*, 074104.
- (91) Pickup, B. T. On the Theory of Fast Photoionization Processes. *Chem. Phys.* **1977**, *19*, 193–208.
- (92) Allan, M.; Kloster-Jensen, E.; Maier, J. P. Emission Spectra of $\text{Cl-C}\equiv\text{C-H}^+$, $\text{Br-C}\equiv\text{C-H}^+$ and $\text{I-C}\equiv\text{C-H}^+$ Radical Cations:

$\tilde{A}^2\Pi \rightarrow \tilde{X}^2\Pi$ Band Systems and the Decay of the $\tilde{A}^2\Pi$ States. *J. Chem. Soc., Faraday Trans. 2* **1977**, *73*, 1406–1416.

(93) Wang, H.; Möhle, T.; Kühn, O.; Bokarev, S. I. Ultrafast Dissipative Spin-State Dynamics Triggered by x-Ray Pulse Trains. *Phys. Rev. A* **2018**, *98*, 013408.

(94) Fruchterman, T. M. J.; Reingold, E. M. Graph Drawing by Force-Directed Placement. *Softw. Pract. Exp.* **1991**, *21*, 1129–1164.

(95) Hagberg, A. A.; Schult, D. A.; Swart, P. J. In *Proceedings of the 7th Python in Science Conference*; Varoquaux, G., Vaught, T., Millman, J., Eds.; SciPy Conference: 2008; pp 11–16.

(96) Bokarev, S. I.; Dantz, M.; Suljoti, E.; Kühn, O.; Aziz, E. F. State-Dependent Electron Delocalization Dynamics at the Solute-Solvent Interface: Soft-X-Ray Absorption Spectroscopy and Ab Initio Calculations. *Phys. Rev. Lett.* **2013**, *111*, 083002.

(97) Douglas, M.; Kroll, N. M. Quantum Electrodynamical Corrections to the Fine Structure of Helium. *Ann. Phys.* **1974**, *82*, 89–155.

(98) Suljoti, E.; Garcia-Diez, R.; Bokarev, S. I.; Lange, K. M.; Schoch, R.; Dierker, B.; Dantz, M.; Yamamoto, K.; Engel, N.; Atak, K.; Kühn, O.; Bauer, M.; Rubensson, J.-E.; Aziz, E. F. Direct Observation of Molecular Orbital Mixing in a Solvated Organometallic Complex. *Angew. Chem., Int. Ed.* **2013**, *52*, 9841–9844.

Recommended by ACS

State-Specific Configuration Interaction for Excited States

Fábris Kossoski and Pierre-François Loos

APRIL 06, 2023

JOURNAL OF CHEMICAL THEORY AND COMPUTATION

READ 

Optimal Mode Combination in the Multiconfiguration Time-Dependent Hartree Method through Multivariate Statistics: Factor Analysis and Hierarchical Clustering

David Mendive-Tapia, Oriol Vendrell, *et al.*

JANUARY 30, 2023

JOURNAL OF CHEMICAL THEORY AND COMPUTATION

READ 

Tensor-Hypercontracted MP2 First Derivatives: Runtime and Memory Efficient Computation of Hyperfine Coupling Constants

Felix H. Bangerter, Christian Ochsenfeld, *et al.*

AUGUST 09, 2022

JOURNAL OF CHEMICAL THEORY AND COMPUTATION

READ 

Assessment of State-Averaged Driven Similarity Renormalization Group on Vertical Excitation Energies: Optimal Flow Parameters and Applications to Nucleobases

Meng Wang, Chenyang Li, *et al.*

DECEMBER 19, 2022

JOURNAL OF CHEMICAL THEORY AND COMPUTATION

READ 

Get More Suggestions >

Supplement. RhoDyn: a TD-RASCI framework to study ultrafast electron dynamics in molecules.

Vladislav Kochetov and Sergey I. Bokarev^{*,†}

*Institut für Physik, Universität Rostock, A.-Einstein-Strasse 23-24, 18059 Rostock,
Germany*

E-mail: sergey.bokarev@uni-rostock.de

Input files

Here we provide representative `OpenMOLCAS` input files for calculations presented in the main text, one for each molecule (complex). One should notice that these files are just examples demonstrating the workflow of calculations with `RHODYN` program. Essentially, they are not complete in the `RASSCF` part. `RASSCF` calculations are usually performed several times to ensure the proper composition of the active space. The `RASSCF` input, presented here, instead gives the general parameters such as spin, `RAS` partitioning, and number of requested states for the sake of clarity.

[TiO₆]⁸⁻

```
&GATEWAY
  coord = 7
  TiO6 rutile
  Ti      0.000000000    0.000000000    0.000000000
  O      0.000000000    1.984000000   -0.000000972
  O      0.000000000   -1.984000000    0.000000972
  O      0.000000000    0.000000000    1.946000000
  O      0.000000000    0.000000000   -1.946000000
  O      1.946000000    0.000000000    0.000000000
  O     -1.946000000    0.000000000    0.000000000
  basis = ano-rcv-vtzp
  group = nosym; Douglas-Kroll; AMFI
&SEWARD
  Cholesky
&RASSCF
  File      = ti_core.rasscf.h5
  Charge    = -8
  Spin      = 1
  Frozen    = 36
  Nactel    = 6 1 1
  RAS1      = 3
  RAS3      = 5
  CRoot     = 16 16 1
> copy $Project.rasscf.h5 JOB001
> copy $Project.rasscf.h5 RASSD1
&RASSCF
  File      = ti_core.rasscf.h5
  Charge    = -8
  Spin      = 3
  Frozen    = 36
  Nactel    = 6 1 1
  RAS1      = 3
  RAS3      = 5
  CRoot     = 15 15 1
> copy $Project.rasscf.h5 JOB002
> copy $Project.rasscf.h5 RASSD2
&RASSI
  NrofJob   = 2 all
  SpinOrbit; MESO; RHODyn
> copy $Project.rassi.h5 RASSISD
&RHODYN
  NRManifolds = 2
  NRDEt,CSF,STATES,SPIN = 16 16 16 1
```

	15	15	15	3
POPulatedstyle	=	SO_THERMAL		
NSTate	=	61 all		
FINALtime	=	10		
Tout	=	0.0005		
IFSO				
NPULses	=	1		
PTYPE	=	Gauss		
AMPLitude	=	1.5		
TAUShift	=	1.5		
SIGMa	=	0.2		
OMEGa	=	470		
Dipole				

H₂

```
&GATEWAY
  coord = 2
  H2 molecule
  H      0.00      0.00      -0.37
  H      0.00      0.00       0.37
  basis = H.aug-cc-pVDZ
  group = nosym
&SEWARD
&SCF
&RASSCF
  Ras2    = 1
  Ras3    = 17
  Nactel  = 2 0 1
  Spin    = 1
  Ciroot  = 18 18 1
> copy $Project.rasscf.h5 JOB001
> copy $Project.rasscf.h5 RASSD1
&RASSI
  Nrof JobIphs = 1 all
> copy $Project.rassi.h5 RASSISD
&RHODYN
  NRsManifolds      = 1
  NRDEt,CSF,STATES,SPIN = 18 18 18 1
  POPulatedstyle   = SF
  NSTate            = 18 all
  FINALtime         = 53.3
  Tstep             = 0.001
  Tout              = 0.001
  DMBasis           = SF
  PROPbasis         = SF
  NPULses           = 1
  PTYPE             = cos2
  AMPLitude         = 0.1
  TAUShifts         = 26.65
  SIGMa             = 26.65
  OMEGa             = 1.55
  POLARization      = (0,0) (0,0) (1,0)
  Dipole
```

C₆H₆

```
&GATEWAY
  coord = 12
  C6H6
  C1      0.000000      0.000000      1.390753
  H1      0.000000      0.000000      2.472798
  C2      0.000000      1.204431      0.695377
  H2      0.000000      2.141508      1.236402
  C3      0.000000      1.204431     -0.695377
  H3      0.000000      2.141508     -1.236402
  C4      0.000000      0.000000     -1.390753
  H4      0.000000      0.000000     -2.472798
  C5      0.000000     -1.204431     -0.695377
  H5      0.000000     -2.141508     -1.236402
  C6      0.000000     -1.204431      0.695377
  H6      0.000000     -2.141508      1.236402
  basis = ANO-L-VTZ
  group = nosym
&SEWARD
&SCF
&RASSCF
  Inactive = 18
  Ras2     = 6
  Nactel   = 5
  Spin     = 2
  Ciroot   = 210 210 1
&CASPT2
  Imag = 0.1
> copy $Project.caspt2.h5 JOB001
> copy $Project.caspt2.h5 RASSD1
&RASSI
  NrOF = 1 all
  RHODyn
> copy $Project.rassi.h5 RASSISD
&RHODYN
  NRSManifolds      = 1
  NRDEt, CSF, STATES, SPIN = 300 210 210 2
  NSTate            = 210 all
  POPUlated_style   = CSF
  NRPOpulated       = 1
  FINAltime         = 5
  TOUT              = 0.005
  PROPbasis         = CSF
  DMBasis           = CSF
```

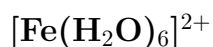
NPULses = 0

HCCI

```

&GATEWAY
  coord = 4
  HCCI
  I      0.0000   0.0000   0.0000
  C 0.0000   0.0000   2.0069
  C 0.0000   0.0000   3.2233
  H 0.0000   0.0000   4.2892
  basis = ano-rcc-vtzp
  group = nosym; Douglas-Kroll; AMFI
&SEWARD
  cholesky
&RASSCF
  File      = s1.rasscf.h5
  Spin      = 2
  Inactive  = 27
  Nactel    = 11
  RAS2      = 9
  ciroot    = 50 50 1
&CASPT2
  File = $Project.rasscf.h5
  Imag = 0.1
> copy $Project.caspt2.h5 JOB001
> copy $Project.caspt2.h5 RASSD1
&RASSI
  Nrof JobIphs = 1 all
  SpinOrbit; MESO
> copy $Project.rassi.h5 RASSISD
&RHODYN
  RUNMode          = 4
  NRSManifolds     = 1
  NRDEt, CSF, STATES, SPIN = 10584 6048 50 2
  NSTate           = 101 all
  POPUlated_style = CSF
  NRPOpulated      = 1
  FINALtime        = 12
  TOUT             = 0.005
  IFSO
  PROPbasis        = SO
  DMBasis          = CSF_SO
  NPULses          = 0

```



&GATEWAY

coord = 19

[Fe(H2O)6]2+

Fe	0.000000000	0.000000000	0.000000000
O1	0.000000000	2.042601000	-0.000001000
O2	0.000000000	-2.042601000	0.000001000
O3	0.000000000	0.000000000	2.269196000
O4	0.000000000	0.000000000	-2.269196000
O5	2.019643000	0.000000000	0.000000000
O6	-2.019643000	0.000000000	0.000000000
H1	2.584262000	0.000000000	0.794308000
H2	-2.584262000	0.000000000	-0.794308000
H3	-0.789169000	2.616296000	0.000000000
H4	0.789169000	-2.616296000	0.000000000
H5	0.789169000	2.616296000	0.000000000
H6	-0.789169000	-2.616296000	0.000000000
H7	-0.000001000	-0.778301000	2.856312000
H8	0.000001000	0.778301000	-2.856312000
H9	0.000001000	0.778300000	2.856312000
H10	-0.000001000	-0.778300000	-2.856312000
H11	2.584262000	0.000000000	-0.794308000
H12	-2.584262000	0.000000000	0.794308000

basis = ano-rcc-vtzip

group = nosym; Douglas-Kroll; AMFI

&SEWARD

Cholesky

&RASSCF

Spin = 5

Nactel = 12 1 0

Frozen = 36

Ras1 = 3

Ras2 = 5

Ciroot = 35 35 1

> copy \$Project.rasscf.h5 JOB001

> copy \$Project.rasscf.h5 RASSD1

&RASSCF

Spin = 3

Nactel = 12 1 0

Frozen = 36

Ras1 = 3

Ras2 = 5

Ciroot = 195 195 1

> copy \$Project.rasscf.h5 JOB002

```

> copy $Project.rasscf.h5 RASSD2
&RASSI
  Nrof JobIphs=2 all
  SpinOrbit; MESO; RHODyn
> copy $Project.rassi.h5 RASSISD
&RHODYN
NRSManifolds          = 2
NRDEt,CSF,STATES,SPIN = 35  35  35  5
                      230 195 195  3

POPulatedstyle       = SF
NSTate               = 128 1 6 12 17 22 26 32 37 41 ...
FINALtime            = 6
PROPbasis             = SF
DMBAxis              = SF
METHod               = RKCK
IFSO
NPULses              = 1
PTYPE                 = Gauss
AMPLitude            = 6.0
TAUShifts            = 1.0
POLArization         = (1.0,0.0) (0.0,0.0) (0.0,0.0)
SIGMa                 = 0.2
OMEGa                 = 716

```



```
&GATEWAY
  coord = 11
  Fe(CO)5
  Fe      0.000000      0.000000      0.000000
  C1      0.885331     -1.533438      0.000000
  C2      0.000000      0.000000     -1.682062
  C3      0.000000      0.000000      1.682062
  C4     -1.770662      0.000000      0.000000
  C5      0.885331      1.533438      0.000000
  O1      1.462429     -2.533001      0.000000
  O2      0.000000      0.000000     -2.848455
  O3      0.000000      0.000000      2.848455
  O4     -2.924857      0.000000      0.000000
  O5      1.462429      2.533001      0.000000
  basis = ano-rcc-vtzip
  group = nosym; Douglas-Kroll; AMFI
&SEWARD
  Cholesky
&RASSCF
  FileOrb = s1_orb.rasscf.h5
  Spin    = 1
  Nactel  = 16 1 1
  Frozen  = 40
  Ras1    = 3
  Ras2    = 6
  Ras3    = 4
  CIroot  = 751 751 1
> copy $Project.rasscf.h5 JOB001
> copy $Project.rasscf.h5 RASSD1
&RASSCF
  FileOrb = s1_orb.rasscf.h5
  Spin    = 3
  Nactel  = 16 1 1
  Frozen  = 40
  Ras1    = 3
  Ras2    = 6
  Ras3    = 4
  CIroot  = 1005 1005 1
> copy $Project.rasscf.h5 JOB002
> copy $Project.rasscf.h5 RASSD2
&RASSI
  Nrof JobIphs=2 all
  SpinOrbit; MESO; RHODyn
```

```

> copy $Project.rassi.h5 RASSISD
&RHODYN
NRsManifolds          = 2
NRDEt,CSF,STATES,SPIN = 1011   751   751   1
                       1265   1005  1005   3

IFSO
POPulatedstyle       = SO_THERMAL
PROPbasis            = SF
DMBasis              = SF
Nstate               = 656 1 2 3 7 13 16 21 22 27 29 32 36 ...
FINALtime            = 6
TSTEP                = 0.0005
NPULses              = 1
PTYPE                = Gauss
AMPLitude            = 6.0
TAUShifts            = 1.0
SIGMa                = 0.2
OMEGa                = 728

```


[VK3] SPIN-FLIP DYNAMICS IN CORE-EXCITED STATES IN THE BASIS OF
IRREDUCIBLE SPHERICAL TENSOR OPERATORS

THIES ROMIG, VLADISLAV KOCHETOV, and SERGEY I. BOKAREV

Reprinted from

THIES ROMIG, VLADISLAV KOCHETOV, and SERGEY I. BOKAREV,
arXiv:2306.06737 [physics.comp-ph] (2023).

Spin-flip dynamics in core-excited states in the basis of irreducible spherical tensor operators

Thies Romig,¹ Vladislav Kochetov,¹ and Sergey I. Bokarev^{2,1, a)}

¹⁾*Institut für Physik, Universität Rostock, A.-Einstein-Strasse 23-24, 18059 Rostock, Germany*

²⁾*Chemistry Department, School of Natural Sciences, Technical University of Munich, Lichtenbergstr. 4, 85748 Garching, Germany*

(Dated: June 13, 2023)

Recent experimental advances in ultrafast science put different processes occurring on the electronic timescale below a few femtoseconds in focus. In the present theoretical work, we demonstrate how the transformation and propagation of the density matrix in the basis of irreducible spherical tensors can be conveniently used to study sub-few fs spin-flip dynamics in the core-excited transition metal compounds. With the help of the Wigner-Eckart theorem, such a transformation separates the essential dynamical information from the geometric factors governed by the angular momentum algebra. We show that an additional reduction can be performed by the physically motivated truncation of the spherical tensor basis. In particular, depending on the degree of coherence, the ultrafast dynamics can be considered semi-quantitative in the notably reduced spherical basis when only total populations of the basis states of the given spin are of interest. Such truncation should be especially beneficial when the number of the high-spin basis states is vast, as it substantially reduces computational costs.

I. INTRODUCTION

Electron dynamics is a fundamental phenomenon determining the mechanism of many processes in molecules and condensed matter.¹⁻⁴ It represents an initial elementary step involving electronic reorganization, while nuclei start to move only in response to it, leading, in turn, to electronic decoherence. One of the most important effects is charge transfer,^{5,6} playing a decisive role in many chemical and biochemical transformations, such as photosynthesis, with the electron correlation- and relaxation-driven charge migration^{7,8} being its elementary step. Electronic response to strong fields can also lead to highly non-linear processes such as high harmonic generation.^{9,10}

Another process that is driven by electronic coupling is spin-flip dynamics.¹¹⁻¹³ In the weak interaction regime, it should be necessarily driven by nuclear motion to bring interacting states close enough for the intersystem crossing to happen. The situation changes when the coupling is strong due to electronic excitation from core shells with non-zero angular momentum, e.g., 2p levels.^{14,15} In this case, the coupling may be larger, starting from several eV for lighter elements, and does not necessarily require a nuclear motion for spin-flip to happen.¹⁶ The spin dynamics can be especially intricate when successive ionizations occur under ultra-intense X-ray irradiation.¹⁷ In this case, one has to consider multiple spin manifolds calling for an efficient theoretical treatment.

One of the ways is to separate geometric, due to the angular symmetry of the system, and essential dynamical parts of the time-evolution of the system's wave function

or density matrix. It can be afforded, for instance, by expanding the density operator in terms of irreducible tensor operators.¹⁸ Fano first suggested the systematic use of tensor operators,¹⁹ and later their use was extensively enlarged to applications in angular correlation theory in atomic physics^{20,21} and the description of atom-light interactions.²²⁻²⁵

When talking about a large number of states of different multiplicities, one might be interested in some reduced representation of a system that should factor geometric parts out. In an energy (state) basis, the zero-order pure-spin states are characterized by their spin S and its projection onto the quantization axis M . When several thousands of states are in focus, i.e., when the state density and the width of the excitation pulse are significant, one would wish to neglect the dynamics of magnetic sublevels and is primarily interested in the population of the groups of these sublevels belonging to the same spin-free state or even collectively the population of all the states with the same spin. The averaging over M reduces the information available and should require simplified propagation, which can be still very costly for many states.

Here, we attempt such a description using the spherical tensor basis to represent the density matrix employing the density-matrix-based Time-Dependent Restricted Active Space Configuration Interaction (TD-RASCI) method.^{15,26} In particular, we consider the ultrafast dynamics in three transition metal compounds, TiCl_4 , $[\text{Fe}(\text{H}_2\text{O})_6]^{2+}$, and $[\text{Cr}(\text{H}_2\text{O})_6]^{3+}$. Upon an excitation from the ground state of these systems to a superposition of $L_{2,3}$ 2p-hole core-excited states, the ultrafast spin-mixing occurs, resulting in a substantial population of spin-flipped states of different multiplicities. Finally, we note that the method is implemented in the `OpenMolcas` program package²⁷ in the module `RhoDyn`,¹⁵ allowing for

^{a)}Electronic mail: sergey.bokarev@tum.de

both full and reduced propagation in the state or spherical tensor bases.

II. THEORY AND IMPLEMENTATION

A. Equation of Motion (EOM) in the tensor basis

Below we utilize the density-matrix-based TD-RASCI formalism.¹⁵ The state of the system is characterized by a density operator $\hat{\rho}$, the time evolution of which obeys the Liouville-von-Neumann (LvN) equation of motion

$$\dot{\hat{\rho}} = -i[\hat{H}_{\text{CI}} + \hat{V} - \hat{\boldsymbol{\mu}} \cdot \boldsymbol{\mathcal{E}}, \hat{\rho}]. \quad (1)$$

Here, the Hamiltonian is split into three terms: \hat{H}_{CI} represents the interelectronic interaction and thus governs dynamics driven by electronic correlation and relaxation. This part is treated here through the Configuration Interaction (CI) method. Next, \hat{V} is the Spin–Orbit Coupling (SOC) operator, and the last semi-classical term corresponds to the interaction of the system with an external time-dependent electric field $\boldsymbol{\mathcal{E}}$ via its dipole moment $\hat{\boldsymbol{\mu}}$, i.e., employing long-wavelength approximation. In this article, nuclei stay fixed, and we neglect energy and phase relaxation processes for simplicity of discussion, i.e., the system stays closed at all times; this limitation can be readily lifted,¹⁴ thanks to the density-matrix formulation of the theory.

The original pure-spin state basis consists of the states $|aSM\rangle$, where a is the index of the spatial part collectively denoting all relevant quantum numbers, and S and M are the total spin and its projection onto the quantization axis. One can consider the spatial part as being, e.g., the eigenstates of \hat{H}_{CI} , which will be called Spin-Free (SF) states below, while the $|aSM\rangle$ states will be called basis spin states. The SF states have no explicit M -dependence and thus need to be extended to include the respective spin part when spin-dependent interactions are to be considered. It increases the state vector size by the spin multiplicity factor and the density matrix by its square. We separate spatial and spin parts in the basis states $|aS\rangle \otimes |SM\rangle$; the total spin naturally relates to the spin part but is fixed by the spatial index a , so the summation over a will be in the following denoted as a summation over aS . Thus, the spin-independent operators attain the structure $\hat{H}_{\text{CI}} \otimes \hat{1}$ and $\hat{\boldsymbol{\mu}} \cdot \boldsymbol{\mathcal{E}} \otimes \hat{1}$. In contrast, \hat{V} couples both parts and can be represented as

$$\hat{V} = \sum_{m=0,\pm 1} (-1)^m \hat{L}_{-m}^1 \otimes \hat{S}_m^1, \quad (2)$$

where $L_{(0,\pm 1)}^1$ and $S_{(0,\pm 1)}^1$ are standard components of angular momentum and spin tensor operators of rank 1.

Assuming this setting, the uncorrelated initial density operator can be represented as the direct product of spatial $\hat{\pi}(0)$ and spin $\hat{\sigma}(0)$ parts at time $t = 0$

$$\hat{\rho}(0) = \hat{\pi}(0) \otimes \hat{\sigma}(0). \quad (3)$$

At later times when SOC is switched on, the factorization does not hold. However, when writing these operators in the matrix form in a state basis, one can consider this structure to still hold within the subblocks of the total density matrix. Further, we will consider only a separate block $\boldsymbol{\rho}_{aS,bS'} = \pi_{ab} \otimes \boldsymbol{\sigma}_{SS'}$ and express the $\boldsymbol{\sigma}$ matrix in terms of irreducible tensor matrix elements $\mathbf{T}_q^k(S, S')$. Note that $\boldsymbol{\rho}_{aS,bS'}$ and $\boldsymbol{\sigma}_{SS'}$ denote the whole $(2S+1) \times (2S'+1)$ subblocks and $\pi_{a,b}$ a single spatial matrix element. With this, the entire block can be written as

$$\boldsymbol{\rho}_{aS,bS'} = \sum_{kq} \langle \rho_{aS,bS'}^{kq} \rangle \mathbf{T}_q^k(S, S') \quad (4)$$

Here, the dynamical factor (state multipole) $\langle \rho_{aS,bS'}^{kq} \rangle = \pi_{ab} \cdot \langle \sigma^{kq}(S, S') \rangle$ absorbs both the spatial part π_{ab} and the expansion coefficient $\langle \sigma^{kq}(S, S') \rangle = \text{Tr}\{\hat{\sigma} \hat{T}_q^{k\dagger}(S, S')\}$, where the trace is taken with respect to the $|SM\rangle$ spin basis states. To do so, we recall that for the matrix element of the irreducible spherical tensor operator \hat{T}_q^k of rank k and projection q , the relation

$$\begin{aligned} \langle SM | \hat{T}_q^k(S, S') | S'M' \rangle = \\ (-1)^{S-M} \sqrt{2k+1} \begin{pmatrix} S & k & S' \\ -M & q & M' \end{pmatrix}, \end{aligned} \quad (5)$$

holds according to the Wigner–Eckart (WE) theorem;²⁸ parentheses denote the Wigner 3j symbol.

Next, we notice that

$$\langle aSM | \hat{H}_{\text{CI}} \otimes \hat{1} | bS'M' \rangle = E_a^{\text{SF}} \delta_{ab} \delta_{SS'} \delta_{MM'} \quad (6)$$

$$\langle aSM | \hat{\boldsymbol{\mu}} \cdot \boldsymbol{\mathcal{E}} \otimes \hat{1} | bS'M' \rangle = \boldsymbol{\mu}_{ab}^{\text{SF}} \cdot \boldsymbol{\mathcal{E}} \delta_{SS'} \delta_{MM'}; \quad (7)$$

since energies and transition dipole matrix elements are estimated solely in the SF basis, they attain the respective label. For SOC, we write

$$\begin{aligned} \langle aSM | \hat{V} | bS'M' \rangle = \\ \sum_{m=0,\pm 1} (-1)^m \langle aS | \hat{L}_{-m}^1 | bS' \rangle \langle SM | \hat{S}_m^1 | S'M' \rangle = \\ \sqrt{3} \sum_{m=0,\pm 1} (-1)^{S-M+m} \begin{pmatrix} S & 1 & S' \\ -M & m & M' \end{pmatrix} \langle aS | \hat{V}^m | bS' \rangle, \end{aligned} \quad (8)$$

where

$$\langle aS | \hat{V}^m | bS' \rangle = V_{aS,bS'}^m = \langle a | \hat{L}_{-m}^1 | b \rangle \langle S | \hat{S}_m^1 | S' \rangle \quad (9)$$

is the WE semi-reduced SOC matrix element; note the residual dependence on the m number. These elements form a reduced SOC matrix (tensor) denoted below as $\mathbf{V} = (\mathbf{V}^m)$.

We obtain an equation for the evolution of state multipoles $\langle \rho_{aS,bS'}^{kq} \rangle$ by multiplying both sides of the LvN

Eq. (1) with the $\hat{1} \otimes \hat{T}_q^{k\dagger}(S, S')$ operator, tracing out spin degrees of freedom, and sandwiching between the SF $|aS\rangle$ basis states. For details of derivation, see Appendix A.

For a general density, the equation for its state multipoles in matrix form reads

$$i\langle \dot{\rho}^{kq} \rangle = [\mathbf{H}_{\text{CI}} - \hat{\boldsymbol{\mu}} \cdot \boldsymbol{\mathcal{E}}, \langle \rho^{kq} \rangle] + \sum_{\substack{K=k, k\pm 1 \\ |Q| \leq K}} \{\mathbb{V}, \langle \rho^{KQ} \rangle\}, \quad (10)$$

where $k = 0, \dots, 2 \cdot \max\{S, S', S''\}$, $q = -k, \dots, k$, and

$K \leq 2 \cdot \max\{S, S', S''\}$. The first conventional commutator on the right-hand side of the Eq. (10) corresponds to the influence of electron correlation and coupling to the external field. In the basis of eigenstates of \hat{H}_{CI} , the \mathbf{H}_{CI} matrix is diagonal with SF energies E_a^{SF} on it, Eq. (6). The commutator-like SOC terms in curly braces on the right-hand side of Eq. (10) mix state multipoles of different ranks and projections. These terms involve weighted matrix-matrix multiplication

$$\{\mathbb{V}, \langle \rho^{KQ} \rangle\}_{aS, bS'} = \sum_{cS''} \sum_{m=0, \pm 1} \mathcal{Y}_1 V_{aS, cS''}^m \langle \rho_{cS'', bS'}^{KQ} \rangle + \mathcal{Y}_2 \langle \rho_{aS, cS''}^{KQ} \rangle V_{cS'', bS'}^m, \quad (11)$$

with geometric weighting factors depending on all spins, ranks, and their projections via Wigner 3j and 6j symbols

$$\mathcal{Y}_1 = (-1)^{S+S'-Q} \sqrt{3(2k+1)(2K+1)} \begin{pmatrix} K & 1 & k \\ Q & m & -q \end{pmatrix} \begin{Bmatrix} K & 1 & k \\ S & S' & S'' \end{Bmatrix} \quad (12)$$

$$\mathcal{Y}_2 = (-1)^{S+S'-Q+K+k} \sqrt{3(2k+1)(2K+1)} \begin{pmatrix} K & 1 & k \\ Q & m & -q \end{pmatrix} \begin{Bmatrix} 1 & K & k \\ S & S' & S'' \end{Bmatrix}. \quad (13)$$

In the resulting Eq. (10), the $\langle \rho^{kq} \rangle$ matrices have dimensions $N_{\text{SF}} \times N_{\text{SF}}$, where N_{SF} is the number of SF states and, thus, the complexity of the problem is reduced approximately by a factor of the squared mean multiplicity. However, the dependence on M is replaced by the dependence on k and q , leading to an increased number of smaller problems.

This Equation of Motion (EOM) in terms of the state multipoles is equivalent to the propagation in the basis of $|aSM\rangle$ spin states if one takes all necessary ranks k into account. Because of this equivalence, one can resolve the dynamics of individual M components of the density matrix delivered by the back transformation from the spherical tensor basis to the spin-state basis. It allows explicitly treating cases with circularly polarized light, interaction with magnetic fields, or when the initial condition implies significantly different populations of M -sublevels. However, it does improve computational effort, and at least for small and medium numbers of states, the scaling is worse than the propagation in the state basis. This calls for simplifications and reduction of complexity.

B. Reduced EOM

If the distribution between different magnetic quantum numbers M is not of interest, only the reduced density matrix $\tilde{\rho}$ must be propagated. It is obtained from the full

density matrix tracing out M -dependence $\tilde{\rho} = \text{Tr} \rho$. The derivation procedure is entirely analogous to that for the full density matrix as sketched in Appendix A, but the elements of the tensor operator matrices, Eq. (5), need to be considered explicitly. This is owing to an additional condition: in Eqs. (4) and (5), only summed diagonal elements of $\mathbf{T}_q^k(S, S')$ are regarded, i.e., $M = M'$, leading to the expression for the reduced matrix element

$$\begin{aligned} \tilde{\rho}_{aS, bS'} &= \text{Tr} \rho_{aS, bS'} \\ &= \sum_M \sum_k \langle \rho_{aS, bS'}^{k0} \rangle (-1)^{S-M} \sqrt{2k+1} \begin{pmatrix} S & k & S' \\ -M & 0 & M \end{pmatrix}, \end{aligned} \quad (14)$$

where the selection rules of the 3j symbol demand $q = 0$. The fact that only $q = 0$ contributes for every k is in accord with the interpretation of $\langle \rho_{aS, bS'}^{k0} \rangle$ as representing diagonal elements of the original density matrix in the state basis, see Appendix B. Taking this into account leads to the reduced EOM

$$i\langle \dot{\rho}^{k0} \rangle = [\mathbf{H}_{\text{CI}} - \hat{\boldsymbol{\mu}} \cdot \boldsymbol{\mathcal{E}}, \langle \rho^{k0} \rangle] + \sum_{\substack{K=k, k\pm 1 \\ |Q| \leq 1}} \|\mathbb{V}, \langle \rho^{KQ} \rangle\|, \quad (15)$$

with the slightly modified SOC commutator-like term and different geometric factors

$$\|\mathbb{V}, \langle \rho^{KQ} \rangle\|_{aS, bS'} = \sum_{cS''} \mathcal{X}_1 V_{aS, cS''}^{-Q} \langle \rho_{cS'', bS'}^{KQ} \rangle + \mathcal{X}_2 \langle \rho_{aS, cS''}^{KQ} \rangle V_{cS'', bS'}^{-Q}, \quad (16)$$

$$\mathcal{X}_1 = (-1)^{S+S'-Q} \sqrt{3(2k+1)(2K+1)} \begin{pmatrix} K & 1 & k \\ Q & -Q & 0 \end{pmatrix} \begin{Bmatrix} K & 1 & k \\ S & S' & S'' \end{Bmatrix} \quad (17)$$

$$\mathcal{X}_2 = (-1)^{S+S'-Q+K+k} \sqrt{3(2k+1)(2K+1)} \begin{pmatrix} K & 1 & k \\ Q & -Q & 0 \end{pmatrix} \begin{Bmatrix} 1 & K & k \\ S & S' & S'' \end{Bmatrix}. \quad (18)$$

However, as the derivative of the $\langle \rho^{k0} \rangle$ also depends on matrices with $Q = 0, \pm 1$, Eq. (15) is not closed and, therefore, cannot be used to propagate the reduced density matrix in the present form. This fact can also be regarded as a consequence of the semi-reduced nature of \mathbb{V} retaining the m -dependence through the angular momentum part of the SOC operator, Eq. (8). Moreover, the submatrices \mathbf{V}^m of the semi-reduced SOC Hamiltonian couple $\langle \rho^{kq} \rangle$ to $\langle \rho^{k(q+m)} \rangle$, meaning that, to account for SOC, for a given k , the $q = \pm 1$ elements require the $q = \pm 2$ projections to be propagated, which, in turn, depend on $q = \pm 3$ and so forth. As this iteratively leads to full propagation, one does not benefit from the reduction.

Nevertheless, the structure of Eq. (15) can inspire physically motivated rank and component truncation in the full EOM, Eq. (10). First, only the lowest $\pm q$ projections for each rank k (or K) can be considered the most important, e.g., $q = 0, \pm 1$. Second, the ranks themselves can be truncated at some value below the maximum $2\text{-max}\{S, S', S''\}$, thus, neglecting all of the computationally demanding higher-rank contributions. In this case, the equations for the truncated expansion are closed, providing substantial savings in the computational effort.

C. Implementation details

Obtaining wave functions of states $|aSM\rangle$ and matrix elements of the \hat{H}_{CI} , $\hat{\mu}$, and \hat{V} operators was performed with the `OpenMolcas` code.²⁷ The propagation itself was performed with the `RhoDyn` module of the same package,¹⁵ which has been extended to allow for the decomposition and time propagation of the density matrix in the spherical tensor basis.

Particular emphasis should be put on accurately evaluating the numerical value on the right-hand side of Eq. (10), namely the sums over the $\{\mathbb{V}, \langle \rho^{KQ} \rangle\}$ SOC terms, see Fig. 1. Element-wise propagation of each matrix element of the state multipoles is not efficient. It is replaced by the propagation of $\langle \rho^{kq} \rangle$ matrices as a whole and involves matrix-matrix multiplications, which are efficiently realized in mathematical libraries. However, incorporating such a multiplication is more complex due to 3j-symbols in \mathcal{Y}_1 and \mathcal{Y}_2 coupling different ranks.

To circumvent this complication, we first note that geometrical factors \mathcal{Y}_i depend on ranks and projections k, q, K, Q , as well as on spins S, S', S'' and m . Therefore, the computation must be performed separately for every k, q, K , and Q combination. When fixing S' (or S for the second term) and, thus, splitting the $\langle \rho^{KQ} \rangle$ into slabs, Fig. 1b), one can compute matrices \mathcal{Y}_1^m (\mathcal{Y}_2^m) de-

pending only on the number m , see Eqs. (12) and (13). Now, Hadamard products $\mathcal{Y}_i^m * \mathbf{V}^m$ can be computed as schematically shown in Fig. 1c); the result is multiplied by a slab of $\langle \rho^{KQ} \rangle$, and the resulting slabs are assembled into the full matrices contributing to the given $\langle \rho^{kq} \rangle$ derivative.

In addition, one can utilize the hermiticity of the density matrices $\langle \rho^{k-q} \rangle = (-1)^{S-S'-q} \langle \rho^{kq} \rangle^*$. Therefore, either $\langle \rho^{kq} \rangle$ or $\langle \rho^{k-q} \rangle$ is calculated using Eq. (10), and the other can be easily obtained. In the discussion below, we will denote both $\langle \rho^{k\pm q} \rangle$ as $\langle \rho^{kq} \rangle$ unless specified otherwise. The algorithm, involving matrix multiplication and accounting for hermiticity, substantially speeds up the calculations.

D. Computational details

The TiCl_4 molecular geometry, a tetragonal structure of T_d point symmetry with Ti-Cl distances of 2.170 Å, was taken from Ref.²⁹ and was obtained by gas electron diffraction. The $[\text{Fe}(\text{H}_2\text{O})_6]^{2+}$ and $[\text{Cr}(\text{H}_2\text{O})_6]^{3+}$ structures were obtained at the DFT level with the B3LYP functional and aug-cc-pVTZ basis set in the `Gaussian` program package;³⁰ see Ref.¹⁴ for more details. Hexa-aqua complexes possess approximate O_h symmetry, lowered by the presence of H atoms and the Jahn-Teller effect in $[\text{Fe}(\text{H}_2\text{O})_6]^{2+}$. Metal-oxygen distances are 2.04, 2.27 Å for $[\text{Fe}(\text{H}_2\text{O})_6]^{2+}$, and 2.00 Å for $[\text{Cr}(\text{H}_2\text{O})_6]^{3+}$.

Calculations of SF states and interstate couplings are performed at the Restricted Active Space Self-Consistent Field (RASSCF) level of theory. Scalar relativistic effects are accounted for via a Douglas-Kroll-Hess transformation³¹ up to the second order within the perturbation theory framework. The ANO-RCC basis set of TZ quality is used for all atoms. The active space of 8 orbitals (three $2p$ and five $3d$ orbitals of transition metals) gave a good approximation for the core-excited states of ionic complexes³² and is used for all species. Full-CI has been done for the $3d$ subspace (RAS2), while only one hole has been allowed for the $2p$ subspace (RAS1). The RAS3 subspace has been left empty, apart from TiCl_4 ; see Sec. III A. Quantities needed for propagation are obtained from the `h5` output file from the `OpenMolcas` Restricted Active Space State Interaction (RASSI) module. SOC matrix elements are computed by making use of Atomic Mean Field Integrals.³³ Propagation of the state multipoles according to Eq. (10) was performed by the Runge-Kutta method of the fourth order.

For simplicity, the incoming electric field has been chosen to be a single linearly polarized pulse with a temporal

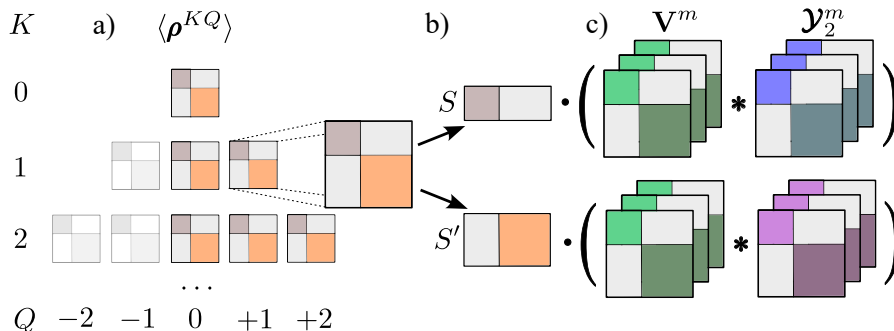


Figure 1. Computational scheme for evaluating SOC-dependent terms in the right-hand side of EOM employing matrix-matrix multiplication, Eq. (10). a) only part of elements of $\langle \rho^{KQ} \rangle$ is computed due to hermiticity; b) for every $K Q$, the state multipole (density) matrix is split into slabs with the same spin in rows; c) every slab is matrix-matrix (denoted as \cdot) multiplied with the Hadamar products (denoted as $*$) of V^m and respective Y_2^m .

Gaussian envelope

$$\mathcal{E}(t) = A \mathbf{e} \exp\left\{-\frac{(t - t_0)^2}{2\sigma^2}\right\} \sin(\Omega t), \quad (19)$$

where A , \mathbf{e} , t_0 , and Ω are the amplitude, polarization, center of the envelope, and carrier frequency. In all cases, the pulse envelope is centered at $t_0 = 0.5$ fs and has $\sigma = 0.125$ fs. The pulse width σ has been chosen to cover a wide range of valence-core excitations; thus, it corresponds to the ultrashort pulse in the time domain. The carrier frequency Ω has been chosen for each case to be centered in the middle of the $L_{2,3}$ absorption edge in the frequency domain and to cover all bright transitions. Dynamics have been simulated in a time interval of 3 fs which is enough to see the main features and is slightly smaller than the typical $2p$ core-hole lifetime.

III. RESULTS AND DISCUSSION

We consider three cases from simplest to more complicated. In the TiCl_4 molecule, one has a small number of participating singlet ($S = 0$) and triplet ($S = 1$) states. Although this case is quite instructive in understanding the internal symmetries of the state multipoles (ρ^{kq}) and their physical meaning, it does not exhaust other, more interesting situations. $[\text{Fe}(\text{H}_2\text{O})_6]^{2+}$ is a high spin complex with the quintet ($S = 2$) ground state, where we have considered the coupling of the quintet manifold to the triplet ($S = 1$) one. $[\text{Cr}(\text{H}_2\text{O})_6]^{3+}$ is a further example where the coupling of three different manifolds – initially populated quartet ($S = 3/2$) to doublet ($S = 1/2$) and sextet ($S = 5/2$) – is regarded. These two cases are more illustrative when it deals with truncating ranks and projections of spherical tensors due to a much larger number of participating states than in the case of TiCl_4 .

Further, we will distinguish two initial conditions representing: i) equal population of $\pm M$ components for a given M , e.g., according to Boltzmann equilibrium distribution at finite temperature $T=273$ K; ii) asymmetric

populations, e.g., when a single component (either $+M$ or $-M$) is populated, whereas the other is not. The latter case corresponds to breaking the time-reversal symmetry, e.g., due to external magnetic fields or 'spin filtering' with some kind of Stern-Gerlach experiment. It should be stressed that we populate an initial density matrix in the state basis and only then perform the expansion of it into a series of state multipoles (ρ^{kq}) according to Eq. (4).

Below, we restrict ourselves to analyzing solely the diagonal elements of the density matrix in the spherical tensor basis. These elements are directly connected to state populations and coherences between them, see Appendix B. Absolute values of diagonal elements are summed over diagonal subblocks ($\sum_a |\langle \rho_{aS,aS}^{kq} \rangle|$) with a certain multiplicity. They are denoted as X^{kq} , where X stands for Q (quintets), T (triplets), S (singlets) for integer spins and S (sextets), Q (quartets), and D (doublets) for half-integer spins.

A. Highly coherent case: TiCl_4 system

For the RASSCF calculations of TiCl_4 , three $2p$ orbitals of titanium make up the RAS1 subspace, and five $3d$ orbitals make up the RAS3 subspace, while RAS2 is left empty. For RAS1, one hole is allowed, and for RAS3, one excited electron is allowed that corresponds to a single core excitation to the empty $3d$ orbitals. Thus, the setup is equivalent to the CI-Singlets level of theory. With such a setup, 16 singlet and 15 triplet states are obtained, leading to 31 spin-free and 61 basis spin states. The pulse that triggers the spin dynamics has the form of Eq. (19), with parameters $A = 1.5$ a.u. and $\Omega = 461$ eV. It is chosen to be centered in the middle of the $L_{2,3}$ absorption edge in the frequency domain and to cover all states (see Fig. 2). The full density matrix for the TiCl_4 molecule was propagated both according to Eq. (10), where each matrix $\langle \rho^{kq} \rangle$ has the dimensions of 31×31 SF states, as

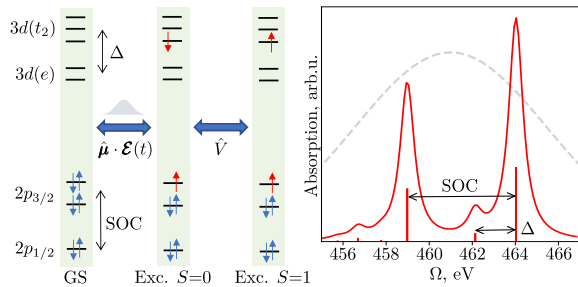


Figure 2. (Left) Schematic depiction of the participating states for the TiCl₄ system and the couplings between these states due to external field and SOC; (Right) X-ray absorption spectrum, red line, and the envelope of the Fourier transformed pulse, dashed gray line. In the MO active space, the orbitals that are depicted close together are degenerate; Δ corresponds to the orbital ligand-field splitting (left).

well as using the conventional approach of LvN Eq. (1) in the basis of 61 spin states.

The X-ray absorption spectrum of TiCl₄ is displayed in Fig. 2, and the principal scheme demonstrates the electronic structure of involved states. The spectrum represents the two groups of bands corresponding to 2p_{3/2} and 2p_{1/2} hole states split by strong SOC. There is also a smaller splitting Δ due to the tetrahedral field of the Cl atoms. The pulse is broad enough to populate all the bright states. In the SF picture, these are two bright singlet core-excited states having a multiconfigurational character and consisting of singly-excited configurations $(2p)^{-1}(t_2)^1$ and $(2p)^{-1}(e)^1$. By t_2 and e , we denote manifolds of virtual valence orbitals of mainly Ti 3d character. The intensity of the peak with a primary t_2 contribution is much higher than the other one with a primary e contribution.^{34,35} The pulse characteristics are chosen to deplete the ground state within the pulse duration almost completely. SOC couples the initially excited singlet states to a handful of triplet states, whereas almost two-thirds of triplet states do not participate in the dynamics, see the analysis in Ref.¹⁴ for a similar system. This coupling drives the transition of the population from singlet to triplet manifolds leading to quantum beating similar to Rabi oscillations, Fig. 3. Due to the relatively small number of participating states, these oscillations correspond to an almost complete population transfer between manifolds. For the same reason, these oscillations do not decay, and the dynamics remain in a highly coherent regime, see discussion in Sec. III B.

Fig. 3 compares the collective population of singlet and triplet states computed in the basis of 61 spin states (red and green dots) with the evolution of different state multipoles. S^{00} and T^{00} correspond to the sums of diagonal elements of the singlet-singlet and triplet-triplet blocks of $\langle \rho^{00} \rangle$; when scaled with the square root of multiplicity, T^{00} is equivalent to the overall population of the triplet manifold in a state basis. The period of the oscillation

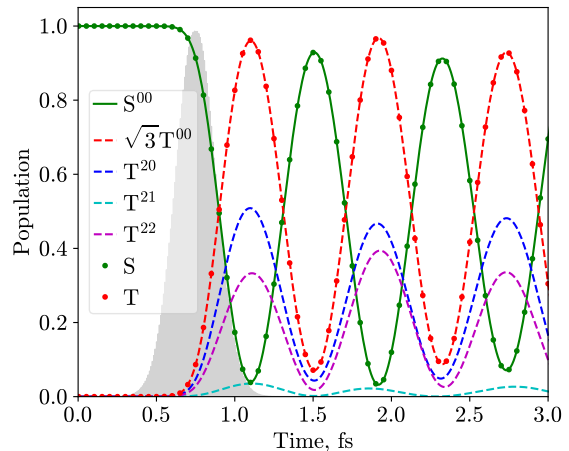


Figure 3. TiCl₄: The evolution of the summed diagonal elements ($\sum_a |\langle \rho_{aS,aS}^{kq} \rangle|$ for a given spin S) of state multipoles according to Eq. (10) (lines) and populations in the spin-state basis from the conventional dynamics (points). Singlet (S) states are denoted with solid line, while triplets (T) – with dashed lines. T^{00} is scaled with $\sqrt{3}$ to obtain populations, see Eq. (B2).

between the singlet and triplet states is roughly 0.82 fs, which corresponds to an energy of 5.04 eV that is in accord with the SOC splitting between 2p_{1/2} and 2p_{3/2} hole states of 5.05 eV, Fig. 2. The results in the basis of spherical tensors and states coincide, which serves as an essential internal consistency check.

For singlet states, the S^{kq} are strictly zero for $k > 0$. For the triplet-triplet block, higher ranks are also possible. However, the evolution of $\langle \rho^{1q} \rangle$ is not shown in Fig. 3, as these state multipoles always stay zero, even for triplet states. The $q = 0$ component for $k = 1$ characterizes the asymmetry in the population of M and $-M$ states, i.e., the system's polarization which stays zero because of the time-reversal symmetry (no magnetic interactions) and initial conditions. Respectively, the diagonal elements of the $q = \pm 1$ projections, characterizing the coherences between M and $M \pm 1$ projections of the same basis state, stay strictly zero, see Eq. B4. The diagonal $\langle \rho^{22} \rangle$ describes coherences between states with $\Delta M = \pm 2$, i.e., $M = 1$ and $M = -1$, where the direct transition is not possible. Nevertheless, they can be simultaneously populated or depopulated, mediated by the intermediate singlet state with $M = 0$. The $\langle \rho^{21} \rangle$ corresponds to a similar process but reflects the coherence between $M = \pm 1$ and $M = 0$, mediated by some other state. Note that in contrast to $\langle \rho^{11} \rangle$, $\langle \rho^{21} \rangle$ does not break the time-reversal symmetry. The off-diagonal elements correspond to coherences and are not easy to analyze. Since we are interested in the population dynamics, they will not be further discussed.

In general, the applicability of the method has been

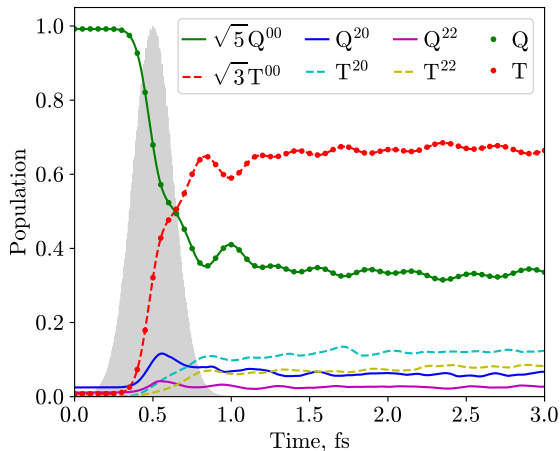


Figure 4. $[\text{Fe}(\text{H}_2\text{O})_6]^{2+}$: The evolution of summed diagonal elements of state multipoles (solid and dashed lines) and diagonal elements of the density matrix in the spin-state basis (dots). The initial populations are according to equilibrium distribution at $T = 273$ K. State multipoles with $k > 2$ are not shown because of their smallness. To estimate the magnitude of their contributions, see Fig. 6(a).

tested for TiCl_4 . The flexibility of the density matrix approach allows one to describe this highly coherent case exhibiting distinct quantum beatings. However, in this case, the reduced dynamical description with limited highest ranks and projections is impossible as discussed further in Sec. III C. Below we consider less coherent cases where the larger number of involved states, serving as the discrete electronic “reservoir”, leads to the (reversible) phase relaxation.

B. Less coherent cases: $[\text{Fe}(\text{H}_2\text{O})_6]^{2+}$ and $[\text{Cr}(\text{H}_2\text{O})_6]^{3+}$

Next, we consider two less coherent cases – spin dynamics in hexaaqua Fe^{2+} and Cr^{3+} complexes. $[\text{Fe}(\text{H}_2\text{O})_6]^{2+}$ has a d^6 electronic configuration and a high-spin quintet ($S = 2$) ground state. The full SF basis in the $2p3d$ active space, see Sec. II D, constitutes 35 quintet and 195 triplet states. Upon account for the spin part, a natural state basis consists of 760 states. The maximum rank of the state multipoles $k_{\text{max}} = 4$ is required to represent the quintet–quintet block of the density matrix exactly and to reproduce the dynamics in the state basis. The evolution of populations in the spin-state basis and diagonal state multipoles for quintets (Q) and triplets (T) is depicted in Fig. 4 with points and lines, respectively. Pulse characteristics used in this case are $A = 6$ a.u. and $\Omega = 712$ eV; see Eq. (19).

The other system, $[\text{Cr}(\text{H}_2\text{O})_6]^{3+}$, has a richer electronic structure regarding the number of participating states and different multiplicities. In the $2p3d$ active

space, one has in total 15 sextet, 160 quartet (including the ground state), and 325 doublet SF states giving rise to 90, 640, and 650 spin states, respectively. Thus, the dimensions of the SF and spin bases are 500 and 1380. Pulse characteristics used for the $[\text{Cr}(\text{H}_2\text{O})_6]^{3+}$ complex in Eq. (19) are $A = 2.5$ a.u. and $\Omega = 588$ eV. The population of state multipoles can be inferred from Fig. 5.

Again, as for TiCl_4 , approximately only half of the total number of states are notably participating in dynamics for both $[\text{Fe}(\text{H}_2\text{O})_6]^{2+}$ and $[\text{Cr}(\text{H}_2\text{O})_6]^{3+}$ complexes, but in the latter cases, their number is at least an order of magnitude larger than for TiCl_4 . This fact determines the different character of dynamics: on the one hand, one also sees a fast rise of the populations of the flipped-spin states, e.g., triplets in the case of $[\text{Fe}(\text{H}_2\text{O})_6]^{2+}$, see Fig. 4. On the other hand, oscillations are less prominent and generally tend to decay about 1 fs after the pulse. One can consider it an “equilibration” in a discrete quasi-reservoir of electronic states. However, this dephasing is reversible, and a rephasing should happen later as the system is closed.

It is not easy to quantify the degree of coherence for the considered cases. As some conditional quantification, we have computed the Shannon entropy, mean (averaged over all $N(N-1)/2$ elements) time-averaged absolute value of the off-diagonal elements of the density matrix (analog of the $\|\rho\|_1$ norm), and maximum absolute off-diagonal element (analog of the $\|\rho\|_\infty$ norm). For TiCl_4 , the entropy stays around 0 during the propagation, the mean off-diagonal element is around $3 \cdot 10^{-3}$, and the maximum off-diagonal element is 0.3. In contrast, for $[\text{Fe}(\text{H}_2\text{O})_6]^{2+}$ assuming thermal population, the entropy is around 1.75, the mean coherence is an order of magnitude smaller around $2.5 \cdot 10^{-4}$, as the maximum coherence is 0.05. These diagnostics show that the case of $[\text{Fe}(\text{H}_2\text{O})_6]^{2+}$ is much less coherent than TiCl_4 . The reasons are the initial incoherent population of states according to Boltzmann distribution and the larger number of participating states acting as quasi-reservoir.

Illustrative is the participation of different state multipoles in the dynamics. It is analyzed here for the diagonal contributions summed over different diagonal subblocks of the density matrix, see, e.g., Figs. 4 and 5 for the time evolution and Figs. 6(a) and 7 for the decomposition of the initial density matrix and the contributions averaged over the full simulation time for $[\text{Fe}(\text{H}_2\text{O})_6]^{2+}$ and $[\text{Cr}(\text{H}_2\text{O})_6]^{3+}$. The first thing to notice is that for the equilibrium population of the initial states, a relatively small number of kq components contribute. For instance, in Fig. 4, only contributions substantially different from zero are plotted, namely, $k = 0$ and $k = 2$ with even projections $q = 0, 2$ for both quintet and triplet states. Others are either strictly zero or rather small. Fig. 6(a) further illustrates this observation. One sees that the decomposition of the initial density matrix according to Eq. (4) (light green bar) involves only $\langle \rho^{00} \rangle$ multipoles. In the course of dynamics, the system is in a superposition of triplet (red) and quintet (green) excited

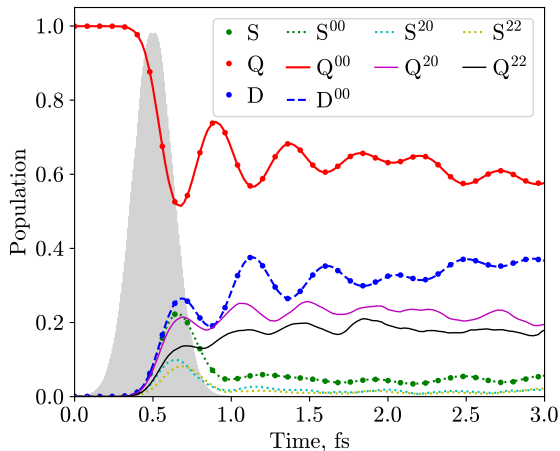


Figure 5. $[\text{Cr}(\text{H}_2\text{O})_6]^{3+}$: Evolution of diagonal elements of the state multipoles for the initial equilibrium distribution at $T = 273$ K of the initial density matrix. Quartet (Q) states are denoted with solid lines, while doublets (D) – with dashed lines, and sextets (S) with dotted lines. The results of the propagation in the state basis are displayed with points. State multipoles with $k > 2$ are not shown.

states with a population ratio of about 3:2.

A similar situation is observed for $[\text{Cr}(\text{H}_2\text{O})_6]^{3+}$, Fig. 7. The importance of higher ranks quickly decreases, with doublets being restricted only to the first rank, quartets to the third rank, and sextets going to the highest fifth rank.

To conclude on these cases, the uniform distribution of the initial population is followed by consecutive “uniform” dynamics, mainly involving the low-rank state multipoles. The analysis of diagonal contributions for less coherent cases shows that one can cut not only the ranks but their components as well. This builds a basis for reduced propagation, see Sec. III C.

To explore the situation when the initial population of $\pm M$ -microstates is uneven, e.g., due to interaction with the magnetic field, we populate only a single ground-state M -component. It has to be noted that the overall dynamics in the state basis for equilibrium and non-equilibrium initial conditions are almost identical, as was shown in our previous work.¹⁴ However, one can discern variations in the evolution of spin-state components with distinct spin projections by analysis of state multipoles. From this viewpoint, the non-equilibrium initial condition leads to a different scenario. The situation is notably more coherent as the entropy stays around 0 during the propagation, the mean coherence is around $3.5 \cdot 10^{-4}$, and the maximum coherence is 0.25, comparable to that of TiCl_4 . It can be rationalized by a smaller number of initially excited states because the coupling to the electromagnetic field conserves M , Eq. 7. The mean contributions of the state multipoles are shown in Fig. 6(b).

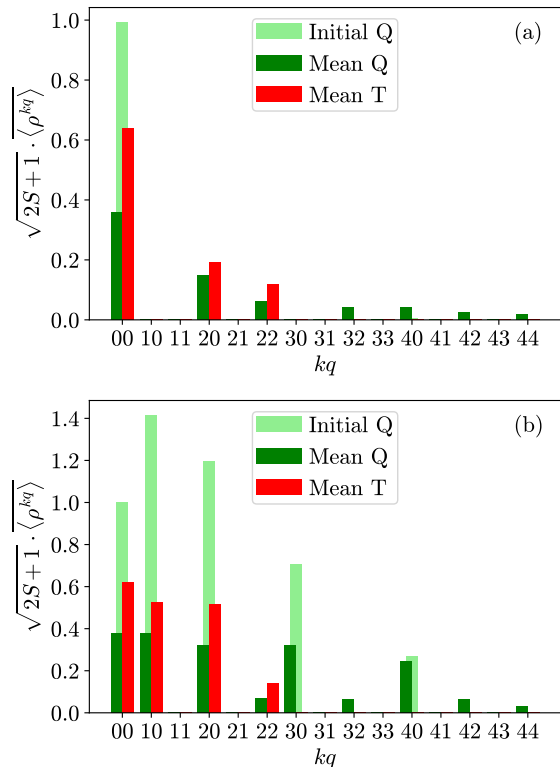


Figure 6. $[\text{Fe}(\text{H}_2\text{O})_6]^{2+}$: Mean contributions (i.e., absolute values of diagonal elements summed according to spin multiplicity and averaged over time) of state multipoles to the density matrix. Averaging over time is performed from the center of the pulse till the endpoint at 3 fs. The initial density matrix (a) is populated according to equilibrium distribution at $T = 273$ K; (b) includes a total population in a single M component of the ground state. The decomposition of ρ values at $t = 0$ fs is denoted with light-green bars. All values are scaled with the factor $\sqrt{2S+1}$ such that 00 contributions correspond to populations.

The initial population distribution, which is asymmetric for different M -projections, involves all ranks of the quintet subblocks, $\langle \rho^{k0} \rangle$ (light green bars). This leads to more diverse population redistribution between different ranks during the dynamics. For instance, contributions from the $\langle \rho^{10} \rangle$ and $\langle \rho^{30} \rangle$ multipoles become non-zero, evidencing a significant degree of asymmetry between M and $-M$ states. In other words, such non-equilibrium initial conditions offer fewer possibilities for rank and projection truncation, as discussed in Sec. III C, since higher ranks and projection play a more critical role.

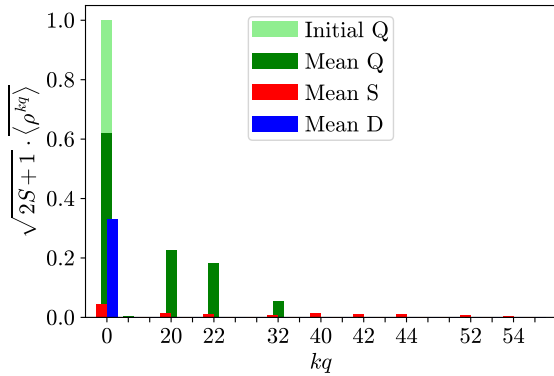


Figure 7. $[\text{Cr}(\text{H}_2\text{O})_6]^{3+}$: Mean contributions of the state multipoles to the density matrix for the equilibrium initial population at $T = 273$ K. See also the caption to Fig. 6.

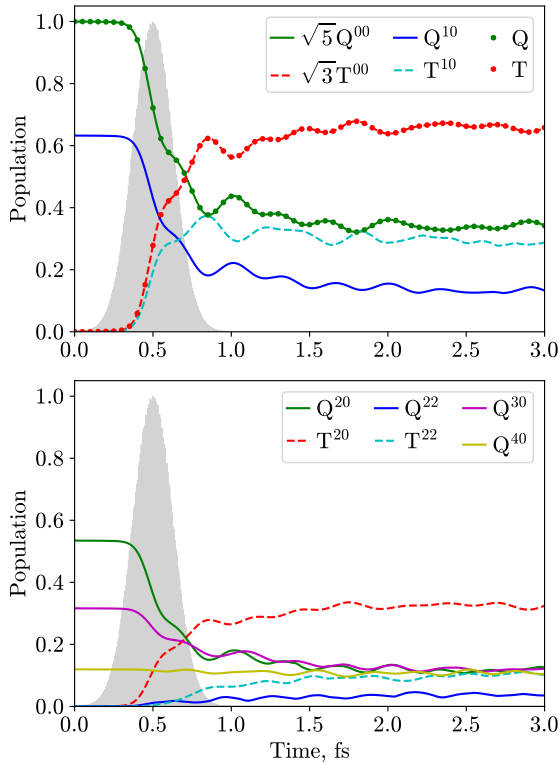


Figure 8. $[\text{Fe}(\text{H}_2\text{O})_6]^{2+}$: Evolution of diagonal elements of state multipoles and the populations obtained by performing dynamics in the state basis (dots); see also caption to Fig. 4. Only a single M -component of the ground state is initially populated. The non-zero components Q^{32} , Q^{42} , and Q^{44} are not shown; their magnitude can be estimated from Fig. 6(b).

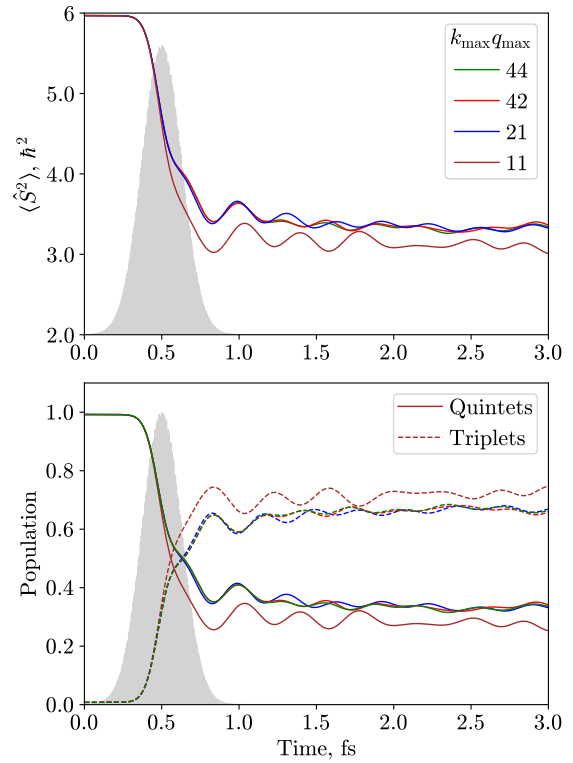


Figure 9. $[\text{Fe}(\text{H}_2\text{O})_6]^{2+}$: Evolution of $\langle \hat{S}^2 \rangle$ (upper panel) and populations (lower panel) for the full $k_{\text{max}} q_{\text{max}} = 44$, and truncated propagation. Quintet states' population is denoted with solid lines, while triplet – with dashed lines. The initial population corresponds to $T = 273$ K.

C. Reduced Propagation

This section discusses the results of truncating the state multipole expansion at certain k and q below maximum. We will call the respective dynamics “reduced”. Nevertheless, it is obtained using the full equation, Eq. (10), but not the reduced one, Eq. (15), as the latter is not closed. The reduced EOM is used only to guide the truncation. The truncation is performed simply by setting all multipoles for k and q larger than the threshold value to zero and constraining the sum over K and Q in Eq. (10). The results of the reduced propagation are displayed in Figs. 9 and 10 of $[\text{Fe}(\text{H}_2\text{O})_6]^{2+}$ and $[\text{Cr}(\text{H}_2\text{O})_6]^{3+}$, respectively. From these figures, one can also infer the time-dependent expectation value of the spin-squared operator $\langle \hat{S}^2 \rangle$.

First, we note that the projections for $k > 0$ should include at least ± 1 , which follows from the reduced EOM, Eq. 15. Indeed, although the dynamics including only $\langle \rho^{k0} \rangle$ (not shown) also predicts spin flip, they substantially differ from the exact. There must be more than just

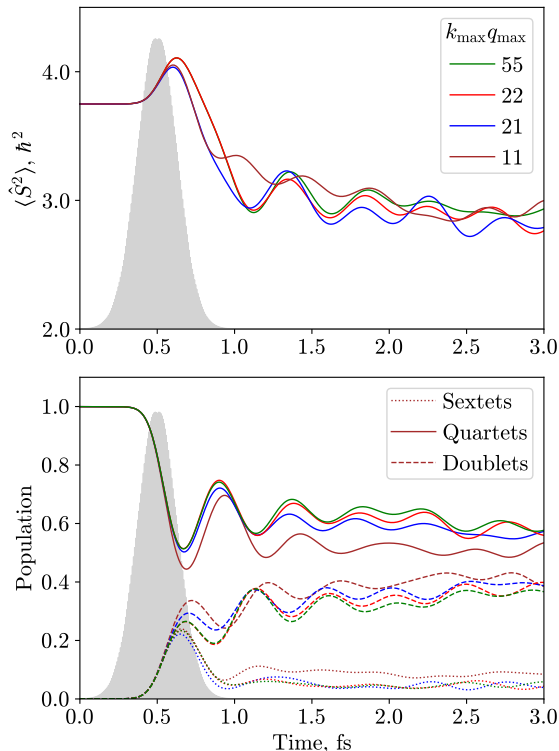


Figure 10. $[\text{Cr}(\text{H}_2\text{O})_6]^{3+}$: Evolution of $\langle \hat{S}^2 \rangle$ (upper panel) and populations (lower panel) for the full $k_{\max} q_{\max} = 55$, and truncated propagation. The initial population corresponds to $T = 273\text{ K}$.

$k = 1$ terms, as $k = 2$ also notably contributes. The truncation at $k = 2$ and $q = 1$ is sufficient to reproduce the dynamics semiquantitatively. Although from Figs. 6(a) and 7, it seems logical to cut at $kq = 20$ or at 22 both for $[\text{Fe}(\text{H}_2\text{O})_6]^{2+}$ and $[\text{Cr}(\text{H}_2\text{O})_6]^{3+}$, one should keep in mind that shown are only the diagonal elements that do not account for essential coherences. The latter are sufficiently represented by the $\langle \rho^{11} \rangle$ and $\langle \rho^{21} \rangle$ multipoles. The $[\text{Cr}(\text{H}_2\text{O})_6]^{3+}$ case is especially illustrative regarding truncation since the higher ranks up to $k = 5$ seem formally important. They correspond to a relatively small number of sextet states and can be neglected, leading to substantial savings in the effort.

Importantly, this truncation is most prominent for less coherent cases. E.g., in $[\text{Fe}(\text{H}_2\text{O})_6]^{2+}$ with non-equilibrium initial population, the ranks cannot be truncated. Only minor savings in computational time can be achieved by excluding some projections for higher ranks. Further, the reduction is impossible for the highly coherent example of the TiCl_4 molecule, as the truncation at $k = 2, q = 1$ produces wrong results (not shown). The $\langle \rho^{22} \rangle$ component describes critical coherent pathways governing the population redistribution that cannot

be neglected.

The observation of the decisive role of coherence and a typical truncation at $kq = 21$ can be rationalized as follows: The entirely incoherent dynamics can be represented solely by the $\langle \rho^{00} \rangle$ as it governs the diagonal of the density matrix, and off-diagonal elements are zeros. With increasing coherence, higher ranks set in to resolve the increasing role of the off-diagonal elements, see Appendix B. By construction, the SOC operator \hat{V} couples states with magnetic numbers M and $M \pm 1$ owing to $m = 0, \pm 1$ in Eq. (2). Thus, apart from diagonal $\langle \rho^{00} \rangle$, the $\langle \rho^{k1} \rangle$ multipoles are most important, as indicated by the reduced EOM, Eq. (15). In turn, higher ranks are responsible for the redistribution of populations between states in the high-spin-high-spin block of the density matrix. If only the total population of the respective manifold is of interest, these ranks can be truncated. From our simulations, we infer that the more states participate in such kind of dynamics and the more “equilibrated” and uniform it is, the easier it can be represented in terms of mean and lower distribution moments, which correspond to lower-rank state multipoles.

We emphasize that the truncation is especially important when myriads of SF basis states have to be included without knowing whether they will be essentially populated or not. The initial prescreening based on the SF energies and dipole and SOC coupling matrix elements can be employed to lower the computational cost by excluding a notable portion of states prior to propagation; see our previous work.¹⁵ The reason is that one uses correlated many-body states to reduce the need to resolve correlation during propagation. The analysis of the present study indicates that one can additionally use angular momentum symmetries to reduce the amount of dynamical information and effort. However, such a reduction becomes prominent only when many high-spin states are involved. In this case, a single large problem of the $N_{\text{spin}} \times N_{\text{spin}}$ size is recast into a smaller $N_{\text{SF}} \times N_{\text{SF}}$ problem for every combination of k and q .

IV. CONCLUSIONS

In this work, the SOC-driven dynamics in different core-excited transition metal complexes have been recast from the state basis to the basis of irreducible spherical tensors. Further, the WE theorem has been used to separate the degrees of freedom into the dynamical part of the interest and the geometrical part that is irrelevant when only total populations of spin states are considered. Although the direct reduction of information does not lead to closed equations, they can be used for the physically inspired truncation of the maximal ranks and projections in the full EOM.

The efficiency of this reduction depends on the coherence degree of the problem and, thus, depends on the system, its initial state, and preparation conditions, i.e., the state prior to interaction with an electromagnetic field

and the details of such interaction. For the highly coherent cases, as the TiCl_4 system considered here, no substantial saving in the computational effort can be expected. When a large number of participating states leads to lower coherence due to quasi-equilibration in the electronic reservoir, this reduction is substantial, and the full dynamics can be rather closely reproduced with a relatively low rank and projection threshold. For instance, for the $[\text{Fe}(\text{H}_2\text{O})_6]^{2+}$ and $[\text{Cr}(\text{H}_2\text{O})_6]^{3+}$ systems, the combination of $k_{\max} = 2$ and $q_{\max} = 1$ produces reasonable results – the limits which are notably lower than the values needed to reproduce the dynamics exactly. These limits can be rationalized by considering the physics of the problem and the details of the SOC operator. Since the transformation of the EOM from the state basis to the basis of spherical tensors replaces a single large problem with a series of smaller problems, the efficiency of the truncated propagation should stand out for a large number of basis states of high multiplicity.

Appendix A: Derivation of the particular terms in the EOM

The density operator can be transformed from the state basis $|aSM\rangle$ to the basis of purely SF functions $|aS\rangle$ for the spatial part and irreducible spherical tensors \hat{T}_Q^K for the spin part

$$\begin{aligned} \hat{\rho} &= \sum_{\substack{aS, bS' \\ M, M'}} \langle aS | \hat{\pi} | bS' \rangle \langle SM | \hat{\sigma} | S'M' \rangle |aS\rangle \langle bS'| \otimes |SM\rangle \langle S'M'| \\ &= \sum_{aS, bS'} \sum_{KQ} \langle \rho_{aS, bS'}^{KQ} \rangle |aS\rangle \langle bS'| \otimes \hat{T}_Q^K(S, S'), \end{aligned}$$

where

$$\begin{aligned} \langle \rho_{aS, bS'}^{KQ} \rangle &= \sum_{MM'} \langle aS | \hat{\pi} | bS' \rangle \langle SM | \hat{\sigma} | S'M' \rangle \times \\ &\quad \times (-1)^{S-M} \sqrt{2K+1} \begin{pmatrix} S & S' & K \\ M & -M' & -Q \end{pmatrix} \end{aligned}$$

is the (time-dependent) expansion coefficient – state multipole. To derive the EOM for these coefficients, we project different terms in LvN Eq. (1) onto the basis operator $\hat{1} \otimes \hat{T}_q^{k\dagger}(S, S')$ by taking the trace over the spin part $\text{Tr}\{\dots\} = \sum_M \dots$. For instance, for the density operator itself

$$\begin{aligned} \text{Tr}\{\hat{1} \otimes \hat{T}_q^{k\dagger}(S, S')\hat{\rho}\} &= \\ \text{Tr}\left\{ \sum_{aS, bS'} \sum_{KQ} \langle \rho_{aS, bS'}^{KQ} \rangle |aS\rangle \langle bS'| \otimes \hat{T}_q^{k\dagger}(S, S') \hat{T}_Q^K(S, S') \right\} &= \\ \sum_{aS, bS'} \langle \rho_{aS, bS'}^{kq} \rangle \{S k S'\} |aS\rangle \langle bS'|, & \end{aligned}$$

where $\{S k S'\}$ is the triangular delta – angular momentum coupling selection rule. To arrive at this result, we have used¹⁸

$$\text{Tr}\{\hat{1} \otimes \hat{T}_q^{k\dagger}(S, S') \hat{T}_Q^K(S, S')\} = \delta_{kK} \delta_{qQ} \{S k S'\}.$$

An SF element of the projected density matrix then reads

$$\langle cS_c | \text{Tr}\{(\hat{1} \otimes \hat{T}_q^{k\dagger}(S, S'))\hat{\rho}\} |dS_d\rangle = \langle \rho_{cS_c, dS_d}^{kq} \rangle \{S_c k S_d\}.$$

The same expression can be used for its time derivative.

Further,

$$\begin{aligned} \hat{H}_{\text{CI}} &= \sum_{\substack{cS_c, dS_d \\ M_c, M_d}} \langle cS_c | \hat{H}_{\text{CI}}^{\text{SF}} |dS_d\rangle \langle S_c M_c | S_d M_d \rangle \times \\ &\quad \times |cS_c\rangle \langle dS_d| \otimes |S_c M_c\rangle \langle S_d M_d| \\ &= \sum_{cS_c} E_c^{\text{SF}} |cS_c\rangle \langle cS_c| \otimes \hat{1}, \end{aligned}$$

where we employed the closure $\sum_{M_c} |S_c M_c\rangle \langle S_c M_c| = \hat{1}$. Below we omit the (S, S') dependence at spherical tensors for brevity since the considered block of the density matrix uniquely determines it. Then,

$$\begin{aligned} \text{Tr}\{(\hat{1} \otimes \hat{T}_q^{k\dagger}) \hat{H}_{\text{CI}} \hat{\rho}\} &= \\ \sum_{cS_c, eS_e} E_c^{\text{SF}} \langle \rho_{cS_c, eS_e}^{kq} \rangle \{S_c k S_e\} |cS_c\rangle \langle eS_e| \end{aligned}$$

and the SF matrix element of the first term in the commutator on the r.h.s. of Eq. (1) reads

$$\langle aS | \text{Tr}\{(\hat{1} \otimes \hat{T}_q^{k\dagger}) \hat{H}_{\text{CI}} \hat{\rho}\} |bS'\rangle = E_a^{\text{SF}} \langle \rho_{aS, bS'}^{kq} \rangle \{S k S'\}.$$

Next, for the dipole moment term, fully analogously, we obtain

$$\begin{aligned} \hat{\mu} &= \sum_{cS_c, dS_d} \boldsymbol{\mu}_{cd}^{\text{SF}} |cS_c\rangle \langle dS_d| \otimes \hat{1} \\ \langle aS | \text{Tr}\{(\hat{1} \otimes \hat{T}_q^{k\dagger}) \hat{\mu} \hat{\rho}\} |bS'\rangle &= \sum_{cS_c} \boldsymbol{\mu}_{ac}^{\text{SF}} \langle \rho_{cS_c, bS'}^{kq} \rangle \{S_c k S'\} \end{aligned}$$

Finally, for the SOC term,

$$\begin{aligned}
 \hat{V} &= \sum_m (-1)^m \sum_{cS_c, dS_d} \langle cS_c | \hat{L}_{-m}^1 | dS_d \rangle \langle S_c M_c | \hat{S}_m^1 | S_d M_d \rangle | cS_c \rangle \langle dS_d | \otimes | S_c M_c \rangle \langle S_d M_d | = \\
 &= \sqrt{3} \sum_m (-1)^{S_c - M_c + m} \begin{pmatrix} S_c & 1 & S_d \\ -M_c & m & M_d \end{pmatrix} \langle cS_c | \hat{L}_{-m}^1 | dS_d \rangle \langle S_c | \hat{S}^1 | S_d \rangle | cS_c \rangle \langle dS_d | \otimes \\
 &\otimes \sum_{KQ} \sum_{M_c M_d} (-1)^{S_c - M_c} \sqrt{2K+1} \begin{pmatrix} S_c & S_d & K \\ M_c & -M_d & -Q \end{pmatrix} \hat{T}_Q^K(S_c, S_d) = \\
 &= \sum_{KQ} \sum_{cS_c, dS_d} \sum_{M_c, M_d} (-1)^m \sqrt{3(2K+1)} \begin{pmatrix} S_c & 1 & S_d \\ -M_c & m & M_d \end{pmatrix} \begin{pmatrix} S_c & S_d & K \\ M_c & -M_d & -Q \end{pmatrix} V_{cS_c, dS_d}^m | cS_c \rangle \langle dS_d | \otimes \hat{T}_Q^K(S_c, S_d).
 \end{aligned}$$

Here, we have used the definition of the semi-reduced SOC matrix element from Eq. (9). When inserting it into $\text{Tr}\{(\hat{1} \otimes \hat{T}_q^{k\dagger}) \hat{V} \hat{\rho}\}$, one obtains a product of three spherical tensors

$$\begin{aligned}
 \text{Tr}\{(\hat{1} \otimes \hat{T}_q^{k\dagger}) \hat{V} \hat{\rho}\} &= \\
 &= \text{Tr} \left\{ \sum_{KQK'Q'} \sum_{cS_c, dS_d, eS_e} \sum_{M_c, M_d} (-1)^m \sqrt{3(2K+1)} \begin{pmatrix} S_c & 1 & S_d \\ -M_c & m & M_d \end{pmatrix} \begin{pmatrix} S_c & S_d & K \\ M_c & -M_d & -Q \end{pmatrix} V_{cS_c, dS_d}^m \langle \rho_{dS_d, eS_e}^{K'Q'} \rangle | cS_c \rangle \langle eS_e | \otimes \right. \\
 &\left. \otimes \hat{T}_q^{k\dagger}(S_c, S_e) \hat{T}_Q^K(S_c, S_d) \hat{T}_{Q'}^{K'}(S_d, S_e) \right\}
 \end{aligned}$$

To tackle them, we apply the product rule for spherical tensors³⁶

$$\begin{aligned}
 \hat{T}_Q^K(S_c, S_d) \hat{T}_{Q'}^{K'}(S_d, S_e) &= \\
 &= \sum_{\mathcal{K}Q} (-1)^{S_c + S_f + \mathcal{K} - K + K' - Q} \sqrt{(2K+1)(2K'+1)(2\mathcal{K}+1)} \begin{pmatrix} K & K' & \mathcal{K} \\ Q & Q' & -Q \end{pmatrix} \begin{Bmatrix} K & K' & \mathcal{K} \\ S_c & S_e & S_d \end{Bmatrix} \hat{T}_{\mathcal{Q}}^{\mathcal{K}}(S_c, S_e).
 \end{aligned}$$

Thus, $\text{Tr}\{\hat{T}_q^{k\dagger}(S_c, S_e) \hat{T}_{\mathcal{Q}}^{\mathcal{K}}(S_c, S_e)\} = \delta_{k\mathcal{K}} \delta_{q\mathcal{Q}} \{S_c k S_e\}$. In addition, we apply the orthogonality rule for the Wigner 3j symbols

$$\sum_{M_c M_d} (2K+1) \begin{pmatrix} S_c & 1 & S_d \\ -M_c & m & M_d \end{pmatrix} \begin{pmatrix} S_c & S_d & K \\ M_c & -M_d & -Q \end{pmatrix} = \delta_{K1} \delta_{Qm} \{S_c S_d K\}$$

As a result, one gets

$$\begin{aligned}
 \langle aS | \text{Tr}\{\hat{1} \otimes \hat{T}_q^{k\dagger} \hat{V} \hat{\rho}\} | bS' \rangle &= \\
 &= \sum_m \sum_{dS_d} \sum_{K'Q'} V_{aS, dS_d}^m \langle \rho_{dS_d, bS'}^{K'Q'} \rangle (-1)^{S+S'-Q'} \sqrt{3(2k+1)(2K'+1)} \begin{pmatrix} K' & 1 & k \\ Q' & m & -q \end{pmatrix} \begin{Bmatrix} 1 & K' & k \\ S & S' & S_d \end{Bmatrix} \{S k S'\} \{S S_d 1\}
 \end{aligned}$$

In the derivation above, we also used permutational and time-reversal symmetries of 3j symbols and selection rules for the projections in these symbols, e.g., $m + Q' = q$. In addition, we utilized the fact that k , K' , and $S_c + S_d$ are integer numbers which allowed us to simplify the phase factor.

The same procedure can be followed for each operator for the second term in the respective commutators. We omit the derivation and refer to the result in Eqs. (10)-(13).

Appendix B: Meaning of different k and q

A physical meaning can be ascribed to state multipoles with different ranks and components,¹⁸ we give the most important examples for the discussion in the main text. An explicit expression for the state multipoles can be obtained from Eqs. (4) and (5):

$$\begin{aligned}
 \langle \rho_{aS, bS'}^{kq} \rangle &= \sum_{MM'} \rho_{aSM, bS'M'} \times \\
 &(-1)^{S-M'+q+2k} \sqrt{2k+1} \begin{pmatrix} S' & k & S \\ -M' & -q & M \end{pmatrix}. \quad (\text{B1})
 \end{aligned}$$

First, for the rank $k = 0$ for subblocks with $S = S'$, Eq. (B1) is simplified as follows

$$\langle \rho_{aS,bS}^{00} \rangle = \sum_M \rho_{aS M, bS' M'} \frac{1}{\sqrt{2S+1}}, \quad (\text{B2})$$

Thus, the diagonal element $\langle \rho_{aS,aS}^{00} \rangle$ describes the population in the spin-free state $|aS\rangle$ scaled with the factor $1/\sqrt{2S+1}$, while off-diagonal elements describe coherence between $|aS M\rangle$ and $|bS M\rangle$.

For $k = 1$ and $q = 0$ one obtains (note, that only $S > 0$ contributes for $k = 1$)

$$\begin{aligned} \langle \rho_{aS,bS}^{10} \rangle = \\ \sum_{M>0} (\rho_{aS M, bS M} - \rho_{aS(-M), bS(-M)}) \frac{M\sqrt{3}}{\sqrt{S(S+1)(2S+1)}}. \end{aligned} \quad (\text{B3})$$

Thus, $\langle \rho_{aS,aS}^{10} \rangle$ describes how large is the difference between the populations in the states $|aS M\rangle$ and $|aS(-M)\rangle$.

As all projections $q \neq 0$ depend only on the off-diagonal elements of the density matrix in the spin-state basis $|aS M\rangle$, they describe coherences between states, as also discussed in Ref. 18. For the rank $k = 1$, the projections $q = \pm 1$, given by

$$\begin{aligned} \langle \rho_{aS,bS}^{1\pm 1} \rangle = \\ \pm \sum_{M \leq \pm(S-1)} \rho_{aS M, bS(M \pm 1)} \sqrt{\frac{3(S \mp M)(S \pm M + 1)}{2S(S+1)(2S+1)}}, \end{aligned} \quad (\text{B4})$$

describe the coherence between $|aS M\rangle$ and $|bS(M \pm 1)\rangle$. Thus, $\langle \rho_{aS,aS}^{1\pm 1} \rangle$ describes coherences between $|aS M\rangle$ and $|aS(M \pm 1)\rangle$. As such direct transitions break time-reversal symmetry, the diagonal values of these multipoles are zero in our case. Eqs. (B3) and (B4) can be combined using spin ladder operators \hat{S}_{\pm} and defining $\hat{S}_0 = \hat{S}_z$ to obtain

$$\sum_{aS} \langle \rho_{aS,aS}^{1Q} \rangle = \sqrt{\frac{3}{S(S+1)(2S+1)}} \text{Tr}\{\hat{S}_Q \hat{\rho}\}, \quad (\text{B5})$$

strictly imposing $\sum_{aS} \langle \rho_{aS,aS}^{1Q} \rangle = 0$.

In the case of $k = 2$ with $q = 0$ (for simplicity in the following, we set $S = 1$ and only consider diagonal elements),

$$\langle \rho_{a1,a1}^{20} \rangle = - \sum_M \rho_{a1 M, a1 M} (2 - 3M^2) \frac{1}{\sqrt{6}}. \quad (\text{B6})$$

A positive value means that the $M = 1$ and $M = -1$, on average, have a higher population than the $M = 0$ projection, and for a negative value vice versa.

Moreover, the projections $q = \pm 1$ of the rank $k = 2$ compare the coherence between $|a10\rangle$ and $|a1(\pm 1)\rangle$ to the coherence between $|a1(\mp 1)\rangle$ and $|a10\rangle$

$$\langle \rho_{a1,a1}^{2\pm 1} \rangle = \frac{1}{\sqrt{2}} (\rho_{a10, a1(\pm 1)} - \rho_{a1(\mp 1), a10}). \quad (\text{B7})$$

In turn, $\langle \rho_{aS,bS}^{2\pm 2} \rangle$ describe the coherence between $|aS M\rangle$ and $|aS(M \pm 2)\rangle$

$$\langle \rho_{a1,a1}^{2\pm 2} \rangle = \rho_{a1(\mp 1), a1(\pm 1)}. \quad (\text{B8})$$

DATA AVAILABILITY STATEMENT

The data that support the findings of this study are available from the corresponding author upon reasonable request.

REFERENCES

- ¹M. A. Halcrow, ed., *Spin-Crossover Materials: Properties and Applications* (Wiley, Chichester, West Sussex, United Kingdom, 2013).
- ²T. Schultz and M. Vrakking, eds., *Attosecond and XUV Physics: Ultrafast Dynamics and Spectroscopy* (Wiley-VCH, Weinheim, 2014).
- ³L. Young, K. Ueda, M. Gühr, P. H. Bucksbaum, M. Simon, S. Mukamel, N. Rohringer, K. C. Prince, C. Masciovecchio, M. Meyer, A. Rudenko, D. Rolles, C. Bostedt, M. Fuchs, D. A. Reis, R. Santra, H. Kapteyn, M. Murnane, H. Ibrahim, F. Légaré, M. Vrakking, M. Isinger, D. Kroon, M. Gisselbrecht, A. L'Huillier, H. J. Wörner, and S. R. Leone, "Roadmap of ultrafast x-ray atomic and molecular physics," *J. Phys. B* **51**, 032003 (2018).
- ⁴A. Bande, "Developing electron dynamics into a tool for 21st century chemistry simulations," in *Chemical Modelling*, Vol. 17, edited by H. Bahmann and J. C. Tremblay (Royal Society of Chemistry, Cambridge, 2022) pp. 91–152.
- ⁵V. May and O. Kühn, *Charge and Energy Transfer Dynamics in Molecular Systems* (Wiley-VCH, Weinheim, 2011).
- ⁶H. J. Wörner, C. A. Arrell, N. Banerji, A. Cannizzo, M. Cherqui, A. K. Das, P. Hamm, U. Keller, P. M. Kraus, E. Liberatore, P. Lopez-Tarifa, M. Lucchini, M. Meuwly, C. Milne, J.-E. Moser, U. Rothlisberger, G. Smolentsev, J. Teuscher, J. A. van Bokhoven, and O. Wenger, "Charge migration and charge transfer in molecular systems," *Struct. Dyn.* **4**, 061508 (2017).
- ⁷A. I. Kuleff and L. S. Cederbaum, "Ultrafast correlation-driven electron dynamics," *J. Phys. B* **47**, 124002 (2014).
- ⁸M. Nisoli, P. Decleva, F. Calegari, A. Palacios, and F. Martín, "Attosecond Electron Dynamics in Molecules," *Chem. Rev.* **117**, 10760–10825 (2017).
- ⁹M. Hentschel, R. Kienberger, Ch. Spielmann, G. A. Reider, N. Milosevic, T. Brabec, P. Corkum, U. Heinzmann, M. Drescher, and F. Krausz, "Attosecond metrology," *Nature* **414**, 509–513 (2001).
- ¹⁰P. B. Corkum and F. Krausz, "Attosecond science," *Nat. Phys.* **3**, 381–387 (2007).
- ¹¹C. M. Marian, "Spin-orbit coupling and intersystem crossing in molecules," *WIREs Comput. Mol. Sci.* **2**, 187–203 (2012).
- ¹²S. Mai and L. González, "Unconventional two-step spin relaxation dynamics of $[\text{Re}(\text{CO})_3(\text{im})(\text{phen})]^+$ in aqueous solution," *Chem. Sci.* **10**, 10405–10411 (2019).
- ¹³Y. Jiang, L. C. Liu, A. Sarracini, K. M. Krawczyk, J. S. Wentzell, C. Lu, R. L. Field, S. F. Matar, W. Gawelda, H. M. Müller-Werkmeister, and R. J. D. Miller, "Direct observation of nuclear

- reorganization driven by ultrafast spin transitions,” *Nat. Commun.* **11**, 1530 (2020).
- ¹⁴V. Kochetov, H. Wang, and S. I. Bokarev, “Effect of chemical structure on the ultrafast spin dynamics in core-excited states,” *J. Chem. Phys.* **153**, 044304 (2020).
- ¹⁵V. Kochetov and S. I. Bokarev, “RhoDyn: A ρ -TD-RASCI Framework to Study Ultrafast Electron Dynamics in Molecules,” *J. Chem. Theory Comput.* **18**, 46–58 (2022).
- ¹⁶H. Wang, S. I. Bokarev, S. G. Aziz, and O. Kühn, “Ultrafast Spin-State Dynamics in Transition-Metal Complexes Triggered by Soft-X-Ray Light,” *Phys. Rev. Lett.* **118**, 023001 (2017).
- ¹⁷A. Rudenko, L. Inhester, K. Hanasaki, X. Li, S. J. Robatjazi, B. Erk, R. Boll, K. Toyota, Y. Hao, O. Vendrell, C. Bomme, E. Savelyev, B. Rudek, L. Foucar, S. H. Southworth, C. S. Lehmann, B. Kraessig, T. Marchenko, M. Simon, K. Ueda, K. R. Ferguson, M. Bucher, T. Gorkhover, S. Carron, R. Alonso-Mori, J. E. Koglin, J. Correa, G. J. Williams, S. Boutet, L. Young, C. Bostedt, S.-K. Son, R. Santra, and D. Rolles, “Femtosecond response of polyatomic molecules to ultra-intense hard X-rays,” *Nature* **546**, 129–132 (2017).
- ¹⁸K. Blum, *Density Matrix Theory and Applications*, Springer Series on Atomic, Optical, and Plasma Physics, Vol. 64 (Springer Berlin Heidelberg, Berlin, Heidelberg, 2012).
- ¹⁹U. Fano, “Geometrical Characterization of Nuclear States and the Theory of Angular Correlations,” *Phys. Rev.* **90**, 577–579 (1953).
- ²⁰R. Steffen and K. Alder, *Extranuclear Perturbations of Angular Distributions and Correlations* (North-Holland, Netherlands, 1975).
- ²¹K. Blum and H. Kleinpoppen, “Electron-photon angular correlation in atomic physics,” *Physics Reports* **52**, 203–261 (1979).
- ²²U. Fano and J. H. Macek, “Impact Excitation and Polarization of the Emitted Light,” *Rev. Mod. Phys.* **45**, 553–573 (1973).
- ²³A. Omont, “Irreducible components of the density matrix. Application to optical pumping,” *Prog. Quantum Electron.* **5**, 69–138 (1977).
- ²⁴I. V. Hertel and W. Stoll, “Collision Experiments with Laser Excited Atoms in Crossed Beams,” in *Advances in Atomic and Molecular Physics*, Vol. 13, edited by D. R. Bates and B. Bederson (Academic Press, 1978) pp. 113–228.
- ²⁵M. Givon, Y. Margalit, A. Waxman, T. David, D. Groswasser, Y. Japha, and R. Folman, “Magic Frequencies in Atom-Light Interaction for Precision Probing of the Density Matrix,” *Phys. Rev. Lett.* **111**, 053004 (2013).
- ²⁶H. Wang, S. I. Bokarev, S. G. Aziz, and O. Kühn, “Density matrix-based time-dependent configuration interaction approach to ultrafast spin-flip dynamics,” *Mol. Phys.* **115**, 1898–1907 (2017).
- ²⁷G. Li Manni, I. Fdez. Galván, A. Alavi, F. Aleotti, F. Aquilante, J. Autschbach, D. Avagliano, A. Baiardi, J. J. Bao, S. Battaglia, L. Birnoschi, A. Blanco-González, S. I. Bokarev, R. Broer, R. Cacciari, P. B. Calio, R. K. Carlson, R. Carvalho Couto, L. Cerdán, L. F. Chibotaru, N. F. Chilton, J. R. Church, I. Conti, S. Coriani, J. Cuéllar-Zuquin, R. E. Daoud, N. Dattani, P. Decleva, C. De Graaf, M. G. Delcey, L. De Vico, W. Dobrautz, S. S. Dong, R. Feng, N. Ferré, M. Filatov (Gulak), L. Gagliardi, M. Garavelli, L. González, Y. Guan, M. Guo, M. R. Hennefarth, M. R. Hermes, C. E. Hoyer, M. Huix-Rotllant, V. K. Jaiswal, A. Kaiser, D. S. Kaliakin, M. Khamesian, D. S. King, V. Kochetov, M. Krośnicki, A. A. Kumaar, E. D. Larsson, S. Lehtola, M.-B. Lepetit, H. Lischka, P. López Ríos, M. Lundberg, D. Ma, S. Mai, P. Marquetand, I. C. D. Merritt, F. Montorsi, M. Mörchen, A. Nenov, V. H. A. Nguyen, Y. Nishimoto, M. S. Oakley, M. Olivucci, M. Oppel, D. Padula, R. Pandharkar, Q. M. Phung, F. Plasser, G. Raggi, E. Rebolini, M. Reiher, I. Rivalta, D. Roca-Sanjuán, T. Romig, A. A. Safari, A. Sánchez-Mansilla, A. M. Sand, I. Schapiro, T. R. Scott, J. Segarra-Martí, F. Segatta, D.-C. Sergentu, P. Sharma, R. Shepard, Y. Shu, J. K. Staab, T. P. Straatsma, L. K. Sørensen, B. N. C. Tenorio, D. G. Truhlar, L. Ungur, M. Vacher, V. Varyazov, T. A. Voš, O. Weser, D. Wu, X. Yang, D. Yarkony, C. Zhou, J. P. Zobel, and R. Lindh, “The OpenMolcas Web : A Community-Driven Approach to Advancing Computational Chemistry,” *J. Chem. Theory Comput.* (2023), 10.1021/acs.jctc.3c00182.
- ²⁸A. R. Edmonds, *Angular Momentum in Quantum Mechanics* (Princeton University Press, Princeton, 1957).
- ²⁹Y. Morino and H. Uehara, “Vibronic Interactions in Vanadium Tetrachloride by Gas Electron Diffraction,” *J. Chem. Phys.* **45**, 4543–4550 (1966).
- ³⁰M. J. Frisch, G. W. Trucks, H. B. Schlegel, G. E. Scuseria, M. A. Robb, J. R. Cheeseman, G. Scalmani, V. Barone, G. A. Petersson, H. Nakatsuji, X. Li, M. Caricato, A. V. Marenich, J. Bloino, B. G. Janesko, R. Gomperts, B. Mennucci, H. P. Hratchian, J. V. Ortiz, A. F. Izmaylov, J. L. Sonnenberg, Williams, F. Ding, F. Lipparini, F. Egidi, J. Goings, B. Peng, A. Petrone, T. Henderson, D. Ranasinghe, V. G. Zakrzewski, J. Gao, N. Rega, G. Zheng, W. Liang, M. Hada, M. Ehara, K. Toyota, R. Fukuda, J. Hasegawa, M. Ishida, T. Nakajima, Y. Honda, O. Kitao, H. Nakai, T. Vreven, K. Throssell, J. A. Montgomery Jr., J. E. Peralta, F. Ogliaro, M. J. Bearpark, J. J. Heyd, E. N. Brothers, K. N. Kudin, V. N. Staroverov, T. A. Keith, R. Kobayashi, J. Normand, K. Raghavachari, A. P. Rendell, J. C. Burant, S. S. Iyengar, J. Tomasi, M. Cossi, J. M. Millam, M. Klene, C. Adamo, R. Cammi, J. W. Ochterski, R. L. Martin, K. Morokuma, O. Farkas, J. B. Foresman, and D. J. Fox, “Gaussian 16 Rev. C.01,” (2016).
- ³¹M. Douglas and N. M. Kroll, “Quantum electrodynamical corrections to the fine structure of helium,” *Ann. Phys.* **82**, 89–155 (1974).
- ³²S. I. Bokarev and O. Kühn, “Theoretical X-ray spectroscopy of transition metal compounds,” *WIREs Comput. Mol. Sci.* **10**, e1433 (2020).
- ³³B. Schimmelpfennig, “AMFI, An Atomic Mean-Field Spin-Orbit Integral Program,” (1996).
- ³⁴P. Decleva, G. Fronmni, A. Lisini, and M. Stmer, “Molecular orbital description of core excitation spectra in trnsidon metal compnds. An ab initio CI calculation on TiQ and isoelectronic molecules,” *Chem. Phys.* (1994).
- ³⁵M. Stener, G. Fronzoni, and M. De Simone, “Time dependent density functional theory of core electrons excitations,” *Chem. Phys. Lett.* **373**, 115–123 (2003).
- ³⁶S. J. Ashby, G. J. Bowden, and M. J. Prandolini, “Irreducible half-integer rank unit spherical tensors,” *J. Math. Chem.* **15**, 367–387 (1994).

V PUBLICATIONS NOT INCLUDED IN THE THESIS

J. Phys.: Condens. Matter, 2021, 33 (10), 105901

Powder diffraction computed tomography: a combined synchrotron and neutron study

V. KOCHETOV, M.J. MÜHLBAUER, A. SCHÖKEL, T. FISCHER, T. MÜLLER, M. HOFMANN, P. STARON, U. LIENERT, W. PETRY, A. SENYSHYN

Energy Storage Mater., 2021, 41, 546-553

Lithium distribution and transfer in high-power 18650-type Li-ion cells at multiple length scales

D. PETZ, M.J. MÜHLBAUER, V. BARAN, A. SCHÖKEL, V. KOCHETOV, M. HOFMANN, V. DYADKIN, P. STARON, G. VAUGHAN, U. LIENERT, P. MÜLLER-BUSCHBAUM, A. SENYSHYN

Phys. Chem. Chem. Phys., 2022, 24, 15540-15555

Probing the molecular structure of aqueous triiodide via X-ray photoelectron spectroscopy and correlated electron phenomena

MD.S. AHSAN, V. KOCHETOV, D. HEIN, S.I. BOKAREV, AND I. WILKINSON

J. Chem. Theory Comput., 2023

The OpenMolcas Web: A Community-Driven Approach to Advancing Computational Chemistry

G. LIMANNI, I. FDEZ. GALVÁN, A. ALAVI, F. ALEOTTI, F. AQUILANTE, J. AUTSCHBACH, D. AVAGLIANO, A. BAIARDI, J.J. BAO, S. BATTAGLIA, L. BIRNOSCHI, A. BLANCO-GONZÁLEZ, S.I. BOKAREV, R. BROER, R. CACCIARI, P.B. CALIO, R.K. CARLSON, R. CARVALHO COUTO, L. CERDÁN, L.F. CHIBOTARU, N.F. CHILTON, J.R. CHURCH, I. CONTI, S. CORIANI, J. CUÉLLAR-ZUQUIN, R.E. DAUD, N. DATTANI, P. DECLEVA, C. DE GRAAF, M.G. DELCEY, L. DE VICO, W. DOBRAUTZ, S.S.DONG, R. FENG, N. FERRÉ, M. FILATOV(GULAK), L. GAGLIARDI, M. GARAVELLI, L. GONZÁLEZ, Y. GUAN, M. GUO, M.R. HENNEFARTH, M.R. HERMES, C.E. HOYER, M. HUIX-ROTLANT, V.K. JAISWAL, A. KAISER, D.S. KALIAKIN, M. KHAMESIAN, D.S. KING, V. KOCHETOV, M. KROŚNICKI, A.A. KUMAAR, E.D. LARSSON, S. LEHTOLA, M.-B. LEPETIT, H. LISCHKA, P. LÓPEZ RÍOS, M. LUNDBERG, D. MA, S. MAI, P. MARQUETAND, I.C.D. MERRITT, F. MONTORSI, M. MÖRCHEN, A. NENOV, V.H.A. NGUYEN, Y. NISHIMOTO, M.S. OAKLEY, M. OLIVUCCI, M. OPPEL, D. PADULA, R. PANDHARKAR, Q.M. PHUNG, F. PLASSER, G. RAGGI, E. REBOLINI, M. REIHER, I. RIVALTA, D. ROCA-SANJUÁN, T. ROMIG, A.A. SAFARI, A. SÁNCHEZ-MANSILLA, A.M. SAND, I. SCHAPIRO, T.R. SCOTT, J. SEGARRA-MARTÍ, F. SEGATTA, D.-C. SERGENTU, P. SHARMA, R. SHEPARD, Y. SHU, J.K. STAAB, T.P. STRAATSMA, L.K. SØRENSEN, B.N.C. TENORIO, D.G. TRUHLAR, L. UNGUR, M. VACHER, V. VERYAZOV, T.A. VOSS, O. WESER, D. WU, X. YANG, D. YARKONY, C. ZHOU, J.P. ZOBEL, AND R. LINDH

Molecules, 2023 (submitted)

Valence and core photoelectron spectra of aqueous I_3^- from multi-reference quantum chemistry

V. KOCHETOV, MD.S. AHSAN, D. HEIN, I. WILKINSON, AND S.I. BOKAREV

Acknowledgments

First of all, I would like to express my gratitude to Prof. Sergey I. Bokarev for his excellent instructions and cordiality when introducing me to the field. His help, enthusiasm, scientific intuition, and brilliant ideas have become essential pillars of this work.

I am thankful to Huihui Wang, who laid the foundations of the topic and passed on invaluable knowledge to me, making this work possible. Also, I am deeply indebted to another coauthor Thies Romig, a brilliant-mind student who made a significant contribution to the development of our work.

I am grateful to Prof. Oliver Kühn for providing me with the opportunity to conduct this research at the Molecular Quantum Dynamics group of Rostock University. I greatly appreciate his support and the friendly atmosphere he has established within the group throughout these years.

Special thanks are extended to all the Molecular Quantum Dynamics Group, including Gilbert Grell, Tobias Marx, and Andy Kaiser, for fruitful discussions, their valuable pieces of advice, and both technical and moral support, which have significantly contributed to the development of this work.

I would also like to acknowledge the financial support of the Deutsche Forschungsgemeinschaft (DFG) (Grant No. BO 4915/1-1).

Lastly, I am deeply grateful to my parents, my whole family, and A. Kylchik for their unwavering support and presence throughout both the positive and challenging times.

Eidesstattliche Versicherung

Ich versichere eidesstattlich durch eigenhändige Unterschrift, dass ich die Arbeit selbstständig und ohne Benutzung anderer als der angegebenen Hilfsmittel angefertigt habe. Alle Stellen, die wörtlich oder sinngemäß aus Veröffentlichungen entnommen sind, habe ich als solche kenntlich gemacht. Die Arbeit ist noch nicht veröffentlicht und ist in gleicher oder ähnlicher Weise noch nicht als Studienleistung zur Anerkennung oder Bewertung vorgelegt worden. Ich weiß, dass bei Abgabe einer falschen Versicherung die Prüfung als nicht bestanden zu gelten hat.

Rostock, 19/06/2023

Vladislav Kochetov